Experimental Verification of the Fire Dynamics Simulator (FDS) Hydrodynamic Model

---

A thesis submitted in partial fulfilment of the
requirements for the degree
of
Doctor of Philosophy in Fire Engineering
at the
University of Canterbury,
Christchurch, New Zealand.

by

Jason Mark Clement

October, 2000

ABSTRACT

The objective of this research has been to verify the hydrodynamic model that is contained within the Fire Dynamics Simulator (FDS). In the first part of the research, a series of buoyant salt water experiments have been conducted, with the purpose of generating experimental data for comparison with computational fluid dynamics (CFD) models. Two types of buoyant flows have been generated in the experiments; a natural transitional flow, and flows that resemble fire induced smoke flow within a residential building. Laser Induced dye Fluorescence (LIF) has been used to measure the fluid density in a single vertical plane of the flow. Measurements have also been made of eddy frequencies on the perimeter of the transitional flows, and of the temporal development of the fire similar flow fields. The uncertainty of the experimental measurements has been quantified. In the second part of the research, the salt water experiments have been simulated with the FDS, to assess the accuracy of the hydrodynamic model. The simulations of the transitional flows are found to be highly dependent upon the resolution of the computational grid. The findings highlight the fact that the numerical methods employed in the FDS can generate fluid behaviour in the computational flow field that does not occur in the real salt water flows. This "numerical fluid behaviour" is clearly seen in the transitional flow computations, because at the source of the flow, the buoyancy and the momentum of the fluid are orientated in perpendicular directions to each other. The comparison of the computational and experimental results for the transitional flows show that the trajectory of the computed buoyant plume is steeper than the trajectory of the real salt water plume. It is speculated that the disagreement in the plume trajectory may be due to the spatial distribution of pressure within the computational domain. Due to limited computational facilities, this research has been unable to determine if the FDS hydrodynamic model can accurately compute the natural transition to turbulence. Further simulations of the transitional flows are required with grid cell dimensions that are less than the compartment height divided by 100, to determine if the transition can be correctly computed. The simulations of the fire similar flows have shown, that the FDS performs well in modelling fully turbulent flow fields, as found in residential building fires. From the fire similar flow simulations a maximum grid cell dimension, of the compartment height divided by 50, has been recommended for the simulation fire induced smoke flows within multicompartment residential scale buildings. At this recommended resolution, and resolutions coarser than this, the Smagorinsky sub-grid scale (SGS) has been found to give more accurate results than the constant viscosity SGS model. A relationship has been determined, for the minimum fluid viscosity that is required for stable computations, in simulations that use the constant viscosity SGS model.

ACKNOWLEDGEMENTS

First, and foremost, I would like to thank the NZ Foundation for Research, Science and Technology for the funding that they provided for this research. I am in no doubt that the fire research undertaken at the University of Canterbury is improving fire safety within New Zealand, and that the money provided for this research program is well invested.

Similarly, I would like to thank the New Zealand Fire Service Commission for their financial support for the Fire Engineering program at the University of Canterbury. Without their support, the program may never have got off the ground, and I may never have been introduced to the field of Fire Safety Engineering. I hope that the financial and moral support for the program will continue as evidence of the NZ Fire Service proactive approach to fire safety. I would also like to thank the J.R. Templin Travelling Scholarship committee, for providing me with the opportunity to spend six months conducting research at the National Institute of Standards and Technology, in Maryland, USA. Without that period of study, I could never have conducted this research.

To my supervisor and good friend Dr Charlie Fleischmann, thanks very much. I greatly appreciate your patience and your willingness to listen when I was finding progress difficult. Your enthusiasm for fire engineering played a large part in attracting me to the subject. Your string of stories on "the process of natural selection" continues to stagger me and to amuse me. However, in practicing what I've learnt, I will endeavour to minimise the growth rate of your story list.

I would also like to express my appreciation for the patience and open door policy of Professor David Wilkinson (1944-1998), and Emeritus Professor Ian Wood. Both of who showed extreme patience in helping me to understand the relatively simple fluid dynamics that was involved in this research. Both have been an inspiration during the times when the going got hard.

To Dr Andy Buchanan, thanks very much for all your effort in establishing the Fire program at the University, and for the perspective and enthusiasm that you continually bring to the course and the students. Your directions and advice always seemed to hit the spot when I couldn't see the exit for the smoke. To the Fluids Laboratory technicians, Ian Sheppard and Alan Pointer, and to the electronics boys, Mike Weavers and Richard Newton, thanks for all the support during my experimental work. Thanks also to the staff from the Engineering Library, particularly Pat Roddick – best wishes for your retirement Pat.

During my six month study term at NIST in Maryland, I was lucky enough to be placed under the guidance of Dr Kevin McGrattan. Since that time, I have consistently pestered Kevin with queries regarding the Fire Dynamics Simulator. Therefore, to Kevin, I would like to express my immense

thanks for your tolerance, enthusiasm and hospitality; I really enjoyed my stay in Gaithersburg, and I hope that this research helps you out. To Laura, Brian and Suz, thanks also for the great hospitality while I was in Gaithersburg, I hope that someday I can return the favour when you head down-under.

To my good friend Tim Shea, thanks buddy for introducing me to Mr Sam Adams, and for the ensuing good laughs that we had during my stay in the US - stay in touch.

To Mike Spearpoint, thanks for reviewing the draft. I know it's not really a topic that you would look for in a bookstore. Your efforts are really appreciated.

I have always believed that people make a place, and during my time at the University of Canterbury I have been lucky enough to go through the Fire Engineering program surrounded by good people. Thanks very much to all those friends; Tony Enright, Ee Yii, Rob Presland and Tony Parkes, to name but a few. Of particular importance, however I would like to thank Alastair Chambers, Graeme Stark, Erica Dalziell and Nick D'Adamo for all the good times, for all the good laughs, and for providing me with all the explanations and excuses that I needed to justify them.

To my family, Mum, Dad, Jeremy and Justin, thanks very much. Your support and patience was fantastic, I couldn't have done it without you. Cheers for the down to earth backing and the ever-present reality checks.

Finally, to my partner Sheelagh, thanks very much for your constant love and support. Looking ahead things look fantastic from here, and you're the primary reason for that.

It's all over.....another door opens.

During the final couple of months of writing up my thesis, I continually found comfort in two quotes.

"The most important thing in the Olympic Games
is not to win but to take part.
Just as the most important thing in life
is not the triumph but the struggle."

- Baron Pierre de Coubertin,
  (The founder of the modern Olympics)
  Printed in the Christchurch Press, Sept 2000

"They don't just give em away"

- Nick D'Adamo
  (Oceanographer and struggling Philosopher)

TABLE OF CONTENTS

Chapter 4 - Uncertainty Analysis

Chapter 5 - Experimental Results

Chapter 6 - Discussion

Chapter 7 - Simulation of Transitional Flows

Chapter 8 - Simulation of Fire Similar Buoyant Flows

Chapter 9 - Conclusions and Future Research

Appendices

NOMENCLATURE

Symbol	Defined
b	Radius where the mean velocity equals the mean centreline velocity divided by the exponential (u/e)
c	Count of clock pulses in the PAAR Density Meter apparatus
c_p	Specific heat of gas
C	Concentration of agent in solution
C_{Drift}	Correction term for the drift in the stability of the LIF apparatus
d	Diameter
D_C	Plume structure (characteristic) length scale
D_{Decay}	Decay Gradient for the drift in the stability of the LIF apparatus
D_s	Diffusion coefficient for salt mass in freshwater
F	Fluorescence emitted by solution
Fr	Densimetric Froude Number
g	Acceleration of gravity = 9.81 m/s^2
g'	Effective gravity $g' = \frac{\Delta\rho}{\rho} g$
G	Grey scale value of pixel (after it has been translated via the Input Look-Up Table (ILUT) in the Global Lab software).
h	Depth of the fluid layer
H	Height of the compartment
l	Characteristic Dimension of the Computational Grid $l = \left(l_x \times l_y \times l_z\right)^{\frac{1}{3}}$
l_x	Dimension of the grid cell in the x-direction
l_y	Dimension of the grid cell in the y-direction
l_z	Dimension of the grid cell in the z-direction
l_M	Morton length scale for buoyant jets
$\dot{m}$	Mass flow

$\dot{m}_{Salt}$	Mass flow of salt in the solution
M_o	Momentum flux at the source
n	Number of measurements
n_{cells}	Number of grid cells in the computational domain
P_{Atm}	Atmospheric Pressure
Pr	Prandtl number
$q_{\Delta\rho}$	Buoyancy flux at the source
Q	Heat release rate of the fire
R	Grey scale value of pixel (before it has been translated via the Input Look-Up Table (ILUT) in the Global Lab software).
Re	Reynolds number
r	Radius
s	Speed of fluid
s_ρ	Buoyant speed of fluid
Sc	Schmidt number
S_{ij}	Local strain rate in the fluid
$\lvert S_{ij} \rvert$	Magnitude of the deformation tensor
t	Time
$t_{Duration}$	Duration of the computations
t_e	Time it takes for an eddy to move past a fixed point
t_{sim}	Time interval to be simulated with the FDS (i.e., TWFIN in FDS notation)
Δt_{avg}	Duration of time-averaging
Δt_{comp}	Duration of a computational time step
Δt_{Delay}	The time interval between the capture of the calibration image, and the capture of the flow images during each experiment
T	Temperature
u	x-component of the velocity vector
U	Velocity scale
v	y-component of the velocity vector
V	Volume

$\dot{V}$	Volumetric flow rate
w	z-component of the velocity vector
W_{door}	Width of opening
x	Length coordinate
y	Width/Depth coordinate
z	Vertical coordinate
β	Density difference ratio $\beta = \frac{\rho_s - \rho_\infty}{\rho_s}$
δ	Absolute error in the measurement
σ	Standard deviation of the measurement
μ	Dynamic viscosity
ν	Kinematic viscosity
ν_T	Eddy viscosity (or turbulent viscosity)
ρ	Density
ρ_{water}	Density of distilled water sample (taken from tabulated values)
ρ_z	Density on the centreline of the plume, at height z
$\Delta\rho$	Density difference
τ_{ij}	Viscous stress tensor

Constants

C_{Smag}	= 0.14	Constant for Smagorinsky SGS model
K_{pb}	= 0.105	Plume constant for growth in width
$K_{p\Delta}$	= 11.1	Plume constant for decay of centreline buoyancy
λ	= 1.067	Plume constant for Gaussian distribution of buoyancy across width

General Superscripts

*	Nondimensionalised

General Subscripts

B-Cal	From an image of the background light intensities for calibration
B-Flow	From an image of the background light intensities for the experiment
Cal	From an image of the fluorescence calibration solution
Calibration	Property of the calibration solution
Flow	From an image of the experimental flows
o	Conditions at the source
r	Radius
s	Saline
∞	Ambient condition
(x,y,z)	Property at a point

Acronyms

CFD	Computational Fluid Dynamics
FDS	Fire Dynamics Simulator
FFT	Fast Fourier Transform
ILUT	Input Look Up Table - (A feature of the Global Lab Software used in experiments)
KBAR	Number of cells in the vertical extent of the computational domain - (A variable in the FDS input file)
LES	Large Eddy Simulation
LIF	Laser Induced dye Fluorescence
RANS	Reynolds Averaged Numerical Simulation
SGS	Sub-Grid Scale
VBC	Velocity Boundary Condition - (a variable in the FDS input file)

Chapter 1 - INTRODUCTION

1.1 *Impetus for the Research*

Within the field of fire safety engineering, computer models are often used to model the spread of smoke from a fire within a building. Given the location and characteristics of the fire, the computer models predict how the toxic smoke and heat will spread throughout the buildings internal geometry. Thus, a fire engineer can model the likely development and impact of fire scenarios, provided that they know the layout and the probable contents of a building. The predictions of the fire model can then be used to assess the threat that likely fire scenarios pose to the building occupants. This is generally done by comparing the time that it takes occupants to leave areas of the building, with the time it takes for a fire scenario to create untenable conditions in those areas. The egress of occupants can also be modelled using other computer programs (generally referred to as building evacuation models). In modelling evacuations, it is common to assume that the occupant egress behaviour is triggered by the activation of a fire detection device, such as a smoke detector or a sprinkler. The fire models, which predict the movement and properties of the smoke, are also often used to estimate this detection time (for a detector in the fire room). Thus, fire models often form an integral part of a fire engineer's life safety evaluation of a building (in terms of the threat that fire poses to the occupants).

Generally speaking there are two types of deterministic fire models, zone models, and field models. Historically, the zone model has been the fire model most commonly used by fire engineers. Its popularity has been due to its relative simplicity, and its ability to provide estimates of the general fire conditions quickly. However, at the present point in time, fire modelling is going through a stage of rapid development. The increasing availability of computational power is making field modelling a progressively more feasible option to use in fire research and consultancy. At the forefront of recent fire model development is the Fire Dynamics Simulator (FDS)[1], which was officially released on the Internet in February 2000 (http://fire.nist.gov/fds). The FDS is a field model that uses the Large Eddy Simulation (LES) technique to model the fire-generated conditions within a building. The recent release of the model, coupled with the promising results that have been seen in LES fire research to date[2], has created a demand for knowledge of the FDS. Of particular interest to potential users and fire safety design authorities is the accuracy of the computational results.

At the University of Canterbury, the Fire Engineering program has received funding to conduct research that will assist in reducing fire deaths within New Zealand residential buildings[3]. As part of this residential fire safety research program, the FDS is to be used to evaluate the life safety of likely fire scenarios within typical New Zealand residential dwellings. Specifically, the computational model is to be used to investigate the potential of smoke detectors to save lives. To

undertake this research program with the FDS, preliminary research is required into two areas. Firstly, how accurately the computational model simulates smoke movement in the early stages of a residential building fire, and secondly, how the activation of a smoke detector can be accurately modelled with the FDS. The research detailed within this document has therefore been conducted as the first step toward achieving this residential fire safety objective. That is, this research studies the accuracy of the FDS predictions, and determines some of the computational settings that are required to accurately capture the fluid dynamics of the smoke flow. Future research at the University of Canterbury will attempt to develop a smoke detection algorithm that can be used with the FDS. Thus, the primary impetus for this research has come from a need to know how accurately the FDS can model the early stages of smoke movement in residential building fires. A secondary impetus comes from the demand of the wider fire engineering community, for knowledge on the accuracy of the FDS fire model.

1.2 *Aim of the Research*

Accurately modelling fire induced smoke flow is a complex task. As smoke moves through the internal structure of a building, the hot gases lose thermal energy to the surrounding environment via conduction, convection and radiation. It is also possible that smoke may contain pockets of unburnt flammable gases, which can combust and release thermal energy into the flow if air is mixed into the smoke in the right proportions. Accurately accounting for these thermal energy transfer processes in a smoke flow model is important, because the amount of energy that is contained in the flow affects how the smoke moves. To complicate matters however, the amount of thermal energy that is gained via combustion, or lost via conduction, convection and radiation, is dependent on the localised fluid movement. Thus, within fire induced smoke flows, the heat transfer, combustion, and fluid movement, are all highly dependent upon one another. For example, consider convective heat loss; the amount of thermal energy that is transferred from hot smoke to a cool solid object submerged in the smoke, is highly dependent on the velocity of the gases around the object. Thus, the heat transfer is dependent on the fluid movement. Similarly, considering the process of combustion as another example, unburnt fuel within the smoke flow will only combust and release energy, if oxygen rich air is mixed into the smoke in the correct proportions. It is the fluid movement that governs the mixing of the gases. Thus, correctly simulating fire induced smoke flow, involves accurately modelling a number of complex coupled processes.

The complex interaction of heat loss, combustion and fluid movement in a smoke flow model means that it is extremely difficult to identify the source of inaccuracies in fire modelling. It is difficult to know whether the performance of the combustion model, the convective heat loss model, the conduction model, the radiation model, or the fluid movement model is responsible for any inaccuracies. Most likely it is a combination of the performance of all these sub-models; however, without an ability to correctly proportion the error between them, it is difficult to know where to focus

improvement efforts. Thus to determine the overall accuracy of a computational smoke flow model, it is desirable to assess the performance of each sub-model independently.

The hydrodynamic model is a fundamental component of a field model. It is that part of the code that approximates the motion, and the properties of the fluid, from the physical forces that are present in the system. That is, it is the sub-model that predicts the fluid movement. In the progressive assessment of the FDS accuracy, determining the performance of this fundamental component is the most logical place to start.

The aim of this research is to assess the accuracy of the hydrodynamic model that is contained within the FDS. As part of the research, the dependence of the hydrodynamic model accuracy on computational settings, such as grid resolution, boundary conditions, and sub-grid scale model, will be investigated. One important outcome of the study is a series of recommendations, on which settings should be employed in the FDS, to achieve the most accurate modelling of smoke flow in residential building fires.

1.3 *Method of Investigation*

To assess the accuracy of the FDS hydrodynamic model, the computational results can be compared to an analytical solution or to experimental measurements. It is beyond our current capabilities to determine a complete analytical solution for turbulent fire induced smoke flow. Therefore, we are forced, in fire research, to simulate a series of fire experiments with a computational model, and then to compare the computational results to the experimental measurements. It is this experimental verification method (rather than an analytical method) that is used in this research to measure the accuracy of the FDS computations.

To independently assess the accuracy of the FDS hydrodynamic model, it is necessary to eliminate the use of other sub-models in the computations. For the FDS, this requires eliminating the use of the sub-models that account for heat transfer and combustion. Therefore, it is ineffective to simulate fire experiments, where these processes affect the real thermal gas flow. To conduct simulations that will only employ the hydrodynamic model, the flow must be buoyant, inert and must retain all the buoyancy that is released at the source (that is, not lose any of the buoyancy agent to the bounding surfaces of the flow – as occurs with heat loss in fire induced convective flows). The buoyant flow of salt water in a quiescent fresh water environment satisfies these conditions. Indeed in previous fire research[4][5][6][7], buoyant salt water flows have been studied, as a means of investigating the movement of fire induced smoke flow through complex geometry enclosures. Therefore, in this research, a series of salt water experiments have been conducted. The experiments are then simulated with the FDS, and the comparison of the experimental measurements with the computational results is used to assess the accuracy of the FDS hydrodynamic model.

1.4 *Scope and Nature of the Research*

The salt water experimental data has been collected using the Laser Induced dye Fluorescence (LIF) flow visualisation technique. In the experiments, the LIF technique uses a sheet of laser light to illuminate a two-dimensional plane of the saline flow. The density of the fluid, within the vertical plane, is measured from the fluorescence emitted by a tracer dye in the saline solution. Thus, the LIF technique provides an unobtrusive means of collecting fluid density measurements from a vertical plane in the flow. The fact that the experimental data comes from a single vertical plane makes the experiments an ideal case study for computational modelling, particularly where the domain is described according to a rectilinear coordinate system; as the FDS domain is. In all, sixteen different salt water experiments are conducted. Additionally, three of the sixteen experiments are each repeated multiple times, to demonstrate the repeatability of the experimental results. The uncertainty of the experimental measurements is quantified.

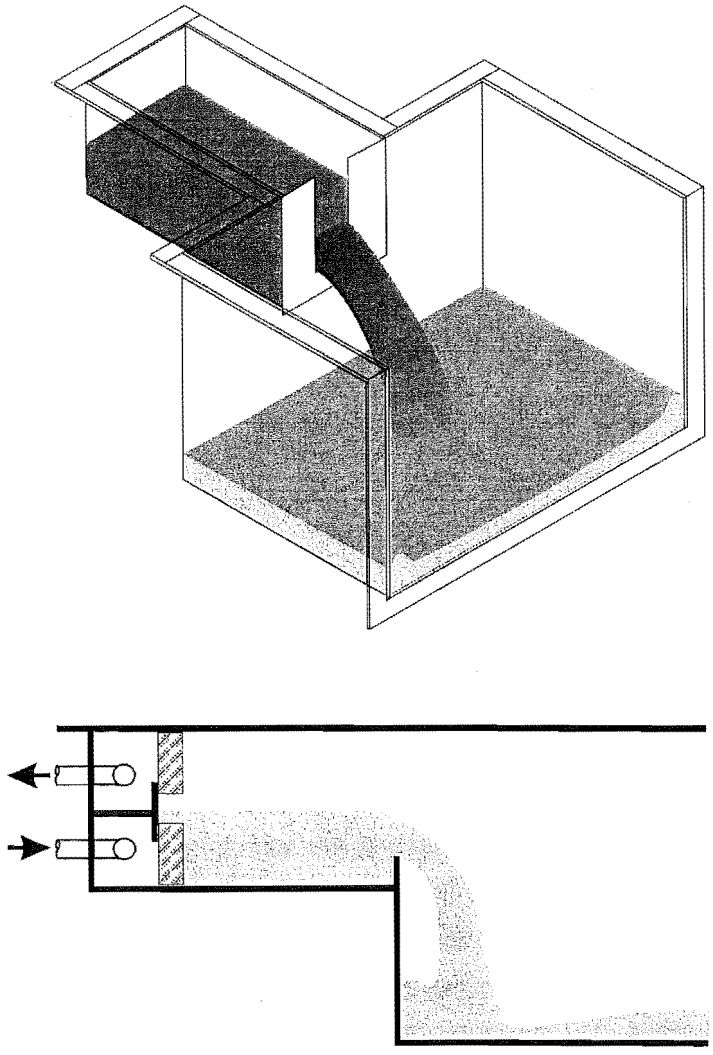

Figure 1-1 ***Illustration of the transitional flows that were generated in the first section of the salt water experimental program. The spilling plume contained a natural transition from laminar to turbulent behaviour.***

The salt water experimental program is split into two different sections; transitional flows, and fire similar flows. In the first section of the experimental program, a buoyant saline flow is generated that contains a transition from laminar to turbulent fluid behaviour. In these experiments, density measurements are taken across a saline plume that spills horizontally from a rectangular opening, and plunges down onto a flat solid surface. The spilling plume undergoes a natural transition from laminar to completely turbulent fluid behaviour. Time averaged density measurements are taken across the flow at different locations to capture the entire transition. The frequency of large-scale eddy structures on the underside and upper surface of the spilling plume are also measured. Natural transitional flows are exceptionally challenging to resolve accurately with computational methods. Thus, the objective of simulating these experiments, with the FDS, is to expose weaknesses in the hydrodynamic model. Figure 1-1 shows a sketch of the model that was used in the transitional flow experiments, and a schematic illustration of the saline flow that was seen in the centreline plane of the model (which was illuminated by the laser sheet).

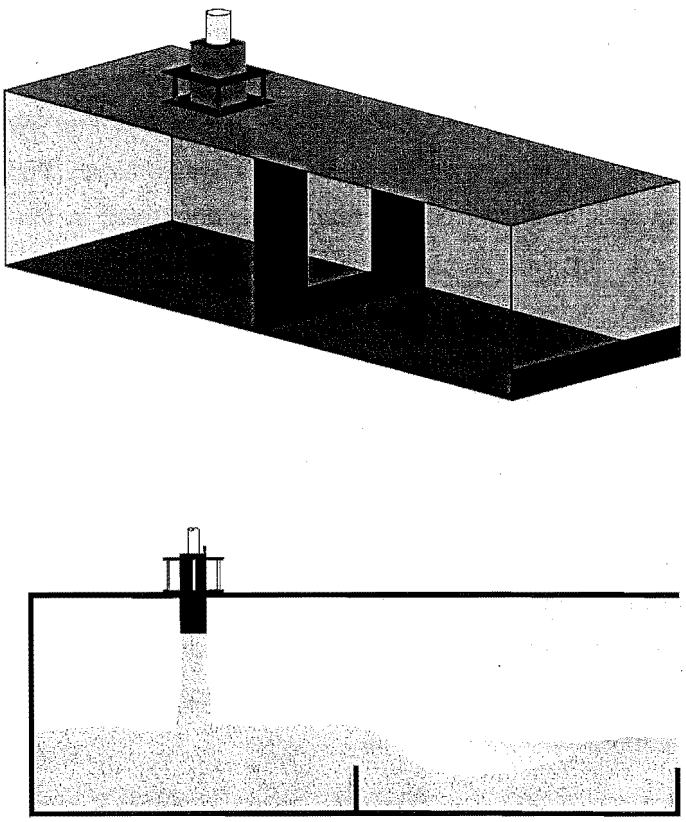

Figure 1-2 ***Illustration of the two room model in which fire similar buoyant flows were generated in the second section of the salt water experimental program. The illustration shows the testing orientation, which is upside down from a real fire situation.***

In the second section of the experimental program, saline flows are generated that resemble the buoyant flow fields found in the early stages of residential building fires. In these experiments a

salt water plume is injected into a two room model, where a simple rectangular opening connects the rooms. The temporal development of the flow field is detailed, and density measurements are taken of the steady state flows in both compartments. The geometry of the opening between the compartments is varied, as is the buoyancy of the source plume. The simulation of these experiments is designed to measure the accuracy of the hydrodynamic model, when the FDS is applied to modelling residential building fires. The results of these simulations (fire similar flows) will be used in future FDS research at the University of Canterbury, to evaluate the potential of smoke detectors to save lives in residential building fires. The results of these simulations are also of interest to the wider fire engineering community, who require knowledge of the accuracy of the FDS. Figure 1-2 shows a sketch of the model that was used in the fire similar flow experiments, and a schematic illustration of the saline flow that was seen in the centreline plane of the model (which was illuminated by the laser sheet).

Since the accuracy of the FDS hydrodynamic model has been assessed through simulating salt water flows, the results of this research are limited to the simulation of Boussinesq flows; that is, buoyant flows where there is a small density difference. Further work is therefore required, to assess the accuracy of the hydrodynamic model in simulations that involve the large density differences found in the near field region of fire induced smoke flows. Further verification work is also required on the heat loss and energy release models used in the FDS, to quantify their accuracy.

1.5 *Outline of Research*

The research detailed in this document can essentially be divided into two parts; firstly, the description of the salt water experiments, and secondly, the simulation of those experiments with the FDS. The documentation of the research has followed this basic structure. The first part of this document details the salt water experiments; that is, the experimental methodology, the uncertainty of the measurements and interpretation of the experimental data. The second part of the document details how the simulations were conducted, and how well the computational results compare with the experimental measurements.

Chapter 2 provides background information on the FDS. The Large Eddy Simulation (LES) technique is described, via a physical interpretation, and the role, and differences of the sub-grid scale models that were used in this research are discussed. The rigorous mathematical derivations that show the internal mechanics of the LES technique and the FDS have been well documented in the past, so that they are not represented in this material. Instead the historical development of the model is highlighted, and the validation work that has been conducted to date is summarised. The chapter is concluded with a brief description of how the FDS was applied to the simulation of salt water flows, and what the computational demands of the simulations were.

Chapter 3 details the method and materials that were used in the salt water experiments. A brief overview is provided of the LIF technique and the apparatus that is used in the experiments. The specific configuration of the equipment and the specification of the measurement devices that are used in each experiment are documented. The geometry and dimensions of the models are given, and finally the conditions at the flow source for each experiment are tabulated.

Chapter 4 details an uncertainty analysis that is conducted on the experimental measurement techniques, to quantify the uncertainty of the experimental data. Particular focus is applied to the uncertainty of the measurement location within the flow field, and to the uncertainty of the density difference that is determined from the LIF analysis. Recommendations are made on how the uncertainty of LIF measurements can be reduced, in future research conducted with the same laboratory equipment.

Chapter 5 summarises the salt water experimental results. Density difference profiles are presented, along with dilution contour maps, eddy frequencies and time intervals that describe the development of the steady state flow field. The repeatability of the density difference profiles from each experimental series is demonstrated. To keep the chapter concise, the density difference profiles from only one experiment in each experimental series is presented; the balance of the experimental results are presented in Appendix 3.

Chapter 6 provides a discussion of the experimental measurements. Observations of the flow are documented, and where appropriate, comparisons are made between the experimental measurements and established buoyant jet theory. The time averaged normalised density difference curves are interpreted, to highlight the fluid dynamic features that they show. The chapter is concluded with a discussion on the value of the experimental data for the purpose of CFD modelling.

Chapter 7 details the simulation of the transitional flows, and the comparison of the salt water measurements with the computational results. A large amount of time is spent in this chapter resolving the impact of the assumptions and parameter settings, which were used in the final transitional flow simulations. The findings in this Chapter, highlight the fact that the numerical methods employed in the FDS can generate fluid behaviour in the computational flow field that does not occur in the real salt water flows. This "numerical fluid behaviour" is clearly seen in the transitional flow computations, because at the source of the flow, the buoyancy and the momentum of the fluid are orientated in perpendicular directions to each other. The comparison of the computational and experimental results also show, that there is disagreement as to the trajectory of the spilling plume.

Chapter 8 details the simulation of the fire similar flows, and the comparison of the salt water measurements with the computational results. The chapter initially focuses on how accurately the

salt water source plume is simulated, and then, on how inaccuracies in the modelling of the plume affect computational flow field downstream (in the second compartment). The conclusions in this chapter recommend a sub-grid scale (SGS) model, and maximum grid cell dimension for the simulation of residential building fires. As with the transitional flow work, there is discussion of the disagreement between the computations and the experiments as to the trajectory of the plume.

Chapter 9 summarises the conclusions drawn from the research and suggests topics, and approaches, for future research that would assist in the progressive verification of the FDS as a tool for enhancing fire safety in buildings.

1.6 *References*

1. McGrattan, K.B. and Forney, G.P. (2000) 'Fire Dynamics Simulator – User's Manual' NISTIR 6469, National Institute of Standards and Technology, U.S. Department of Commerce, Gaithersburg, MD 20899.

2. Baum, H.R. (1999) Large Eddy Simulations of Fires – from Concepts to Computations, *Fire Protection Engineering*, Issue No 6, pp. 36-42.

3. Web Page, October 2000; Civil Engineering Department, University of Canterbury, Christchurch, New Zealand, see - Fire Engineering, Residential Fire Safety Research, http://www.civil.canterbury.ac.nz/fire1/rfsresearch.html.

4. Steckler, K.D., Baum, H.R. and Quintiere J.G. (1986) Salt Water Modelling of Fire Induced Flows in Multicompartment Enclosures, Proceedings of the 21st International Symposium on Combustions, The Combustion Institute, 1986, pp142-149.

5. Fleischmann C. M., Pagni P.J. and Williamson R.B. (1994) Salt Water Modelling of Fire Compartment Gravity Currents, *Proceedings of the Fourth International Symposium of Fire Safety Science*, pp 253-264.

6. Zukoski E. E. and Peterka D.L. (1979) Measurements of Entrainment in a Doorway Flow, California Institute of Technology, Pasadena, California.

7. Fleischmann, C.M. and McGrattan, K.B. (1999) Numerical and Experimental Gravity Currents related to Backdrafts, *Fire Safety Journal*, **33**, 21-34.

Chapter 2 - FIRE DYNAMICS SIMULATOR - BACKGROUND

2.1 Introduction

This chapter serves the purpose of providing background information on the Fire Dynamics Simulator. Section 2.2 provides a basic description of the Large Eddy Simulation technique that is used in the Fire Dynamics Simulator. This background information is necessary for the consideration of the simulation results presented later in Chapters 7 and 8. Section 2.3 reviews the historical development of the Fire Dynamics Simulator, and the previous validation work that has been conducted on the model. The chapter is concluded with Section 2.4, which details how the FDS was used to model the buoyant salt water experiments that are documented in Chapters 3 through 6.

2.2 Large Eddy Simulation – the Technique

2.2.1 Overview

Large Eddy Simulation (LES) is a branch of Computational Fluid Dynamics (CFD). It differs from other CFD approaches, in that LES explicitly calculates the large-scale turbulent flow structures from first principles. The small-scale turbulent motion not calculated directly from the governing equations has its influence on the resolved flow field modelled. The rational behind the LES approach is based upon the knowledge that, in turbulent flow, the large-scale structures are responsible for the majority of the momentum and energy transport. Explicitly determining the dynamics of these structures from first principles should accurately capture the processes that govern the distribution of mass, momentum and energy. Reinforcing this rational is the knowledge that large scale eddies interact strongly with the mean flow, and that the structure of these eddies is highly dependent on geometry. These properties make large scale eddies highly anisotropic, such that they should be resolved explicitly, in order to accurately capture flow dynamics. Small scale eddies on the other hand, are created by non-linear interactions of the large scale structures, and only have a slight influence on the mean flow properties. The structure of these small-scale motions is considered to be more universal, such that in the LES approach, the influence of motion on the small scale is modelled with generality.

The drawback of the LES approach is that it is computationally intensive. The high grid resolution that is required to resolve the instantaneous turbulent structures in the flow means that the LES approach requires powerful computers with large memory facilities. Generally speaking, as the computational grid is refined further and further, the results of the simulations converge to provide a more accurate approximation of the solution to the governing equations. In terms of the resolved flow, a finer grid resolution means more of the turbulence is resolved explicitly from first principles and less generality is applied in modelling the small-scale influence. In practical terms however,

computational hardware limitations and time constraints limit the degree of resolution that it is feasible to use in modelling. Thus in the LES approach, modelling the influence of the small-scale turbulent structures, rather than resolving them explicitly, is a practical consequence, more than it is a reasonable assumption.

There are primarily two other CFD approaches; Direct Numerical Simulation (DNS) and Reynolds Averaged Numerical Simulations (RANS). DNS could be considered as an extreme version of the LES approach, whereby the computational grid is fine enough that all the motion that occurs on a scale influencing the flow field is resolved from the governing equations. DNS employs no turbulence modelling. A consequence of this computationally intensive approach is that DNS investigations are presently restricted to modelling very small physical domains. In fire applications for example, the physical size of the area of interest is generally far too large to obtain a computational grid of sufficient resolution to conduct a DNS. RANS CFD packages[1][2][3][4] however, are quite commonly used in field modelling of fire phenomena. These packages solve what are referred to as the Reynolds Averaged equations, which are both spatially and temporally averaged. In these computations, the influence of all turbulent motion on the mean flow field is modelled. The main criticism levelled at the RANS approach targets the validity of the turbulence models employed to provide closure to the governing equation set. These turbulence models contain empirically determined parameters that can only be considered applicable for the specific flow cases where they have been validated. This narrows the range of validity for the RANS CFD approach.

2.2.2 *Segregation of Large-Scale and Small-Scale Motions*

In LES, the behaviour of those structures large enough to be resolved with the computational grid is calculated directly from the fundamental fluid mechanics contained in the governing equations. The flow structures that are too small to be resolved (referred to as sub-grid scale (SGS) motions), have their effect on the resolved fluid motion modelled. The LES technique therefore divides the treatment of turbulent structures into two different approaches, based upon their size. A spatial filtering operation is used to mathematically separate the large-scale resolvable motions from the SGS motions. The governing equations are spatially filtered so that the resulting equations define the large-scale field[5]. The filtering operation is based upon the characteristic dimension of the computational grid. Consideration of the turbulence energy spectrum indicates that there is a grid resolution at which the LES segregation of large scale and small-scale motions is a fair reflection of reality.

In high Reynolds number flows (that is, highly turbulent flows), there is an internal sub-range in the turbulent energy spectrum. Within this sub-range, there is essentially no turbulence production or viscous dissipation. The existence of this sub-range neatly divides turbulent structures into two distinct groups. The rational behind LES modelling means that it is desirable to locate the boundary that divides the large-scale structures from the small-scale structures within the internal

sub-range. This objective is achieved when the characteristic dimension of the spatial filtering operation l, has a corresponding wave number π/l that lies in the sub-range. Achieving this goal however, is not generally possible for two reasons. Firstly, at low Reynolds numbers, no sub-range exists in the turbulence spectrum, and secondly, the physical size of the domain is generally so large that computational limitations prevent the necessary grid resolution being achievable. The fact that the LES segregation of the flow structures cannot generally be located in the internal sub-range means that a larger proportion of the turbulent structures are modelled in LES than would be ideal. The influence of this limitation diminishes with increased grid resolution.

2.2.3 *Sub-Grid Scale (SGS) Modelling*

In modelling the influence of the sub-grid scale motions, the small-scale turbulent fluctuations of fluid properties at a point are described via a statistical approach[6]. In this method, the instantaneous value of a quantity is described by two components; a volumetric average $\overline{u}$, and a fluctuation component that represents the deviation of the quantity from its volumetric average u'. In problems where three-dimensional numerical methods are employed, the volumetric average of a quantity is obtained by averaging the quantity over the spatial extent of each cell in the computational grid[7][8]. The volume of the grid cell is assumed to be large enough that molecular effects are eliminated, and continuum mechanics pertinent to gases is applicable.

$$u = \overline{u} \pm u' \qquad \text{Equation (2-1)}$$

Where

$$\overline{u} = \frac{1}{dV}\int_{dV} u\, dV \qquad \text{Equation (2-2)}$$

The governing equations of motion can be rewritten in terms of volumetrically averaged quantities. These volume-averaged governing equations then describe the large-scale field that is the output of the LES approach. The momentum equation in this form contains terms that involve the fluctuating components of the velocity. These terms represent the effect of the sub-grid scale motions on the large-scale resolvable motions. That is, they describe the stress that the fluctuating velocities place on the mean flow[9]. These Reynolds stresses remove energy from the mean flow that is ultimately dissipated via viscosity at the level of the sub-grid scale motion. It is these SGS terms in the Navier-Stokes equations that are approximated with a model in the LES approach[10].

Smagorinsky SGS model.

The simplest and most common form of SGS turbulence model used in LES is the Smagorinsky model[10][11]. This is the default SGS model used in the FDS fire code. The Smagorinsky model uses the eddy viscosity approach[9] to quantify the stresses that the turbulent velocity fluctuations place on the mean flow. In this modelling approach, the Reynolds stresses are assumed to relate

to the local mean velocity gradient. The eddy viscosity is the function that relates these two quantities. The eddy viscosity is therefore a property of the flow, rather than a property of the fluid. It may have a constant value, or its value may vary as a function of position in the flow. Equations (2-3) through (2-7) describe the Smagorinsky SGS model.

$$\tau_{ij} = -2\nu_T S_{ij} \qquad \text{Equation (2-3)}$$

$$\nu_T = (C_s l)^2 \left(S_{ij} S_{ij}\right)^{\frac{1}{2}} S_{ij} = (C_s l)^2 |S_{ij}| \qquad \text{Equation (2-4)}$$

$$l = \left(l_x \times l_y \times l_z\right)^{\frac{1}{3}} \qquad \text{Equation (2-5)}$$

$$S_{ij} = \frac{1}{2}\left(\frac{\partial u_i}{\partial x_j} + \frac{\partial u_j}{\partial x_i}\right) \qquad \text{Equation (2-6)}$$

$$|S|^2 = 2\left(\frac{\partial u}{\partial x}\right)^2 + 2\left(\frac{\partial v}{\partial y}\right)^2 + 2\left(\frac{\partial w}{\partial z}\right)^2 + \left(\frac{\partial u}{\partial y} + \frac{\partial v}{\partial x}\right)^2 + \left(\frac{\partial u}{\partial z} + \frac{\partial w}{\partial x}\right)^2 + \left(\frac{\partial v}{\partial z} + \frac{\partial w}{\partial y}\right)^2 \qquad \text{Equation (2-7)}$$

Where

τ_{ij} is the viscous stress tensor used in the Navier-Stokes equations.

ν_T is the SGS eddy viscosity.

l is the characteristic dimension of the computational grid used by the FDS, but not necessarily called for by the Smagorinsky method in this form.

S_{ij} is the local strain rate in the fluid.

$|S|$ is the magnitude of the deformation tensor.

C_s is the only empirical parameter in the Smagorinsky model; it has a generally accepted constant value of 0.21. In the FDS code, the Smagorinsky constant has been given a default value of 0.14, because this value has been found to provide good results in the simulation of fire plumes. It is generally accepted however, that LES results are relatively insensitive to small variations in the value of the constant[12].

The eddy viscosity nature of the Smagorinsky model means that in simulations the fluid viscosity varies spatially. The model places a high amount of viscosity (and consequently a high drain of energy from the large-scale motions) in regions where there is a high strain rate in the large-scale

field. Additionally, the developers of FDS model have placed a lower bound on the fluid viscosity given by the Smagorinsky model. By default the lower bound is equal to the viscosity of air, however the user has the option to change this. The lower bound was implemented to eliminate instabilities seen in the computations when the velocity gradients were relatively small.

Constant Viscosity SGS model

The FDS code provides the facility to specify a constant fluid viscosity rather than using the default Smagorinsky eddy viscosity model. In the user manual, this option is described as a DNS. It is the authors' opinion that this description is inappropriate in virtually all fire simulations, because the grid resolution will not be fine enough to resolve all the motion that has an influence on the flow field. Describing this constant viscosity option as a DNS implies a false sense of accuracy for the simulations, through association with true DNS research. The difference is merely an issue of grid resolution. If the resolution is fine enough, then simulations are truly a DNS. However, given the size of the domain typically modelled in fire applications, it seems highly unlikely that this resolution will be achieved with computational hardware presently available (and affordable). Therefore, in this document the use of this SGS modelling approach will be referred to as using a constant viscosity SGS model.

In real fluid flow, viscosity dissipates the energy that cascades down from the large-scale motions to the small-scale structures. At the smallest scale, the inertia of the fluid packages is small enough that viscous forces are significant, and momentum can be ultimately dissipated as heat. In true Direct Numerical Simulations (DNS), the resolution of the computational grid is sufficient that all fluid motion on an influencing scale can be resolved. Consequently, in DNS computations there is no need for SGS modelling, and the actual fluid viscosity can be used in the Reynolds stress tensor.

In the LES approach, if a constant viscosity environment is specified, then care must be taken to ensure that the computations remain stable. The stability is related to the grid resolution and the viscosity that is specified for the fluid. This relationship can be appreciated by considering the energy cascade described in the paragraph above. Energy cascades from the largest structures down to the smaller structures, where it must be dissipated via the fluid viscosity. In LES, only the large-scale motions are resolved. Thus, in order to dissipate the energy that is passed down from these resolved motions, the viscosity of the fluid must be large enough that it is comparable to the inertia of the smallest resolved structures. If the fluid is not sufficiently viscous to dissipate all the energy at the smallest scale, then excess energy builds up over time, which creates instabilities in the computations. The instability of the computations can be seen in animations of the results as physically implausible fluid behaviour; this is illustrated later in Section 7.2.3. In terms of the FDS code, this means that where a constant viscosity environment is specified, the fluid viscosity must be sufficiently severe to remove all the energy that cascades down to the smallest resolvable scale.

The nature of the LES approach requires this viscosity to be larger than the actual viscosity of the fluid being simulated.

A large volume of previous LES work has shown that for low Reynolds number flows the results produced by the LES approach are relatively insensitive to the sub-grid scale model employed. Conversely however, in highly complex high Reynolds number flows the influence of the sub-grid scale model on the LES results can be more pronounced[10]. Ferziger[13] provides an excellent description of the LES and DNS approaches to CFD.

2.3 The Fire Dynamics Simulator

2.3.1 Historical Development

In the late 1970's Rehm and Baum [14] derived a set of approximate equations of motion to describe the buoyant movement of fire-induced thermal gas flows. In the research community, these equations are sometimes referred to as the low Mach number form of the Navier-Stokes equations. The equations are described as approximate (or simplified), because they do not contain any description of the high frequency acoustic waves that can occur in an elastic fluid. During the derivation of the equations, perturbation analysis was used to show that the spatial variation in pressure is extremely small when the rate of heat addition to the fluid is relatively slow (as is the case for fires). In this condition, the time scale associated with pressure waves equilibrating the pressure in the immediate environment is small when compared with the time scale on which the buoyant motion in the fluid occurs. For this reason, the reference pressure of the environment was simplified in the equations to be spatially uniform, so that the short-term pressure variations of high frequency acoustic waves are not described by the equations. This simplification was advantageous for the application of computational methods in solving the governing equations of motion. It meant that the time step employed in computations was set relative to the time scale of the buoyant fluid motion, rather than the much smaller time scale associated with the propagation of acoustic waves. The result of this is that computations are completed sooner.

In their documentation of the low Mach number governing equations, Rehm and Baum demonstrated that when the heat addition from the volumetric fire source was mild (such that the density variations produced by the heat source were small), the governing equations reduce to the Boussinesq equations. This was an important point, as it meant that for Boussinesq flows the known ambient density could be used in computations in place of the unknown buoyant fluid density. This simplification greatly reduced the number of computations that needed to be employed to solve the equation set. To clear the way for finite difference schemes to be used to predict fluid motion from the governing equations, Rehm and Baum also determined relations for

the uniform reference pressure level, and the spatial distribution of the overpressures[†]. This meant that numerical methods could be applied to the equation set to compute the density and velocity of the buoyant flow field as a function of time.

The first LES style computations that were conducted using these governing equations were published in the early 1980's[15][16][17]. The computations were two-dimensional, and used the Boussinesq set of equations to describe the motion of an inviscid, non-conducting gas. In line with the derivation of the governing equations, the fluid in the computations was described as thermally expandable but not compressible. That is, the local density of the fluid would decrease as the local temperature increased (in accordance with the ideal gas law), but pressure variations in the environment would not cause any density variations in the fluid. This initial two-dimensional modelling work included an attempt to simulate the features of smoke particle coagulation. Fictitious particles were randomly injected into the computational domain near the prescribed heat source. Each particle represented a blob of smoke that contained a prescribed size distribution of aerosol particles. The movement of the particles was given by the hydrodynamic equations that describe the large-scale motion of the buoyant fluid. The particles were tracked in the domain, so that the size distribution of aerosol particles in any computational grid cell could be determined at any time.

In 1984 the previous two-dimensional work was extended into three dimensions[18][19]. Boussinesq flows were modelled to enable an efficient Fast Fourier Transform (FFT) method to be employed to solve the Poisson pressure equation. For the thermally expandable fluid described by the governing equations, the elliptic pressure equation is non-separable and self-adjoint, such that the linear algebraic system that arises from its discretisation in computations must be solved by an iterative method. If, however, the Boussinesq assumption is employed, the linear algebraic system that arises from the discretization has constant coefficients and can be solved by fast direct methods (that is, non-iterative). This is an important point, as the solution of the pressure equation constitutes the bulk of the numerical computations. The Boussinesq approximation is still employed in the present code where the ambient density is used in the pressure term of the momentum equation. This simplification is used to increase the computational efficiency of the model. In these three dimensional simulations, fictitious particles were again used to model smoke aerosol coagulation. The fluid was still an inviscid, non-conducting gas, such that a Lanczos smoothing algorithm was employed in the computations to remove the sub-grid energy build-up that was observed.

[†] *Although a uniform reference pressure can be used in both the energy equation and the equation of state, the pressure perturbations (overpressures) are large enough that they must be included in the momentum equation.*

In the 1990's the availability of faster and cheaper computers meant that the computations could be expanded to account for the small-scale processes of viscosity and thermal conduction[20]. The increase required in grid resolution to do this however, meant that these initial simulations had to be two-dimensional. The expansion of the properties of the fluid to include viscosity and thermal conduction meant that boundary condition problems related to these properties had to be solved. A no-slip or full-slip boundary condition option was provided for the fluid velocity at the domain boundaries. An adiabatic or constant temperature wall condition was provided for the thermal conductivity. Neither of these thermal boundary conditions accounted for convective heat loss to the walls. In addition to the viscosity and thermal conductivity, new features were also added to the code to increase its practicality in application. The orientation of gravity became a variable, so that it could be specified relative to the boundaries of the rectangular domain. This enabled flows to be studied in rooms that had an inclined geometry, such as stairwells or escalators. An ambient stratification feature was also added to the code, whereby the ambient atmosphere in the domain could be divided into two distinct layers of different density. This feature was used to study the effect of stratification on the rise of a fire plume in an atrium. By this stage in the model development, the fictitious particles that were originally injected to model smoke coagulation were now being primarily used to visualise the transient dynamics of the flow in animations.

In a further attempt to increase the practicality of the computational model, the algorithm was generalised to enable the computational domain to be described as a polygon shape[21]. This allowed geometric features such as windows, soffits and stairwells to be included in the simulations[22]. In an attempt to maintain the efficient computational methods that had been employed in the model to date (where there were rectangular grids), a conformal map was used to transform the spatial coordinates of the polygon grid to a rectangle description. The disadvantage in the conformal mapping approach was that grid distortion created small grid cells in the domain that severely limited the time step of the computations[†].

In the early 1990's a model was implemented into the LES code to represent the fluctuating source volume that is the flaming combustion zone[23][24][25]. Prior to this time, the spatial distribution of the heat release was prescribed in simulations. The new heat release model utilised the concept of having small thermal elements release energy as they are convected upward in the buoyant plume above the fuel. Each thermal element is analogous to a small neutrally buoyant package that is a combustible mixture of gases and vapours given off by the pyrolysis occurring on the fuel surface. Each thermal element releases the chemical energy that it holds, over a time interval that is determined from empirical plume correlations[26]. The length of the time interval is such that the energy is completely released before the thermal elements are convected beyond the intermittent region of the fire plume. The time history of the energy release can be prescribed. This approach

---

[†] *Stability of the computational scheme imposes a limit on the time step relative to the size of the cells in the grid.*

means that the spatial extent of the source (that represents the flaming region) is defined by the combination of the thermal element burnout time, and the convective velocities that are induced in the region of energy release.

By the mid 1990's, computer hardware had advanced sufficiently to permit full three-dimensional simulations to be conducted that accounted for the viscosity and thermal conductivity of the fluid[25][27][28]. The polygon description of the domain was removed from the algorithm, to recapture some of the computational efficiency lost in the conformal mapping. Masked rectangular cells were now used to described internal boundaries in the domain that were impermeable to the flow. Maximal conduction heat loss from the fluid to constant temperature surfaces was also incorporated into the model, to assess the effect of heat loss on flow dynamics[28]. Both Boussinesq and non-Boussinesq flows were simulated, however the ambient density was still used in the pressure term of the momentum equation, to enable the FFT methods to be retained in directly solving the pressure equation. Unpublished work was done to assess the impact of this assumption. The assessment revealed that for large-scale fire work where the transport of hot gases (100°C -300°C) is the emphasis, the approximation is reasonable. Only in the combustion region where temperatures are of the order of 700°C is the approximation a problem. Improvements in this approximation are a possible area of work in the future development of the model.

With the rapid development of computing power in the 1990's, radiation was identified as the most pressing small-scale process that needed to be accounted for in the large-scale fire simulations. Work was therefore undertaken to develop a radiative transport model suitable for incorporation into the large eddy simulations of fire[29][30]. Basically, the radiation model that has been developed to date uses the thermal elements of the LES heat release model as radiation emitters that are convected about in a grey gas environment. The energy emitted from the thermal elements is absorbed by the surrounding gas and the solid boundaries of the domain. The proportion of the chemical heat release that is emitted from the thermal particles is a prescribed parameter in the model. The absorption coefficient of the grey gas can be constant, or can vary spatially. The radiation model with variable absorption coefficients was successfully used in two-dimensional LES simulations in 1998[30].

2.3.2 Present Capabilities of the Model

The user manuals for the FDS model[31][32] detail the entire present capabilities of the program. This section will therefore only briefly highlight the features that the model incorporates. The reader is referred to the user manuals for further details and background references.

The FDS model is capable of simulating the three-dimensional buoyant motion of a thermally conducting and thermally expanding Newtonian fluid. The model does not simulate acoustic pressure waves in the domain. Rapid heat addition applications such as explosions or jet engines

are therefore outside the range of application for the model. The spatial geometry of the domain is described via rectilinear coordinates to facilitate computational efficiency. By default, the computational grid is uniformly distributed in each of the three coordinate directions. It is possible however, to vary the spatial discretisation in up to two coordinate directions in order to focus the grid resolution on a specific area of the domain. A plane of symmetry function is provided in the model, whereby the spatial extent that needs to be simulated can be halved in cases where the domain is symmetrical.

The combustion zone that represents the fire in the simulations can be modelled in two different ways (depending on the resolution of the simulations). It is important to note that the model does not determine the driving heat release rate history of a fire; the user is required to prescribe this as input to the model. At crude grid resolutions, the combustion zone is best simulated using a series of thermal elements that represent burning pockets of combustible gas ejected from the flaming fuel surface. The thermal elements release their allocated energy as they are convected upward in the fire plume. After the elements have released their energy, they remain in the thermal convection and are tracked by the computations as a representation of combustion generated aerosol particles (soot). At finer grid resolutions where a true Direct Numerical Simulation is feasible, combustion can be modelled as a simple one-step reaction between fuel and oxygen species that are tracked in the simulations. Fictitious inert particles can still be used in these simulations to represent the combustion-generated soot. In both approaches, a prescribed fraction of the chemical heat release from combustion can be emitted via radiation. The radiative energy is absorbed by solid boundaries and smoke laden gas throughout the domain.

There are four different thermal boundary conditions for the model. The simplest is that of adiabatic flow, where there is no heat loss from the flow to the bounding walls. Solid surfaces in the domain can also be modelled as constant temperature surfaces. This provides a useful means for assessing the impact of maximal heat losses from the flow. The final two thermal boundary conditions model solid surfaces as either thermally thick or thermally thin heat sinks. The thermally thick case uses a one dimensional heat transfer calculation requiring the specification of the boundary wall depth and conduction properties. Heat losses and gains to the bounding surfaces occur via convection and radiation. It is important to note however, that although the surfaces emit radiation in the computations, the emitted energy is not absorbed anywhere else, so that it is lost from the system.

The model is capable of handling passive external openings in the domain boundaries. These openings can be used to represent open doors and windows from a room. Volume inflows and outflows from the domain can also be prescribed to represent ventilation influences or the injection of certain gas species. The velocity boundary conditions can be set as no-slip, free-slip, or any degree intermediate to the two. The model is capable of tracing the mass fraction of different species throughout the domain.

Thermal detector activation and sprinkler suppression can also be modelled with the FDS model. The activation of thermal detectors uses the RTI of the device in a calculation that accounts for convection, conduction and radiation heat transfer, as well as possible cooling from water droplets present in the gas from the activation of sprinkler heads. The trajectories of the water droplets from the sprinkler are computed. The computations account for the drag force between the spherical droplet and atmosphere, and the forced convection heating of the droplet as it falls through the hot gases. The suppression influence of the water spray on a burning surface has been modelled from global observations of the heat release rate suppression on rack storage fires conducted at Factory Mutual. The observed exponential suppression influence of sprinkler spray has been preserved, and applied locally in the LES approach to modelling. On non-combusting surfaces, the water from the sprinkler spray acts as a heat sink, absorbing convective and radiative heat transfer. Baum[33] provides a recent review on the use of the Large Eddy Simulation approach in modelling fires.

2.3.3 Previous Validation Work

To date, there has been no single piece of work that has focussed on comprehensively validating the FDS model. This is of no surprise however, when you consider that the model has been in a state of rapid development for the last twenty years. Useful verification of the model will require progressive determination of the accuracy of the component elements in the model, and the relative contribution of each element to the final accuracy of the simulations. The scope of this task is too large to be completely dealt with in a single piece of work. The research documented in this thesis therefore has the objective of providing information on the accuracy of the hydrodynamic element of the FDS code. Previous validation work documented for the model is summarised below.

Numerical Methods

Following on from the derivation of the governing equations of motion, Rehm and Baum went on to study the use of several candidate finite difference schemes to obtain solutions to their equations[34]. Their analysis assessed the accuracy and stability requirements of each of the finite difference approximations. This work entailed a comparing a continuous solution for the linear equations that describe internal waves in a stratified fluid, with the finite difference approximate solutions to these equations. The finite difference schemes considered were second order accurate in space, and incorporated either first order or second order time differencing. The results of the comparison determined that a second order accurate central difference scheme be employed in the initial FDS buoyant convection algorithm[35]. Simulations of buoyant convection in an enclosure with this scheme demonstrated symmetry in the flow field about the centreline of a symmetrical enclosure. This observation was proposed as a measure of the accuracy of the computations (given that the computations were applied as if no symmetry existed). The frequency of vortices seen in the computed buoyant plume was also found to agree with the frequency of puffs observed in real fire plume experiments[36]. The non-linear algorithm for convection was then

verified in later work conducted by Rehm, Barnett, Baum and Corley[37]. Here, solutions for two specialised cases with full non-linear equations of motion were used to check the accuracy of the finite difference approximation to the equations. The discretisation error from the comparison was given as a few percent for the buoyant convection calculations performed on a 30 by 30 computational grid. It should be noted that certain criteria were placed upon the selection of the finite difference scheme[35] that restricted the possible candidates.

Salt Water Plumes

In the early stages of the model development, two-dimensional simulations were conducted of an inviscid salt-water plume[15][16]. The simulations modelled the vertical descent of a line plume in a fresh water tank. The non-dimensional rate of descent of the plume front was compared with experimental data from previous research[38], and experiments that had been conducted by the researchers themselves. The experimental data and the computations both displayed a constant rate of descent for the plume until it impinged on the model floor. The computations however, determined that the plume had a faster rate of fall (1.15) than the experimental data demonstrated (0.75 and 0.96). In light of the limited grid resolution, and the approximation of the fluid environment in the computations, the comparison was described as "reasonably good".

Gravity Currents

The FDS code has been used a number of times to simulate the propagation of gravity currents along a horizontal surface of a long channel[20][22][28]. Early two-dimensional viscous fluid simulations were able to resolve the characteristic head on the gravity current. Later simulations then compared the speed of the computed gravity current head with the speed of salt-water gravity currents given by the experimental data of Zukoski[39]. The agreement was excellent. The simulations also showed that the results were insensitive to the value of the Schmidt number that characterised molecular diffusion of the buoyancy agent. This was an important point, as diffusion could not be modelled exactly in the simulations due to stability limitations associated with the grid resolution and the Pèclet number. The propagation of thermal gravity currents down a long corridor has also been simulated with the FDS code, in both two and three dimensions. These simulations looked at the impact of convective heat losses to the ceiling on the speed of the gravity current nose. The computations were able to resolve the three-dimensional lobes and cleft patterns that have been seen in real gravity currents[40]. The heat loss to the ceiling was found to be heavily dependent on these three-dimensional structures, such that simulations that intend to account for heat transfer effects should be three-dimensional. The speed of the gravity current was reduced by heat loss, as had been seen in previous experimental work[41].

A quantitative comparison of simulation and experimental data was conducted for the gravity currents seen in the backdraft research of Fleischmann[42]. In this work, two-dimensional simulations were conducted of the gravity current that enters a compartment as a precursor to a backdraft. The results of the simulations were compared with both salt water modelling

experiments[43] and half-scale fire tests[44], conducted as part of Fleischmann's research. The transit time for the gravity current to strike the back wall of the fire compartment was compared in simulations of the salt-water experiments. The agreement between the transit times was excellent for a full opening on the fire compartment, but slightly less favourable when a horizontal slot opening was simulated. In the case of the horizontal slot, the LES computations consistently over predicted the transit time. Comparisons were also made of the quasi-steady vent flow velocities in simulations of the half scale backdraft experiments. In this case, there was good agreement between the data and simulations, although the computed vent flow velocities were higher than those measured in experiments. The difference between the velocities was, however, within the uncertainty bounds of the experimental data.

Isolated Fire Plumes

The fire plume plays a pivotal role in the dynamics of a compartment fire. The correct characterisation of the plume behaviour has therefore been given a very high priority in fire science research. A number of simulations of an isolated fire plume have been conducted with the FDS model. In the three dimensional simulations, a minimum grid resolution has been recommended to adequately capture the plume dynamics. The resolution is related to a plume structure length scale D_C that was used in the determination of McCaffrey's plume correlations[26]. The length scale is given by Equation (2-8), and can be derived from a critical Froude number consideration.

$$D_C = \left(\frac{Q}{\rho_\infty c_p T_\infty \sqrt{g}} \right)^{\frac{2}{5}} \qquad \text{Equation (2-8)}$$

Using the minimum resolution of $0.1D_C$, the time averaged velocities and temperatures of the simulated plumes showed excellent agreement with McCaffrey's centreline plume correlations[27][45]. The Gaussian spread of temperature and velocity across a section of the plume was also shown to agree excellently with McCaffrey's plume radius correlation[27].

The numerical methods employed in the FDS model have been observed to naturally produce a symmetrical flow field when the domain and source for the computations are described as symmetrical. This symmetry has been evident in early publications of the model development[18][19]. In reality, the instantaneous structure of a fire plume is asymmetric. To produce a fire plume with the realistic instantaneous asymmetrical appearance, a small cube can be prescribed into the FDS domain to break the symmetry of the computations (this is later referred to as a symmetry breaker). This approach produces a fire plume that has a realistic chaotic turbulent appearance. Instantaneous images have been published of the FDS computed fire plume[25][27][33][45]. The fact that the instantaneous plume structure looks realistic in these images, and the data produces accurate time averaged properties, lends credence to the use of the LES computational approach in modelling fires.

Enclosure Fire Dynamics

Enclosing the plume in a large compartment, such as an aircraft hanger, was the next advance in simulating the dynamics of a fire plume[25][27][45]. Unfortunately, in some of the cases where this has been done, a comprehensive comparison with experimental data has not been conducted. This is likely to be due to the unavailability of suitable data for these fire tests.

FDS computations have been conducted of the ever-popular Steckler *et al*[46][47] fire compartment experiments[25][45]. The published results of the simulations show the similarity of the velocity distribution across the area of the doorway that divides the two compartments. The velocities at the edge of the vent flows are seen to be larger than the centreline velocities, as was seen in the experimental measurements. A quantitative comparison of the time averaged centreline temperatures and velocities in the doorway also show good agreement between the experimental data and computations.

The most comprehensive comparison of enclosure fire experimental data and simulations was performed for a series of 39 large-scale fire tests conducted at the Underwriters Laboratories in Northbrook, Illinois over a two year period in the late 1990's[46]. The objective of the tests was to study the influence and interaction of sprinklers, roof vents and draft curtains on fires that occur in large warehouse type enclosures.

To demonstrate the accuracy of the FDS model, initial simulations were conducted of a series of well-defined fire experiments. These simulations modelled experiments in which a Heptane spray burner was used as the fire source in a 7.6m high flat-ceiling warehouse. The results of the computations showed that the model accurately predicted both the gas temperatures near the ceiling, and the activation times of the sprinkler heads near the fire. Gas temperatures in the region just beneath the ceiling were predicted to within 15%. Sprinkler activation times for the first ring of sprinklers around the burner location were predicted to within 15%. The activation time for the second ring of sprinklers was predicted to within 25%. In a second series of simulations, the heat release rate of multiple boxes containing a well-defined plastic commodity was simulated, using an ignition temperature fire growth rate model. These simulations predicted the heat release rate time history of the boxes to within 20% of the calorimetry burns. Having demonstrated the accuracy of the model in well-defined applications, the model was then used to study apparent anomalies in the experimental results from five full-scale rack storage tests that were conducted. The deterministic nature of the model allowed researchers to identify the specific reason that unusual behaviour was seen in the experiments. This contribution was important, given that it was the interaction of multiple fire protection features that was being studied. The model successfully demonstrated the effect that a delay in initial sprinkler head activation has on the total number of sprinklers that activate in a fire. It also reproduced the sprinkler activation and suppression behaviour that was seen in experiments where the fire was located directly below a roof vent or the

intersection of draft curtains. Readers are referred to the official research report of this work for the necessary details on the model verification in this specific application [48].

Qualitative Observations

In addition to the quantitative comparisons that were made between the computational results and experimental data, observations of the transient flow dynamics also provided some verification of the model. In most publications of FDS simulations, the good qualitative agreement between the computational flow behaviour and the smoke flows that were seen in real fire experiments was noted. Features such as the pulsing nature of vortices in the plume[19][45], the blowing over of the plume in enclosure fires with vents[19], and the reproduction of the trench effect[20][21] seen in the Kings Cross underground fire[49], all lend credence to the predictive capability of the FDS model.

2.4 Simulation of Salt Water Flows

The FDS has been successfully used in the past to simulate the buoyant flow of salt water in a freshwater environment[28][42]. The model can be used to simulate these liquid flows because the hydrodynamic equations that describe the movement of smoke in the FDS are also valid for buoyant saline flows. This similarity between fire induced smoke flows and buoyant salt water flows has been formally documented and utilised in previous fire research[50]. Section 2.4.1 however, provides a basic overview of the similarity of the flows, and describes how the FDS can be used to simulate saline flows if specific assumptions are employed.

2.4.1 Similarity of Saline and Smoke Flows

The flow of saline fluid in a quiescent freshwater environment is driven by the density difference between the two fluids. Similarly, the flow of hot smoke in cool ambient air is driven by the density difference between the gases. The fact that the fluid movement in both cases is driven by the same phenomenon, a buoyancy force, means that there is similarity between the governing equations of motion for the two cases. The similarity of the governing equations is best illustrated when the equations are non-dimensionalised. The governing equations are non-dimensionalised in accordance with Equations (2-9) through to (2-19).

Distance

$$x^* = \frac{x}{H} \qquad \text{Equation (2-9)}$$

Time

$$t^* = \frac{t}{H}U \qquad \text{Equation (2-10)}$$

Velocity

$$\bar{u}^* = \frac{\bar{u}}{U} \qquad \text{Equation (2-11)}$$

Pressure Perturbation

$$\tilde{P}^* = \frac{\tilde{P}}{\rho_\infty U^2} \qquad \text{Equation (2-12)}$$

Fire Buoyancy

$$\theta^* = \left(\frac{T - T_\infty}{T_\infty}\right)\frac{1}{\xi} \qquad \text{Equation (2-13)}$$

where

$$\xi = \left(\frac{U^2}{gH}\right) \qquad \text{Equation (2-14)}$$

Saline Buoyancy

$$Y_S^* = \frac{Y_S}{\xi} \qquad \text{Equation (2-15)}$$

Velocity Scale

$$U = \left(\frac{\dot{Q}g}{\rho_\infty C_p T H}\right)^{\frac{1}{3}} = \left(\frac{\dot{m}_s g}{\rho_\infty H}\right)^{\frac{1}{3}} \qquad \text{Equation (2-16)}$$

Reynolds Number

$$Re = \frac{HU\rho_\infty}{\mu} \qquad \text{Equation (2-17)}$$

Schmidt Number

$$Sc = \frac{\mu}{\rho D_S} \qquad \text{Equation (2-18)}$$

Prandtl Number

$$Pr = \frac{\mu C_p}{k} \qquad \text{Equation (2-19)}$$

Equations (2-20) through (2-23) show a non-dimensional form of the governing equations for both fire induced smoke flow and buoyant salt water flows. In this non-dimensional form, the conservation of mass equation is exactly the same for both the saline flow and the smoke flow. Similarly, the conservation of momentum equation has exactly the same form in both cases. The third conservation equation for fire induced thermal gas flows is the conservation of thermal energy. For buoyant salt water flows, the third conservation equation is the conservation of salt mass in solution.

Conservation of Mass - (Applicable to both saline flow and smoke flow)

$$\nabla^* \cdot \bar{u}^* = 0 \qquad \text{Equation (2-20)}$$

Conservation of Momentum - (Applicable to both saline flow and smoke flow)

$$\frac{\partial \bar{u}^*}{\partial t^*} + \left(\bar{u}^* \cdot \nabla^*\right)\bar{u}^* + \nabla^* \tilde{P}^* - \theta^* \hat{k} = \left(\frac{1}{Re}\right)\nabla^{*2}\bar{u}^* \qquad \text{Equation (2-21)}$$

Conservation of Thermal Energy - *(Applicable to smoke flow)*

$$\frac{\partial \theta^*}{\partial t^*} + \left(\bar{u}^* \cdot \nabla^*\right)\theta^* = \left(\frac{1}{RePr}\right)\nabla^{*2}\theta^* \qquad \text{Equation (2-22)}$$

Conservation of Salt Mass in Solution - *(Applicable to saline flow)*

$$\frac{\partial Y_S^*}{\partial t^*} + \left(\bar{u}^* \cdot \nabla^*\right)Y_S^* = \left(\frac{1}{ReSc}\right)\nabla^{*2}Y_S^* \qquad \text{Equation (2-23)}$$

The conservation of thermal energy equation has exactly the same form as the conservation of salt mass equation for saline flows. The similarity in form of the three governing equations means that the same solution procedure can be used to solve the equations from each flow case. Thus, the FDS can be used to simulate buoyant saline flows by replacing the conservation of thermal energy relationship with the conservation of salt mass relationship given by Equation (2-23). Instead of solving for the temperature in the simulations, the code is used to solve for a salt mass concentration. This similarity of the non-dimensional governing equations is used in salt water modelling theory to derive the scaling laws that will achieve dynamic similarity between the two flows. Readers are referred to the paper that formally documented the salt water modelling theory[50] for further explanation of the similarity between the flows and the anomalies in the modelling relationship.

2.4.2 *Specification of Fluid Conditions*

The following section discusses the specifications that must be made in the input file of the FDS to correctly simulate salt water flows. Readers are referred to the FDS user manual[31] for the nomenclature referred to within this section and Section 2.4.3.

In all salt water simulations, the ISOTHERMAL=.TRUE. condition must be specified in the species namelist group, to eliminate any temperature dependence calculations. The ISOTHERMAL flag instructs the code to call up the species conservation equation (in this case the conservation of salt mass) in place of the thermal energy conservation equation. In these isothermal simulations the fluid density is extracted from the average molecular weight in the grid cells.

By default, the FDS will use the Smagorinsky SGS model. In simulations where the constant viscosity SGS model is desired, two additional specifications must be made in the miscellaneous namelist group; DNS=.TRUE. and INCOMPRESSIBLE=.TRUE.. When these specifications are made, the incompressible flag forces the code to use a simpler viscous term differencing scheme, which reduces the computations. The simpler differencing scheme can be employed because the isothermal nature of the computations eliminates the temperature dependence of the fluid viscosity. The DNS=.TRUE. flag forces the code to use a constant rate of molecular diffusion given by the diffusion coefficient that is specified by the user. In contrast the Smagorinsky SGS model determines the local rate of molecular diffusion from the Schmidt number that is specified by the user and from the local fluid density and viscosity. Since the fluid viscosity varies spatially, so does the rate of molecular diffusion. This is discussed in further detail in Section 7.2.3.

To correctly replace the default properties of air, the density and viscosity of the ambient freshwater must be specified in the miscellaneous namelist group. For the saline fluid, these same properties must be specified in the species namelist group. Care must be taken when the constant viscosity SGS model is being used, to ensure the fluid is sufficiently viscous to provide stable computations. The real fluid viscosity may be specified when the Smagorinsky SGS model is employed.

In simulations where the Smagorinsky SGS model is used, the Schmidt number (Sc) must be specified, to quantify the eddy diffusion of salt mass in water. A Schmidt number of approximately one must be specified in order to keep the computations stable; this value could possibly be extended as high as two. When a constant fluid viscosity environment is used in simulations, a diffusion coefficient must be specified in the species namelist group instead of a Schmidt number. A value of $1.14\times10^{-6}\,m/s^2$ is recommended for this parameter.

The inflow of salt water into the computational domain is generally modelled using the VOLUME_FLUX and MASS_FRACTION parameters in a surface namelist group. The surface namelist is used to specify the conditions at the face of the forced vent. The mass fraction is

generally set to a value of one, to indicate the saline inflow is of the density specified in the species namelist group.

2.4.3 *Specifications used in Simulations*

In this research, the computational grid has been uniformly distributed in each of the three coordinate directions, such that the translation functions (given by TRNX, TRNY and TRNZ) are not utilised. The discretisation of the domain (via the parameters IBAR, JBAR and KBAR), attempts to obtain the same cell dimension in each direction (i.e. say, 10*mm* cube cells). Exact uniform distribution was limited by the condition of having each of the discretaisation parameters (IBAR, JBAR and KBAR) equal to an integer value of the form $2^l 3^m 5^n$ for computational efficiency.

The specified fluid densities were taken from Tables 2-1, 2-2 and 2-3. The dynamic viscosity of both the saline and the freshwater was specified as 1.14×10^{-3} kg/ms[52] in simulations where the Smagorinsky SGS model was used . A Schmidt number of 0.721 was specified (this value is simply the real Schmidt number divided by one thousand[†]). In simulations where the constant viscosity SGS model was used, the diffusion coefficient was specified as 1.581×10^{-6} m^2/s; which equates to a Schmidt number of approximately 0.721.

The resolution of the computations was never fine enough to accurately resolve the boundary layers that would form at the boundaries of the saltwater flows. As such, the computational boundary condition for the tangential velocity at solid surfaces was set at an intermediate slip condition. The FDS parameter VBC defines the degree of flow resistance for the tangential fluid velocity at solid surfaces. Simply speaking, the tangential component of the fluid velocity at a solid surface is set (by the user) as a fraction of the tangential velocity half a grid cell away from the surface. This is illustrated in Figure 2-1.

Figure 2-1 shows the simple method that is employed in the FDS to account for the tangential resistance to flow, and hence the presence of boundary layers along solid surfaces. A value of -1 for the VBC parameter gives a fluid velocity of zero at the surface of the solid object, and is referred to as a no-slip condition. A VBC value of 1 gives a full slip condition, such that there is no tangential resistance to the fluid flow at solid surfaces. VBC values between –1 and 1 give intermediate slip conditions. The FDS software is not designed for application to resolve boundary layer flow, such that the user is required to specify the VBC boundary condition to reflect the impact that a boundary layer is expected to have on the flow near the solid surface. This requires the consideration of the depth of a boundary layer relative to the dimension of the grid cells adjacent to the solid surface.

[†] *A Schmidt number of 0.7 would have been sufficient; the precision specified (to three decimal places) is misleading.*

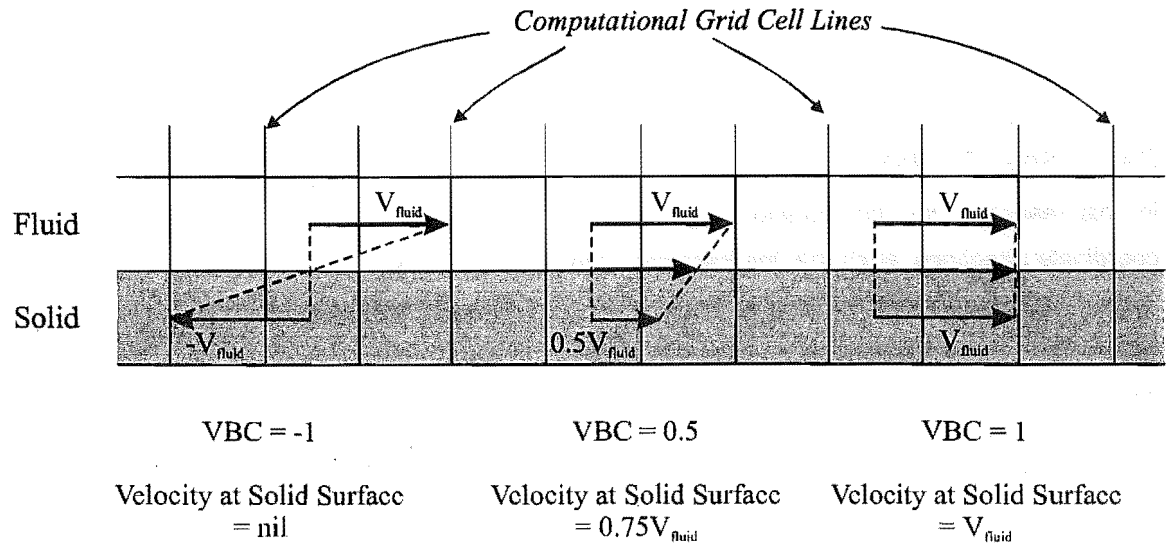

Figure 2-1 ***Schematic illustration of the method by which FDS accounts for the effect of boundary layers on the flow, through the parameter VBC.***

An example of a typical input file for the simulation of experiment T02 (which is defined in Chapter 3) is provided on page 2-19.

2.5 Computational Demands

Simulations were run on two IBM compatible PCs, that each had a 450 MHz Pentium P3 microprocessor and 512 Meg of RAM. The Cache size of the computers was 512 Kbytes. Simulation times varied from 18 minutes through to 4 days, depending on the number of cells in the domain and the length of time to be simulated. Figure 2-2 shows the rate of computation versus the number of cells in the domain for the computational hardware specified above. The rate of computation is expressed as the time that it takes the hardware to compute the solution for one time step at one cell in the domain. Thus, to estimate the total time that it will take for a simulation to run (on a similar machine), the total number of time steps in the computation must be known, along with the total number of cells in the domain. The duration of a single time step can be estimated using Equation (2-24)

$$\Delta t_{Comp} = \frac{l}{\sqrt{\frac{\Delta\rho}{\rho} gH}} \qquad \text{Equation (2-24)}$$

```
&HEAD CHID='T02-Vent',TITLE='Salt Water Experiment T02' /
&GRID IBAR=100,JBAR=64,KBAR=100 /
&PDIM XBAR0=0.000,XBAR=0.400,YBAR0=0.000,YBAR=0.250,ZBAR0=0.000,
     ZBAR=0.400 /
&TIME DT=0.1,TWFIN=60. /
```

Insert appropriate specifications in the MISC and SPEC namelist groups to determine which SGS Model is used

```
&SURF ID='HALF',VBC=0.5 /
&SURF ID='FULL',VBC=1.0 /
&SURF ID='SALT',MASS_FRACTION(1)=1.,VOLUME_FLUX=-0.0001334 /
&SURF ID='OUT',VOLUME_FLUX=0.0000537 /
&OBST XB=0.000,0.400,0.000,0.250,0.400,0.400, SURF_ID='FULL' /
&OBST XB=0.000,0.100,0.000,0.250,0.000,0.250 /
&OBST XB=0.080,0.100,0.000,0.078,0.250,0.400 /
&OBST XB=0.080,0.100,0.172,0.250,0.250,0.400 /
&OBST XB=0.080,0.100,0.078,0.172,0.250,0.295 /
&VENT CB='XBAR',SURF_ID='OPEN' /
&VENT XB=0.100,0.400,0.250,0.250,0.000,0.400,SURF_ID='OPEN' /
&VENT XB=0.100,0.400,0.000,0.000,0.000,0.400,SURF_ID='OPEN' /
&VENT XB=0.000,0.000,0.000,0.250,0.250,0.340,SURF_ID='SALT' /
&VENT XB=0.000,0.000,0.000,0.250,0.360,0.400,SURF_ID='OUT' /
&SLCF XB=0.000,0.400,0.125,0.125,0.000,0.400,QUANTITY='DENSITY' /
&SLCF XB=0.000,0.400,0.140,0.140,0.000,0.400,QUANTITY='DENSITY' /
&SLCF XB=0.000,0.400,0.110,0.110,0.000,0.400,QUANTITY='DENSITY' /
&SLCF XB=0.110,0.110,0.000,0.250,0.000,0.400,QUANTITY='DENSITY' /
&SLCF XB=0.100,0.100,0.078,0.172,0.295,0.400,QUANTITY='U-VELOCITY' /
&PL3D DTSAM=1000. /
```

For the Smagorinsky SGS Model specify the following:

```
&MISC ISOTHERMAL=.TRUE.,CSMAG=0.14,BACKGROUND_SPECIES='FRESH_WATER',
      DENSITY=999.23,VISCOSITY=0.00114,SC=0.721,SURF_DEFAULT='HALF'  /
&SPEC ID='SALINE',DENSITY=1005.70,VISCOSITY=0.00114,
      XB=0.000,0.080,0.000,0.250,0.250,0.340 /
```

For the Constant Viscosity SGS Model specify the following:

```
&MISC ISOTHERMAL=.TRUE.,DNS=.TRUE.,INCOMPRESSIBLE=.TRUE.,
      BACKGROUND_SPECIES='FRESH_WATER',DENSITY=999.23,
      VISCOSITY=0.00322,SURF_DEFAULT='HALF'  /
&SPEC ID='SALINE',DENSITY=1005.70,VISCOSITY=0.00322,
      DIFFUSION_COEFFICIENT=1.581E-6,
      XB=0.000,0.080,0.000,0.250,0.250,0.340 /
```

This relationship estimates the time that it takes for a fluid particle to move across the extent of a single grid cell. In the formulation of Equation (2-24) the real velocity of the fluid is unknown (before the computations), thus the velocity of the fluid particle is estimated using the velocity scale for buoyant motion. The total duration of a simulation could be estimated using Equation (2-25), where the computational rate (that is, the computational time, per cell, per time step) is taken from Figure 2-2.

$$t_{Duration} = (Computational Rate) \times \frac{t_{sim}}{\Delta t_{comp}} n_{cells} \qquad \text{Equation (2-25)}$$

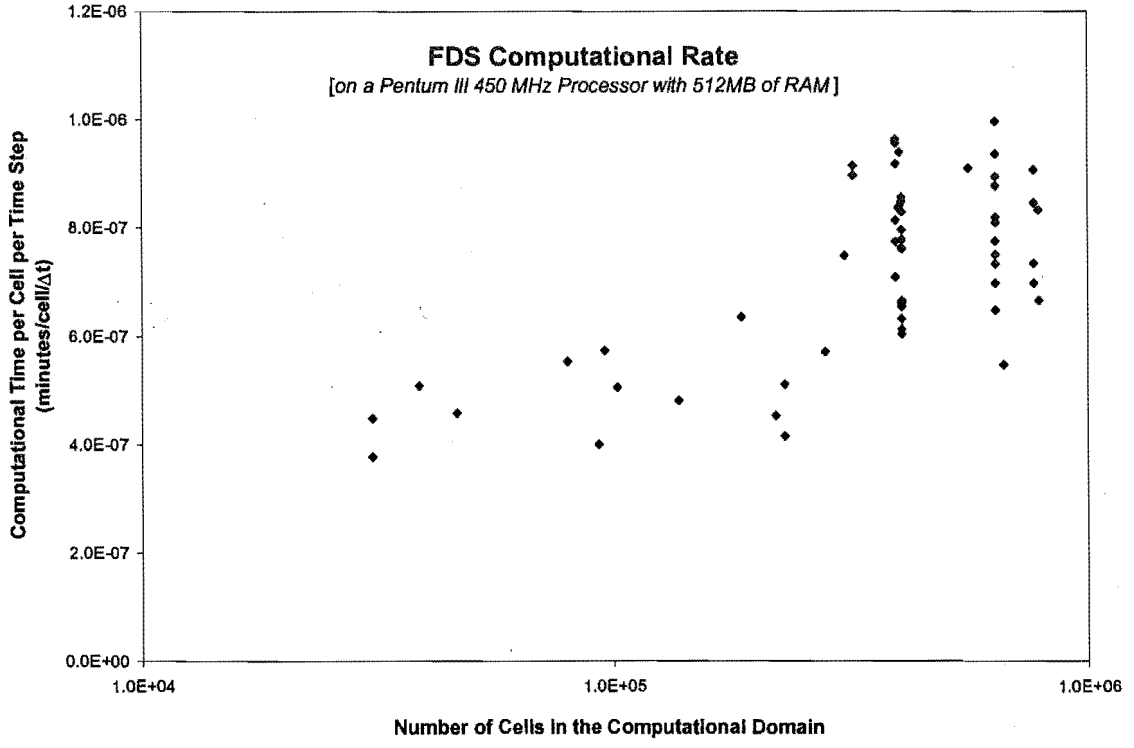

Figure 2-2 Graphical plot showing the rate of FDS computations on the Pentium 3, 450MHz PC that was used in the research

2.6 Smokeview - Graphics Program

In addition to developing the FDS, the National Institute of Standards and Technology (NIST), in Gaithersburg, Maryland (USA), also developed a graphics program for viewing the results of the FDS computations. The graphics program is called *Smokeview*[31], and it has been used throughout this research to visualise the computational flow field.

2.7 References

1. Kerrison, L., MaWhinney, N., Galea, E.R., Hoffmann, N. and Patel, M.K. (1994b) A Comparison of a FLOW3D Based Fire Field Model with Experimental Compartment Fire Data, *Fire Safety Journal*, **23**, 387-411

2. Kumar, S., Hoffmann, N. and Cox, G (1985), Some Validation of Jasmine for Fires in Hospital Wards, *Numerical Solution of Fluid Flow and Heat/Mass Transfer Processes,* Springer-Verlag, Berlin, p.159.

3. Welch, S. and Rubini, P.A. (1996) SOFIE 2.1 User's Manual, Cranfield University, Cranfield, United Kingdom

4. Galea, E.R., Knight, B., Patel, M.K., Ewer, J., Pitridis, M. and Taylor, S., SMARTFIRE v2.0 User Guide and Technical Manual, Fire Safety Engineering Group, University of Greenwich, UK, 1998.

5. Ferziger, J.H. (1977) Large Eddy Simulation of Turbulent Flows, *AIAA Journal* **15**, 1261-1267.

6. Rodi, W. (1994) 'Simulation Approaches for Turbulent Flows' In: *Computational Fluid Dynamics '94.* Eds: S. Wagner, J. Periaux and E.H. Hirschel, John Wiley & Sons Ltd, England. pp 149-158.

7. Shyy, W., Thakur, S.S., Ouyang, H., Hiu, J. and Blosch, E. (1997) *Computational Techniques for Complex Transport Phenomena*, Cambridge University Press, Cambridge, pp 231-242.

8. Deardorff, J.W. (1970) A Numerical Study of Three-Dimensional Turbulent Channel Flow at Large Reynolds Numbers, *Journal of Fluid Mechanics*, **41** Part 2, 453-480.

9. Tritton, D.J. (1977) *Physical Fluid Dynamics*, Van Nostrand Reinhold Company Ltd., Molly Millars Lane, Wokingham, Berkshire, England, pp 238-248.

10. Ferziger, J.H. (1993) 'Subgrid-Scale Modeling' In: *Large Eddy Simulation of Complex Engineering and Geophysical Flows.* Eds: B. Galperin and S.A. Orszag, Cambridge University Press, Cambridge, pp 37-54.

11. Smagorinsky, J. (1963) General Circulation Experiments with the Primitive Equations, *Monthly Weather Review*, **91**, 99-165.

12. Tannehill, J. C., Anderson, D. A. and Pletcher R. H., (1997) *Computational Fluid Dynamics and Heat Transfer*, 2nd Edition, Series in Computational and Physical Processes in Mechanics and Thermal Sciences, Taylor and Francis, Washington DC. pp 320-321.

13. Ferziger, J.H. (1983) Higher-level Simulations of Turbulent Flows, In: *Computational Methods for Turbulent, Transonic and Viscous Flows,* Ed: *J.A.* Essers, A von Karman Institute Book, Hemisphere Publishing Corporation, New York, pp 93-182.

14. Rehm, R.G. and Baum, H.R. (1978) The Equations of Motion for Thermally Driven Buoyant Flows, *Journal of Research of the National Bureau of Standards*, **83** No. 3, 297-308.

15. Baum, H.R. and Rehm, R.G. (1982) Numerical Computation of Large-Scale Fire Induced Flows, In: *Eighth International Conference on Numerical Methods in Fluid Dynamics*, Ed: E. Krause, Lecture Notes in Physics Vol. 170, Springer-Verlag, Berlin, pp 124-130.

16. Baum, H.R., Rehm, R.G. and Mulholland, G.W. (1982) Computation of Fire Induced Flow and Smoke Coagulation, *Nineteenth Symposium (International) on Combustion/The Combustion Institute*, pp 921-931.

17. Baum, H.R., Rehm, R.G., Barnett, P.D. and Corley, D.M. (1981) 'Finite Difference Calculations of Buoyant Convection in an Enclosure Part 1, The Basic Algorithm', The National Bureau of Standards Report NBSIR 81-2385, Gaithersburg, MD 20899, U.S.A.

18. Baum, H.R and Rehm, R.G (1984) Calculations of Three Dimensional Buoyant Plumes in Enclosures, *Combustion Science and Technology*, **40**, 55-77.

19. Rehm, R.G., Baum, H.R., Lozier, D.W. and Corley, D.M. (1988) A Model of Three-Dimensional Buoyant Convection Induced by a Room Fire, *Paper Presented at the First National Fluid Dynamics Congress*, July 24-28, Cincinnati, Ohio.

20. Rehm, R.G., Tang, H.C., Baum, H.R., Sims, J.S. and Corley D.M. (1991) 'A Boussinesq Algorithm for Enclosed Buoyant Convection in Two Dimensions' NISTIR 4540, U.S. Department of Commerce, National Institute of Standards and Technology, Computing and Applied Mathematics Laboratory, Gaithersburg, MD 20899, U.S.A.

21. McGrattan, K.B., Rehm, R.G., Tang, H.C., Baum, H.R. (1992) 'A Boussinesq Algorithm for Buoyant Convection in Polygon Domains' NISTIR 4831, U.S. Department of Commerce,

National Institute of Standards and Technology, Computing and Applied Mathematics Laboratory, Building and Fire Research Laboratory, Gaithersburg, MD 20899, U.S.A.

22. Baum, H.R., McGrattan, K.B., and Rehm, R.G. (1994) Mathematical Modelling and Computer Simulation of Fire Phenomena, *Fire Safety Science – Proceedings of the Fourth International Symposium*, Ottawa, Ontario, Canada, 13-17 June 1994, pp 185-193.

23. Baum, H.R., Ezekoye, O.A., McGrattan, K.B. and Rehm, R.G. (1994) Mathematical Modelling and Computer Simulation of Fire Phenomena, *Theoretical and Computational Fluid Dynamics*, **6**, 125-139.

24. Mell, W.E., McGrattan, K.B. and Baum, H.R. (1996) Numerical Simulation of Combustion in Fire Plumes, *Twenty-Sixth Symposium (International) on Combustion/The Combustion Institute*, pp 1523-1530.

25. Baum, H.R., McGrattan, K.B., and Rehm, R.G. (1996) Large Eddy Simulations of Smoke Movement in Three Dimensions, *Conference Proceedings of the Seventh International Interflam Conference*, Interscience Communications, London, pp 189-198.

26. Baum, H.R and McCaffrey, B.J. (1989) Fire Induced Flow Field - Theory and Experiment, *Fire Safety Science – Proceedings of the Second International Symposium*, pp 129-148.

27. Baum, H.R., McGrattan, K.B., and Rehm, R.G. (1997) Three Dimensional Simulations of Fire Plume Dynamics, *Fire Safety Science – Proceedings of the Fifth International Symposium*, pp 511-522.

28. Rehm, R.G., McGrattan, K.B., Baum, H.R., and Cassel K.W. (1997) Transport by Gravity Currents in Building Fires, *Fire Safety Science – Proceedings of the Fifth International Symposium*, pp 391-402.

29. Mell, W.E., Baum, H.R. and McGrattan, K.B. (1997) Simulation of Fires with Radiative Heat Transfer, *Proceedings – Second International Conference on Fire Research and Engineering*, pp 26-33.

30. Baum, H.R. and Mell, W.E. (1998) A Radiative Transport Model for Large Eddy Fire Simulations, *Combustion Theory Modelling*, **2**, 405-422.

31. McGrattan, K.B. and Forney, G.P. (2000) 'Fire Dynamics Simulator – User's Manual' NISTIR 6469, National Institute of Standards and Technology, U.S. Department of Commerce, Gaithersburg, MD 20899.

32. McGrattan, K.B., Baum, H.R., Rehm, R.G., Hamins, A. and Forney, G.P. (2000) 'Fire Dynamics Simulator – Technical Reference Guide' NISTIR 6467, National Institute of Standards and Technology, U.S. Department of Commerce, Gaithersburg, MD 20899.

33. Baum, H.R. (1999) Large Eddy Simulations of Fires – from Concepts to Computations, *Fire Protection Engineering*, Issue No 6, pp. 36-42.

34. Baum, H.R. and Rehm, R.G. (1984) Finite Difference Solutions for Internals Waves in Enclosures, *SIAM Journal on Scientific and Statistical Computing*, **5** No. 4, 958-977.

35. Baum, H.R., Rehm, R.G., Barnett, D.P. and Corley, D.M. (1983) Finite Difference Calculations of Buoyant Convection in an Enclosure, 1. The Basic Algorithm, *SIAM Journal on Scientific and Statistical Computing*, **4** No. 1, 117-135.

36. Zukoski, E., Kubota, T. and Cetegen, B. (1980) 'Entrainment in Fire Plumes' National Bureau of Standards Report NBS-GCR 80-294, Gaithersburg, MD 20899, U.S.A.

37. Rehm, R.G., Barnett, D.P. Baum, H.R., and Corley, D.M. (1985) Finite Difference Calculations of Buoyant Convection in an Enclosure: Verification of the Non-linear Algorithm, *Applied Numerical Mathematics*, **1**, 515-529.

38. Tsang, G. (1970) Laboratory Study of Two-Dimensional Starting Plumes, *Atmospheric Environment*, **4**, 519-544.

39. Chan, W.R., Zukoski, E.E. and Kubota, T. (1992) 'Experimental and Numerical Studies on Two-Dimensional Gravity Currents in a Horizontal Channel' Guggenheim Jet Propulsion Center, California Institute of Technology, Pasadena, California.

40. Simpson, J.E. (1987) *Gravity Currents in the Environment and the Laboratory*, Published by Halsted Press: a division of Kohn Wiley & Sons, New York.

41. Chobotov, M.V., Zukoski, E.E. and Kubota, T. (1986) 'Gravity Currents with Heat Transfer Effects' National Bureau of Standards Report, NBS-GCR 87-522, Gaithersburg, MD 20899, U.S.A.

42. Fleischmann, C.M. and McGrattan, K.B. (1999) Numerical and Experimental Gravity Currents related to Backdrafts, *Fire Safety Journal*, **33**, 21-34.

43. Fleischmann, C.M., Pagni, P.J. and Williamson, R.B. (1994) Salt Water Modelling of Fire Compartment Gravity Currents, *Proceedings of the Fourth International Symposium of Fire Safety Science*, pp 253-264.

44. Fleischmann, C.M. (1994) 'Backdraft Phenomena' NIST-GCR 94-646, National Institute of Standards and Technology, Gaithersburg, MD 20899, U.S.A.

45. McGrattan, K.B., Baum, H.R. and Rehm, R.G (1998) Large Eddy Simulations of Smoke Movement, *Fire Safety Journal*, **30**, 161-178.

46. Steckler, K.D., Quintiere, J.Q. and Rinkinen, W.D. (1982) Flow Induced by a Fire in a Compartment, *19th International Symposium on Combustion, The Combustion Institute, Pittsburgh*, pp 912-920.

47. Steckler, K.D., Baum, H.R. and Quintiere, J.Q. (1984) Fire Induced Flows through Room Openings – Flow Coefficients, *20th International Symposium on Combustion, The Combustion Institute*, pp 1591-1600.

48. McGrattan, K.B., Hamin, A. and Stroup, D. (1998) 'Sprinkler, Smoke & Heat Vent, Draft Curtain Interaction – Large Scale Experimental Model Development' NISTIR 6196-1, National Institute of Standards and Technology, U.S. Department of Commerce, Gaithersburg, MD 20899.

49. Simcox, S., Wilkes, N.S. and Jones, I.P. (1988) 'Fire at Kings Cross Underground Stations, 18th November 1987: Numerical Simulations of the Buoyant Flow and Heat Transfer', Harwell Report AERE-G 4677, May.

50. Steckler, K.D., Baum, H.R. and Quintiere, J.G. (1986) 'Salt Water Modelling of Fire Induced Flows in Multicompartment Enclosures' NBSIR 86-3327, National Bureau of Standards, National Engineering Laboratory, Center for Fire Research, Gaithersburg, MD 20899.

51. *CRC Handbook of Chemistry and Physics*, 57th Edition, Ed: R.C. Weast, CRC Press, 18901 Cranwood Parkway, Cleveland, Ohio 44128, U.S.A.

52. Streeter, V.L. and Wylie, E.B. (1975) *Fluid Mechanics*, 6th Edition, McGraw-Hill Book Company, New York, pg 712.

Chapter 3 - EXPERIMENTAL METHOD

The salt water experimental program was divided into three parts; T-Series, P-Series and C-Series experiments. Each series is described separately in Sections 3.2, 3.3 and 3.4 respectively. Laser Induced dye Fluorescence (LIF) was used in all of the experiments to map the fluid density. The details of the LIF procedure and the experimental apparatus have been well documented previously[1][2], such that they will not be presented here. It is appropriate however, to provide a basic overview of the LIF technique and analysis, to enable the reader to comprehend the sources of uncertainty that are quantified later in Chapter 4.

3.1 Laser Induced dye Fluorescence

3.1.1 Theory

Laser Induced dye Fluorescence (LIF) is a flow visualisation technique that can be used to quantify concentration. In this research, the technique is used to quantify the concentration of saline as the brine solution flows through a freshwater environment. LIF uses a sheet of laser light to visualise the flow of a specific fluid in a two dimensional plane. The coherent light of the laser excites a tracer dye that is mixed into the fluid being studied. The tracer dye is excited into a fluorescent state, so that only the fluid in the two-dimensional plane of the laser sheet is illuminated.

Previous research[3] has shown that the fluorescence of the Rhodamine 6G tracer dye is linearly related to its concentration in solution. The LIF technique utilises the linear response characteristic of this tracer dye to quantify dilution. The dye is mixed thoroughly through the fluid that is to be visualised, so that it has a uniform concentration at the source of the flow. When the solution is injected into an ambient fluid (that contains no dye), the dilution that occurs to the host fluid reduces the concentration of dye in solution. Nil fluorescence implies that the fluid has ambient conditions. Thus, the concentration of the tracer dye in the host solution is representative of the concentration of the agent that is responsible for the density difference. The fluorescence that is emitted from the flow provides a measure of the concentration of the buoyancy agent in the solution. The linear response characteristic of the tracer dye means that the dye fluorescence can be calibrated, so that the absolute concentration of the buoyancy agent in solution can be determined from the fluorescence emitted by the solution; see Equation (3-1).

$$C_{Solution} = \left(\frac{F_{Solution}}{F_{Calibration}} \right) \times C_{Calibration} \qquad \text{Equation (3-1)}$$

Where

$C_{Solution}$ = Concentration of buoyancy agent in solution

$C_{Calibration}$ = Concentration of buoyancy agent in the calibration solution

$F_{Solution}$ = Fluorescence emitted from solution

$F_{Calibration}$ = Fluorescence emitted from the calibration solution

In the experimental procedure, the solution that was used to calibrate the fluorescence was a diluted sample of the solution that was injected at the source of the flow. Thus, the concentration of the buoyancy agent at any point in the flow could be determined from the fluorescence emitted from the flow, and from the characteristics of the fluid that was injected at the source; see Equation (3-2).

$$C_{(x,y,z)} = \left[\frac{F_{(x,y,z)}}{F_{Calibration}}\right] \times \left[\frac{F_{Calibration}}{F_o}\right] \times C_o \qquad \text{Equation (3-2)}$$

During experiments, a video camera was used to film the plane of the flow illuminated by the laser sheet. Capturing images of the fluorescent light emitted by the fluid provided an unobtrusive means of measuring the fluorescence of the solution. Ensuring that the light intensities captured in images were not distorted in any non-linear way from the light intensities that were emitted from solution (i.e., the image capture equipment and process had a linear response), meant that the fluorescence captured in images could be used to determine dilution information about the flow.

The images captured from the video camera were constructed of a rectangular array of pixels. The brightness of each pixel was described by a grey scale integer value between zero and two hundred and fifty five. The grey scale values of the image pixels were used to measure the fluorescence emitted from a point in the flow. To ensure that the light intensities used in the calculations were only a measure of the light emitted by the fluorescent tracer dye, background light intensities were subtracted from those intensities that were captured in the images of the flow and the calibration solution; see Equation (3-3).

$$C_{(x,y,z)} = \left[\frac{G_{Flow} - G_{B-Flow}}{G_{Cal} - G_{B-Cal}}\right] \times \left[\frac{F_{Calibration}}{F_o}\right] \times C_o \qquad \text{Equation (3-3)}$$

Where

G_{Flow} = Grey scale value of pixels in the image of the flow.

$G_{B\text{-}Flow}$ = Grey scale value of pixels in the image of the background light conditions for the flow apparatus.

G_{Cal} = Grey scale value of pixels in the image of the calibration solution.

$G_{B\text{-}Cal}$ = Grey scale value of pixels in the image of the background light conditions for the calibration apparatus.

Thus, the relative fluorescence emitted from the flow and the calibration solution was determined from image analysis. A Fluorometer[4] was used to measure the relative fluorescence emitted from the calibration solution and the source solution ($F_{Calibration}/F_o$).

For saline (at 20°C), there is a linear relationship between the concentration of salt mass in solution and the density difference between the saline fluid and freshwater. For the flow of salt water in a freshwater environment, the concentration terms in Equation (3-3) can therefore be replaced with density difference terms, to give Equation (3-4). This is the relationship that was used in the LIF analysis to map the density difference of the flow field from images of the flow and knowledge of the density difference between the fluids at the source of the flow. The density difference at the flow source was determined by using a PAAR density meter to measure the density of fluid samples taken from the saline source solution and the ambient freshwater. In this research, density measurements are presented as normalised density difference, where the density difference between the fluids at the source of the flow is the normalising quantity; i.e. $\Delta\rho^* = \Delta\rho/\Delta\rho_o$.

$$\Delta\rho_{(x,y,z)} = \left[\frac{G_{Flow} - G_{B-Flow}}{G_{Cal} - G_{B-Cal}}\right] \times \left[\frac{F_{Calibration}}{F_o}\right] \times \Delta\rho_o \qquad \text{Equation (3-4)}$$

3.1.2 Laboratory Equipment

In each salt water experiment, saline fluid was injected into a transparent perspex (PMMA) model that was submerged in freshwater. The freshwater was contained in a tank that was 6.2*m* long, 1.5*m* wide and 1.0*m* deep. The sides of the tank were a series of glass windows, each 0.70*m* wide by 0.98*m* high. The perspex models sat on a mobile trolley that ran along two tracks, which were fixed to the floor of the tank and aligned parallel to the tank walls. The models were elevated 300*mm* above the floor of the tank to prevent the saline fluid that had passed through the model flowing back into the geometry. A black polythene wave sheet was suspended in the tank behind the models to block any background light sources that could be viewed by the camera during experiments. A fine plastic-mesh wave sheet was suspended across the width of the tank to dissipate any seiche that was set up through the movement of apparatus during experiments. Figure 3-1 shows the general configuration of the LIF experimental apparatus.

All the internal surfaces of the perspex models, with the exception of the side through which the camera viewed the flow, were lined with black, matt-finish metal sheeting. The metal sheeting was 1*mm* thick, and was fixed to the internal surfaces of the models with double sided adhesive tape. The black sheeting prevented fluorescent light from the tracer dye reflecting off the polished internal surfaces of the model.

The laser sheet that was used during experiments was generated from a Coherent Innova 70-5 Ion laser. The laser was operated in a self-regulating mode to produce coherent light with a wavelength of 514.5*nm*, at a constant power of 2.0*W*. The laser sheet was generated from a single beam of laser light. This was accomplished by reflecting the beam off the faces of a rotating octagonal mirror that was located near the focal point of a parabolic mirror. The octagonal mirror was spinning at a rate of 20000*rpm*, which caused the light beam to sweep through a vertical plane with a frequency of 2667*Hz*[1][2]. To the naked eye and the video camera, this appeared as a continuous sheet of laser light.

A Pulnix TM-765E black and white high-resolution CCD camera was used to film the fluorescent light emitted from the Rhodamine dye in the saline solution. The camera was fitted with an image intensifier and a Cosmicar CCTV 16*mm*/F1.4lens. A Schott glass optical filter, type OG530, was positioned in front of the camera to filter out light of wavelengths less than 530*nm*. A Topward TPS-4000 supply box was used to provide the twelve-volt DC power for the camera.

A Data Translation Inc DT2867 frame grabber board was used to capture images from the camera video signal. The board was installed in a Pentium II PC, and was operated via the Windows software package Global Lab Image 2.0[5]. The A/D conversion process of the video signal was performed with Gain, Zero Offset and A/D Reference values of 1, -60 and 1024 respectively. These values were found to be appropriate for the aperture and intensifier settings that were used on the camera for the light levels experienced during experiments. Previous research[1][2] used these same values in LIF work conducted with the same experimental apparatus.

The Input Look Up Tables PRE.ilt and POST.ilt were used to linearise the image capture process. PRE.ilt was used for the T-Series experiments, while POST.ilt was used for the P-Series and C-Series experiments. Section 3.4.1 discusses these Input Look Up Tables (ILUT) further. All images captured during the experiments were 10 second time-averaged images that were saved directly to the hard drive of the PC. The time averaging was done in real time by the frame grabber board, through averaging 250 consecutive frames from the video camera (which had a temporal resolution of 25*Hz*). After the experiments, the Scion Image software package[6] was used to combine ten time-averaged images of the flow to create a single one hundred second time-averaged image.

Images from the camera were recorded onto video-cassette using a Panasonic NV-FS200EC video recorder. A Sony PVM-1442QM Trinitron colour video monitor was used to view the live images from the camera, and the images captured by the frame grabber board.

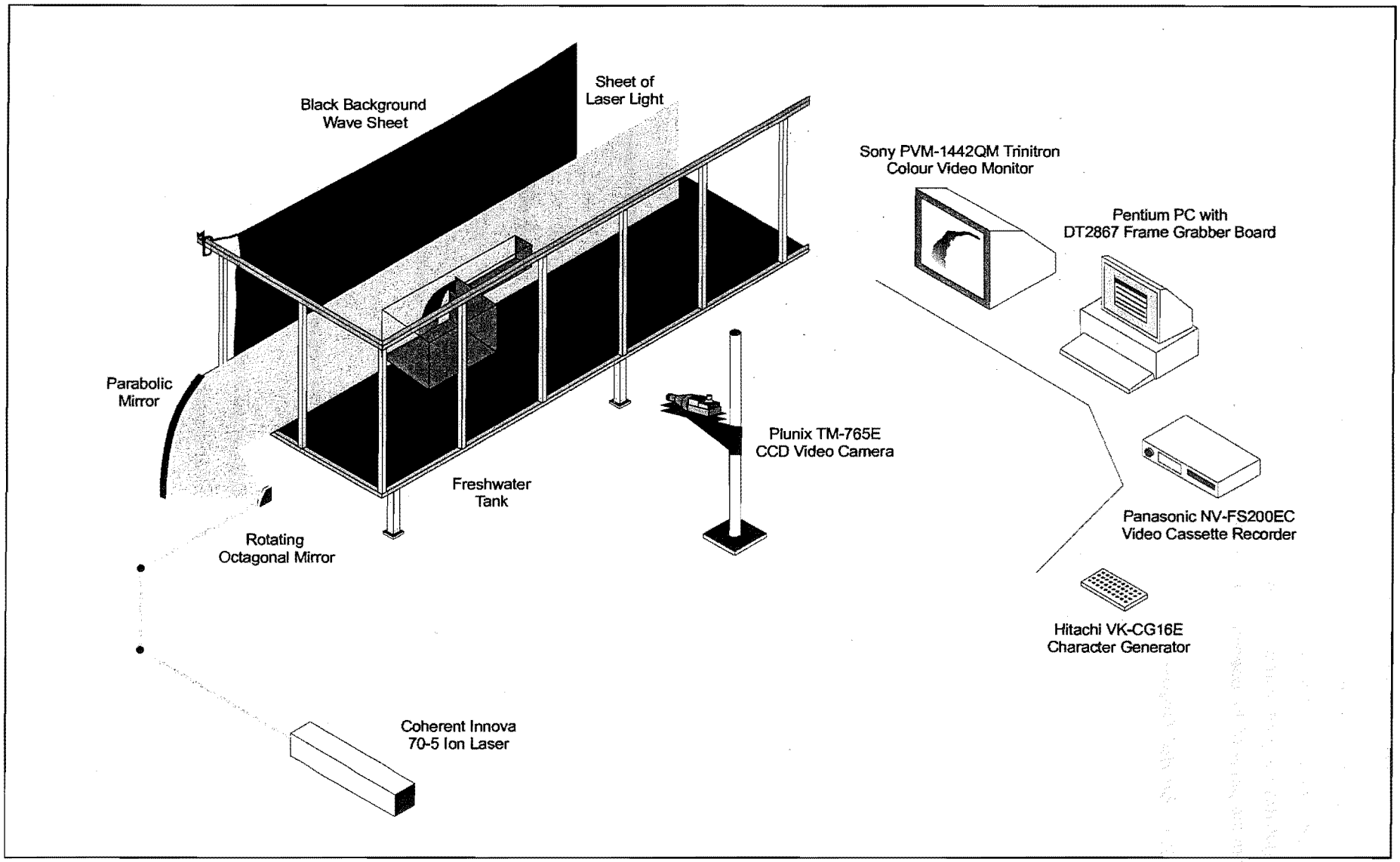

Figure 3-1 Schematic diagram of the Laser Induced dye Fluorescence (LIF) apparatus that was used in the salt water experiments.

3.2 T-Series Experiments

The T-Series (Transitional flow) experiments used the LIF technique to map the density field of a buoyant saline plume that spilt from a rectangular opening between two compartments. The negatively buoyant plume underwent a transition from laminar to fully turbulent behaviour as it spilt from the plane of the opening onto the floor of the second compartment.

3.2.1 Model Geometry

The model that was used in the T-Series experiments consisted of two rectangular compartments that were connected by an opening in the wall between them. The opening had a rectangular geometry with height and width of $0.824H$ and $0.376H$ respectively; where H is the height of the source compartment. The second compartment (into which the plume spilled) was twice as high and three times as wide as the compartment that contained the source for the flow. The geometry and the as-built interior dimensions of the T-Series model are shown in Figure 3-3. The wall that separated the two compartments was $3mm$ thick.

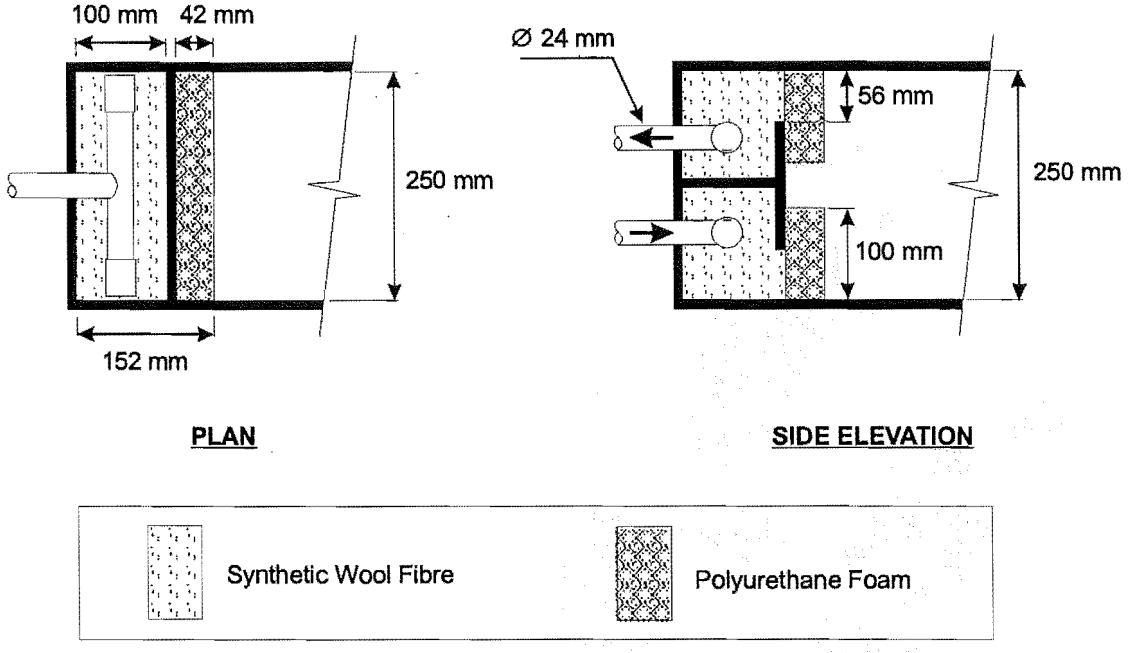

Figure 3-2 Geometry and dimensions of the flow source in the T-Series model.

Figure 3-2 details the geometry and dimensions of the T-Series flow source. The source was built into the rear of the smaller compartment, a clear distance $1.4H$ back from the plane of the opening. It was designed to artificially generate an exchange flow through the opening that connected the two compartments. Ambient freshwater was drawn into the source compartment through the upper portion of the opening, while saline solution spilled out of the compartment through the lower portion. The freshwater flow was drawn out of the source compartment through a porous polyurethane foam block that was lodged against the ceiling of the model.

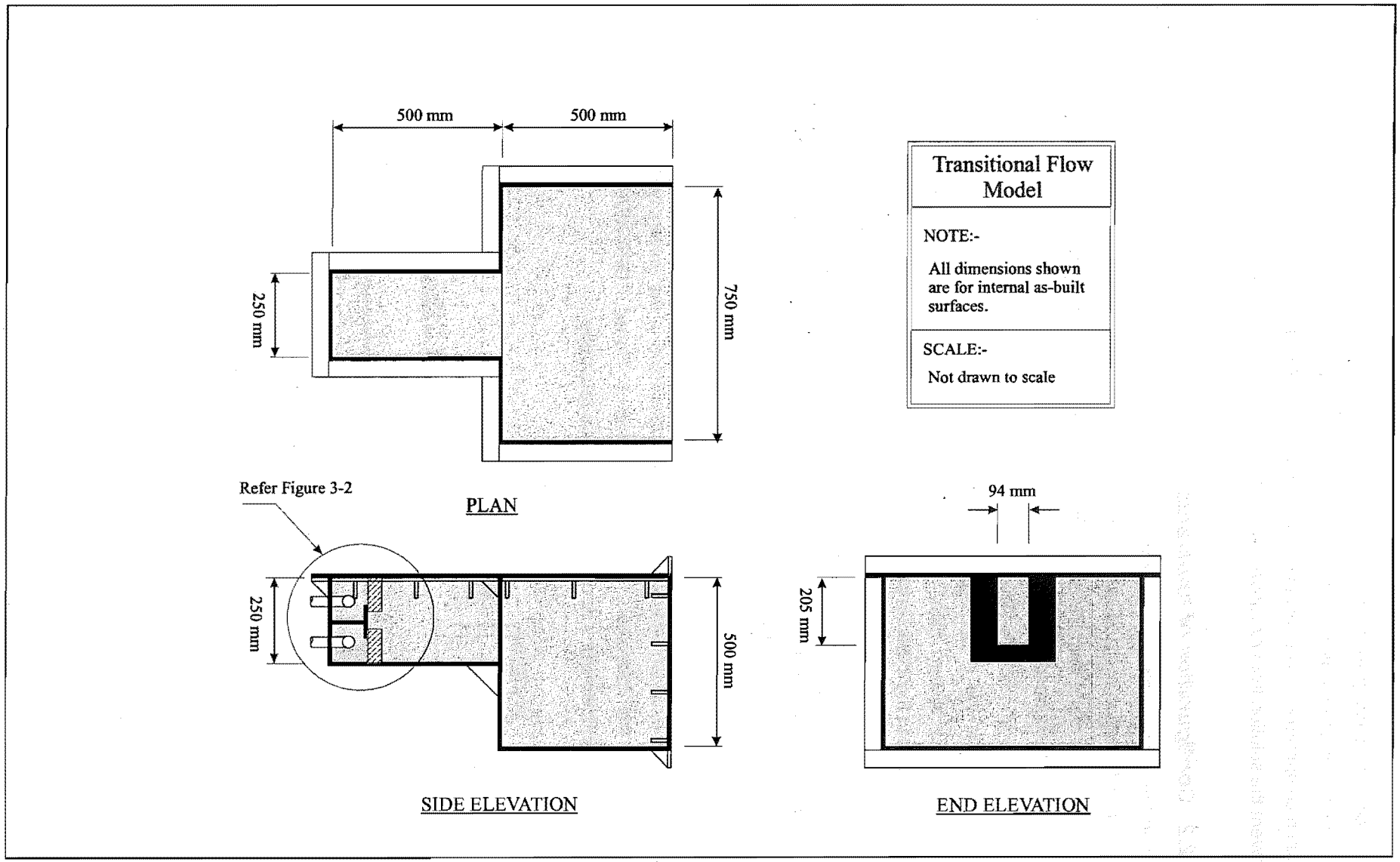

Figure 3-3 Geometry and dimensions of the T-Series model.

Similarly, the saline fluid was injected into the source compartment through another polyurethane foam block that was pressed against the floor of the compartment. The polyurethane foam blocks distributed the volume flow of each solution as uniformly as possible over the entire width of the source compartment. The foam was pressed firmly against the boundaries of the compartment, to prevent the solution from circumventing the flow path through the porous media.

3.2.2 *Configuration of Apparatus*

During the experiments, the light sheet from the laser was shone through the end window of the freshwater tank (below the level of the water surface). The sheet was aligned parallel to the tank walls, and was offset from the internal surface of the windows by approximately 580*mm*. The T-Series model was positioned on the trolley so that the laser sheet illuminated the centreline plane of the model geometry. The video camera was located approximately 790*mm* away from the laser sheet, such that the image captured of the centreline plane of the model was approximately 550*mm* wide by 390*mm* high. Figure 3-4 is a schematic diagram of the configuration of the apparatus used in the T-Series experiments.

Saline solution was gravity fed into the source of the model from a constant head tank located on a mezzanine floor above the laboratory room. The constant head tank had a spilling weir system that provided approximately 4.75*m* of head at the elevation of the tank floor. The volumetric flow rate of the saline solution into the model was measured using a rotameter. The glass housing of the rotameter was a size 24G model manufactured by Rotameter Manufacturing Co Ltd, Croydon, England. A replacement stainless steel float (constructed in the university laboratory workshop) was used in the rotameter. A Bailey Fischer & Porter COPA-XE/MAG-XE, 10DX4011B electromagnetic flowmeter was used to calibrate the rotameter.

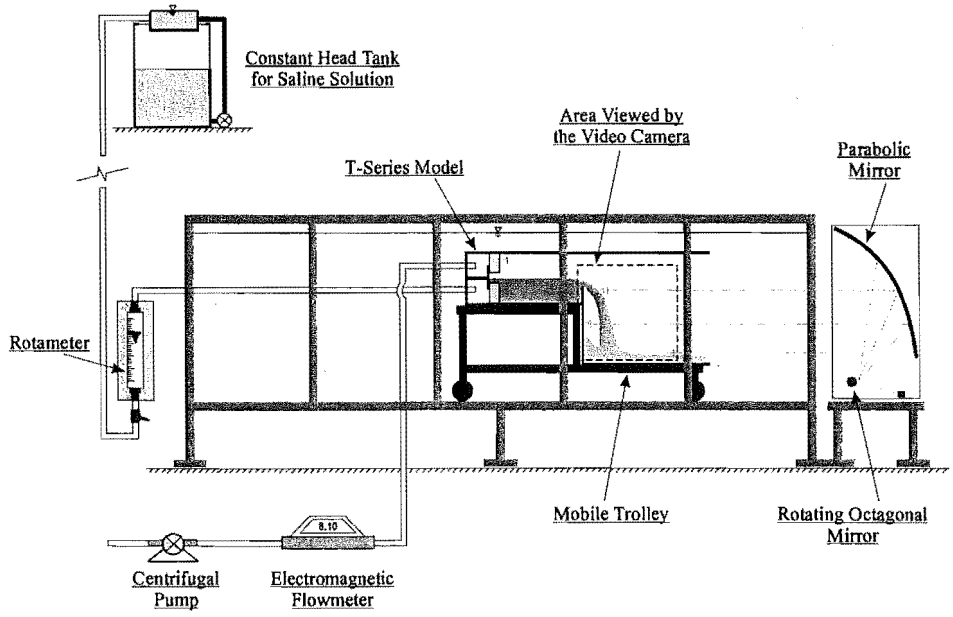

Figure 3-4 Configuration of the experimental apparatus for the T-Series experiments.

The freshwater that was drawn from the flow source in the model was drawn using a Davis centrifugal pump. The flow rate of the freshwater was measured using Bailey Fischer & Porter COPA-XE/MAG-XE, 10DX4011B electromagnetic flowmeter. The flow rate of the freshwater was sampled, and logged directly to a PC at a frequency of 4Hz over the time interval that images of the flow were captured in each experiment.

3.2.3 Matrix of Experiments

Six different experiments were conducted in the T-Series investigation. One of the six experiments, T02, was repeated a further four times, to quantify the repeatability of the experimental results. Table 3-1 details the source conditions for the fluid streams in each T-Series experiment. Three different saline solution densities were used in combination with two different volumetric flow rates to create the six different experiments. The densities of the saline and freshwater solutions for each experiment are shown in Table 3-1; the three saline densities equate to approximate salt mass fractions of 0.5%, 1.0% and 2.0%. In all of the T-Series experiments the volumetric flow rate of saline injected into the model source was approximately equal to the volumetric flow rate of freshwater drawn out of the source. The two volumetric flow rates that were used for the saline and freshwater fluid streams are also shown in Table 3-1; the flow rates shown are equal to 8.0*l/min* and 17.1*l/min*. Throughout this document, the density difference between the fluids at the source of the flow is described via the variable β, which is the density difference ratio, as given by Equation (3-5). The geometry of the model was not altered in any of the T-Series experiments.

$$\beta = \frac{(\rho_s - \rho_\infty)}{\rho_s} \qquad \text{Equation (3-5)}$$

Exp Title	ρ_s (kg/m^3)	ρ_∞ (kg/m^3)	β -	$\dot{V}_s$ (m^3/s $\times 10^4$)	$\dot{V}_\infty$ (m^3/s $\times 10^4$)	T_s (°C)	T_∞ (°C)
T01	1002.15	999.32	0.003	1.334	1.336	18.7	14.0
T02	1005.70	999.23	0.006	1.334	1.338	19.0	14.6
T03	1012.85	999.30	0.013	1.334	1.340	18.5	14.0
T04	1002.16	999.30	0.003	2.851	2.815	19.0	14.0
T05	1005.69	999.19	0.006	2.851	2.883	19.2	14.5
T06	1012.74	999.38	0.013	2.851	2.857	19.3	13.7
T07	*1006.14*	*999.40*	*0.007*	*1.334*	*1.331*	*17.0*	*13.6*
T08	*1005.93*	*999.39*	*0.006*	*1.334*	*1.352*	*18.2*	*13.7*
T09	*1005.52*	*999.37*	*0.006*	*1.334*	*1.340*	*20.2*	*13.9*
T10	*1005.73*	*999.31*	*0.006*	*1.334*	*1.329*	*19.2*	*14.1*

Table 3-1 Fluid conditions at the flow source for each T-Series experiment.

3.3 P-Series Experiments

The P-Series (Plume) experiments used the LIF technique to map the density field of a buoyant salt water plume injected into a compartment that was open to the ambient atmosphere. The salt water plumes that were generated in the P-Series experiments were later used in the C-Series experiments. The C-Series experiments studied the buoyant flow field that forms in a compartment adjacent to the source room. Therefore, the purpose of the P-Series work was to accurately quantify the source plumes that were used in the C-Series experiments.

3.3.1 Model Geometry

The model that was used in the P-Series experiments was a rectangular compartment that was 400*mm* high, 400*mm* wide and 1200*mm* long. The geometry and the as-built interior dimensions of the model are shown in Figure 3-6. The overall dimensions of the model were scaled to represent two ISO fire rooms connected end on end; however no wall was installed in the P-Series model to separate the two rooms. The end of the model that was remote from the plume source was completely open to the ambient environment.

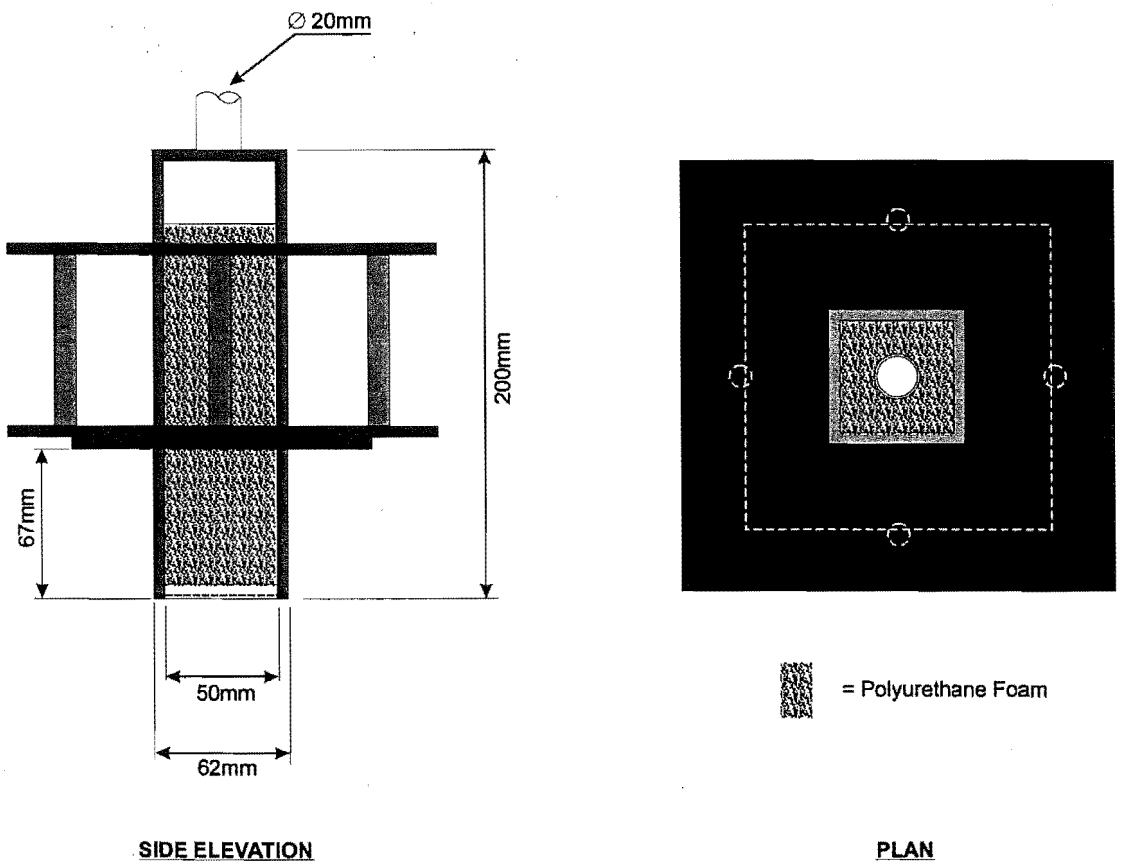

Figure 3-5 ***Geometry and dimensions of the plume source that was used in the P-Series and C-Series experiments***

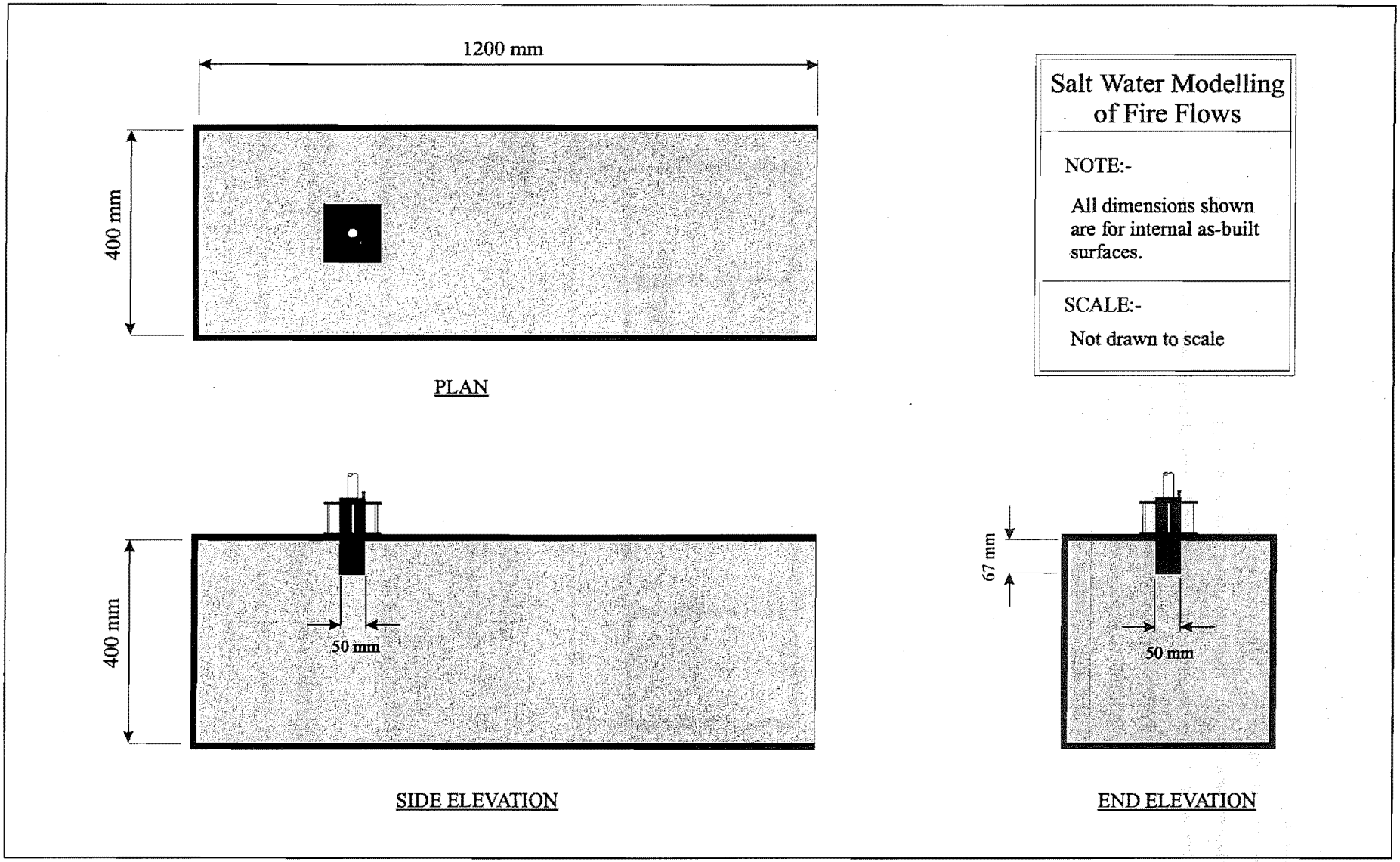

Figure 3-6 Geometry and dimensions of the P-Series model.

Figure 3-5 details the geometry of the salt water plume source. The centre of the source was located on the centreline plane of the model, 300*mm* out from the closed end of the compartment. The source protruded down from the top of the model 67*mm,* and discharged through a horizontal square port of 50*mm* dimension. Three layers of a fine stainless steel mesh were placed across the source opening. The rectangular chamber above the opening was packed with porous polyurethane foam. The foam and fine wire mesh served to distribute the saline flow over the entire area of the square port. The three layers of mesh were stainless steel 40/40x0.010" (No of strands per inch both ways x wire diameter). A fourth, more sturdy layer of mesh was placed at the very base of the source to prevent the foam being forced out of the rectangular chamber, and to minimise the out of plane deflection of the three finer mesh layers. The fourth layer of mesh was stainless steel 10/10x0.023". The plume source was constructed of 6*mm* thick perspex.

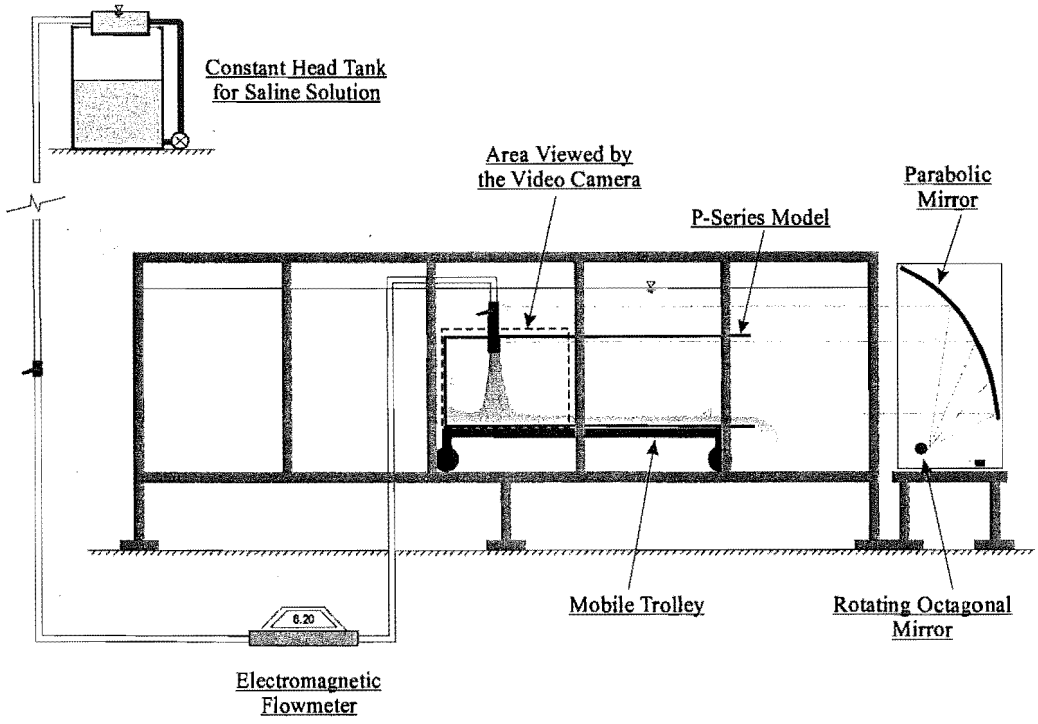

Figure 3-7 Configuration of the experimental apparatus for the P-Series experiments.

3.3.2 Configuration of Apparatus

The configuration of the laser sheet during the P-Series work was the same as that used in the T-Series experiments. The camera however, was set further back from the sheet, at approximately 1050*mm*. The image that was captured by the camera from the plane of the laser sheet was approximately 723*mm* wide by 500*mm* high. Figure 3-7 is a schematic diagram of the configuration of apparatus used in the P-Series experiments.

As with the T-Series experiments, saline solution was gravity fed to the model from a constant head storage tank on a mezzanine floor above the laboratory. A Bailey Fischer & Porter COPA-

XE/MAG-XE, 10DX4011B electromagnetic flowmeter was used to measure the volumetric flow rate of the saline injected at the plume source. The flow rate was sampled, and logged to a PC at a frequency of 4*Hz* for the time interval that images of the flow were captured.

3.3.3 Matrix of Experiments

Two different salt water plumes were generated in the P-Series experiments; P01 and P06. The generation of plume P01 was repeated a further four times to assess the repeatability of the C-Series source conditions. The density of the saline solution was the only property changed between the two source plumes. Table 3-2 details the characteristic properties of the fluids that were used in the P-Series experiments. For each experiment the density of the saline solution and the freshwater are listed in Table 3-2, along with the volumetric flow rate of saline that was injected through the plume source. The buoyancy at the plume source is expressed via the variable β, and the initial temperatures of both fluids are given. The two saline solutions that were used for the plumes had approximate mass fractions of salt mass in solution of 1.5% and 3.0%. A volumetric flow rate of 6.2*l/min* was used for both plumes. The geometry of the model was not altered for any of the P-Series experiments.

Exp Title	ρ_s (kg/m^3)	ρ_∞ (kg/m^3)	β -	$\dot{V}_s$ (m^3/s $\times 10^4$)	T_s (°C)	T_∞ (°C)
P01	1009.31	999.54	0.01	1.033	18.9	12.4
P02	*1009.10*	*999.50*	*0.01*	*1.024*	*19.8*	*12.6*
P03	*1009.53*	*999.56*	*0.01*	*1.039*	*18.0*	*12.3*
P04	*1008.87*	*999.46*	*0.01*	*1.033*	*21.0*	*13.0*
P05	*1009.13*	*999.50*	*0.01*	*1.035*	*19.7*	*12.7*
P06	1020.53	999.52	0.02	1.046	18.0	12.6

Table 3-2 Fluid conditions at the flow source for each P-Series experiment.

3.4 C-Series Experiments

The C-Series (Corridor) experiments used the LIF technique to map the density of the saline layer that formed in a room that was connected to a compartment containing a salt water plume. The C-Series saline flows are representative of the flow field that would occur in the adiabatic movement of low temperature smoke through the internal geometry of a residential scale building.

3.4.1 Model Geometry

The overall dimensions of the model that was used in the C-Series experiments were the same as those of the model used in the P-Series work; i.e. 400*mm* high, 400*mm* wide and 1200*mm* long. The C-Series model however, differed from the P-Series model, in that it was divided at mid-length into two compartments of equal size. Both compartments were a scaled representation of the ISO fire room [7].

The internal geometry of the model was the primary variable altered in the C-Series work. Figure 3-9 shows the four variations of geometry that were used in the experiments. The variations were achieved by changing the geometry of the opening that connected the two rooms, and the geometry of the opening at the far end of the compartment. To imitate the internal geometry of a residential scale building, the openings were scaled to represent a sill (which extended across the full width of the room), or an open single leaf pedestrian doorway. Figure 3-8 shows the dimensions of the vent plates that were inserted into the model to provide the desired openings.

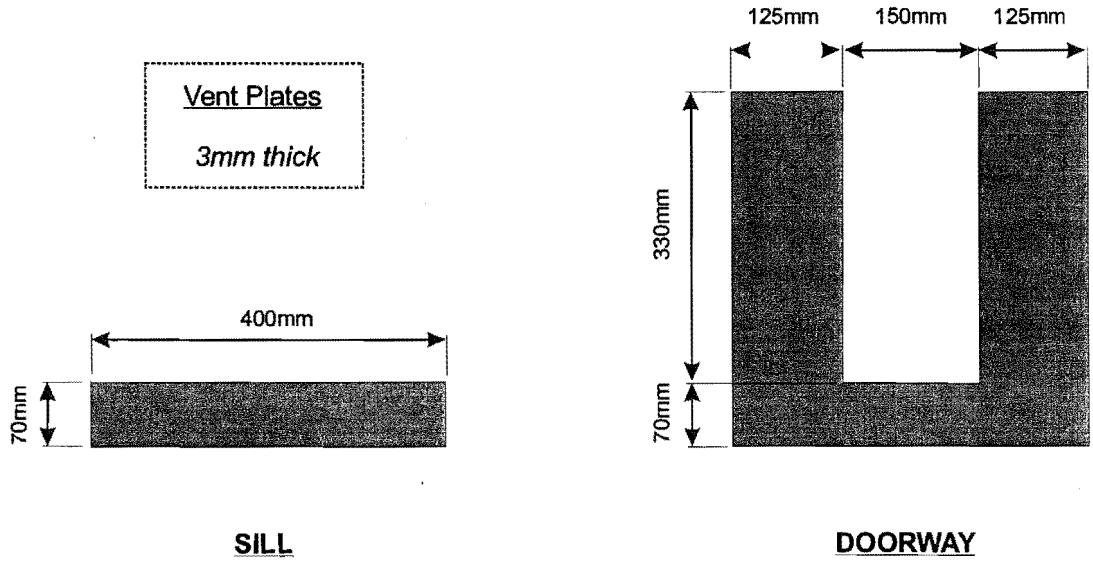

Figure 3-8 ***Geometry and dimensions of the openings that were used in the C-Series models.***

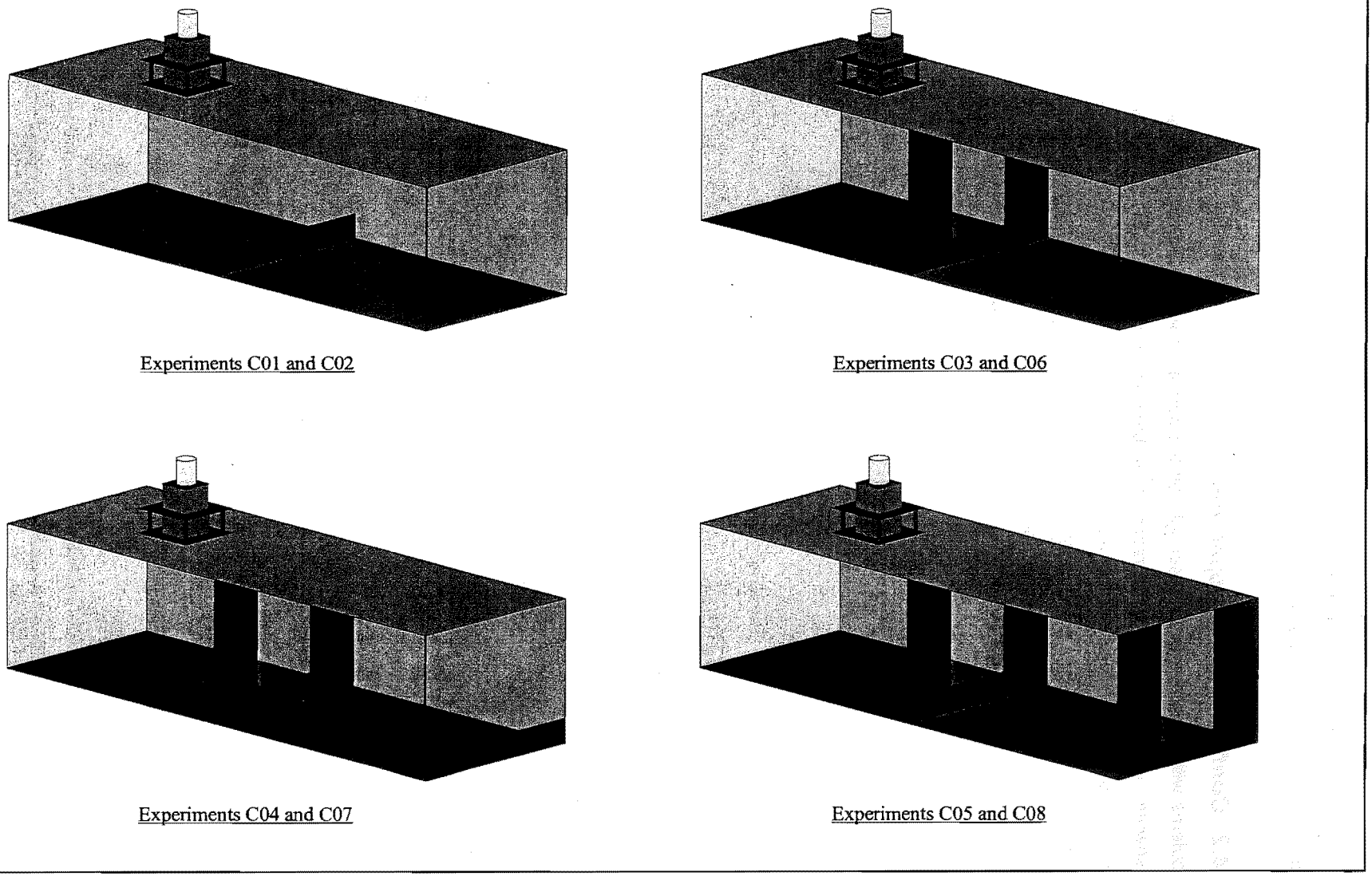

Figure 3-9 Geometry of the four different C-Series models.

The plume source from the P-Series work was reused in the C-Series experiments. None of the properties of the source, including location, were changed. Refer to Section 3.3.1 for detailed discussion of the plume source.

3.4.2 Configuration of Apparatus

Problems with refraction of the laser light off the density interface between the saline layer and the freshwater, meant that the configuration of the laser sheet used in the C-Series work was different from that used in T-Series and P-Series experiments; Section 3.4.3 provides an explanation of the problem. In the C-Series experiments, the laser sheet was elevated above the water level in the tank. At the location of the model, the light sheet was reflected down onto the saline flow with a planer mirror. A 25*mm* wide strip was cut out of the black metal sheeting fixed to the model ceiling, to allow the laser to illuminate the saline flows within the model. The sheet was aligned parallel to the walls of the tank, and was offset from the internal surface of the windows by 580*mm*. The video camera was located approximately 945*mm* away from the laser sheet. The image that the camera captured from the plane of the laser sheet was approximately 656*mm* wide by 451*mm* high.

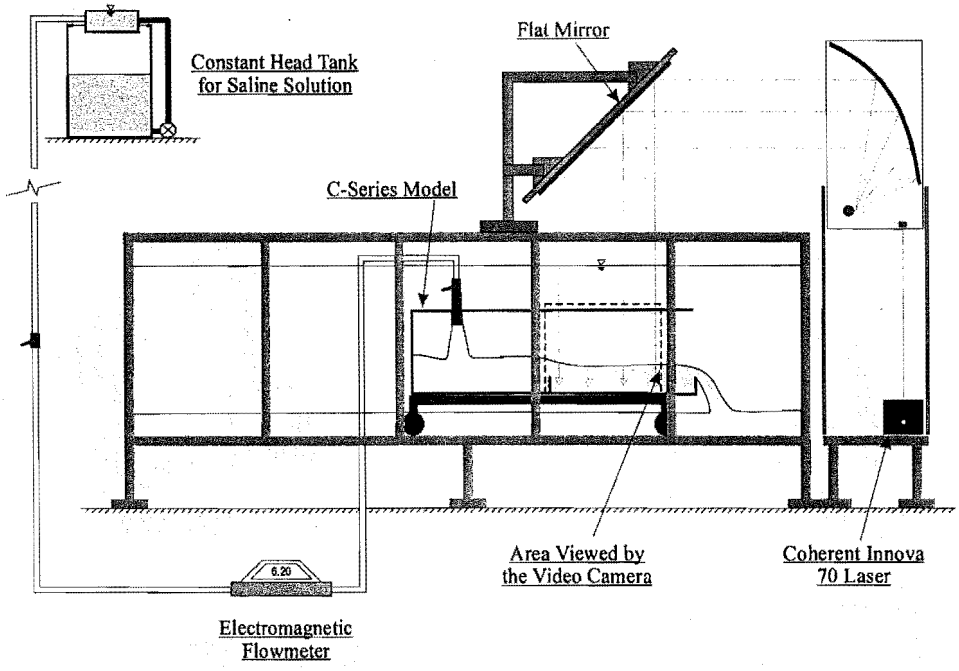

Figure 3-10 Configuration of the experimental apparatus for the C-Series experiments.

Just as in the P-Series experiments, saline solution was gravity fed to the plume source from a constant head storage tank on a mezzanine floor above the laboratory. A Bailey Fischer & Porter COPA-XE/MAG-XE, 10DX4011B electromagnetic flowmeter was used to measure the volumetric flow rate of the saline. The flow rate was sampled, and logged to a PC at a frequency of 4*Hz* for

the time interval that images of the flow were captured. Figure 3-10 schematically shows the configuration of the equipment that was used in the C-Series experiments.

3.4.3 Refraction off the Density Interface

In the P-Series experiments, dark horizontal bands were observed near the top of the saline layer, which formed around the impingement region of the plume. The dark bands were caused by the laser light being reflected off the density interface between the saline fluid and the freshwater in the downstream region of the model. The reflection off the density interface prevented light at the saline layer height reaching the end of the model, thereby causing the horizontal shadow bands that were observed in the experiments. The disruption of the uniform light conditions prevented density measurements being taken from the saline layer. Measurements were, however, still able to be collected of the plume density before the plume plunged into the layer.

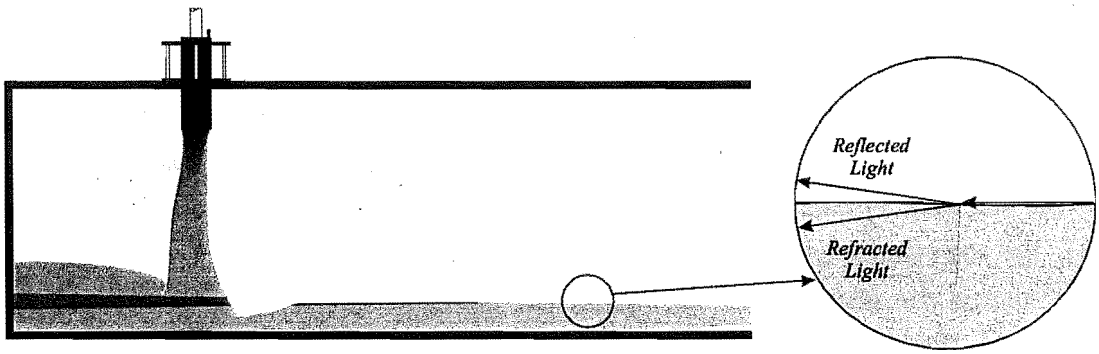

Reflection off the Density Interface in the P-Series Experiments

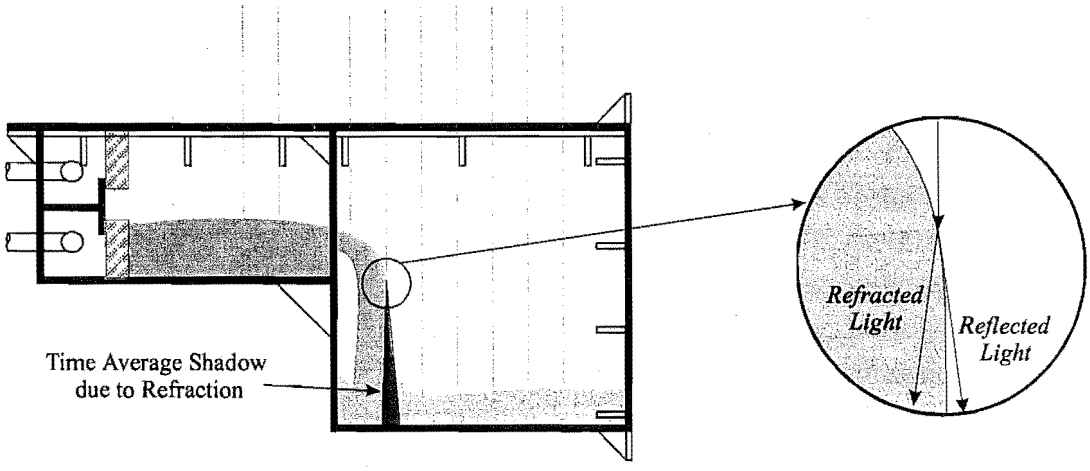

Reflection off the Density Interface in the T-Series Experiments

Figure 3-11 Schematic illustration of the shadow bands caused by the reflection of the laser light off the density interface between the salt water and freshwater.

Problems with reflection off a density interface were also seen in preliminary work for the T-series experiments. In these preliminary experiments, the laser sheet had a vertical orientation similar to that used in the C-series experiments. Here, refraction occurred off the density interface of the laminar section of the spilling plume. As the saline fluid spilled over the edge of the sill, the interface with the ambient freshwater curved downward, before being broken up by turbulence. The vertical light beam from the laser reflected off the edge of the saline flow at the point where the interface between the fluids was very nearly vertical. This created dark vertical shadow bands around the impingement region of the plume. In order to study the plume in the T-series work, the laser sheet orientation had to be changed, so that the flow was illuminated by laser light with a horizontal orientation. With this orientation, there was no reflection of the laser light in any region that would shadow the turbulent region of the plume. Figure 3-11 schematically shows the reflection problems observed in the P-series and T-Series experiments.

3.4.4 Matrix of Experiments

Eight different experiments were conducted in the C-Series experimental investigation. Experiment C06 was additionally repeated once. The two different P-Series plumes were used in combination with the four model geometries shown in Figure 3-9 to constitute the eight different experiments. The two salt water plumes were the same as those detailed in the P-Series work (i.e., P01 and P06). For each C-Series experiment Table 3-3 details the properties of the saline solution at the plume source, the geometry of the model, and the initial temperatures of the fluids in the experiments. The four geometries are represented in Table 3-3 by the following notation: -

S/- A sill between the two compartments with no obstruction on the final opening.

D/- A doorway between the two compartments with no obstruction on the final opening.

D/S A doorway between the two compartments with a sill across the final opening.

D/D A doorway between the two compartments with a doorway on the final opening.

Exp Title	ρ_s (kg/m^3)	ρ_∞ (kg/m^3)	β -	$\dot{V}_s$ (m^3/s x10^4)	Geometry	T_s (°C)	T_∞ (°C)
C01	1008.88	997.96	0.01	1.023	*S/-*	21.0	16.4
C02	1019.49	999.05	0.02	1.023	*S/-*	19.9	15.4
C03	1009.30	999.04	0.01	1.045	*D/-*	19.2	15.3
C04	1008.75	998.90	0.01	1.031	*D/S*	15.7	21.3
C05	1009.34	999.03	0.01	1.016	*D/D*	19.3	15.3
C06	1019.57	998.02	0.02	1.034	*D/-*	20.7	16.3
C07	1019.57	998.02	0.02	1.061	*D/S*	21.4	16.1
C08	1019.35	997.99	0.02	1.013	*D/D*	22.2	16.4
C09	*1020.46*	*999.04*	*0.02*	*1.042*	*D/-*	*19.2*	*16.0*

Table 3-3 ***Model geometry and fluid conditions at the flow source for each C-Series experiment.***

3.5 References

1. Papps, David A. (1995) Merging Buoyant Jets in Stationary and Flowing Ambient Fluids. PhD Thesis, Civil Engineering, University of Canterbury, Christchurch, New Zealand.

2. Gaskin, Susan J. (1995) Single Buoyant Jets in a Crossflow and the Advected Line Thermal. PhD Thesis, Civil Engineering, University of Canterbury, Christchurch, New Zealand.

3. Prasad, R.R. and Sreenivasan, K.R. (1990) Quantitative Three Dimensional Imaging and the Structure of Passive Scalar Fields in Fully Turbulent Flows, *Journal of Fluid Mechanics*, **216**, 1-34.

4. Operating & Service Manual, Model 10 Series Fluorometers, Turner Designs, 2247 Old Middlefield Way, Mountain View, California 94043, Printed in USA October 1981.

5. Global Lab Image Version 2.0, Data Translation Inc., 100 Locke Drive, Marlboro MA 01752-1192, Ph (508) 481-3700, Fax (508) 481-8620.

6. Scion Image - Release Beta 3b, Copyright 1998 Scion Corporation, 82 Worman's Mill Court, Suite H, Frederick, Maryland 21703, Ph (301) 695-7870, E-mail: info@scioncorp.com, http://www.scioncorp.com.

7. International Standard ISO 9705:1993(E). Fire Tests – Full Scale Room Test for Surface Products.

Chapter 4 - UNCERTAINTY ANALYSIS

4.1 Overview

The purpose of conducting the salt water experiments in this research is to generate experimental data that can be used to verify the hydrodynamic model in the Fire Dynamics Simulator. The accuracy of the model is measured according to how well the computational results compare with the salt water experimental measurements. This assessment assumes that the experimental measurements provide a true representation of the fluid dynamics present in the salt water flows. In reality, measurement techniques are subject to error, so that experimental results are not a true measure of the quantity. Therefore, in order to ascertain some knowledge of the hydrodynamic model accuracy from the comparison of the simulation results with experimental data, it is necessary to quantify how close the experimental measurement is to the true value. That is, it is necessary to quantify the uncertainty of the experimental measurements.

In this chapter, the uncertainty of the measurements made in the salt water experiments is quantified. The uncertainty of each measurement is presented as either the limit uncertainty or the probable uncertainty. The limit uncertainty has been quantified for the fluid temperature, volumetric flow rate, source fluid density and the location of the density difference measurements within the flow field. The probable uncertainty has been evaluated for the normalised density difference measurement; it is displayed in the form of confidence envelopes for the measurement. The uncertainties have been evaluated according to the methods details in Baird, D.C. (1962)[1].

4.2 Source Conditions

4.2.1 Volumetric Flow Rate

An electromagnetic flowmeter and a rotameter were used to measure the volumetric flow rates of solutions. The accuracy of the Electromagnetic flowmeter is specified as 0.5% of the flow rate. The reading of the float elevation within the rotameter housing was accurate to within 1 division on the scale provided, such that the flow rate was estimated to be accurate to within 0.1*l/min*.

4.2.2 Fluid Density

An Anton-PAAR density meter was used to measure the density of the fluid samples collected immediately prior to each experiment. The density of each sample was calculated from Equations (4-1) and (4-2). The propagation of the component variable uncertainties in these equations has been considered, to determine the limit uncertainty of the source fluid density. For the range of fluid densities that were used in the salt water experiments, the absolute uncertainty of the density measurement was 0.04 kg/m^3. The component uncertainty of each of the variables in Equations (4-1) and (4-2) is given below.

$$\rho_{sample} = \rho_{water} + \left(\frac{\rho_{water} - \rho_{air}}{c^2_{water} - c^2_{air}} \right) \left(c^2_{sample} - c^2_{water} \right) \qquad \text{Equation (4-1)}$$

Where

$$\rho_{air} = \frac{1.2930}{1 + 0.00367 T_{air}} \frac{P_{atm}}{1013.25} \qquad \text{Equation (4-2)}$$

PAAR Density Meter Count - (c)

The PAAR density meter apparatus consisted of a DMA 60 processing unit, an external DMA 602 remote measuring cell, and a Grant Instruments LTD6-P constant temperature bath. The Period Select DMA 60 processing unit was set at 1k, so that 1000 oscillations of the sample were measured. The sum of the clock pulses (released every 10^{-5}seconds) that were counted over the duration of the 1000 oscillations is precise to one unit.

Density of Freshwater – (ρ_{water})

The density of freshwater at various temperatures was obtained from tabulated standard values[2] to an accuracy of two decimal places. The accuracy of freshwater density is therefore accurate to within 0.001%.

Atmospheric Pressure – (P_{atm})

Atmospheric pressure was measured using a mercury manometer. Mercury levels recorded from the manometer were accurate to within 0.5*mm*, such that the relative accuracy of the atmospheric pressure measurement was less than 0.1%.

Fluid Temperature – (T)

The density of each fluid sample was evaluated at the temperature that the fluid had during the experiment. A digital thermometer was used to ensure that the fluid sample in the remote-measuring cell was in thermal equilibrium while the PAAR density meter readings was taken. The accuracy of the thermometer was 0.1°*C*, such that the temperature measurement had an error of less than 1% (in degrees Celsius).

4.2.3 Fluid Temperature

A glass/mercury thermometer was used to measure the temperature of both the saline fluid in the header tank and the fresh water in the experimental tank. The thermometer scale was precise to 0.1°C, such that the relative error of the temperature measurement was less than 1% when quantified in degrees Celsius.

4.3 Profile Location

Three spatial coordinates describe the location of the density difference measurements in the flow field. Each coordinate has a degree of uncertainty. The horizontal and vertical coordinates, *x* and *z*, describe the location of the measurements within the sheet of the laser light. These are the coordinates that are given in Appendix 1 for the profile locations. Uncertainty in these coordinates is traceable to inaccuracies in the procedure used to spatially calibrate images from the video camera. The third coordinate, *y*, describes the position of the laser sheet within the model. The uncertainty in this coordinate is due to spatial characteristics of the laser sheet.

4.3.1 Uncertainty in the X and Z Coordinates

Spatial calibration of the LIF images was achieved by using an image of a grid to determine the average size of the area represented by each pixel in the image, and the distortion effects of perspective and rotation. In the calibration procedure, an image was captured of a 25*mm* grid sheet that was positioned vertically in the plane of the laser sheet. From the image of the grid, eight pixel locations were selected at the intersection of grid lines. The pixel coordinates and the corresponding grid coordinates (in millimetres) were input into the Global Lab Calibration Tool for all eight points. From these sample points, the software determined a translation function to remap the pixel coordinates of the image to the real world spatial coordinates of the grid. Within this spatial calibration process, there were two primary sources of error.

1. the accuracy with which the calibration grid sheet was positioned in the flow field
2. the accuracy of the translation function determined by the software.

Accuracy in Positioning the Calibration Grid in the Model Geometry

Error in the horizontal and vertical positioning of the calibration grid was minimised by having the grid sheet sit on the floor of the model, butted up against the sill of the vent that divided the two compartments. This positioning enabled the coordinate system of the calibration grid to be linked to the geometry of the model. The error in positioning the grid within the model is estimated to be within 1*mm* (both vertically and horizontally).

In the spatial calibration, it was necessary to locate the grid sheet in the plane of the laser sheet, to ensure that the average pixel size determined from the calibration image was the same as the pixel size in the LIF images. Figure 4-1 schematically shows the impact of positioning the calibration grid at an incorrect depth of field.

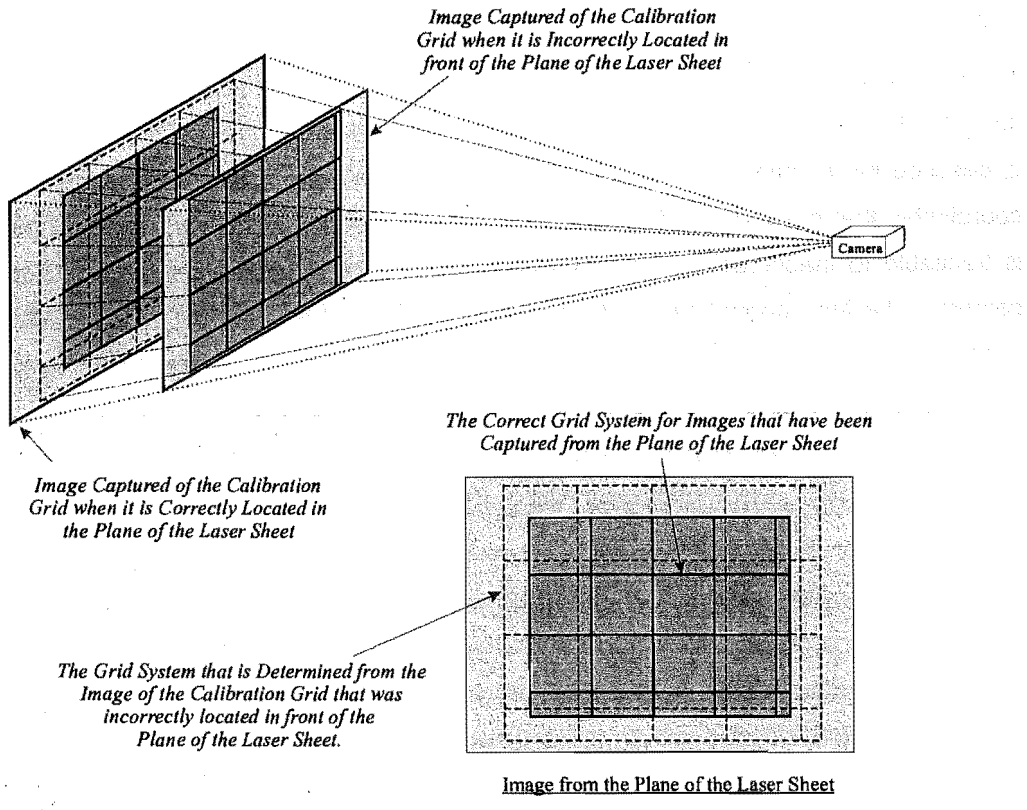

Figure 4-1 ***Schematic diagram showing the parallax error induced in the spatial calibration of the LIF images through locating the calibration grid at an incorrect depth of field.***

Imperfections in mirror alignments meant that the laser sheet that was used in experiments was not completely flat, but rather was warped out of plane in areas. This meant that it was not possible to position the flat calibration grid at the correct depth of field for the entire flow image. The maximum parallax error (in the x and z coordinates) that could result from this imperfection has been evaluated via simple trigonometry and is displayed in Table 4-1. The error was calculated using the containment width of the laser sheet (discussed later in Section 4.3.2), and the distance that the camera was located away from the laser sheet. For each of the three experimental series (T-Series, P-Series and C-Series), Table 4-1 lists the maximum error with which the calibration grid was positioned in the model, the containment width of the laser sheet (refer Section 4.3.2), and the maximum possible parallax error that could be created in the x and z coordinates.

Series	Positional Error (mm)	Containment Width (mm)	Maximum Parallax Error (mm)	
			x-Coordinate	*z*-Coordinate
T-Series	1	15	4.1	3.5
P-Series	1	15	1.4	1.7
C-Series	1	20	5.0	4.4

Table 4-1 ***Maximum error (in the x and z coordinates) created by the incorrect positioning of the calibration grid during the spatial calibration.***

Accuracy of the Translation Function

The translation function converted pixel coordinates in the LIF images to real world coordinates that tied in with the geometry of the model. It was determined that the accuracy of the translation was governed by the resolution and contrast characteristics of the image, rather than the precision of the translation function itself.

The accuracy of the translation was assessed, by comparing the coordinates of known locations in an image with the coordinates given by the translation function. An image of the calibration grid was used for this assessment. The lines on the calibration grid were one millimetre thick. The limited contrasting ability of the image capture equipment however, meant that in the image of the grid, the lines were blurred over a width of four to six pixels, which equated to a width of three to six millimetres. Thus, in an image of a grid, the intersection of two grid lines had to be selected from a square arrangement of four adjacent pixels. The translation function was sufficiently precise that it predicted the coordinates of the intersection within one pixel of the four-pixel cluster that encircled the actual intersection. The accuracy of the coordinate translation is therefore quantified as one and a half times the diagonal dimension of the pixels in the LIF images. The inability of the image capture equipment to accurately resolve the spatial distribution of highly contrasting areas is discussed later in Section 6.1.1. For each experimental series, Table 4-2 lists the size of the flow area that each individual pixel represented. The translation error, for each experimental series, is calculated from these pixel dimensions and is also displayed in Table 4-2.

Series	Pixel Size (mm)		Translation Error (mm)
	x-Dimension	z-Dimension	
T-Series	0.71	0.76	1.6
P-Series	0.94	0.98	2.0
C-Series	0.85	0.90	1.9

Table 4-2 ***Maximum error (in the x and z coordinates) caused by inaccuracies in the translation of pixel coordinates to real world coordinates during spatial calibration.***

4.3.2 Uncertainty in the Y Coordinate

The *y* coordinate describes the position across the model at which the normalised density difference measurement was taken. If the laser sheet had been ideally flat, this coordinate would always be the distance to the centreline plane. However, in the generation of the laser sheet, imperfections in the alignment and the shape of mirrors meant that the light sheet had a slightly warped profile and a diverging width. This introduced some uncertainty into the *y* coordinate.

The spatial characteristics of the laser sheet were assessed at the start and at the end of each of the three experimental series. The light sheet was shone onto a white perspex sheet, marked with 10*mm* grid lines to enable measurements to be made. The length, thickness and the total width of

containment for the laser sheet were recorded according to the measurement protocol shown in Figure 4-2. For each experimental series, Table 4-3 lists the thickness and the total width of containment for the laser sheet. The width of containment can be used as the absolute limit uncertainty for the *y* coordinate.

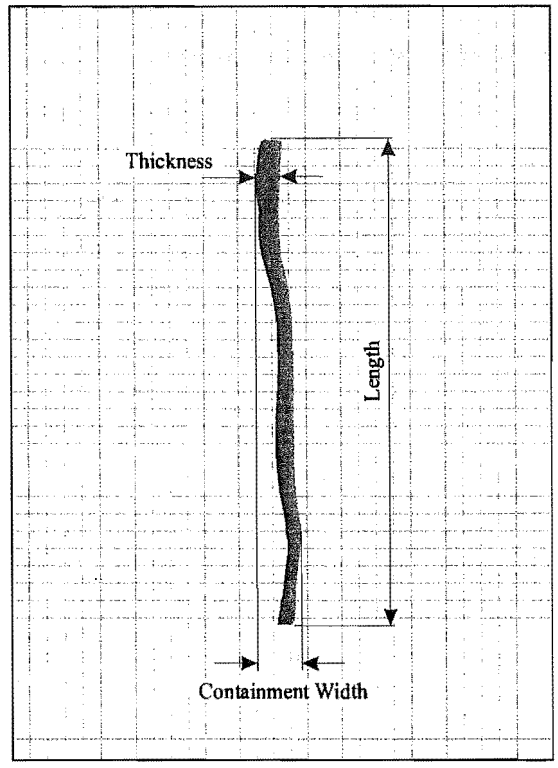

Figure 4-2 ***Schematic diagram of the measurements that were collected between each experimental series to quantify the spatial extent of the light sheet.***

Experimental Series	Thickness (mm)	Containment Width (mm)
T-Series	10	15
P-Series	10	15
C-Series	7	20

Table 4-3 ***Dimensions of the light sheet in the experimental region.***

4.3.3 Summary of the Uncertainty in Measurement Locations

The component errors that have been quantified and displayed in Table 4-1 and Table 4-2 are limit errors for the *x* and *z* coordinates. The simple addition of these component errors to determine a resultant uncertainty would be unrealistically pessimistic. An estimate of the realistic uncertainty in the location of the normalised density difference profiles within the flow field is given by the absolute uncertainties listed in Table 4-4. For each experimental series, Table 4-4 lists the limit

uncertainty in the x, y and z components of the Cartesian coordinates that describe the experimental measurement locations. Evidence of the spatial uncertainty, can be seen in the normalised density difference coordinates that are listed in Appendix 1 for the C-Series experiments. In a number of C-Series experiments, the vertical coordinate at the start of the profile (z_{Start}) lies beneath the floor level of the C-Series model (that is, $z_{Start} > 333mm$ when the C-Series model floor lies at $z = 333mm$).

Experimental Series	δx (mm)	δy (mm)	δz (mm)
T-Series	±4	±15	±4
P-Series	±2	±15	±2
C-Series	±5	±20	±5

Table 4-4 ***Final estimate of the limit uncertainty for each component of the Cartesian coordinates that describe the location of measurements in the flow field.***

4.4 Normalised Density Difference

The probable uncertainty of the normalised density difference measurement has been evaluated in accordance with the method detailed in Baird, D.C. (1962)[1]. In the LIF determination of the normalised density difference (given by Equation (4-3)), there are three primary sources of measurement uncertainty:

1. the grey scale value allocated to each pixel in an image, G,
2. the correction term, C_{Drift}, (discussed with later in Section 4.4.2) and
3. the fluorescence measurements made from samples of solutions, F.

$$\Delta\rho^* = \frac{\Delta\rho}{\Delta\rho_o} = C_{Drift}\left[\frac{G_{Flow}-G_{B-Flow}}{G_{Cal}-G_{B-Cal}}\right]\times\left[\frac{F_{Calibration}}{F_o}\right] \qquad \text{Equation (4-3)}$$

The absolute uncertainty of the calculated normalised density difference can be determined from the uncertainty of the component measurements, according to Equation (4-4). Similarly, the standard deviation of the normalised density difference measurement can be quantified from the standard deviations of the component measurements, according to Equation (4-5). Thus, in order to quantify the uncertainty of the normalised density difference, the uncertainty in the three component measurements G, F and C_{Drift} must be determined.

$$\delta\Delta\rho^* = \frac{\partial\Delta\rho^*}{\partial G}\delta G + \frac{\partial\Delta\rho^*}{\partial C_{Drift}}\delta C_{Drift} + \frac{\partial\Delta\rho^*}{\partial F}\delta F \qquad \text{Equation (4-4)}$$

$$\sigma_{\Delta\rho^*} = \sqrt{\left(\frac{\partial\Delta\rho^*}{\partial G}\right)^2 \sigma_G^2 + \left(\frac{\partial\Delta\rho^*}{\partial C_{Drift}}\right)^2 \sigma_{C_{Drift}}^2 + \left(\frac{\partial\Delta\rho^*}{\partial F}\right)^2 \sigma_F^2} \qquad \text{Equation (4-5)}$$

4.4.1 Uncertainty in the Pixel Grey Scale Value - G

The light intensity values *G* that are allocated to pixels in the experimental images, are adjusted values from the light intensity measurements *R*, which are captured by the image capture equipment. The light intensities are adjusted according to a defined translation function that ensures the equipment has a linear response. The uncertainty of the grey scale value *G* that is finally allocated to a pixel, is therefore a function of both the uncertainty of the captured fluorescence *R*, and the uncertainty of the translation function that remaps *R* to *G*.

Uncertainty in the Captured Fluorescence – (R)

To account for the possible influence of random noise in the image capture apparatus, analysis was undertaken to look at the variation in the fluorescence captured in an image under experimental conditions. The analysis examined how the light intensity values assigned to a pixel location in an image, varied between ten images that were captured of the same article under identical conditions.

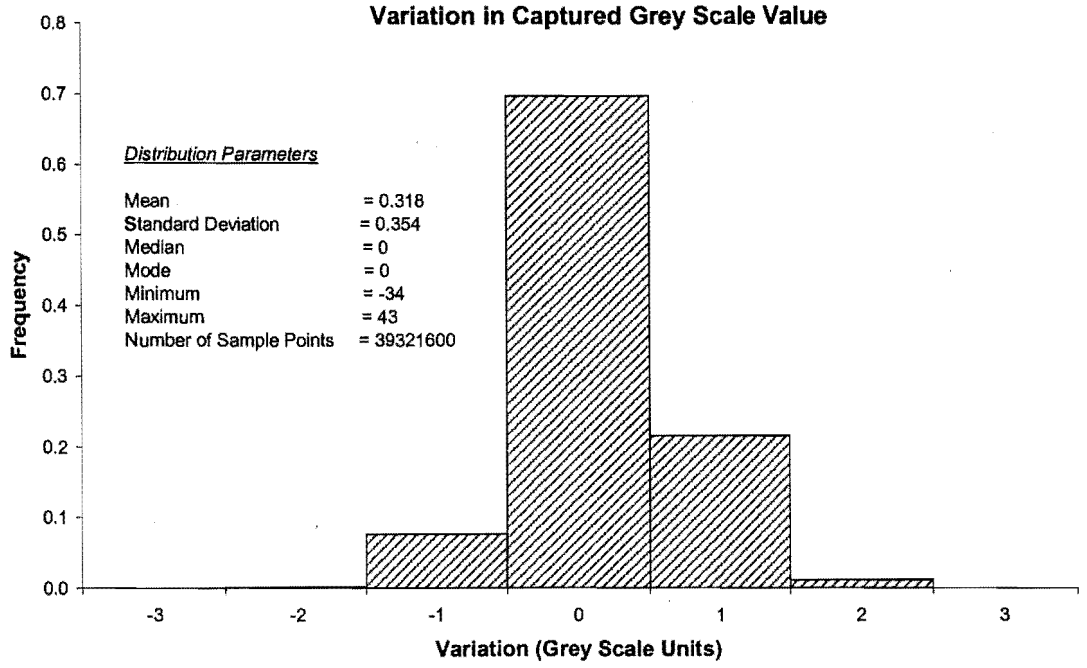

Figure 4-3 ***Frequency distribution of the random variation in the captured grey scale value at any pixel location in a LIF image.***

The variation was assessed, by comparing the grey scale values at the same pixel location in two different images of the same fluorescent calibration solution. The analysis revealed that the

magnitude of the variation in the captured grey scale value was independent of the level of light intensity. The data from one hundred image comparisons was collated into one data set. Figure 4-3 shows the frequency distribution that was determined for the variation in the grey scale value *R* assigned to a pixel during image capture.

In the calculation of the grey scale variation (through the comparison of two images), the order in which the images were captured was considered. The image that was captured at a later time was always subtracted from the image that had been captured earlier. The slight skew in the distribution, and the non-zero mean, is evidence of drift that occurred over the time interval between the capture of the two images; see Section 4.4.2 for discussion of the correction for this problem. The analysis determined that the standard deviation of the captured fluorescence *R* is 0.354 grey scale units, (i.e., $\sigma_R = 0.354$).

Uncertainty in the Linear Response Translation Function

The image capture equipment used in the LIF experiments was required to have a linear response, so that light intensities captured in images were not distorted in any non-linear way from the light intensities that were emitted from solution. Prior to any experiments in this investigation being conducted, the natural response characteristics of the image capture equipment were evaluated, and found to be non-linear. A translation function was therefore determined, to modify the light intensities that were naturally captured in images *R* to light intensities that were appropriate for a linear response *G*. The translation function was applied during the image capture process via the Global Lab Picture Tool, Input Look-Up Table facility, (ILUT)[3].

The natural response characteristics of the image capture equipment were evaluated from images of a fluorescence calibration solution. The response characteristics were evaluated by comparing the fluorescence captured in an image with the power of the laser sheet that was used to illuminate the solution. The comparison was conducted over the range of fluorescence levels that the data capture equipment was exposed to during experiments. Adjusting the power output of the laser varied the fluorescence emitted from solution (according to a linear relationship[4]).

The fluorescence captured in each image was measured, using the grey scale value of pixels at twenty-six sample locations in each image. Twenty of the sample locations were arranged in a grid pattern across the area of the image; the remaining six locations were selected in brighter regions of the image to provide data in the upper range of the light resolution scale. For each sample location, a best-fit linear regression was determined for the relation of the laser power to grey scale value of the pixel. The slope of the best fit linear relation was found to vary throughout the image, such that there was spatial variation in the response characteristics of the image capture equipment. Figure 4-4 schematically shows the method that was used to determine the linear response translation function at each of the sample locations.

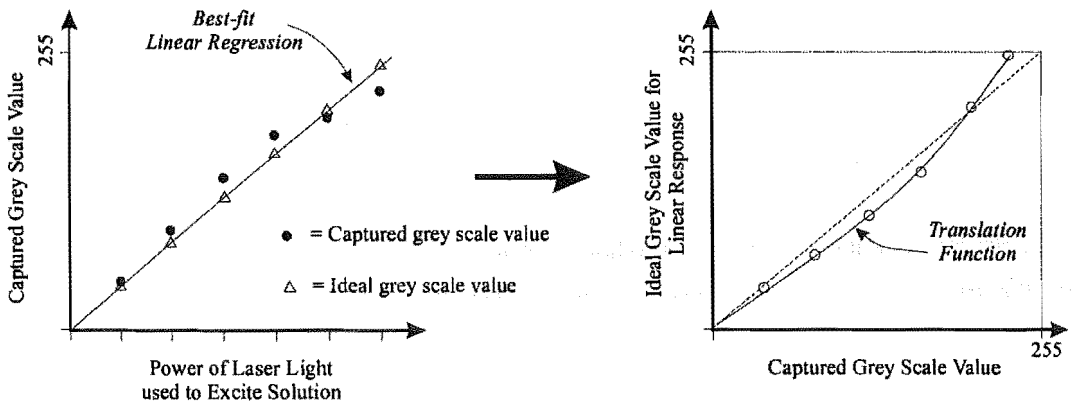

Figure 4-4 ***Schematic diagram showing the method that was used to derive a translation function that would remap the grey scale values of a pixel to values that were appropriate for a linear response.***

The ILUT translation function used in the T-Series experiments was determined prior to the start of any of the salt water work. The data from all twenty six sample locations was collated into one data set, and a best-fit fourth order polynomial was determined to describe the remapping of the incoming grey scale values to the linear response values. Between the completion of the T-Series and the start of the P-Series experiments, the video camera was serviced to rectify synchronisation problems that appeared during experimental work that was later dumped. Following servicing, the response characteristic of the image capture equipment was reassessed and found to be significantly different from that seen prior to the T-Series work. The response evaluation was therefore repeated a further four times to assess the repeatability of the translation function determination. The data points from all of the five derived ILUTs were collated into one data set and used to determine the best-fit ILUT for the image capture equipment after servicing. The data from the five response characteristic evaluations had a 5% relative standard deviation about the best fit polynomial given by Equation (4-6). The scatter of the data represents the spatial variation in the image capture equipment response.

$$G = a_1 R^4 + a_2 R^3 + a_3 R^2 + a_4 R \qquad \text{Equation (4-6)}$$

Where

$a_1 = 5.705 \times 10^{-8}$

$a_2 = -2.292 \times 10^{-5}$

$a_3 = 3.984 \times 10^{-3}$

$a_4 = 0.6892$

As no repeatability analysis was undertaken prior to the camera servicing (that is, prior to the T-Series experiments being conducted), the 5% relative standard deviation error has also been used to describe the accuracy of the translation function that was used in the T-Series experiments.

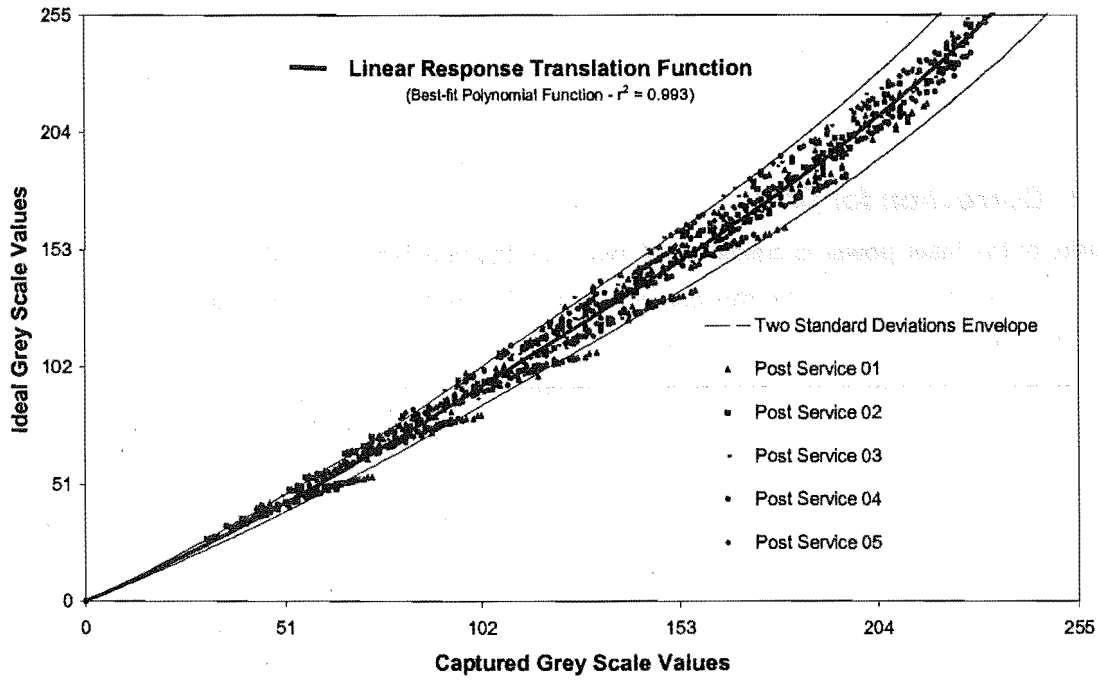

Figure 4-5 ***Diagram showing the scatter of the ideal grey scale value (that would achieve a linear response) around the grey scale value given by the linear response translation function. The scatter represents the spatial variation in the response of the image capture apparatus.***

Summary – Uncertainty in the Pixel Grey Scale Value - G

The relative uncertainty in the remapped grey scale value G is described by Equation (4-7).

$$\delta G = \sqrt{\left\{\left(\frac{\partial G}{\partial R}\right)\sigma_R\right\}^2 + \left[\left\{\left(\frac{\partial G}{\partial a_1}\right)\sigma_{a_1}\right\}^2 + \left\{\left(\frac{\partial G}{\partial a_2}\right)\sigma_{a_2}\right\}^2 + \left\{\left(\frac{\partial G}{\partial a_3}\right)\sigma_{a_3}\right\}^2 + \left\{\left(\frac{\partial G}{\partial a_4}\right)\sigma_{a_4}\right\}^2\right]}$$

Equation (4-7)

Unfortunately however, the uncertainty of the four constants a_1, a_2, a_3 and a_4 in the polynomial given by Equation (3-6) is unknown. The term in the square parentheses of Equation (4-7) can, however, be thought of as the accuracy of the translation function, which has been evaluated as having a relative error of 5% of the allocated grey scale value G. The probable uncertainty of the grey scale value G is therefore described by Equation (4-8).

$$\sigma_G = \sqrt{\left\{0.354\left(\frac{\partial G}{\partial R}\right)\right\}^2 + [0.05G]^2}$$

Equation (4-8)

Where

$$G=5.705\times10^{-8}R^4-2.292\times10^{-5}R^3+3.984\times10^{-3}R^2+0.6892R$$

Equation (4-9)

4.4.2 Correction for Drift

Stability of the laser power is critical in LIF work, as the fluorescence of the tracer dye is assumed to vary only as a function of the dye concentration. To verify that the laser was correctly providing a constant energy source during experiments, stability assessments were made intermittently over the course of the experimental program. In each assessment, the stability of the laser was gauged by recording the variation over time of the fluorescence emitted from a solution that contained a uniform concentration of tracer dye. At regular five-minute intervals over the period of one hour, an image of the fluorescent light emitted from the solution was captured. Each image was a time-average of the fluorescence emitted over a ten second interval. At each five-minute interval, the average grey scale value in the image was determined. Results of the stability analysis showed that there was some drift in the average fluorescence captured in the images over the period of an hour. In hindsight, this method was flawed, in that it was impossible to determine from the results if the drift was due to the performance of the laser or the image capture apparatus. Using a light meter to directly measure the power of the coherent light that was output from the laser would have eliminated this entanglement.

The stability assessment was conducted a number of times over the course of the experimental investigation. For each assessment, a best-fit linear regression was determined for the decay in the average grey scale value as a function of time. Table 4-5 lists the stages in the experimental program at which the stability assessments were conducted, the best-fit linear regression gradient that was determined by each assessment, and the dye concentration in the calibration solution that was the focus of each stability assessment.

Stability Assessment	Best-Fit Gradient - D_{Decay} (*Average Grey Scale Value/Minute*)	Dye Concentration (*mg/l*)
Start of T- Series	-0.0795 (r^2=0.98)	0.005
End of T-Series	-0.1022 (r^2=0.84)	0.005
Start of P- Series	-0.0141 (r^2=0.94)	0.005
End of P-Series	-0.0492 (r^2=0.94)	0.005
Start of C- Series	0.0687 (r^2=0.61)	0.010
Midpoint of C-Series	0.0896 (r^2=0.98)	0.010
End of C-Series	-0.0398 (r^2=0.54)	0.003

Table 4-5 ***The best fit linear gradient for the decay in the average grey scale value of a calibration image over the period of one hour.***

A major concern with the range of gradients in Table 4-5 is the apparent lack of consistency in the direction of the average grey scale drift. The stability analysis conducted at the start and midpoint of the C-series work determined that the average grey scale value was increasing, rather than decaying (as all the other analyses had demonstrated). The only apparent difference between these two assessments and the other assessments was that the solution that was used in the assessment had a higher dye concentration, refer Table 4-5. The consequence of this is that a high level of fluorescence was emitted from these two solutions, so that the camera aperture would have been reduced to prevent overexposure of the image. It is postulated therefore, that the camera may have been the source of the drift in the flow visualisation equipment, and that the stability of the camera was a function of the aperture setting.

Throughout the experimental program, the fluorescence was calibrated from solutions containing a dye concentration between 0.0029*mg/l* to 0.0052*mg/l*. These concentrations are very close to dye concentrations used in the stability assessments conducted during the T-Series and P-Series work, and at the end of the C-Series experiments. All these assessments determined that there was decay in the average grey scale value. For this reason, the decay gradients evaluated at the start and mid point of the C-Series experiments have been disregarded. To account for the decay behaviour observed in the stability assessments, a correction term was incorporated into the calculation of the normalised density difference. The correction term took the form of a scaling factor C_{Drift}; refer Equation (4-10).

$$\Delta\rho^* = \frac{\Delta\rho}{\Delta\rho_o} = C_{Drift}\left[\frac{F_{Calibration}}{F_o}\right]\left[\frac{G_{Flow}-G_{B-Flow}}{G_{Cal}-G_{B-Cal}}\right] \qquad \text{Equation (4-10)}$$

To quantify the magnitude of the scaling factor C_{Drift}, it was necessary to determine how much the average fluorescence had decayed over the time interval between the capture of the calibration image and the capture of the flow images. The amount of decay was quantified using the average decay gradient D_{Decay}, from the gradients shown in Table 4-5, and the time interval between the capture of the calibration image and the capture of the flow images Δt_{Delay}.

The times at which images were captured during the experimental procedure were recorded in the laboratory notebook. During the experiment, ten 10*s* time averaged images of the flow were captured, which were later combined to create one 100*s* time-averaged image of the flow; refer Section 3.1.2. The capture of the ten flow images, during an experiment, took an interval of approximately three minutes. Thus, the time interval Δt_{Delay}, was measured from when the calibration image was captured, to the centre of the time interval over which the flow images were captured.

The magnitude of the scale factor was dependent upon the brightness of the initial calibration image, and the magnitude of the decay that occurred before the flow images were captured. The

brightness of the calibration image was quantified by calculating the average grey scale value of all the pixels in the image $\overline{G}_{Cal}$. Thus the scale factor C_{Drift} was calculated, according to Equation (4-11).

$$C_{Drift} = \frac{\overline{G}_{Cal}}{\left(\overline{G}_{Cal} + D_{Decay}\Delta t_{Delay}\right)} \qquad \text{Equation (4-11)}$$

The standard deviation of the scale factor, was calculated in accordance with Baird, D.C. (1962)[1], from the standard deviation of the decay gradients shown in Table 4-5; refer Equation (4-12).

$$\sigma_C = \sqrt{\left(\frac{\partial C_{Drift}}{\partial D_{Decay}}\right)^2 \sigma_D^2} \qquad \text{Equation (4-12)}$$

Where

$$\frac{\partial C_{Drift}}{\partial D_{Decay}} = \frac{-\Delta t_{Delay}\overline{G}_{Cal}}{\left(\overline{G}_{Cal} + D_{Decay}\Delta t_{Delay}\right)^2} \qquad \text{Equation (4-13)}$$

Exp	Time Interval	Decay	Initial Condition	Scale Factor	
	Δt_{Delay}	$D_{Decay}\Delta t_{Delay}$	$\overline{G}_{Cal}$	C_{Drift}	σ_C
	(min)	*(Grey Scale)*	*(Grey Scale)*	-	-
T01	14.63	-0.83	170.55	1.005	0.0030
T02	15.92	-0.91	132.82	1.007	0.0042
T03	14.29	-0.81	134.18	1.006	0.0037
T04	16.08	-0.92	129.87	1.007	0.0043
T05	10.96	-0.62	134.71	1.005	0.0028
T06	13.13	-0.75	127.31	1.006	0.0036
P01	9.58	-0.55	149.93	1.004	0.0022
P06	17.75	-1.01	154.63	1.007	0.0040
C01	17.50	-1.00	120.94	1.008	0.0051
C02	33.42	-1.90	117.69	1.016	0.0101
C03	21.83	-1.24	111.65	1.011	0.0069
C04	21.92	-1.25	118.26	1.011	0.0065
C05	29.00	-1.65	114.76	1.015	0.0090
C06	19.42	-1.11	109.78	1.010	0.0062
C07	28.21	-1.61	114.94	1.014	0.0087
C08	37.83	-2.15	117.15	1.019	0.0115

Table 4-6 ***Determination of the scaling factor C_{Drift} that is used to correct the normalised density difference calculation for the decay that was observed in the stability assessment.***

Table 4-6 lists the factors that were used in the calculation of the scaling factor for each experiment. These factors are, the time interval over which decay could have occurred in the experiment Δt_{Delay}, the estimate of the amount of decay (in the average grey scale value) over this time interval, and the average grey scale value of the pixels in the calibration image. Table 4-6 also lists the scale factor C_{Drift} that is calculated for each experiment, and the probable uncertainty of the scale factor, (expressed as the standard deviation of the scale factor σ_C)

4.4.3 *Fluorescence of Fluid Samples*

The relative fluorescence emitted from the source solution and the calibration solution was determined by using a Fluorometer to measure the fluorescence of samples taken from both solutions. This analysis was only necessary for the C-Series experiments, as in both the T-Series and P-Series experiments, the source solution was used to calibrate the fluorescence.

In the C-Series experiments, fifteen fluid samples were collected from both the calibration solution and the source solution. Using the fluid samples, the average fluorescence emitted from each solution was determined. This fluorescence was then used to determine the relative fluorescence emitted from the calibration solution and the source solution (that is, $F_{Calibration}/F_o$). The standard deviation of the fluorescence measurement for each solution was determined from the sample analysis. Table 4-7 lists the average fluorescence measurements for each C-Series experiment and the standard deviation of the measurements.

Exp	Calibration Solution		Source Solution		Relative Fluorescence
	$F_{Calibration}$[1]	$\sigma_{Calibration}$	F_o	σ_o	-
C01	31.59	0.71	110.60	2.58	3.50
C02	36.00	0.71	96.78	2.04	2.69
C03	49.06	0.79	94.70	2.20	1.93
C04	29.63	0.67	103.49	4.08	3.49
C05	42.69	0.51	84.63	2.00	1.98
C06	36.97	0.72	109.42	1.96	2.96
C07	47.41	0.71	104.38	2.61	2.20
C08	28.31	0.48	96.08	1.65	3.39
C09	27.44	1.00	88.18	1.55	3.21

Table 4-7 Experimental measurements of the fluorescence emitted from samples of the fluorescence calibration solution and the source solution.

[1]Arbitrary units for the fluorescence measurements.

4.4.4 Summary

The normalised density difference profiles were calculated from the pixel values in the LIF images using the Equation (4-10). For the T and P-Series experiments, the relative fluorescence term was equal to one, as the source solution was used to calibrate the fluorescence. In accordance with Equation (4-10), the standard deviation of the normalised density measurement was calculated according to Equation (4-14). The derivatives in Equation (4-14) are evaluated and listed in Appendix 2.

$$\sigma^2_{\Delta\rho^*} = \sum_i^i \left[\left(\frac{\partial \Delta\rho^*}{\partial G_i} \right)^2 \left(0.125 \left(\frac{\partial G_i}{\partial R_i} \right)^2 + 0.0025 G_i^2 \right) \right] + \left(\frac{\partial \Delta\rho^*}{\partial C_{Drift}} \right)^2 \sigma_C^2 + \left(\frac{\partial \Delta\rho^*}{\partial F_{Calibration}} \right)^2 \sigma^2_{F_{Calibration}} + \left(\frac{\partial \Delta\rho^*}{\partial F_o} \right)^2 \sigma^2_{F_o}$$

Equation (4-14)

Where

i = *Flow*, *B-Flow*, *Cal* and *B-Cal*

4.5 Reducing the Uncertainty

In hindsight, improvements can be made to the experimental apparatus and the experimental method employed during this investigation to reduce the uncertainty of the measurements.

4.5.1 Uncertainty in the Measurement Location

The most dramatic improvement that can be made in reducing the uncertainty of the measurement location can be achieved by improving the profile of the laser sheet. Eliminating the warping of the sheet and reducing the divergence of the light would significantly improve the spatial accuracy described by the containment width in Table 4-3.

4.5.2 Uncertainty in the Normalised Density Difference

Spatial Variation in Response Characteristics

Figure 4-6 shows the relative contribution of the terms in Equation (4-14) to the total uncertainty of the normalised density difference measurement. The two terms that represent the uncertainty of the grey scale value in the flow image and the calibration image make the largest contribution to the total uncertainty by far. The main source of uncertainty in these terms is the 5% relative standard deviation that describes the accuracy of the ILUT translation function. The largest reduction in the uncertainty of the normalised density difference measurement can therefore be achieved by using software in the image capture process that is capable of applying an individual translation function at each pixel in the image. This would account for the spatial variation in the response characteristics of the equipment.

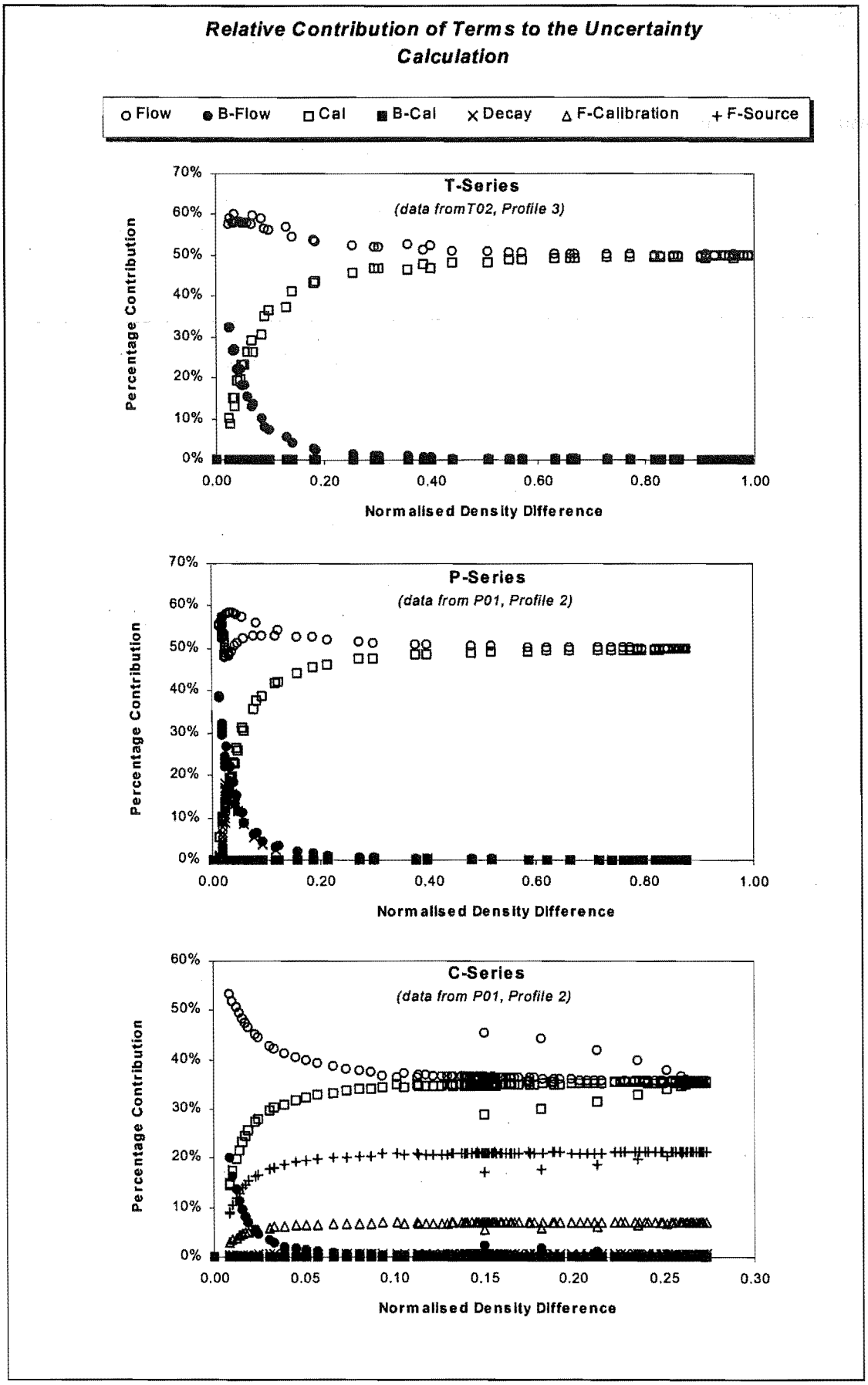

Figure 4-6 ***Graphical plot showing the relative contribution of the component terms in Equation (3-14) toward the total uncertainty.***

Capture Multiple Images

The uncertainty of the experimental measurement can also be reduced if multiple measurements are collected and then the average result of these measurements is presented as the final measure. The uncertainty of the final result is then given by Equation (4-15).

$$\sigma_{Average} = \frac{\sigma_{\Delta\rho^*}}{\sqrt{n}} \qquad \text{Equation (4-15)}$$

Where

n is the number of measurement that were taken, and

$\sigma_{\Delta\rho^*}$ is the uncertainty of any one measurement, given by Equation (4-14).

In the LIF work detailed in this research, a single measurement was collected and presented. If multiple images had been collected for each of the necessary shots, then multiple measures of the normalised density difference could have been determined. Presenting an average result of four measurements would have halved the uncertainty of the normalised density difference measurement, for only a negligible increase in the experimental time, and a small increase in the analysis time.

4.6 References

1. Baird, D.C. (1962) *Experimentation: An Introduction to Measurement Theory and Experiment Design*, Prentice-Hall Inc. Englewood Cliffs, New Jersey,U.S.A.

2. *CRC Handbook of Chemistry and Physics*, 57th Edition, Ed: R.C. Weast, CRC Press, 18901 Cranwood Parkway, Cleveland, Ohio 44128, U.S.A.

3. Global Lab Image Version 2.0, Data Translation Inc., 100 Locke Drive, Marlboro MA 01752-1192, Ph (508) 481-3700, Fax (508) 481-8620.

4. Prasad, R.R. and Sreenivasan, K.R. (1990) Quantitative Three Dimensional Imaging and the Structure of Passive Scalar Fields in Fully Turbulent Flows, *Journal of Fluid Mechanics*, **216**, 1-34.

Chapter 5 - EXPERIMENTAL RESULTS

Experimental measurements from the salt water experiments are presented in this chapter. Measures of the density difference, frequency of eddies in the flow, and the temporal development of the fire similar flow fields are presented.

Normalised Density Difference

Density difference measurements have been taken from the centreline plane of the models. Measurements were collected along line segments contained within this vertical plane. Eight profiles were collected in each experiment. A Cartesian coordinate system has been used to describe the location of the density profiles within the model geometry. The coordinates that describe the location of each profile are specified in Appendix 1. Each profile is a one hundred second time average measurement of the steady state density difference. The density difference has been normalised by the density difference of the fluids at the source of the flow.

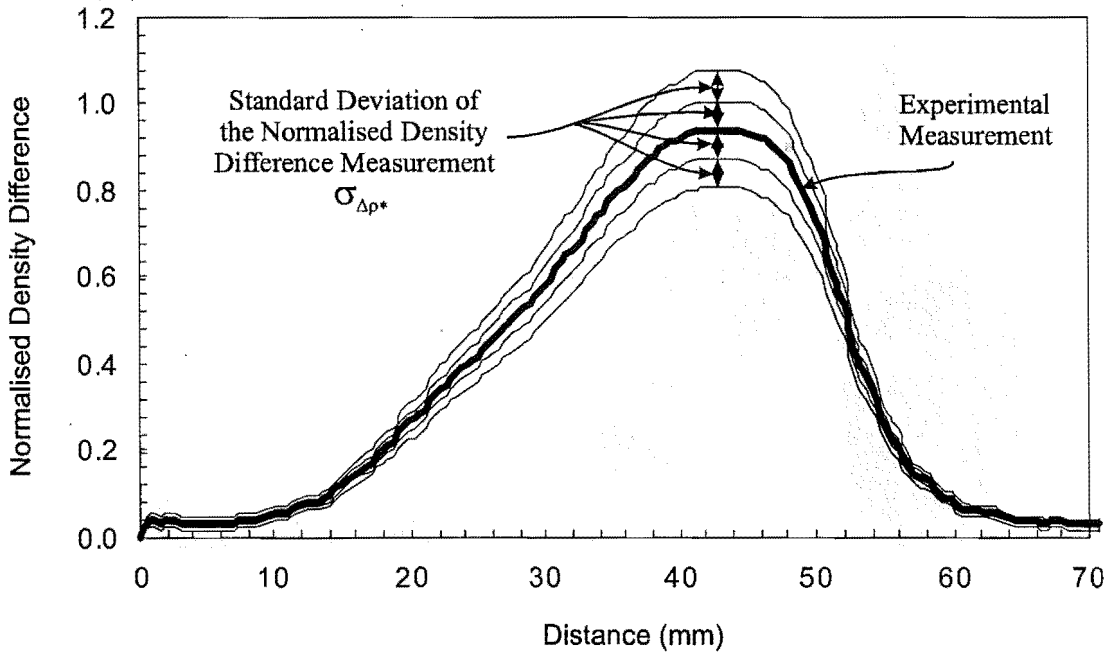

Figure 5-1 Format of the graphs that are used to present the experimental measurement of the normalised density difference and its associated uncertainty.

The density measurements are presented in graphical form. The normalised density difference is plotted against distance along the line segment. The uncertainty of the results is displayed through the 68th and 95th percentile confidence envelopes. Figure 5-1 shows the format of the density difference plots.

5.2 T-Series

5.2.1 *Normalised Density Difference Profiles*

The eight normalised density difference profiles for each T-Series experiment were collected from the region of saline flow between the plane of the opening and the impingement region on the floor of the model. Figure 5-2 shows the typical location of the eight profiles in the flow.

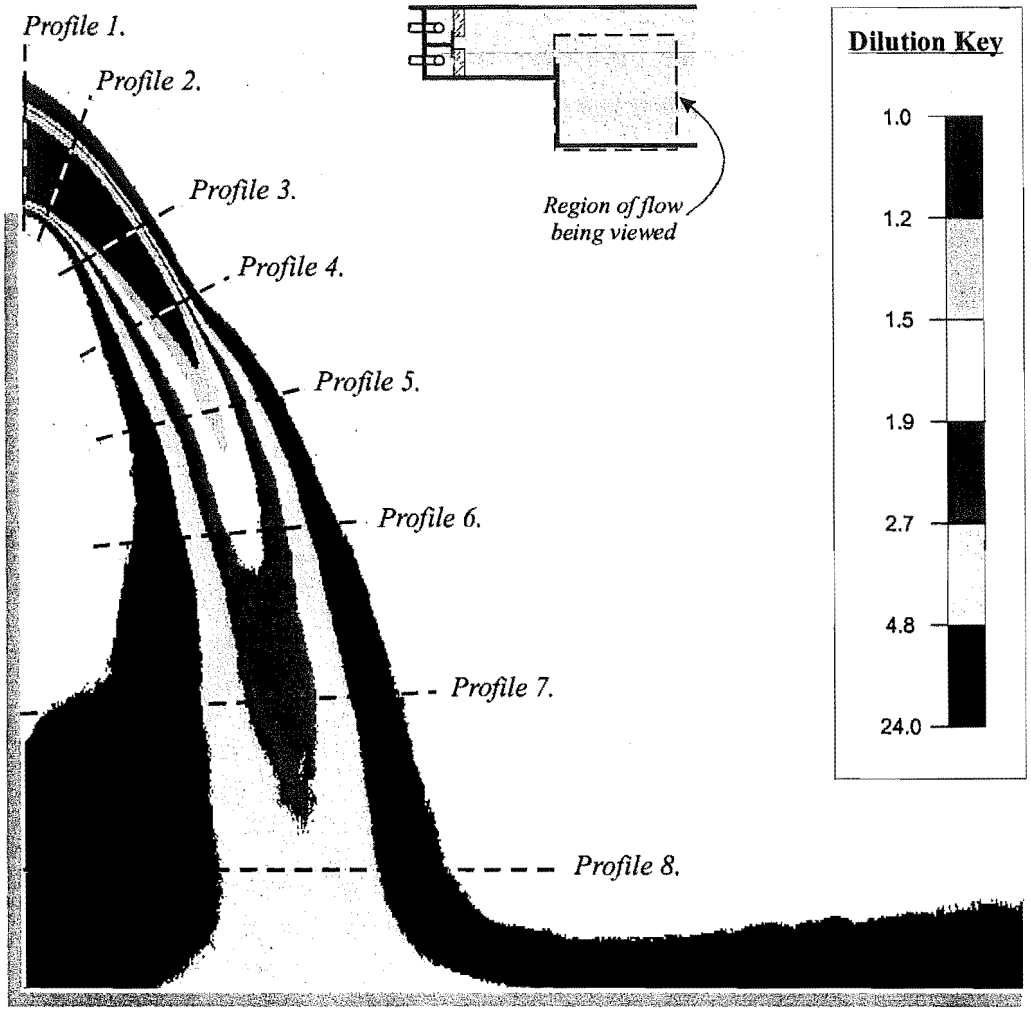

Figure 5-2 ***A time averaged image of a transitional flow showing the approximate location of the eight normalised density difference profiles that section the plume.***

The Cartesian coordinate system that describes the location of each profile has the origin located at the leading edge of the sill between the two compartments. The units for the coordinate system are millimetres. Figure -5-3 illustrates how the coordinate system ties to the geometry of the T-Series model.

The normalised density difference profiles from experiment T02 (β = 0.006 and V = 8.0*l/min*) are shown in Figure 5-5. The shapes of the profiles within this figure are typical of the profiles obtained for all of the T-Series experiments. Therefore, in order to keep this chapter concise and avoid repetition in the presentation, the balance of the T-Series results from experiments T01 through T6 are displayed in Appendix 3.

Coordinate System for the T-Series Profiles

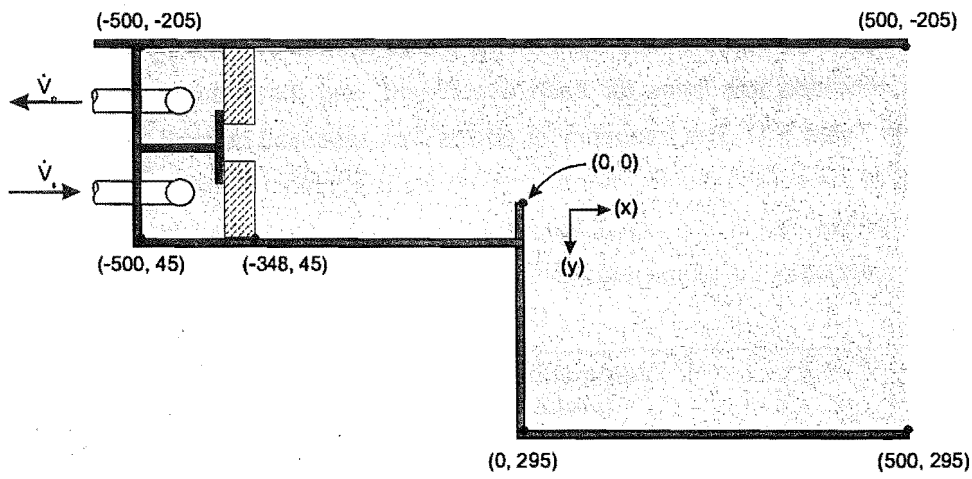

Coordinate System for the P-Series and C-Series Profiles

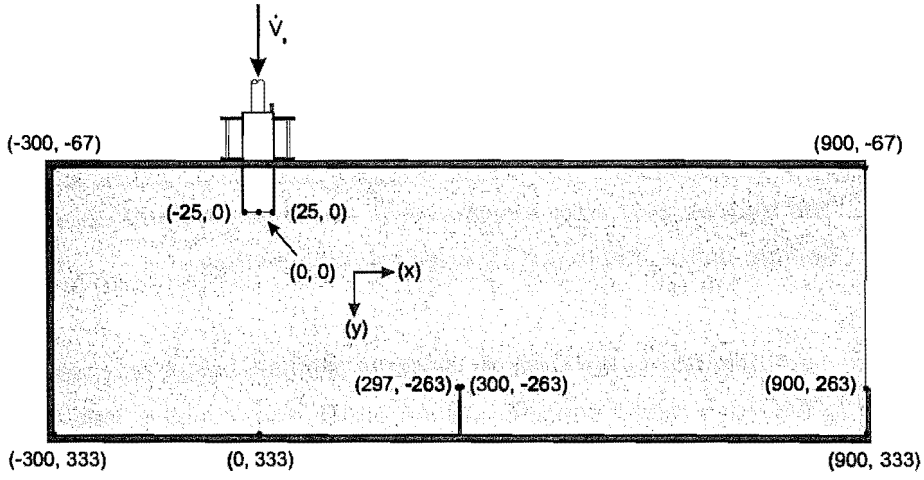

Figure -5-3 ***A schematic diagram showing how the Cartesian coordinate system that describes the locations of measurement links to the model geometry.***

Experiment T02 (β = 0.006 and V = 8.0*l/min*) was repeated a further four times to assess the repeatability of the density profiles. Figure 5-7 shows the agreement of the profiles from these five experiments.

5.2.2 *Eddy Frequency*

During experiments, the Images from the video camera were recorded onto videocassette. The video record of the flow was later analysed to determine the frequency of the eddy structures that form on the perimeter of the spilling plume. The frequency was determined by counting the number of eddies that passed a fixed point on the plume surface over a sixty-second interval. This analysis was repeated five times for each experiment, and the average result determined for presentation in Table 5-1. The frequency of eddies was assessed on both the underside and the upper surface of the spilling plume. For each T-Series experiment Table 5-1 shows the buoyancy of the saline, the volumetric flow rate of the fluid streams, and the frequency of the eddy structures on both the underside of the plume, and on the upper surface of the plume.

Title	β -	Volume Flow (*l/min*)	Eddy Frequency (Hz)	
			Underside	Upper Surface
T01	0.003	8.0	1.09	0.72
T02	0.006	8.0	1.61	1.06
T03	0.013	8.0	1.90	1.64
T04	0.003	17.1	1.21	0.53
T05	0.006	17.1	1.53	0.68
T06	0.013	17.1	2.10	1.38
T07	*0.007*	*8.0*	*1.62*	*1.16*
T08	*0.006*	*8.0*	*1.68*	*1.12*
T09	*0.006*	*8.0*	*1.62*	*1.16*
T10	*0.006*	*8.0*	*1.61*	*1.15*

Table 5-1 ***The frequency of eddy structures on the underside and upper surface of the spilling plume that is the T-Series transitional flow.***

Eddy structures were generally of the order of 15-20*mm* diameter before they were visible enough to be counted in the video record analysis. Even at this size, counting was difficult when the frequency exceeded 1.5*Hz*. A number of features of the eddy behaviour made counting the structures that passed a fixed point on the plume boundary difficult.

- Disturbances that passed the counting location did not always completely develop into the classic eddy roll up structure; some would collapse downstream.

- Some eddies would start to roll up but then collapse before reaching the location at which the structures were being counted.

- Often two adjacent eddies would form simultaneously, and sometimes the lower eddy would roll up and completely engulf the structure above it.

Due to the complications in counting the eddy structures, the frequency with which eddies were generated did not appear to be regular over the sixty-second interval. The frequency data in Table 5-1 is still useful however, in that it gives an estimation of the frequency with which the structures were generated. The repeatability of the frequencies from experiments T02 and T07 through T10 gives confidence in the measurement technique.

5.2.3 Instantaneous Flow Structure

Figure 5-4 is a photo of the saline flow from one of the transitional flow experiments. Four other photographs of the T-Series flow are appended as Appendix 4, so that the large scale structures seen in the transitional flows may be qualitatively compared to those flow structures resolved by the computational model.

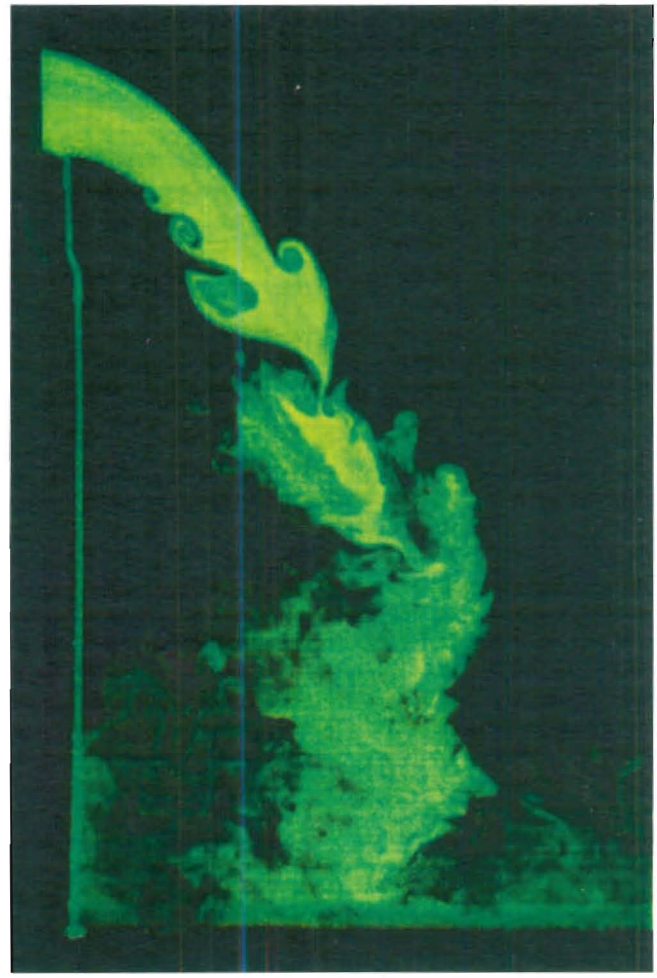

Figure 5-4 ***A photograph of a transitional flow showing the eddy structures that were observed on the perimeter of the spilling plume.***

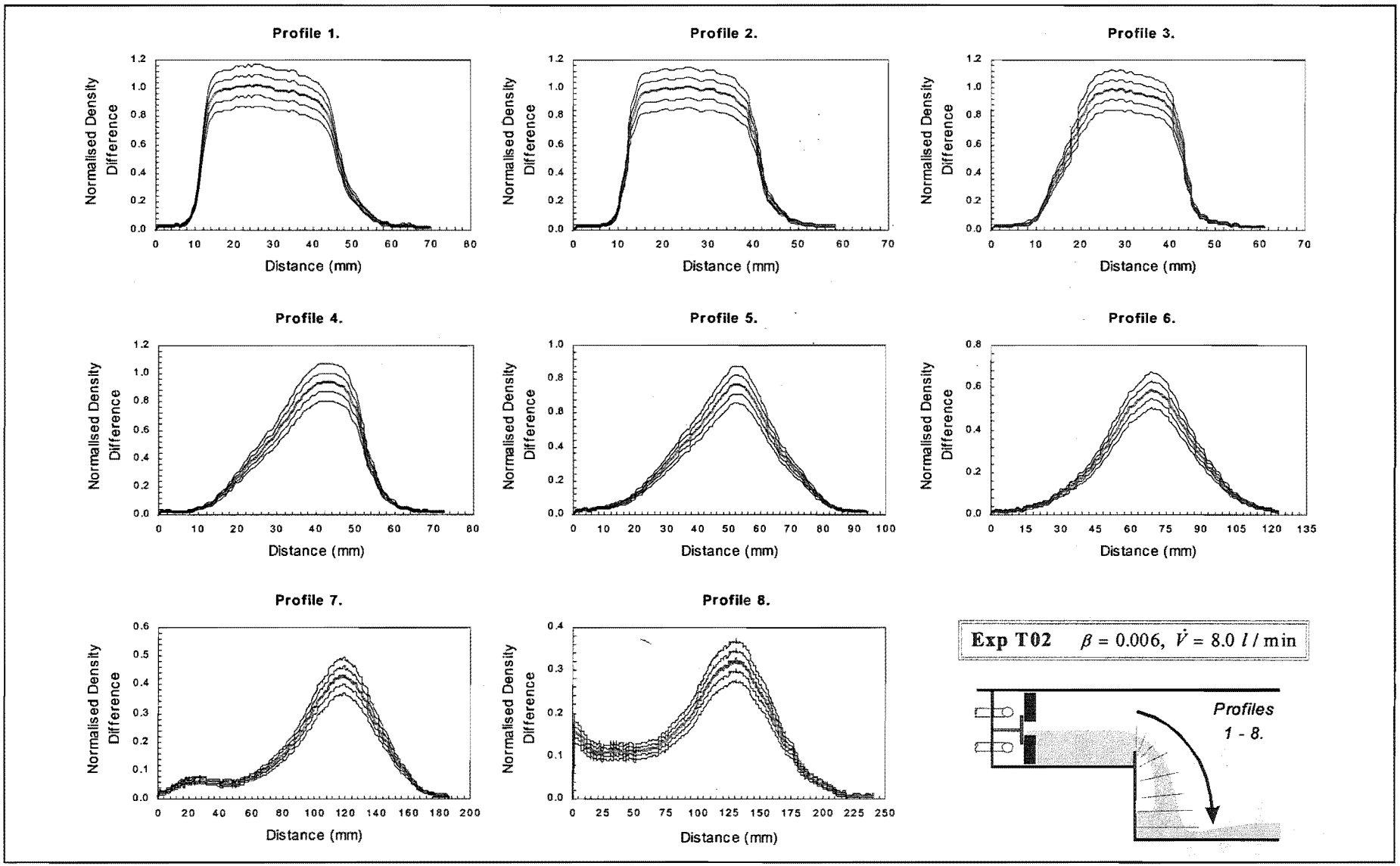

Figure 5-5 ***Normalised density difference profiles from transitional experiment T02.***

5.2.4 Dilution Contours

Figure 5-6 shows the dilution contours of the flow field for the six different experiments T01 through T06. The approximate location of the onset of turbulent mixing on the upper boundary of the plume is marked with a black arrow for each experiment.

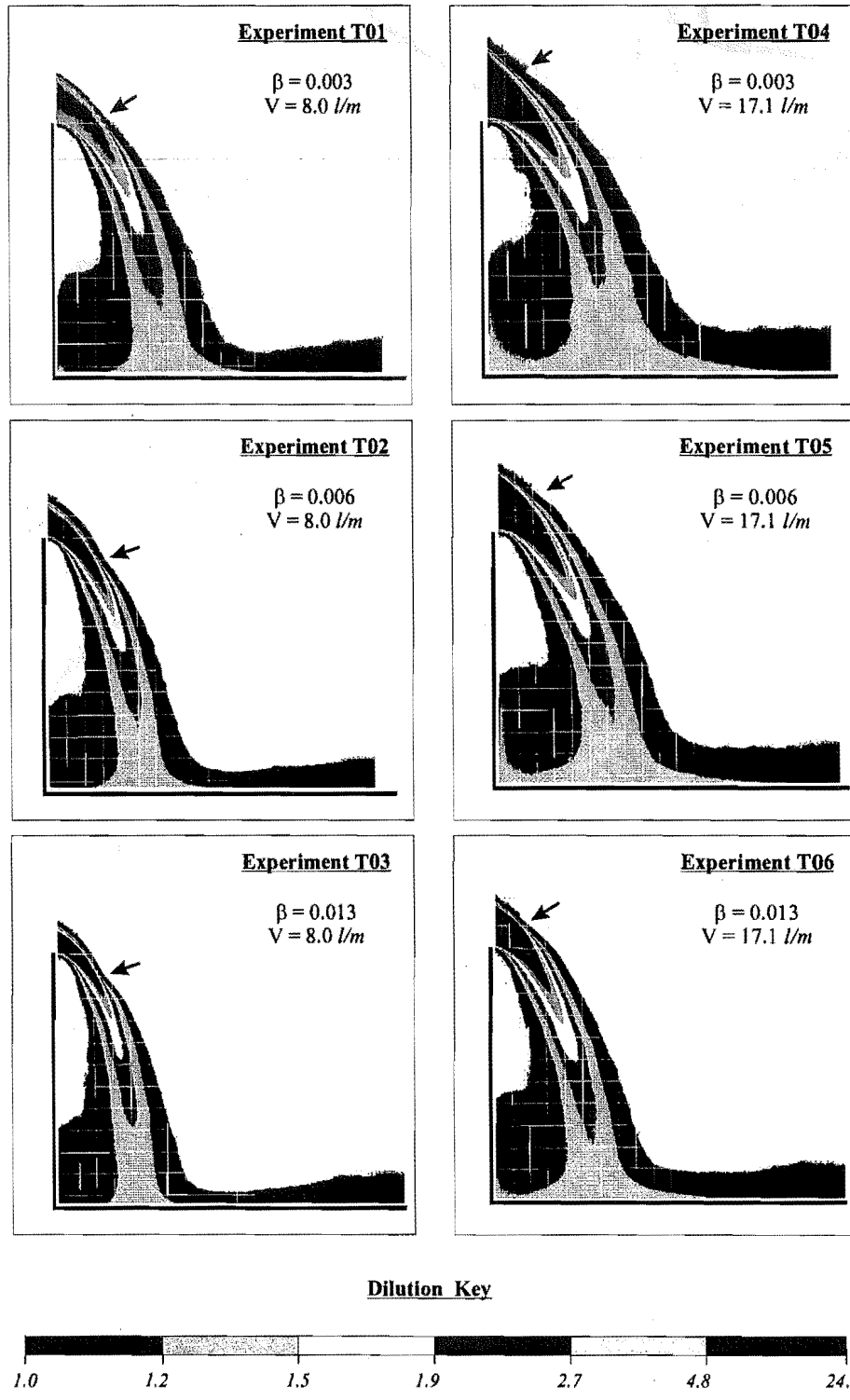

Figure 5-6 Time averaged dilution maps of the saline flow in each T-Series experiment.

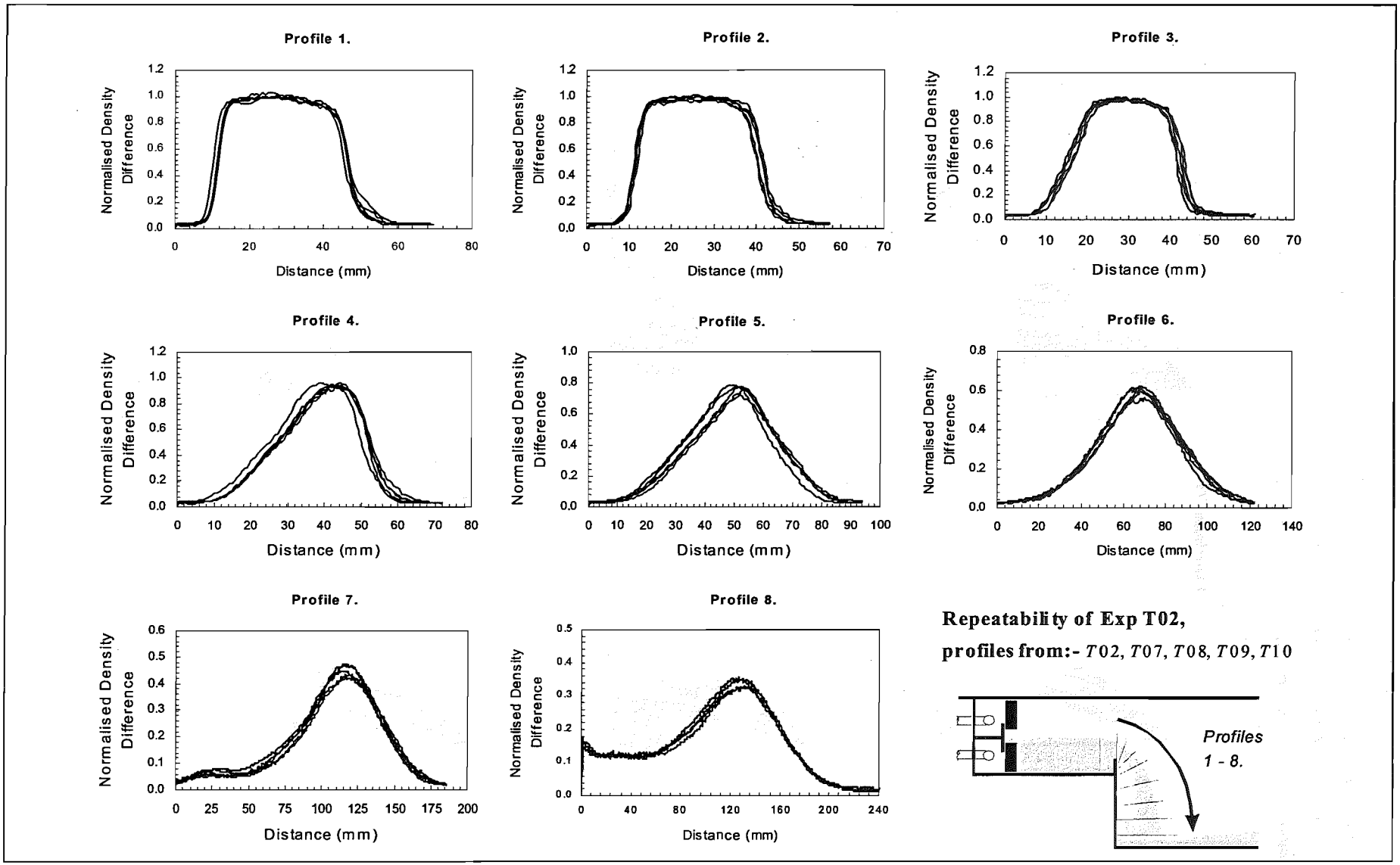

Figure 5-7 Repeatability of the T-Series experimental measurement of the normalised density difference.

5.3 P-Series

5.3.1 *Normalised Density Difference Profiles*

The eight profiles from each experiment were collected over the height of the salt water plume before it plunged into the saline layer. Due to problems with refraction, no density difference measurements were made in the saline layer; refer Section 2.4.3. Figure 5-8 shows the typical locations of the profiles within both P-series plumes. The origin of the Cartesian coordinate system that describes the location of the profiles is sited at the centre of the plume source opening. Figure -5-3 illustrates the coordinate system. The normalised density difference profiles from experiment P01 (β = 0.01) are shown in Figure 5-10. As with the T-Series experimental results; the balance of the P-Series results are displayed in Appendix 3 to avoid repetition.

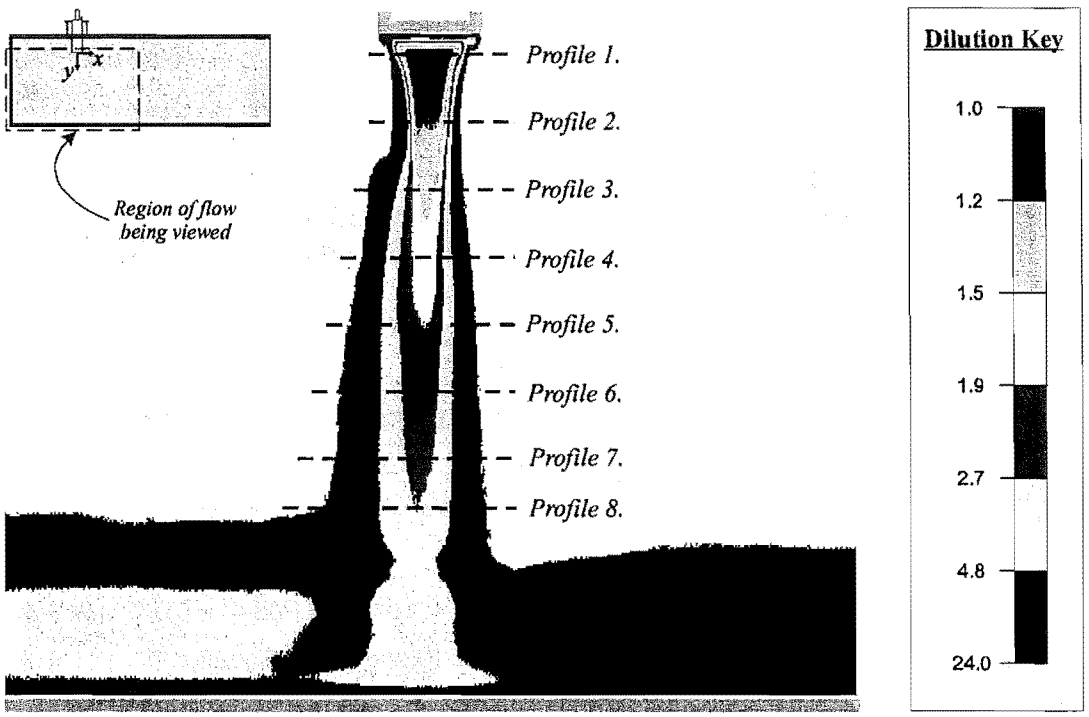

Figure 5-8 ***A time averaged image of a P-Series plume, showing the approximate location of the eight normalised density difference profiles that section the flow.***

The repeatability of the density difference measurement was assessed by repeating experiment P01 (β = 0.01) a further four times. Figure 5-11 shows the repeatability of the P-Series profiles.

5.3.2 *Dilution Contours*

Figure 5-9 shows dilution contours for the two different source plumes P01 and P06. The Froude number (Fr^2) at the source of the plumes P01 (β = 0.01) and P06 (β = 0.02) was 0.56 and 0.39 respectively. The non-dimensional parameter was calculated in accordance with Equation (5-1). The bulk velocity (s) of the saline flow at the source was used in the calculation along with an equivalent source diameter, (equal circular area).

$$Fr = \frac{s_s}{\sqrt{g' d_o}} \qquad \text{Equation (5-1)}$$

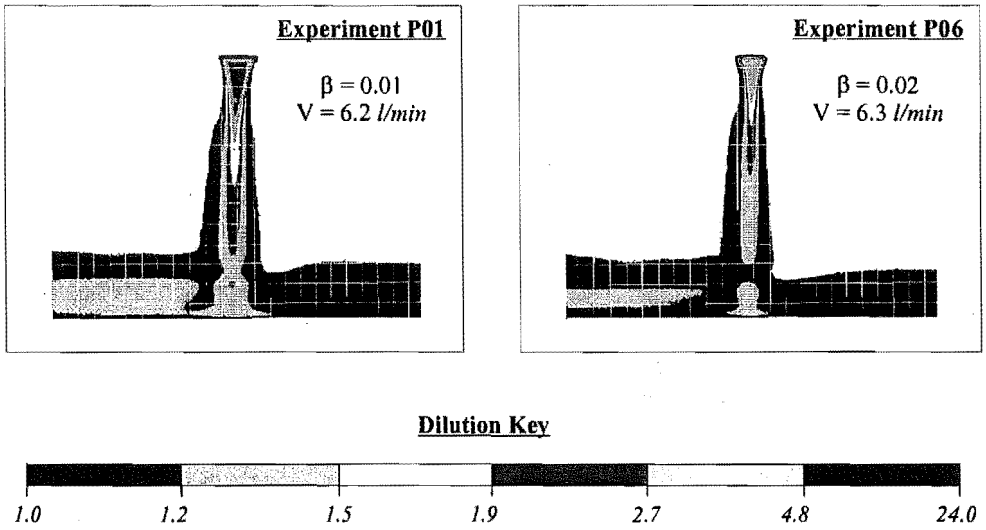

Figure 5-9 Time averaged dilution contours for the two source plumes P01 and P06.

The Reynolds number for the two source plumes P01 (β = 0.01) and P06 (β = 0.02), was calculated according to two different formula, given by Equations (5-2) and (5-3). Equation (5-2) describes the plume Reynolds number as it is normally quantified in fluid mechanics research on buoyant plumes[1]. In this form, the Reynolds number for all the P-Series source the plumes was 2.2×10^4. Equation (5-3), on the other hand, describes the Reynolds number, as it is defined in Steckler *et al*[2], which details the scaling theory for the salt water modelling of fire induced smoke flow. In this form, the Reynolds number for the plumes P01 and P06 was 1.2×10^4 and 1.6×10^4 respectively.

$$Re_d = \frac{\rho_s s_s d_o}{\mu} \qquad \text{Equation (5-2)}$$

$$Re_H = \frac{\rho_o U H}{\mu} \qquad \text{Equation (5-3)}$$

Where

$$U = \left(\frac{\dot{m}_{salt} g}{\rho_o H} \right)^{\frac{1}{3}} \qquad \text{Equation (5-4)}$$

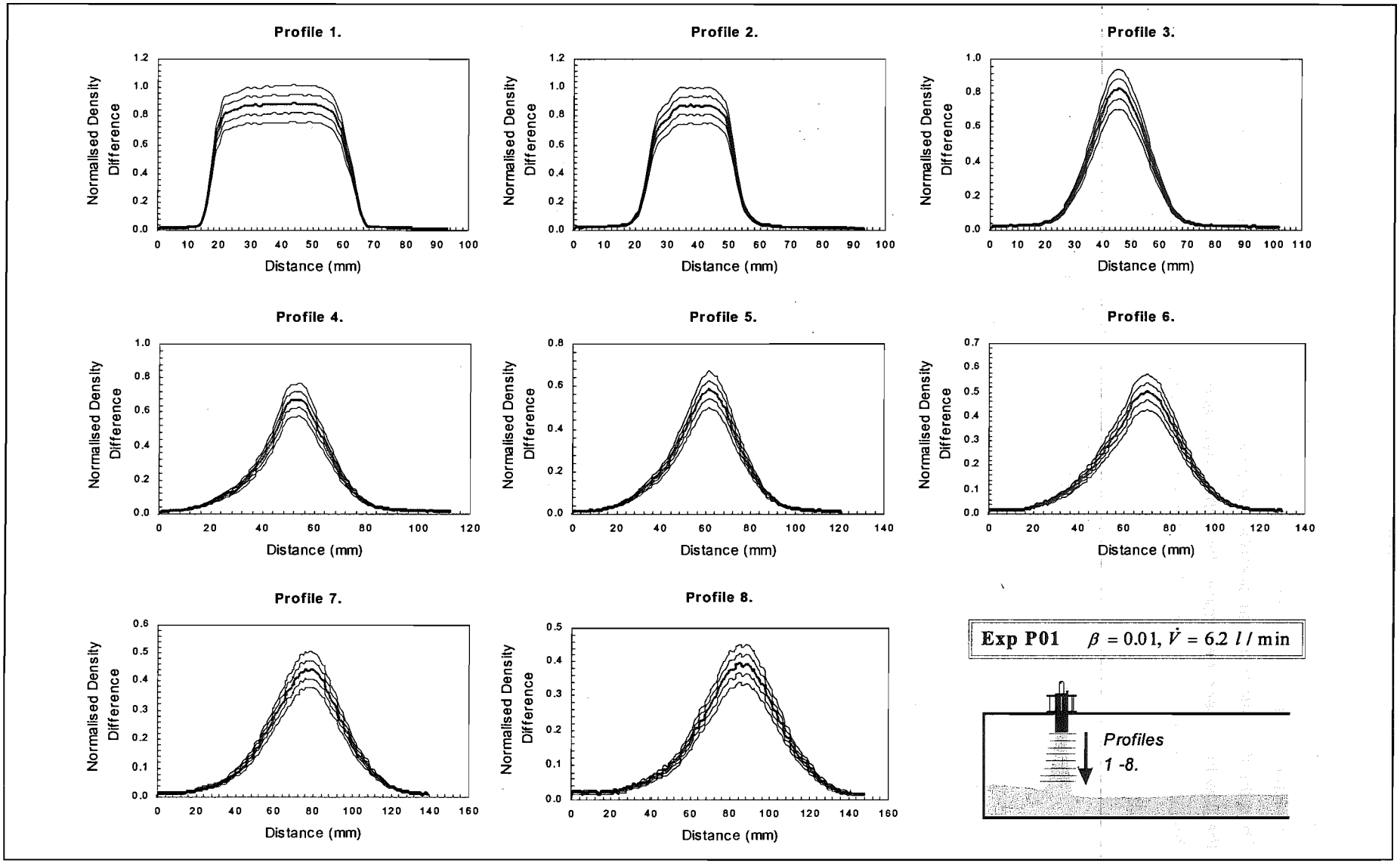

Figure 5-10 Normalised density difference profiles from source plume P01.

5.3.3 *Flow Field Development*

The temporal development of the flow field was measured for the C-Series experiments; Figure 5-13 shows the stages that were marked in time. However the first three stages of the development occurred in the source compartment, which was the focus of the P-Series work. Thus the time intervals that describe the occurrence of the first three events in the development of the flow have been determined from the video record of the P-Series experiments. The complete development of the P-Series flow field was only recorded onto videocassette for experiment P02, which was part of the repeatability analysis that was conducted for experiment P01 (β = 0.01). During the development of the plume source however, two trial experiments were also conducted where the development of the flow field was recorded. The plume source in these experiments was different from the final source design, in that the source did not contain the three layers of fine wire mesh (refer to Section 3.3.1). The fluid source conditions in these experiments however were the same as experiment P01 (β = 0.01 and $\dot{V}_s$ = 6.2*l/min*). Thus, to provide a measure of the flow field development in the source compartment, Table 5-2 details the time intervals that were measured from the three experiments that had P01 source conditions (β = 0.01 and V = 6.2*l/min*). The time interval Δt_1 shown Table 5-2 describes that time that it takes for the plume front to fall from the source onto the floor of the model. The time interval $\Delta t_{1\text{-}2}$ is the time that it takes for the nose of the ceiling jet to travel from the impingement point of the plume to the back wall of the source compartment. Finally, the time interval $\Delta t_{2\text{-}3}$ is the time that it takes for the reflected ceiling jet to travel from the rear wall of the source compartment, back to the salt water plume. No video record was available to determine the flow field development for source plume P06 (β = 0.02)

Title	Time Interval between Events in the Source Compartment (s)		
	Δt_1	$\Delta t_{1\text{-}2}$	$\Delta t_{2\text{-}3}$
P02	5	11	14
Trial exp 1	8	10	14
Trial exp 2	8	10	15

Table 5-2 ***Temporal development of the flow field in the source compartment for source plume P01 (β = 0.01 and V = 6.2l/min).***

Table 5-2 shows that there is a notable difference between experiment P02 and the two trial experiments in the time that it takes for the saline plume to strike the floor of the model, i.e. Δt_1. This is probably due to the presence of the fine wire mesh in the plume source for experiment P02. The fine mesh distributed the saline flow over a larger area of the source than had occurred in the trial experiments. Thus, the mesh reduced the initial momentum with which the fluid exited the source. The time intervals that describe the spread of the ceiling jet in the source compartment however, (that is, time intervals $\Delta t_{1\text{-}2}$ and $\Delta t_{2\text{-}3}$), agree well for all three experiments. The following time intervals are therefore recommended as a measure of the flow field development in the source compartment for plume P02.

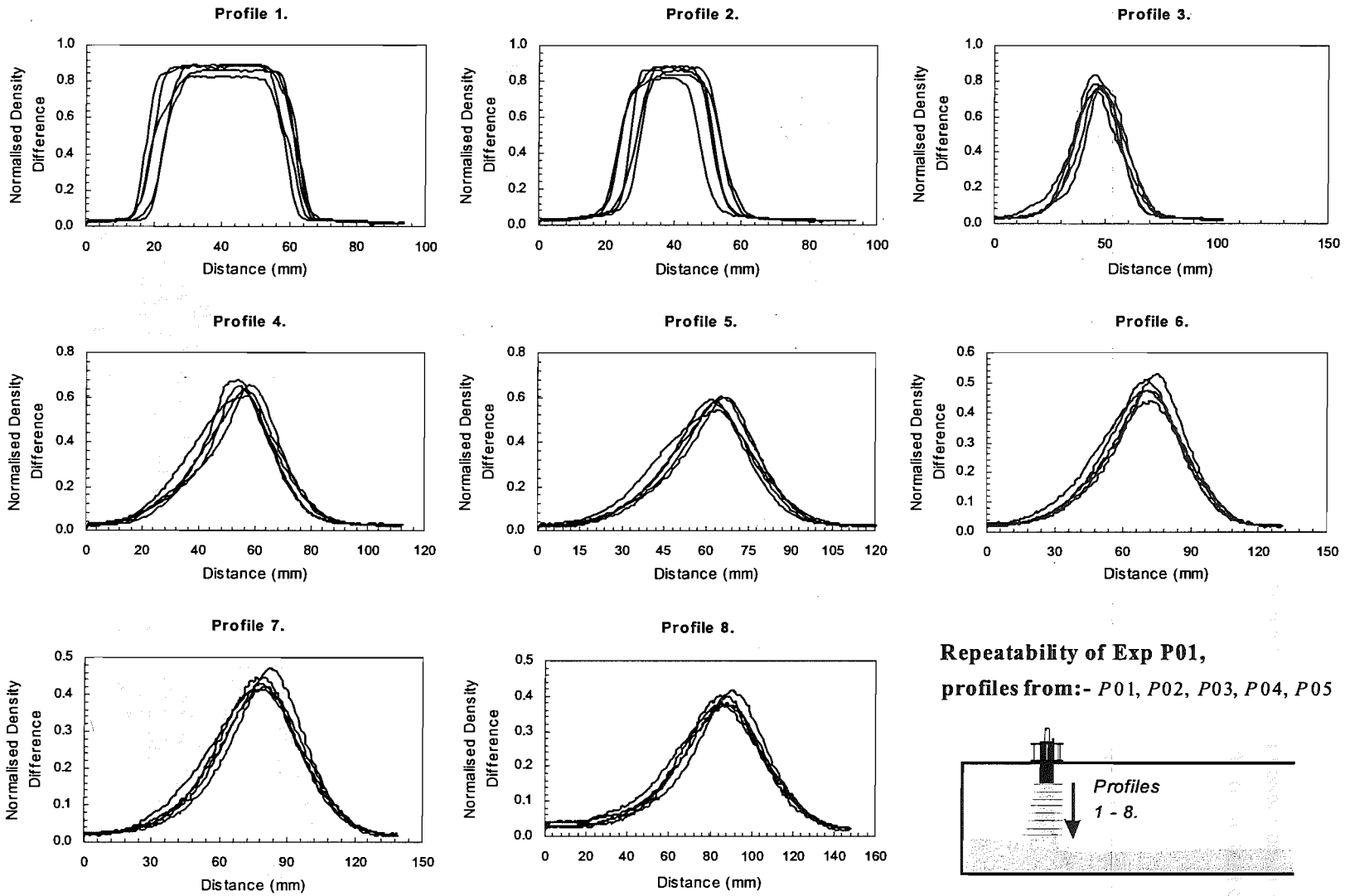

Figure 5-11 Repeatability of the P-Series experimental measurement of the normalised density difference.

Δt_1 = 5 seconds

$\Delta t_{1\text{-}2}$ = 10 seconds

$\Delta t_{2\text{-}3}$ =14 seconds

There is no measure of the development of the flow field in the source compartment for source plume P06 (β = 0.02).

5.4 C-Series

5.4.1 Normalised Density Difference Profiles

The eight profiles for each of the C-Series experiments were collected from the compartment that was adjacent to the room containing the salt water plume. ***Figure*** 5-12 shows the typical locations of the eight profiles in the saline layer that formed in this compartment. The same Cartesian coordinate system used to describe the P-Series profile locations is used to describe the location of the profiles in the C-series flows; refer Figure -5-3. The normalised density difference profiles from experiment C04 are shown in Figure 5-15. The balance of the normalised density difference profiles for the C-Series experiments are displayed in Appendix 3. Experiment C06 was repeated once as experiment C09. Figure 5-16 shows the agreement between the normalised density difference profiles for these two experiments.

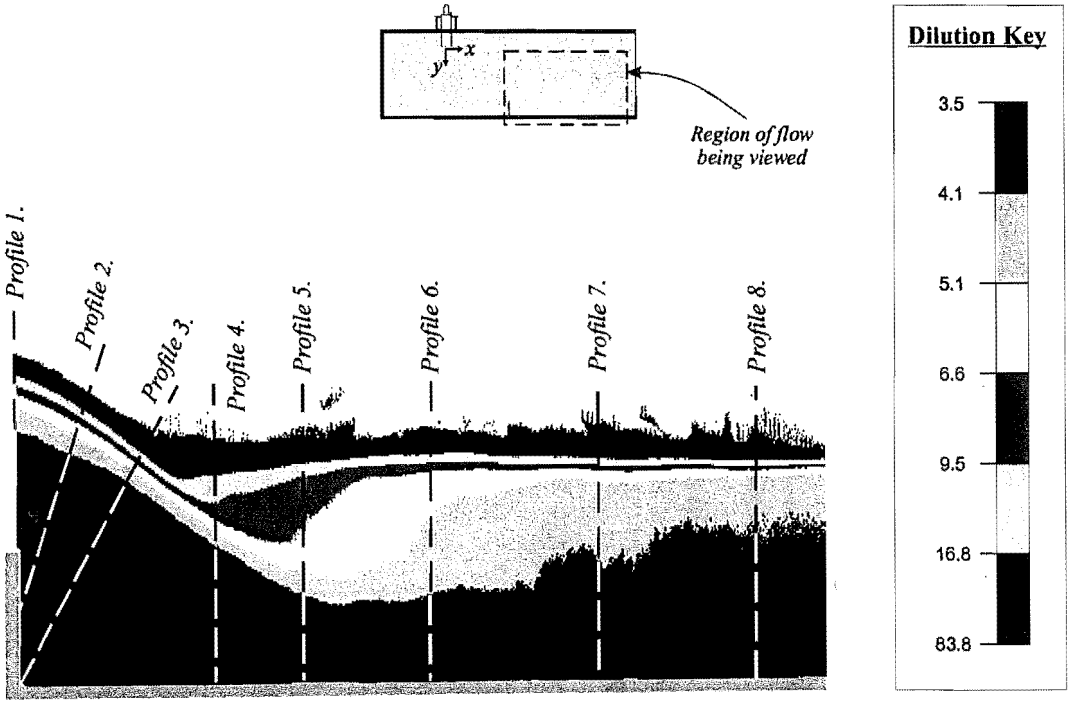

Figure 5-12 ***A time averaged image of the flow in a C-Series experiment (C04), showing the approximate location of the eight normalised density difference profiles that section the saline layer in the second compartment.***

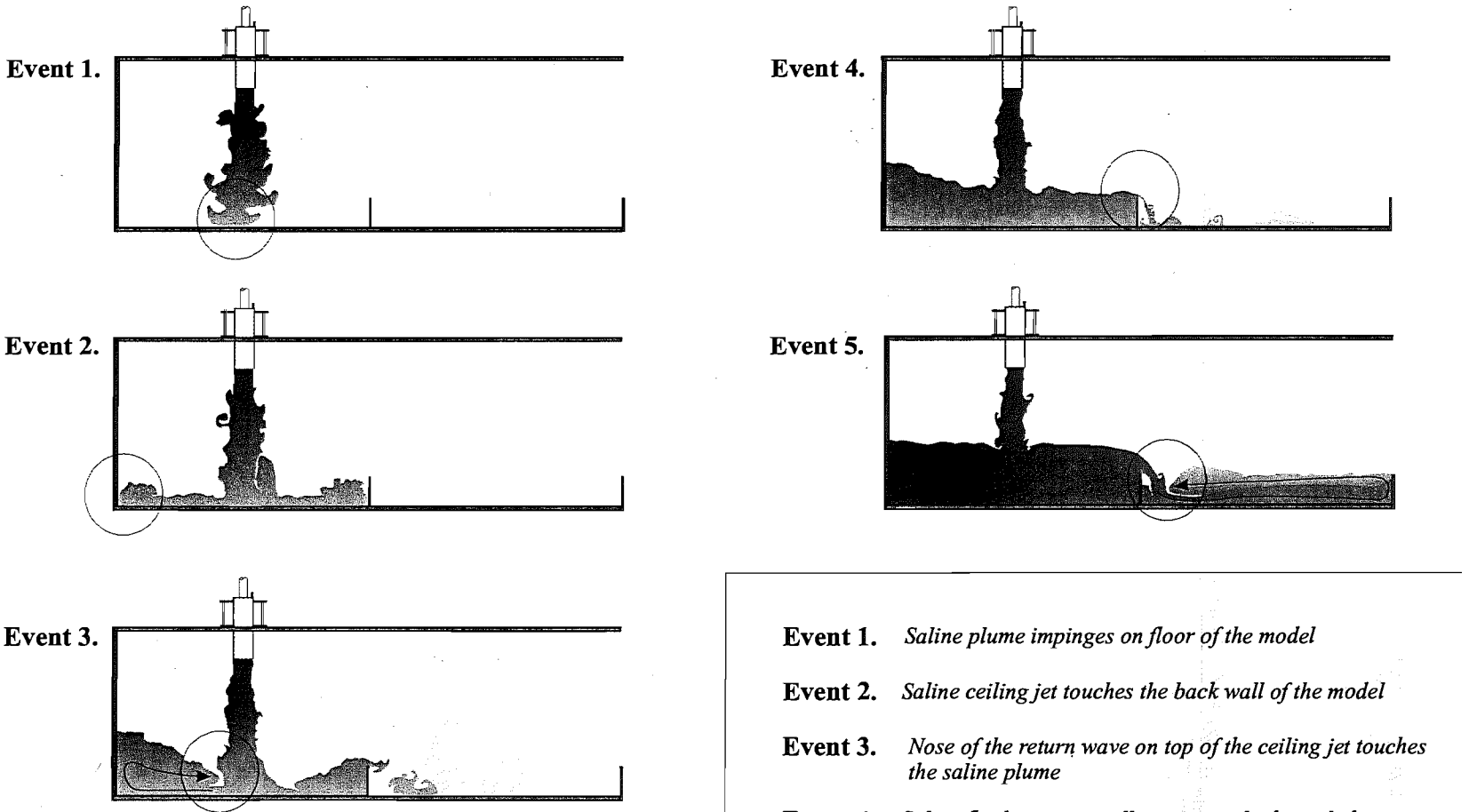

Figure 5-13 Schematic diagram showing the events in the C-Series flow field development that were marked in time.

5.4.2 Dilution Contours

Figure 5-14 shows contour plots of the steady state flow field for the C-Series experiments.

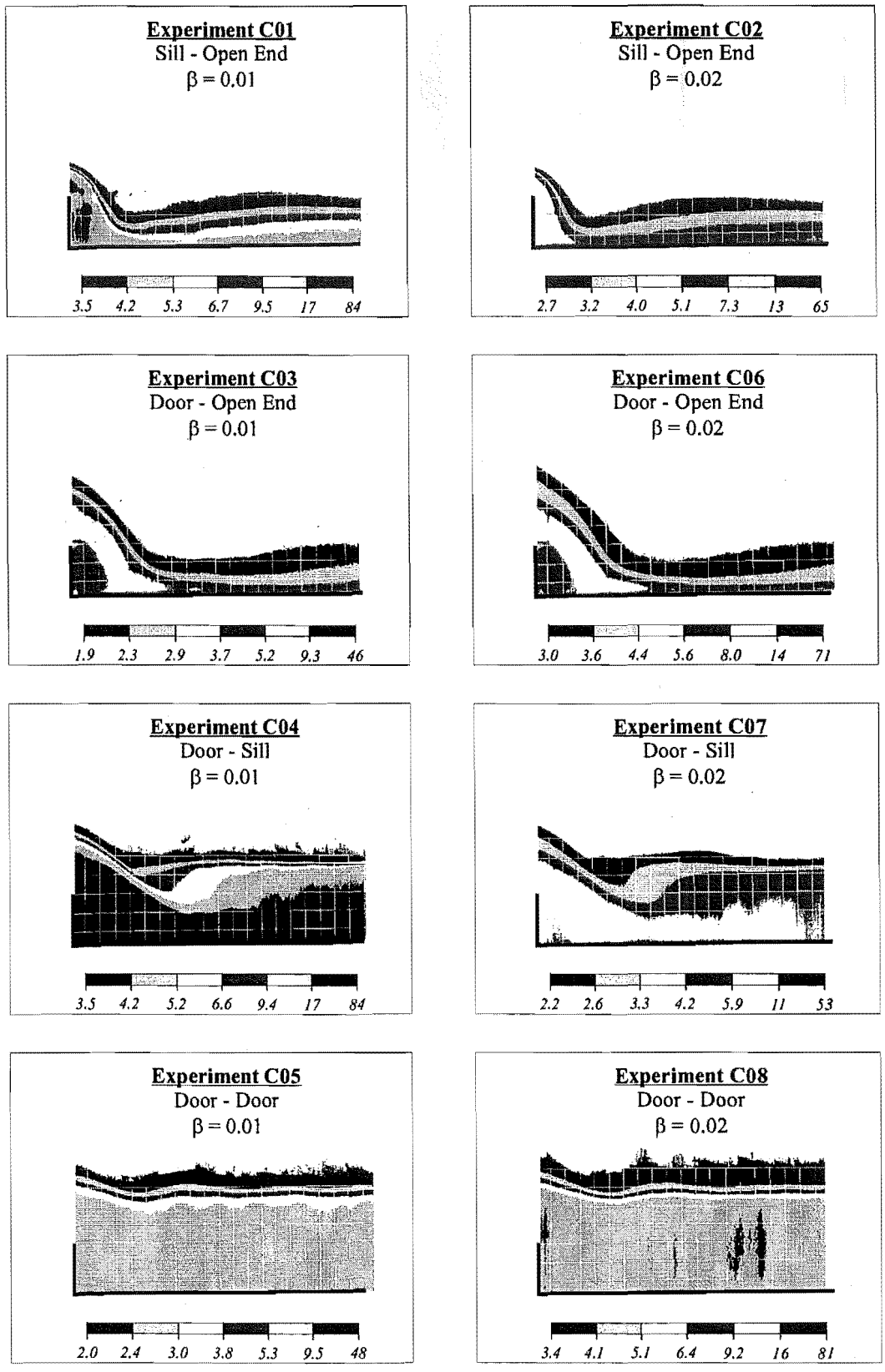

Figure 5-14 Time averaged dilution contour maps of the C-Series experiments

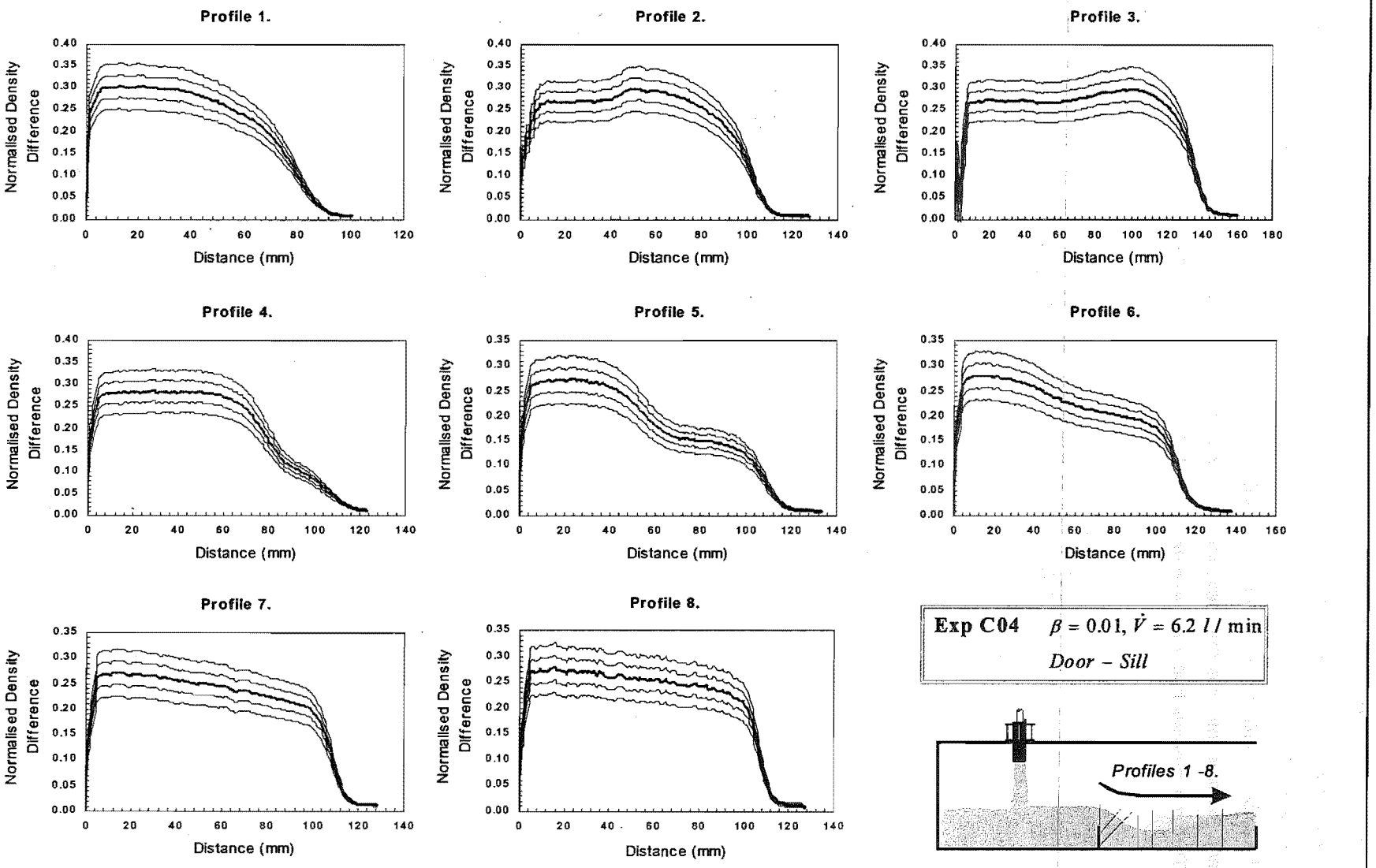

Figure 5-15 Normalised density difference profiles from C-Series experiment C04.

5.4.3 Flow Field Development

A temporal development of the saline flow field in the compartment adjacent to the source room was determined from the video record of the C-Series experiments. For each C-Series experiment Table 5-3 details the buoyancy of the saline fluid at the plume source, the geometry of the model, and the time intervals that describe the development of the flow field in the second compartment. The time intervals that are presented in Table 5-3 are defined in Figure 5-13.

Title	β -	Vent Plate Arrangement	Time Interval between Events (s)		
			$\Delta t_{2\text{-}4}$	$\Delta t_{4\text{-}5}$	$\Delta t_{2\text{-Steady State}}$
C01	0.01	Sill – Open End	27	*NA*	180
C02	0.02	Sill – Open End	21		150
C03	0.01	Door – Open End	29		210
C04	0.01	Door – Sill	27	78	270
C05	0.01	Door – Door	28	74	390
C06	0.02	Door – Open End	22	*NA*	180
C07	0.02	Door – Sill	21	61	240
C08	0.02	Door – Door	21	60	330

Table 5-3 ***Temporal development of the flow field in the second compartment for all the C-Series experiments.***

The time intervals presented in Table 5-3 are linked to the development of the flow field in the source compartment through the occurrence of event two (the saline ceiling jet touching the back wall of the model). The salt water plume was located in the centre of the source compartment, such that the ceiling jet from the plume touched the back wall of the model at approximately the same time that it impacted on the wall dividing the two compartments. As the ceiling jet impacted on the dividing wall, a small amount of saline was washed up the wall and often over the sill of the opening into the adjacent room. In the analysis of the C-Series video record, it was possible to see the saline fluid that washed up the wall as the ceiling jet impacted on the end of the compartment. This time was noted and assumed to be the time of occurrence of event two. The uncertainty in this time is 1-2 seconds.

The visual estimation method that was used to determine the time intervals presented in Table 5-3 could not provide a definite measure of the time taken for the flow field to achieve steady state conditions. The density of the saline layer that formed in the second compartment asymptotically approached the steady state density with time. Thus, it was difficult to visually discern an exact time at which steady state conditions were achieved. Thus, the time that is presented in Table 5-3 for steady state conditions has a high degree of uncertainty (as much as 30-60 seconds).

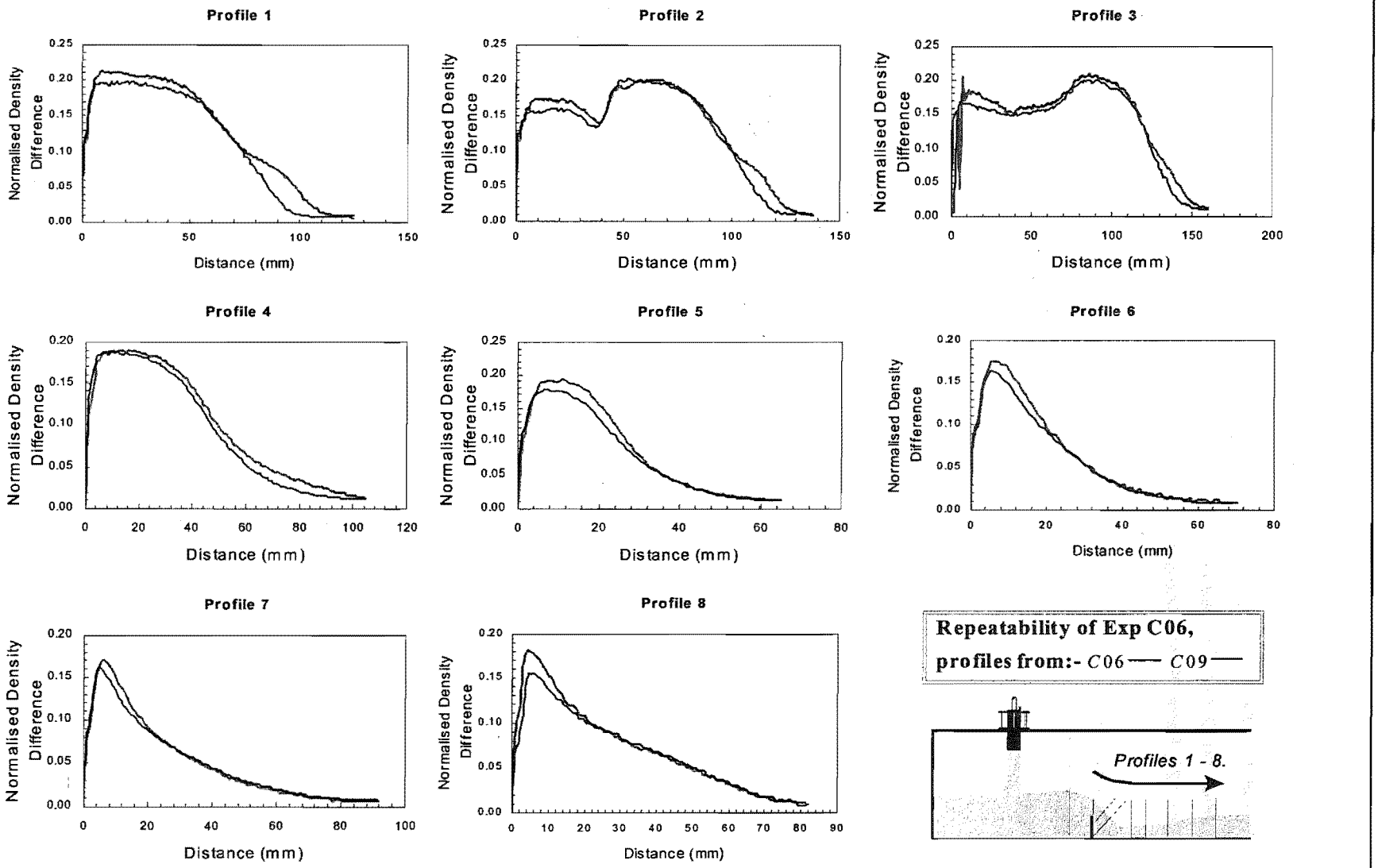

Figure 5-16 Repeatability of the C-Series experimental measurement of the normalised density difference.

5.5 References

1. Wood, I.R., Bell, R.G and Wilkinson, D.L. (1993) *Ocean Disposal of Wastewater,* Advanced Series on Ocean Engineering – Volume 8, World Scientific Publishing Co. Pte. Ltd, P O Box 128, Farrer Road, Singapore 9128.

2. Steckler, K.D., Baum, H.R. and Quintiere, J.G. (1986) 'Salt Water Modelling of Fire Induced Flows in Multicompartment Enclosures' NBSIR 86-3327, National Bureau of Standards, National Engineering Laboratory, Center for Fire Research, Gaithersburg, MD 20899.

Chapter 6 - DISCUSSION

6.1 Introduction

The saline flows from the salt water experiments are analogous to adiabatic, non-reacting, boussinesq smoke flows[1]. In this chapter however, the results of the salt water experiments are not discussed in terms of the equivalent smoke flow properties, but rather in terms of the fluid dynamics that was observed in the flow. This is due to the objective of this research being to verify the hydrodynamic section of Fire Dynamics Simulator (FDS), rather than investigate the movement of fire induced smoke flow. Therefore, the discussion presented in this chapter provides a description of the flow dynamics, to compliment the quantitative measurements taken in the experiments. The chapter is concluded with a discussion of the value of the data set for the purpose of Computational Fluid Dynamics (CFD) model verification.

6.1.1 Sharp Density Interface Anomaly

During experiments, it was found that the image capture equipment did not accurately replicate an abrupt boundary between a bright light source and a dark background. The captured image would blur the sharp boundary into a gradual transition in contrast, which occurred over a width of four to six pixels. This limitation was confirmed by examining an image of a sheet of paper that had two distinct black and white halves. In the image of the paper, the transition from black to white occurred over a width of six pixels. Studying the images of the spatial calibration grids that were used in experiments reinforced this finding. The dark blue lines that were one millimetre thick on the calibration grids were found to be four to six pixels wide in the images, which equated to a distance of four to six millimetres. The Laser Induced dye Fluorescence (LIF) experimental technique used in the salt water experiments was therefore unable to accurately capture sharp density interfaces in the flow. The sharpest interface that could be accurately captured in the LIF images is approximately 5*mm* thick. Thus, in cases where the results show that the density interface was of the order of 5*mm* thick, the real density interface may have been sharper.

6.2 T-Series

6.2.1 General Observations of the Flow

The foam blocks that were used in the flow source of the T-Series model worked well at distributing the momentum of the fluid streams over as large a cross sectional area of each fluid layer as possible. The foam blocks successfully prevented any turbulent mixing occurring between the saline and freshwater within the source compartment. The density interface between the fluids in the source compartment was therefore stable and flat. The depth of the density interface in the source compartment was visually estimated as near 3*mm*.

Once the saline fluid exited the source compartment the underside of the spilling fluid remained detached from the wall that separated the two compartments. The underside of the flow was initially projected upward; perhaps 3*mm* above the level of the sill before it started to drop down to the floor of the model. There was a constant stream of eddies forming on this edge of the flow. The eddy structures appeared to form right from the leading edge of the sill, and they grew in diameter with distance from the opening; see Figure 6-1.

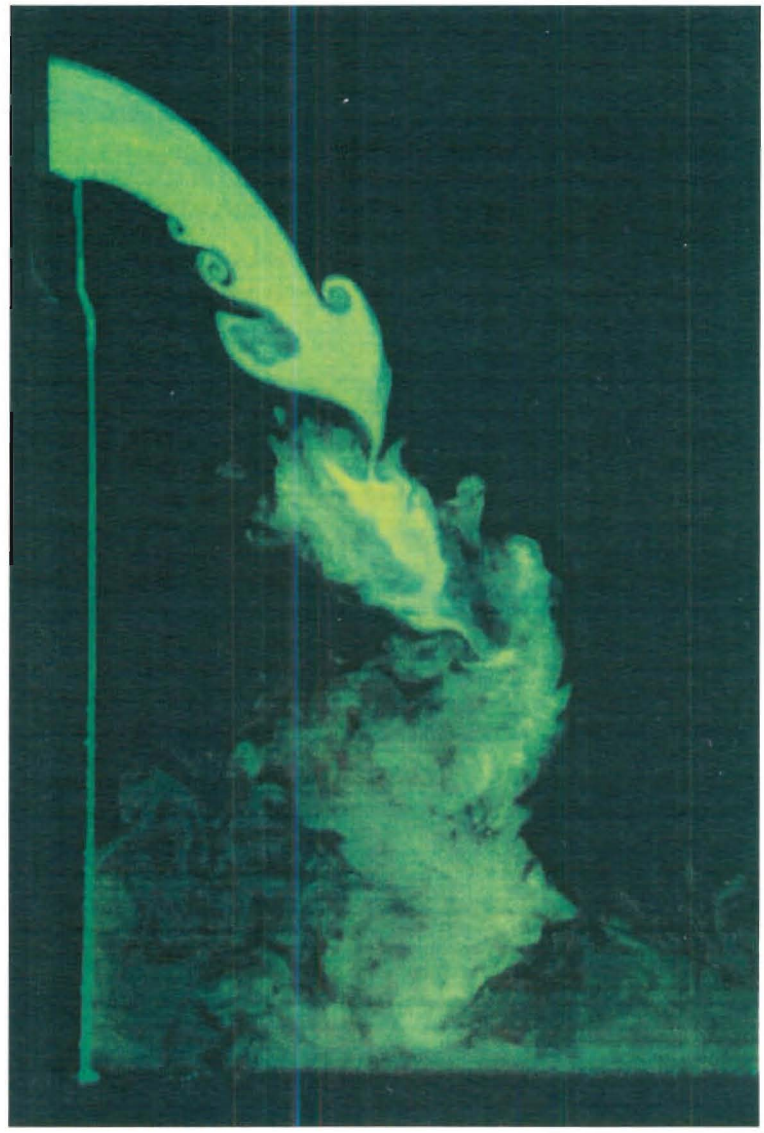

Figure 6-1 Photograph of the spilling saline plume that is the T-Series transitional flow.

Eddy structures only formed on the upper surface of the spilling plume after the flow was beyond the plane of the opening. In the region immediately after the opening, there was a length on the upper surface of the saline flow that remained sharp and stable. After a distance however, small depressions would form on this interface that would grow in size to form an eddy; see Figure 6-2. The point at which the depressions on the upper surface of the flow started to roll up into eddies

varied between experiments. This can be seen clearly in the dilution maps in Figure 4-5. The abrupt bump on the upper surface of the plume boundary in these dilution maps can be considered as the onset of turbulent mixing. In general, the smaller the density difference and the larger the volumetric flow rate, the closer to the plane of the opening the turbulent eddy structures would start to form.

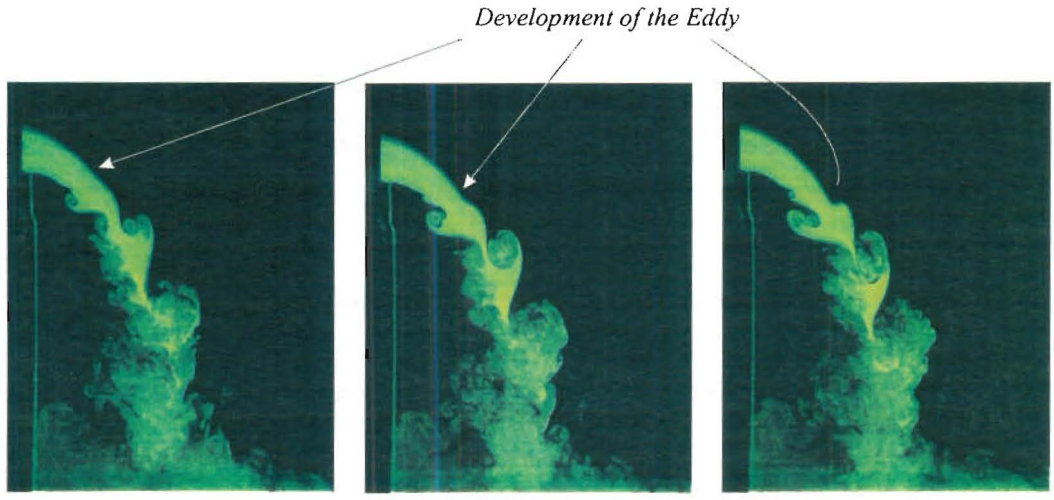

Figure 6-2 ***Photographs showing the progressive formation of an eddy on the upper surface of the spilling saline flow.***

6.2.2 Interpretation of Normalised Density Difference Profiles

Potential Core Region

Generally, the first two or three profiles in the T-Series experimental results have a flat plateau top, which shows the existence of a potential core region within the plume. Figure 6-3 shows the first two profiles from experiment T02 to illustrate this point. The potential core region within the plume is the fluid that has not yet been diluted through mixing with ambient fluid.

In experiments, as the plume spilt away from the plane of the opening, the shear induced turbulence along the boundaries of the flow gradually ate into the cross section of the spilling saline. At some point downstream, the turbulence on the perimeter of the spilling plume converged to meet near the centre of the flow. Below this point, all the saline fluid was subject to dilution by ambient fluid drawn into the saline flow by the turbulence along the plume boundaries. The potential core region exists to the point where the density across the entire cross-section of the flow is influenced by the turbulent mixing. In the T-Series experiments this point generally lay between the third and fourth profiles, as can be seen in Figure 6-4.

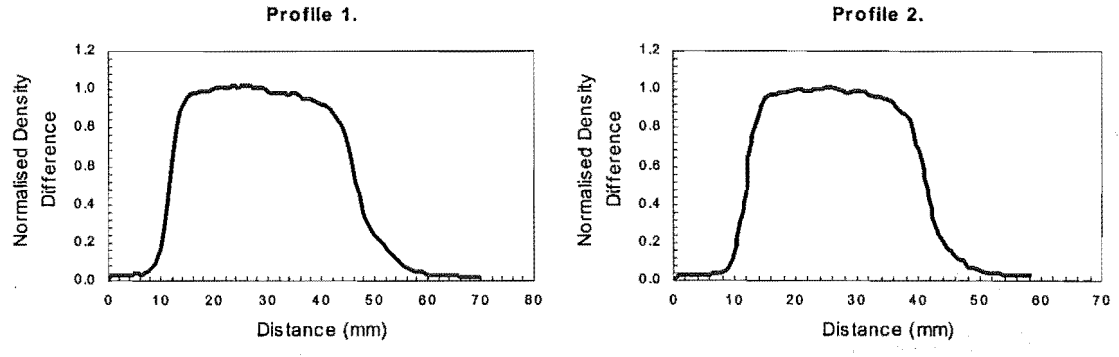

Figure 6-3 ***Profiles one and two from experiment T02, showing the potential core region in the transitional flow.***

The steep sections in the first and second profiles of each experiment show that the saline flow had a sharp density interface with the ambient freshwater. In reality, the edges of these initial profiles may be steeper than what is shown in the plotted results; refer Section 6.1.1.

Lopsided Profiles

Typically in the T-Series results, the third and fourth profiles were noticeably lopsided. These profiles showed that there was mixing occurring on the underside of the plume, while there was no mixing occurring on its upper boundary. This differential mixing was observed in experiments, where eddies on the underside of the saline flow were seen to form immediately from the downstream edge of the sill, while eddy structures on the upper surface of the flow did not form until some distance downstream from the opening. Figure 6-4 illustrates this point with the third and fourth profiles from experiment T02. As with the first and second profiles, it is possible that the right hand side of these profiles (the upper interface) may be steeper than is actually presented in the results.

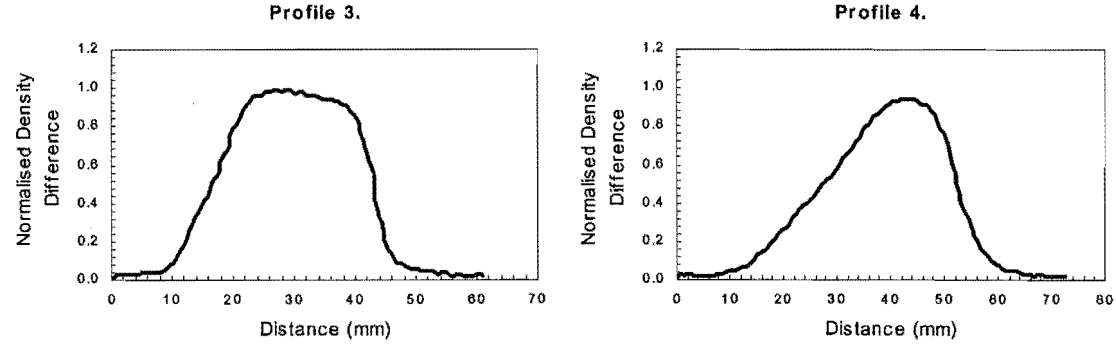

Figure 6-4 ***Profiles three and four from experiment T02, showing their lopsided nature immediately after the potential core region.***

Gaussian Distribution

Once the potential core region of the spilling saline was consumed, the entire cross section of the plume was turbulent. Across[†] a fully developed turbulent plume, the density has a Gaussian distribution[2]. The fifth and sixth profiles of each T-Series experiment were collected from the region of the flow that was completely turbulent. There was generally a noticeable difference between the shape of the fifth and sixth profiles, indicating that the flow had not yet completely achieved self-similarity at these sections, or that the presence of the end wall of the model was influencing the flow. The fifth and sixth profiles however, did appear to be converging toward a Gaussian distribution with distance from the opening. Figure 6-5 shows the theoretical Gaussian curve overlayed onto the fifth and sixth profiles from experiment T02. The Gaussian curve is given by Equation (6-1)[2]. The variable b is the radius at which the mean velocity is equal to the mean centreline velocity divided by the exponential (e^1 = 2.718). As there was no velocity information obtained from the experiments, to compliment the normalised density difference profiles, the values of b used in the calculation of the Gaussian the curves (shown in Figure 6-5) are best-fit values.

$$\frac{\Delta\rho_r}{\Delta\rho_o} = \left(\frac{\Delta\rho_r}{\Delta\rho_z}\right) \times \left(\frac{\Delta\rho_z}{\Delta\rho_o}\right) = \exp -\left(r^2/\lambda^2 b^2\right) \qquad \text{Equation (6-1)}$$

Where

λ = 1.067 - plumes [2]

b = 18.6mm – best fit value for Profile 5

b = 24.0mm – best fit value for Profile 6

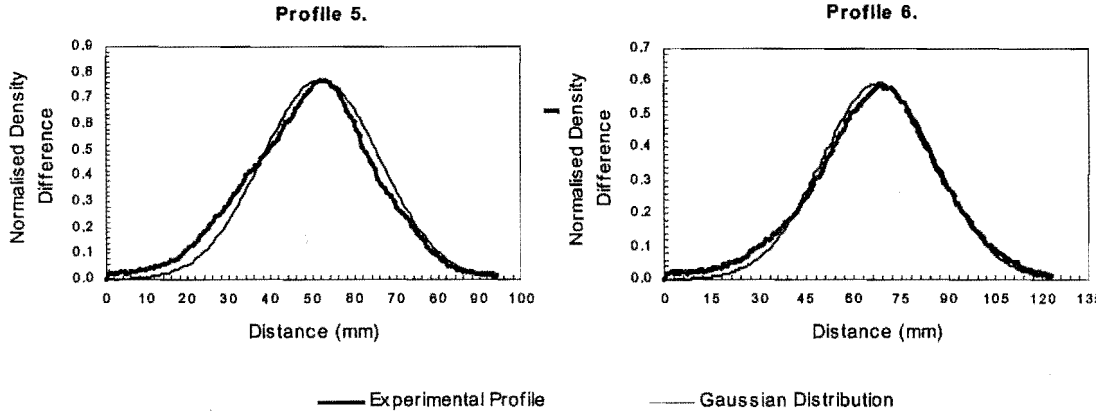

Figure 6-5 ***Profiles five and six from experiment T02, showing the near Gaussian distribution of the fully developed turbulent flow.***

[†] *Sectioning the flow at an angle perpendicular to the trajectory.*

Impingement and Recirculation Region

The seventh and eighth profiles for the T-Series experiments were generally located within the region of the flow generated by the plume impinging onto the horizontal surface of the model. The seventh profile typically sectioned the plume at an elevation just below the top of the roller region that formed underneath the spilling saline. This profile typically shows that the saline in the centre of the roller region is of a lower density than the fluid on the perimeter. The eighth profile is generally a horizontal section through the flow that is taken just above the depth of the ceiling jet that forms on the right side of the impingement region. The left side of this profile captures the density of the saline fluid that flows up the wall of the model and into the recirculation region. The seventh and eight profiles from experiment T02 are shown in Figure 6-6 to illustrate these points.

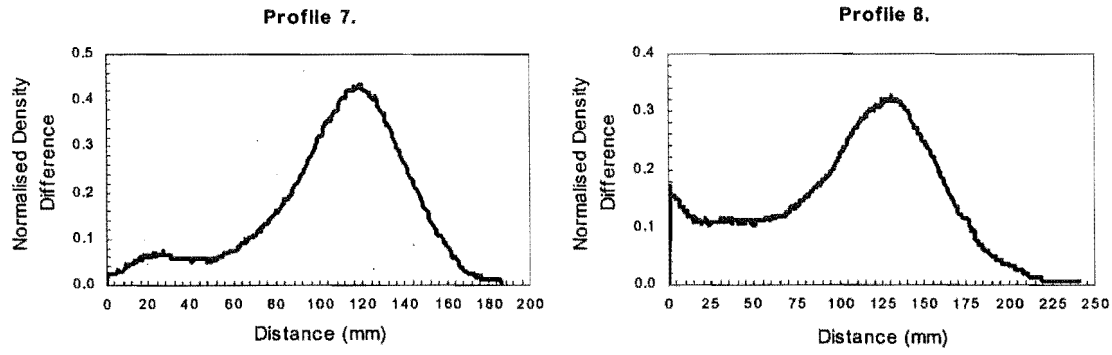

Figure 6-6 ***Profiles seven and eight from experiment T02, showing the existence of a recirculation region beneath the spilling saline.***

6.2.3 Repeatability

The repeatability of the T-Series experiments is shown in Figure 5-6. The agreement between the normalised density difference measurements from each experiment is excellent. This means that the uncertainty of the normalised density difference measurements would have been significantly reduced had multiple measurements been collected during each experiment; refer Section 4.5.2.

6.2.4 Vent Flow Characteristics

The T-series flows were a series of artificially generated exchange flows through an opening that was geometrically similar to a doorway. An artificial pressure gradient was imposed on the system by using pumps to control the volumetric flow rate of the two fluid streams through this opening. The opening between the compartments acted as a hydraulic control on the system, setting the interface depth between the two fluid streams for the buoyancy and volumetric flow rates imposed by the pumps. Exchange flow theory [3][4][5] states that, in idealised conditions, the sum of the squared Froude number from each of the streams will equal unity in the plane of the contraction, refer Equation (6-2). However, although the opening in the model does act as a hydraulic control on the system, the exchange flow theory is not applicable in this case, because the flow in the region of the doorway is rapidly varying due to the abrupt contraction of the geometry [6].

The densimetric Froude number and the bulk layer properties for each of the fluid streams in the plane of the opening are presented in Table 6-1. For the freshwater and the saline fluid streams, the layer depth, the bulk velocity, the effective gravity and the Froude number have been listed in Table 6-1. The Froude number has been calculated in accordance with Equation (6-3). The depth of each fluid stream has been measured according to the density interface between the fluids. Using this measure of the depths, the saline fluid stream occupied a range of depths between 15% and 40% of the vent height.

$$\left(\frac{s_\infty}{\sqrt{g'h_\infty}}\right)^2 + \left(\frac{s_s}{\sqrt{g'h_s}}\right)^2 = 1 \qquad \text{Equation (6-2)}$$

Exp	Layer Depth (m)		Bulk Velocity (m/s)		Effective Gravity (m/s^2)	Froude Number -		Hydraulic Diameter (m)
	h_s	h_∞	s_s	s_∞	$g' = \beta g$	Fr^2_{Saline}	Fr^2_{Fresh}	d_h
T01	0.050	0.155	0.028	0.009	0.03	0.58	0.02	0.065
T02	0.038	0.167	0.037	0.009	0.06	0.58	0.01	0.054
T03	0.030	0.175	0.047	0.008	0.13	0.56	0.00	0.046
T04	0.083	0.122	0.037	0.025	0.03	0.57	0.18	0.088
T05	0.068	0.137	0.045	0.022	0.06	0.46	0.06	0.079
T06	0.051	0.154	0.059	0.020	0.13	0.53	0.02	0.066
T07	*0.038*	*0.167*	*0.037*	*0.008*	*0.07*	*0.56*	*0.01*	*0.054*
T08	*0.039*	*0.166*	*0.036*	*0.009*	*0.06*	*0.53*	*0.01*	*0.055*
T09	*0.040*	*0.165*	*0.035*	*0.009*	*0.06*	*0.52*	*0.01*	*0.056*
T10	*0.038*	*0.167*	*0.037*	*0.008*	*0.06*	*0.58*	*0.01*	*0.054*

Table 6-1 ***Listing the bulk flow characteristics within the plane of the opening for all the T-Series experiments.***

$$\mathrm{Fr} = \frac{s}{\sqrt{g'd_o}} \qquad \text{Equation (6-3)}$$

The Reynolds number of the saline flow in the plane of the opening was calculated according to Equation (6-4), using the bulk velocity of the fluid and the depth of the flow. For experiments T01 through T03, the Reynolds number of the saline flow was 1314. For experiments T04, T05 and T06, the Reynolds number was 2808.

$$\mathrm{Re} = \frac{\rho_s s_s h_s}{\mu} \qquad \text{Equation (6-4)}$$

Hydrogen bubble work done prior to the LIF experiments revealed that, within the plane of the opening, the plane of zero velocity did not coincide with the density interface. Although the saline and the freshwater fluid streams had the same volume flux, they had different depths and consequently different bulk velocities. The saline fluid was denser and moved faster than the freshwater in the plane of the opening. This velocity profiles that were seen in the hydrogen bubble work are schematically illustrated in Figure 6-7.

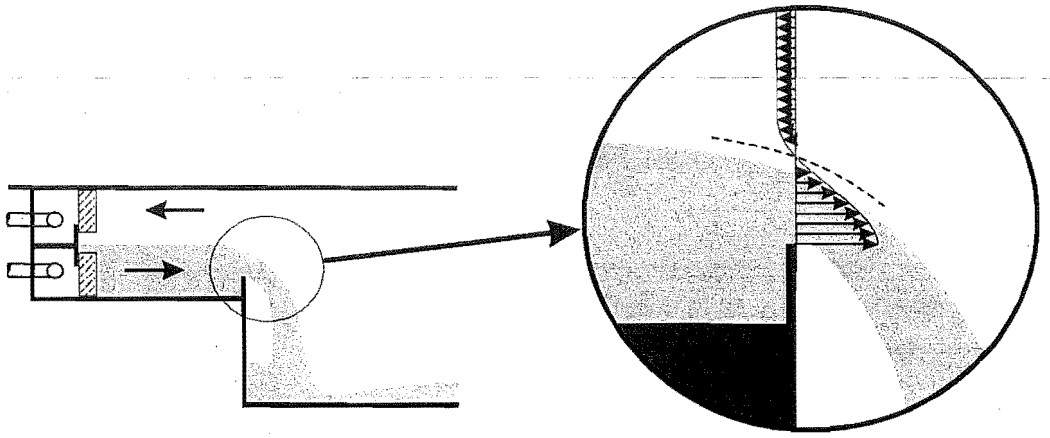

Figure 6-7 ***Schematic illustration showing the offset of the zero velocity plane from the density interface in the plane of the opening.***

6.2.5 Trajectory

The trajectory of the spilling plume was analysed by calculating the location of the peak concentration in each of the eight density profiles from each experiment. The vertical height of fall has been measured downward from the mid height of the saline layer in the plane of the vent. The horizontal coordinate has been measured from the downstream edge of the opening between the compartments. Both spatial coordinates have been normalised using the hydraulic diameter (d_h), given by Equation (6-5).

$$d_h = \frac{4 \times (\text{Flow Area})}{(\text{Wetted Perimeter})} = \frac{4 h_s W_{door}}{(2h_s + 2W_{door})} \qquad \text{Equation (6-5)}$$

The hydraulic diameter has been used to non-dimensionalise the spatial coordinates to account for the different aspect ratios of the rectangular flow source. For example, in experiments T01-T03 the saline flow was between 30*mm* and 50*mm* deep in the plane of the opening; while for experiments T04-T06 the flow depths were between 51*mm* and 83*mm* deep. By comparison, the width of the opening (source) was 94*mm*.

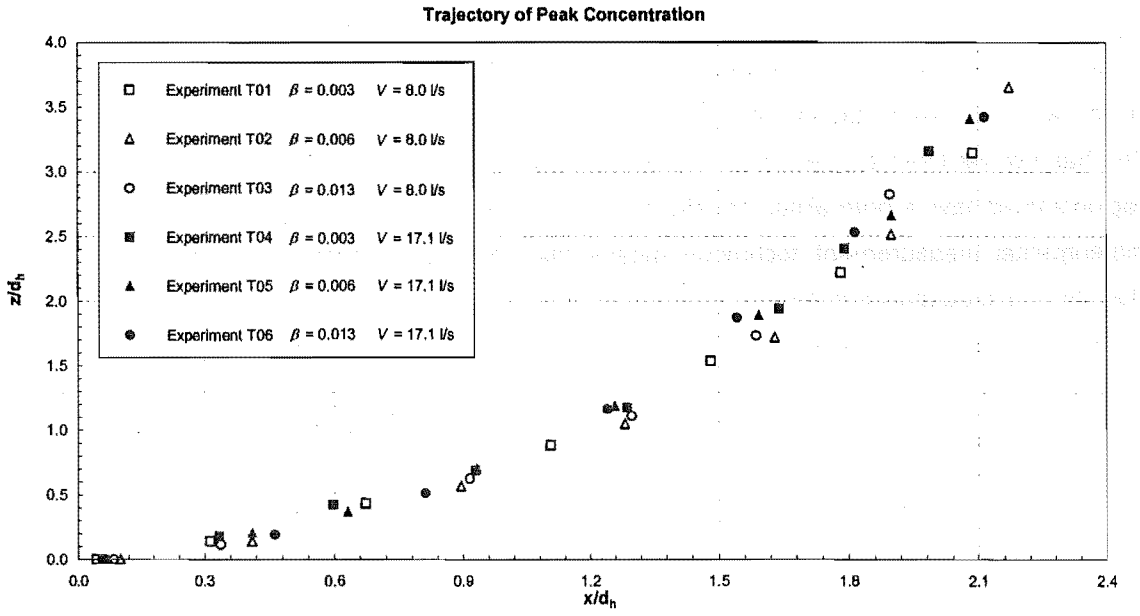

Figure 6-8 ***Graphs showing the non-dimensionalised trajectory of the six different T-Series flows.***

Figure 6-8 shows that the trajectory for each of the six different transitional flows collapse onto a single curve when the spatial coordinates are non-dimensionalised with the hydraulic diameter at the rectangular source. The agreement in the non-dimensional trajectory, across all six transitional flows, is excellent.

6.2.6 *Uncertainty of T-Series Results*

All the T-Series time averaged density difference profiles show the existence of a potential core region within the saline plume, refer Section 6.2.2. The potential core region contains source fluid that has not yet been diluted through mixing with the ambient fluid. Thus, the saline fluid in this region should have a normalised density difference value equal to one. In reality, uncertainty in the experimental measurement technique means that the experimental measurement of the fluid density can produce normalised profiles that have a peak value not equal to one. Chapter 4 discusses and evaluates the uncertainty of the experimental measurement technique.

Appendix 3 contains the normalised density difference profiles from each of the six different T-Series experiments. These experimental profiles show the measurement of the normalised density difference in the potential core region of the flow did not always produce profiles with a peak value of one. In all cases however, the correct normalised density difference value of one lies within two standard deviations of the experimental measurement. In fact, in four of the six cases the correct value lies within one standard deviation of the experimental measurement.

Scaling of the Experimental Profiles

In comparing the experimental measurements with computational results, there is an argument for scaling the T-Series profiles, so that the flat plateau of the initial profiles lies at the correct value of one. If the experimental results are not scaled, the comparison with the computational results can appear poor, thereby implying that the computational model predictions are inaccurate, when in fact the main source of the disagreement is due to the uncertainty in the experimental measurements. Thus, for the comparison of computational results with the experimental profiles, the T-Series normalised density difference profiles have been scaled, so that the flat plateau on the first profile lies at the correct value of one. The factors that were used to scale the experimental measurements are shown in Table 6-2. The scaling has the most impact on the profiles from experiments T01 and T06, where the flat tops of the initial experimental profiles had an average value of approximately 0.86 and 1.10 respectively.

Exp	T01	T02	T03	T04	T05	T06
Scale Factor	1.159	0.981	0.971	1.011	0.939	0.922

Table 6-2 ***Scale factors that are required to correct the T-Series normalised density difference profiles given by the experimental measurements.***

6.3 P-Series

6.3.1 General Observations of the Flow

The flow rate of the saline fluid was successfully distributed over the entire area of the plume source. However, as soon as the fluid exited the port, it converged to form a stream that was narrower than the 50*mm* source width. Eddy structures formed on the perimeter of the flow that gradually ate into the fluid stream, until they met near the centreline of the plume. As with the T-Series experiments, the flow above this point contained a potential core region, which can be clearly seen in Figure 5-9. The fluid within the potential core had the same density as the source fluid. The decay in the width of the potential core region reflects the growth rate of the eddy structures on the perimeter of the flow.

Once discharged from the source, the P-Series plumes sloped mildly toward the enclosed end of the compartment. The drift in the plume trajectory was caused by the restricted direction from which ambient fluid was available to satisfy the entrainment demand of the plume. The enclosed rear end of the compartment meant that ambient fluid had to be drawn past the plume into the rear end of the model. The momentum of this ambient fluid flow pushed the buoyant plume over ever so slightly.

In the time averaged dilution plots of the source plumes in Figure 5-9, there is an abrupt bump on the perimeter of the saline flow that is closest to the enclosed end of the model (the left side of the plots). This point is approximately where the saline flow ceased to converge after leaving the source, and where the small eddy structures started to grow rapidly.

6.3.2 Interpretation of the Normalised Density Difference Profiles

Scaling Profiles

The normalised density difference profiles that were taken just beneath the discharge port of the plume source have a flat top shape. The flat top demonstrates the presence of a potential core region in the flow, as was seen in the T-Series results. Fluid within the potential core region should have a normalised density difference value of one, because it has not yet been affected by turbulent mixing on the perimeter of the flow. Profiles with the flat top shape are seen in the P-Series results in Figure 5-10, however, the profiles plateau at a value of approximately 0.85, rather than 1.0. The consistency of this anomaly has revealed an error in the experimental method.

Previous research[7] has found that the Rhodamine 6G tracer dye adheres to plastic surfaces. This characteristic can reduce the concentration of the dye in solution when the solution is stored in plastic containers. It is hypothesised that during the P-series experiments (and likely the C-Series experiments as well), dye from the saline solution adhered to the porous foam block that was squashed into the plume source. This behaviour would explain the reduced fluorescence seen in the potential core region of the flow (that is, a normalised density difference value of 0.85 rather

than 1.0). Another possible explanation is that there was a shift in the power output of the laser between the capture of the calibration image and the capture of the flow images. This explanation can be eliminated however, by considering the results of the repeatability analysis; refer Figure 5-11. The initial profiles from all five experiments have a flat top at a normalised density difference value of approximately 0.85. The consistency of this result eliminates the possibility that a random fluctuation in the laser power is responsible for the error.

Foam blocks of the same polyurethane material were used in the source structure of the T-Series model. These blocks however, were used in a very large number of preliminary LIF experiments conducted prior to the T-Series experimental program. During the preliminary experiments, the foam was consistently flushed with solutions containing Rhodamine dye concentrations much higher than 0.005*mg/l*. When the T-Series experiments were finally conducted, the foam blocks had a red stained appearance. Rhodamine 6G dye has a red/orange colour in solution at a concentration of 0.005*mg/l*. It is therefore hypothesised that the foam blocks were effectively saturated with the tracer dye prior to the T-Series experiments, and consequently did not remove any significant mass of dye from the T-Series solutions. A clean block of new foam was used in the plume source for the P-Series and C-Series experiments, so that it may have absorbed some of the dye mass.

In the following analysis of the P-Series experimental data, the normalised density difference results have been scaled by a factor to bring the flat plateau up to an average value of approximately 1.0. The correction factors that have been used for this scaling are shown in Table 6-3.

Experiment	P01	P02	P03	P04	P05	P06
Scale Factor	1.128	1.125	1.138	1.168	1.218	1.297

Table 6-3 ***Scale factors that are required to correct the P-Series normalised density difference profiles given by the experimental measurements.***

Region of Converging Flow

The first two normalised density difference profiles for each P-Series experiment show that the saline flow was converging to form a fluid stream narrower than the width of the source port; refer Figure 6-9. The bulk velocity of the fluid discharged from the plume source for plumes P01 ($\beta = 0.1$) and P06 ($\beta = 0.1$) was 0.04*m/s* at the exit point. If Equation (6-6) is used to estimate the buoyant velocity of the source fluid, then the natural buoyant velocity of the fluids from plumes P01 ($\beta = 0.1$) and P06 ($\beta = 0.1$) is 0.07 *m/s* and 0.11*m/s* respectively. Thus the convergence of the fluid stream occurred because the natural buoyant velocity of the source fluid was larger than the velocity with which the fluid was discharged from the port. Therefore, the fluid accelerated toward

the buoyant velocity after it was discharged, and consequently the cross sectional area of the flow was reduced.

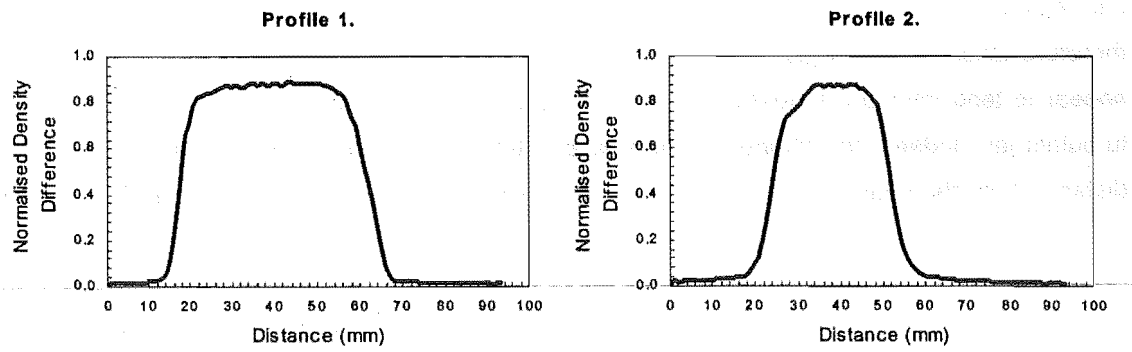

Figure 6-9 ***Profiles one and two from experiment P01, showing the convergence of the saline flow after it leaves the flow source.***

$$s_\rho = \sqrt{\frac{\Delta\rho}{\rho} g d_o} \qquad \text{Equation (6-6)}$$

As the flow from the plume source initially converged, small eddies were observed on the perimeter of the flow. It is likely that the formation of these eddies was induced by the presence of small screws that protruded through the walls of the plume source and into the cross sectional area of the port. Four screws were used to prevent the wire mesh at the bottom of the source popping out. Each screw was located at the centre of each wall and protruded approximately 5*mm* into the cross sectional area of the port. The thread was machined off each screw, such that the diameter of the cylindrical protrusions was 2*mm*. Figure 6-10 shows a plan view of the source opening.

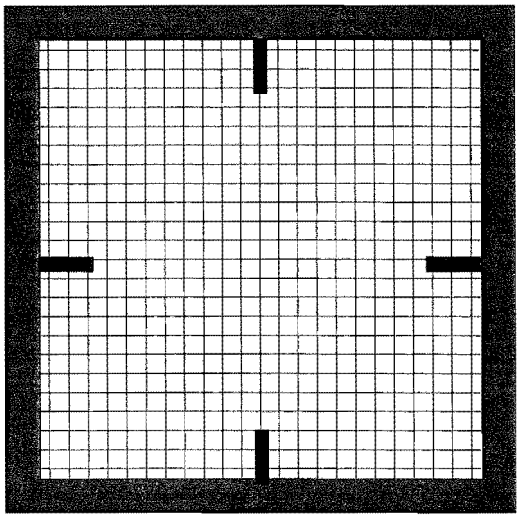

Figure 6-10 ***Plan view of the plume source port, showing the small cylindrical obstructions (machined screws) on the inner walls of the source.***

Gaussian Distribution

In all of the P-Series experiments, the fourth normalised density difference profile was taken from the region of flow below the potential core region. The fourth through to eighth profiles are therefore taken from a region of the flow that is completely turbulent. In general, these profiles appear to tend toward a Gaussian distribution as is found in a fully developed buoyant plume or turbulent jet. Indeed, the change in the shape between adjacent profiles appears to reduce with distance from the source, indicating that the flow is possibly tending toward self-similarity. Figure 6-11 shows the theoretical Gaussian distribution overlaid on the fourth through to eighth profiles of experiment P01. The vertical distance from the source z is known for the P-Series profiles, so that the theoretical radius of the plume b has been determined from Equation (6-7)[2]. The Gaussian distribution is described by Equation (6-1).

$$\frac{b}{z} = K_{pb} \qquad \text{Equation (6-7)}$$

Where

$K_{pb} = 0.105$ [8]

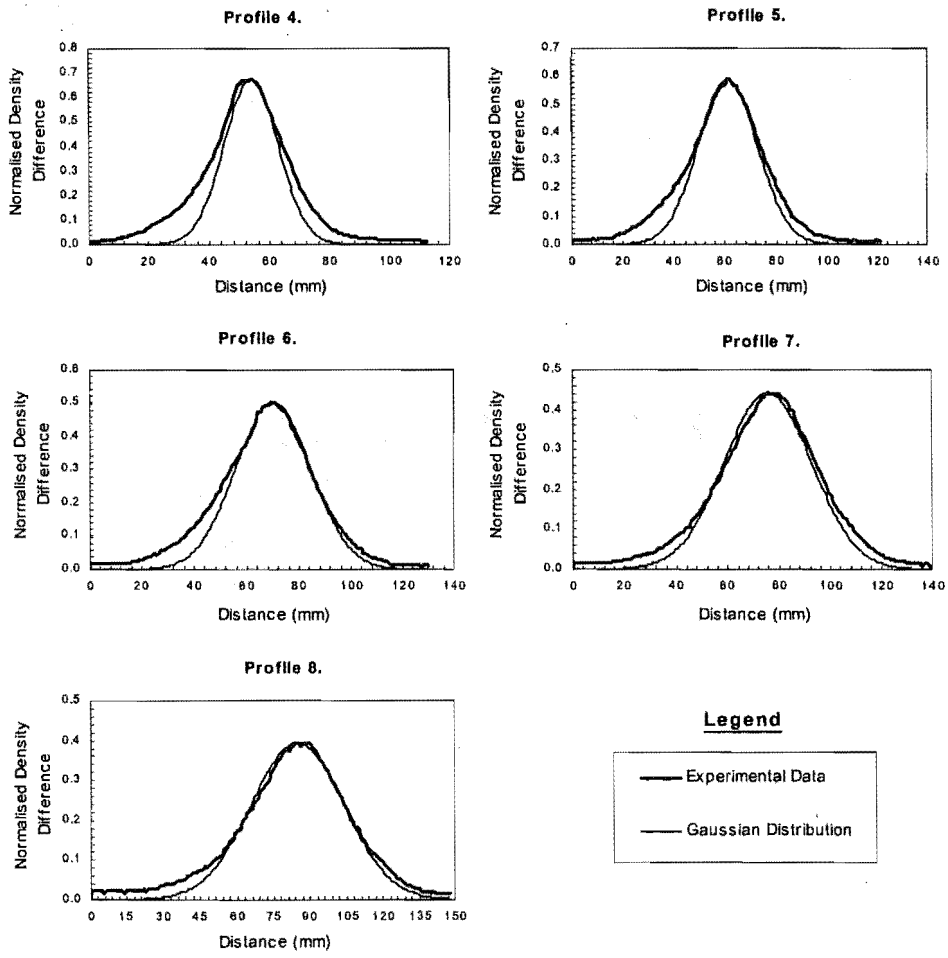

Figure 6-11 Plots of the theoretical Gaussian distribution overlayed on the P-Series experimental profiles from the turbulent region of the plume P01.

6.3.3 Repeatability

The repeatability of the P-Series experiments is shown in Figure 5-11. The agreement between the normalised density profiles is excellent, although not quite as good as the T-Series result. In the comparison of profiles four, five and eight, the profiles from experiment P01 stand out a little from the balance, however there is no obvious reason for this small disagreement. As with the T-Series results, the excellent repeatability of the profiles means that the uncertainty of the normalised density difference measurements could have been significantly reduced had multiple measurements been collected during each experiment.

6.3.4 Source Momentum

The saline source plume used in these experiments was not a true buoyant plume; rather it was a buoyant jet, because it was injected with some initial momentum. In a buoyant jet, the flow undergoes a transition from jet like behaviour where the source momentum dominates the flow, to plume like behaviour where buoyancy is the dominant factor. The transition takes place within a region of the flow where the spatial extent is traditionally described according to the Morton length scale l_M [9].

$$l_M = \frac{M_o^{3/4}}{q_{\Delta o}^{1/2}} \qquad \text{Equation (6-8)}$$

Where

M_o=Specific Momentum Flux $\qquad M_o = \frac{\pi}{4} d_o^2 s_o^2$ Equation (6-9)

$q_{\Delta o}$=Specific Buoyancy Flux $\qquad q_{\Delta o} = \frac{\Delta\rho}{\rho_\infty} g \dot{V}_o$ Equation (6-10)

According to theory, jet like behaviour should be seen in the region of the flow where $z < l_M$, and plume like behaviour is seen where $z > 5l_M$ [10]. For the source plumes P01 (β = 0.01) and P06 (β = 0.02), this means that plume like behaviour should be seen at distances greater than 105*mm* and 150*mm* respectively (1.9 and 2.7 source diameters). Beyond these distances, the buoyancy of the fluid is the dominant driving force. Figure 6-12 shows the decay in the peak concentration of the tracer dye in the salt water plumes. In a fully developed axisymmetric buoyant plume, the peak concentration should decay in accordance with Equation (6-11) [1]. This theoretical relationship is also plotted in Figure 6-12

$$\frac{\Delta\rho_z}{\Delta\rho_o} = K_{p\Delta} \left(\frac{\pi}{4}\right)^{\frac{2}{3}} Fr_o^{\frac{2}{3}} \left(\frac{z}{d_o}\right)^{\frac{-5}{3}} \qquad \text{Equation (6-11)}$$

Where

$K_{p\Delta}$ = 11.1 [8]

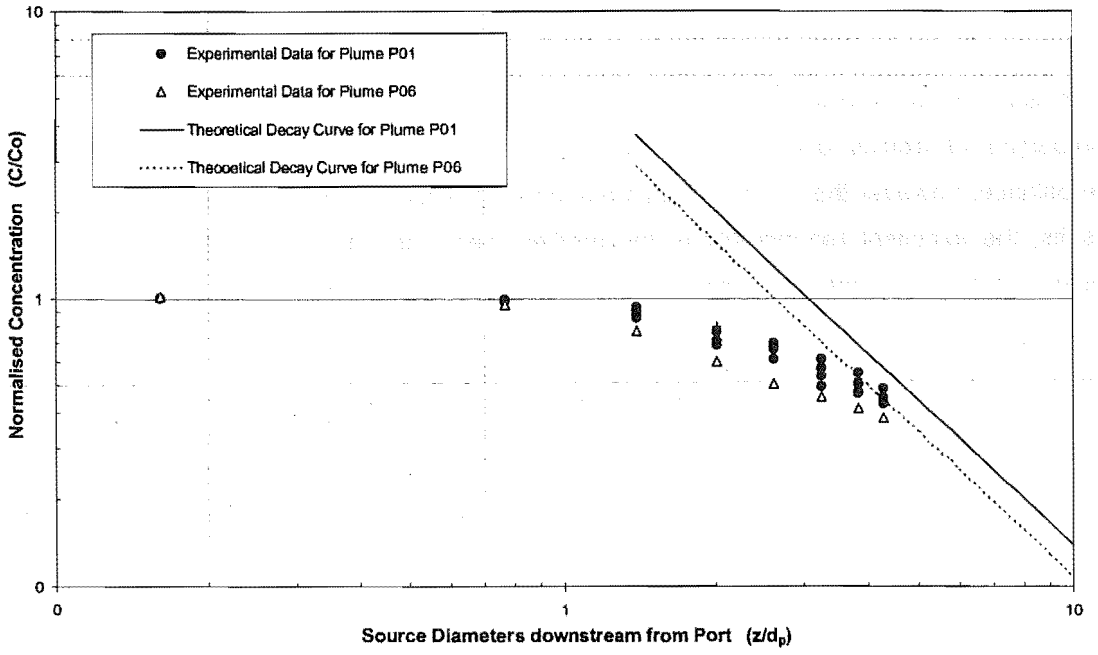

Figure 6-12 Comparison of the decay in the peak concentrations within the P-Series source plumes with buoyant plume theory.

The comparison of the experimental data with established plume theory in Figure 6-12, shows that the source plumes P01 (β = 0.01) and P06 (β = 0.02) are not fully developed before they plunge into the saline layer that forms on the floor of the model. Although buoyancy dominates the flow at distances greater than three source diameters, the velocity field in the flow is still transforming from source distribution toward a Gaussian distribution. If there were no buoyancy in the injected fluid, submerged jet theory would predict that the zone of flow establishment would extend an order of seven port diameters downstream[2]. This distance would equate to 390*mm* for the P-Series flow source, which is well beyond the floor of the model.

The analysis above shows that the P-Series salt water plumes do not behave as a pure buoyant plume at any stage before they plunge into the saline fluid that surrounds the impingement region of the flow. The height of fall for the plumes is too small relative to the source diameter to enable the flows to become fully developed with a self-similar velocity distribution.

Reynolds Number

The Reynolds number of the saline flow was evaluated at the plume source, using the bulk velocity of the flow and an equivalent plume source diameter (refer Equation 5-4). The Reynolds number for the six saline plumes was 2.2×10^4 .

Froude Number

The densimetric Froude number (given by Equation (6-3)) for source plumes P01 (β = 0.01) and P06 (β = 0.02) was 0.56 and 0.39 respectively.

6.3.5 *Uncertainty of P-Series Profiles*

As with the T-Series experiments, the P-Series profiles show the existence of a potential core region just beneath the discharge port of the plume source, refer Section 6.3.2. Profiles that section this potential core region in the source plumes, should have a peak normalised density difference value of one. In reality, uncertainty in the experimental measurement technique means that the fluid in the potential core region of the flow may not have the correct normalised density difference value. The first profile for all of the six experiments conducted as part of the P-Series work had an average peak density difference value of 0.85. This peak value was often greater than two standard deviations away from the correct value of one. The consistency of the peak experimental value, and the fact that the correct value lays more than two standard deviations away from the experimental value, implied that the uncertainty analysis might not have been complete. In retrospect, it is believed that the P-Series experimental results were influenced by a factor not accounted for in the uncertainty analysis (that is, the extraction of some tracer dye from the saline fluid as it flowed through a porous foam block; refer Section 6.3.2). The influence of the dye extraction on the experimental measurements can be simply corrected by scaling the experimental profiles. As with the T-Series profiles, the existence of the potential core region within the P-Series source plumes provides a means for determining the correct scaling for the experimental profiles, refer Section 6.2.6. Therefore, wherever the P-Series profiles are compared to computational results, the experimental profiles have been scaled by the factors listed in Table 6-3. In the uncertainty analysis, the extraction of dye from the saline fluid would have increased the value of the scaling factor C_{Drift}, and possibly have increased the uncertainty of this parameter, such that the uncertainty envelopes would encompassed the correct value of one.

6.4 C-Series

6.4.1 General Observations of the Flow

Figure 6-13 contains four images that illustrate the saline flow seen in each of the four C-Series model geometries. Each of the four images is an instantaneous sketch that shows the turbulent eddy structures seen in the flow. Figure 6-13 should be referred to, to compliment the verbal description of the flows given in this section.

Experiments C01 and C02 – (*Sill - Open End*)

The saline that spilt out of the source compartment over the sill remained attached to the downstream side of the sill. The two dimensional geometry of the opening prevented ambient fluid moving around the edges of the spilling fluid to feed any entrainment demand on the underside of a detached flow. Thus, the entrainment demand on the underside of the spilling flow drew the saline fluid back onto the solid sill wall. The suction of flow onto a solid boundary is often referred to as the conda effect[11][12]. After the saline impinged on the model floor (at the base of the sill), the fluid flowed out of the impingement region as a thin jet-like layer. The thin layer of saline fluid formed a hydraulic jump structure[13][14][15] downstream, which gradually crept back upstream (toward the sill). The jet-like layer of saline that exited the impingement region initially flowed underneath the nose of the hydraulic jump. Downstream however, the turbulence of the jump broke down the jet like layer and mixed the saline fluid thoroughly with ambient fluid that was entrained into the turbulence. Thus, the saline fluid that flowed over the free overfall at the end of the C-Series model was of a lower density, and had a greater depth, than the fluid that had exited the impingement region at the base of the sill.

Experiments C03 and C06 – (*Doorway - Open End*)

The saline fluid that spilt through the opening between the compartments detached itself from the downstream side of the sill. When this flow impinged on the floor of the model, the fluid spread out radially as a thin jet-like layer. Some of the saline fluid in the jet-like layer flowed upstream toward the sill of the opening. This supply of saline caused a roller region to form beneath the spilling flow at the base of the sill. The fluid that was circulated within the roller region was of a lower density than the spilling vent flow, because ambient fluid was drawn into the recirculation from around the edges of the spilling plume. This entrainment (around the spilling vent flow) was evident, because a small pocket of ambient fluid was intermittently visible on top of the roller region at the edge of the sill.

Small eddies were observed to form constantly along the underside of the spilling vent flow. The eddy structures formed immediately after the leading edge of the sill, and engulfed fluid from within the roller region. On the upper surface of the spilling plume, eddies would only form intermittently. These eddies were larger in diameter than those seen on the underside, and only appeared to form once the flow was through the plane of the vent and the upper interface of the plume had a steep incline (i.e., as the fluid approached the impingement region).

(a.)

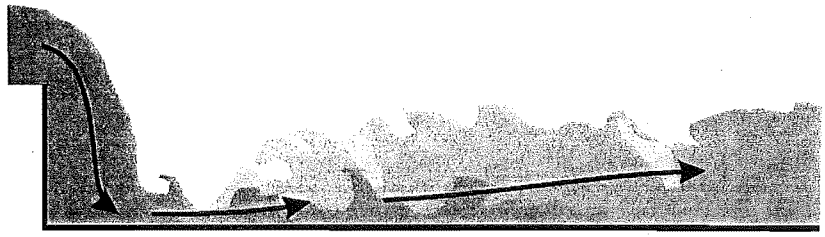

Experiments C01 & C02 - (*Sill - Open End*)

(b.)

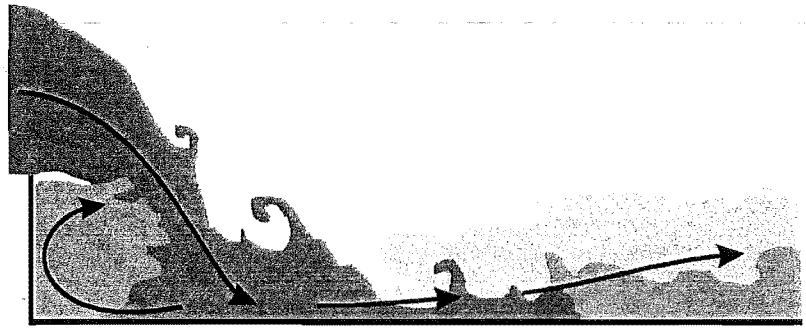

Experiments C03 & C06 - (*Doorway - Open End*)

(c.)

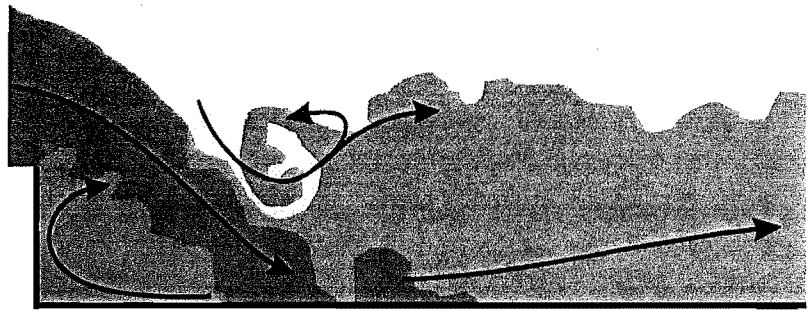

Experiments C04 and C07 - (*Doorway - Sill*)

(d.)

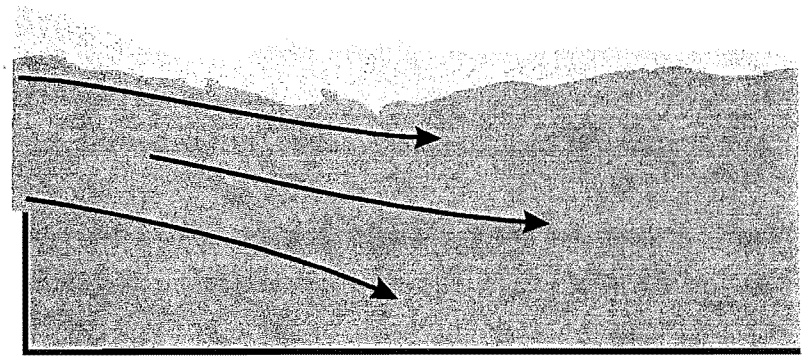

Experiments C05 and C08 - (*Doorway - Doorway*)

Figure 6-13 ***Sketches of the typical instantaneous flows observed in the C-Series experiments***

Since the spilling saline flow was detached from the sill of the opening, the saline plume impinged on the floor of the model away from the base of the sill. Downstream of the impingement point, a thin jet like layer exited the impingement region and formed a hydraulic jump structure. As with the case described previously (*Sill – Open End*), the turbulent hydraulic jump gradually broke down the jet like layer and mixed the saline fluid thoroughly with ambient fluid that was drawn into the turbulence. Thus, with distance downstream from the opening, the saline layer became deeper and less buoyant.

Experiments C04 and C07 – (*Doorway - Sill*)

The initial stages of the flow field development within this geometry resemble the flow described previously (*Doorway - Open End*). However, in this geometry, the flow in the second compartment is eventually altered by the presence of a downstream sill, which causes a saline layer to form.

In this model geometry, the saline that initially spills through the opening falls onto the floor of the second compartment and flows radially out of the impingement region as a thin jet. The front of the saline fluid that flows downstream gradually forms a gravity current head. At the end of the C-Series model, the head of the gravity current is reflected off the sill, and starts to travel back upstream as a layer on top of the thin jet-like flow that flows from the impingement region. When the reflected wave reaches the spilling vent flow, a saline layer starts to form in the second compartment. The saline layer gradually increases in depth, until the volumetric flow over the sill is the same as the volumetric flow rate from the opening between the two compartments. Although the sill of both openings are at the same height, the depth of the layer in the second compartment is always less than the depth of the layer in the source room, because the flow over the sill does not have a contraction in width.

As the vent flow plunges into the saline layer that forms in the second compartment, it draws ambient fluid into the layer that is mixed with saline. However, rather than being thoroughly mixed throughout the entire layer, the ambient fluid appears to only be mixed into the saline fluid that surrounds the perimeter of the plunging vent flow. Thus, a pocket of low-density saline fluid is created on top of the saline layer, at the point where the vent flow plunges into the layer. The low-density fluid from this region appears to flow downstream on top of the layer. The vent flow, on the other hand, plunges into the layer, and flows along the floor of the model toward the sill.

The trajectory of the vent flow within the layer changes as the saline layer develops in the second compartment. In the initial stages of the layer development, the saline fluid from the vent flow descends nearly vertically through the saline in the layer. However, as the layer develops, its average density approaches the density of vent flow fluid. This means that within the layer the effective buoyancy of the vent flow fluid is reduced. Consequently, the horizontal momentum of the spilling fluid becomes more dominant, and the vent flow fluid develops a flatter trajectory within the saline layer.

The roller region of fluid that existed beneath the detached spilling plume in the previous geometry (*Doorway – Open End*) was still present in this geometry. However, in this case, the roller region was not always able to entrain ambient fluid from around the perimeter of the spilling flow. As the layer developed in the second compartment, the supply of ambient fluid to the recirculation region was drowned out. However, the fluid in this region was still able to entrain low-density saline fluid from the pocket of low-density saline that surrounded the plunging region of the vent flow. This meant that the density of the fluid within the roller region (and consequently the density of the fluid entrained into the underside of the plume) was still less than the density of the spilling vent flow.

Experiments C05 and C08 – (*Doorway and Doorway*)

The initial stages of the flow field development within this geometry resemble the flow that was described for the previously (*Doorway – Sill*). In this geometry however, the doorway on the end of the model provides a more severe obstruction to the flow than the sill did in the previous model. This results in a deeper saline layer forming in the second compartment of the model. In fact, the layer in the second compartment has very nearly the same depth as the layer in the source compartment. There is a localised depression in the layer where the vent flow enters the second compartment; otherwise it is almost flat. The near equivalent depth of the layers in the two compartments means that the vent flow does not plunge down into the second compartment layer, as much as it appears to flow sedately into the layer, causing very little entrainment, if any. A consequence of this is that the trajectory of the vent flow fluid within the layer is flatter again than the one described for the previous geometry. This is because there is very little entrainment into the vent flow, so that the saline layer in the second compartment has an average density very close to that of the vent flow fluid.

6.4.2 Interpretation of the Normalised Density Difference Profiles

This section highlights the flow features evident in the C-Series normalised density difference profiles, which are shown in Appendix 3. The profiles are discussed for each of the four different model geometries, rather than for each of the eight different experiments. Figure 6-14 shows the approximate locations of the normalised density difference profiles within the steady state flow field generated within each model.

Boundary Layer Falsity

In the C-Series experimental profiles, the normalised density difference appears to decay in any region of the flow that is adjacent to a solid surface of the model. This "apparent" boundary layer in the density field is an error brought about by the contrasting limitations of the image capture equipment; refer Section 6.1.1. In every C-Series profile, this fictitious boundary layer is approximately 5*mm* thick (4 to 6 pixels across). Therefore, in considering the C-Series profiles, disregard the section of the profiles that show decay within approximately 5*mm* of any solid surface of the model.

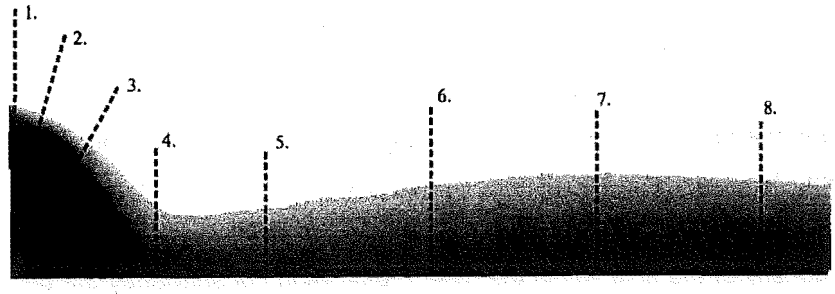

Experiments C01 and C02

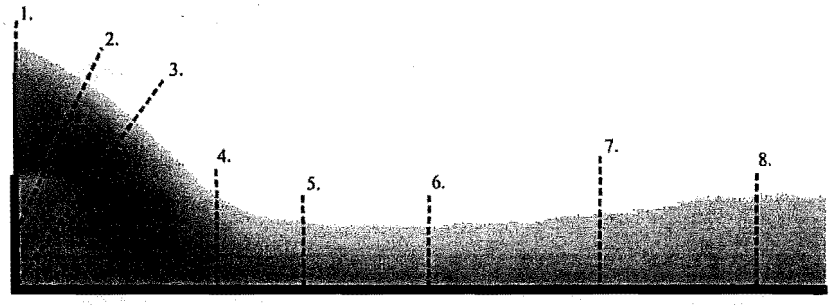

Experiments C03 and C06

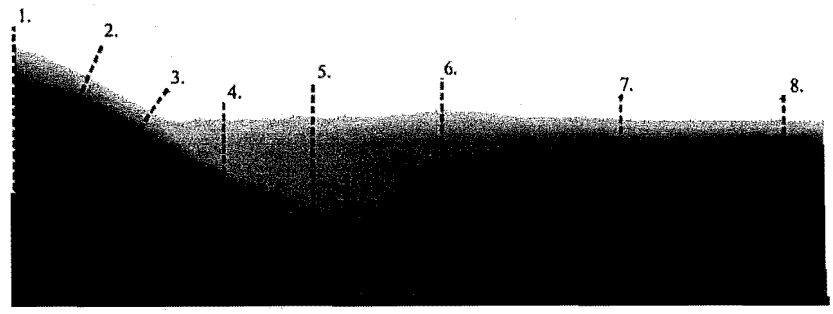

Experiments C04 and C07

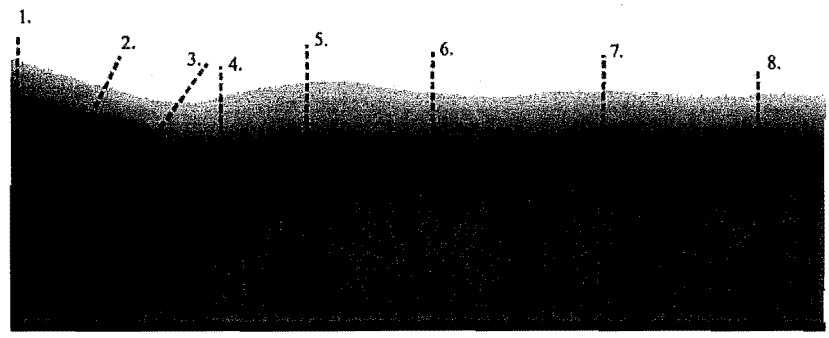

Experiments C05 and C08

Figure 6-14 ***Approximate locations of the eight density difference profiles within the saline layer that developed in the second compartment of the four different model geometries used in the C-Series experiments.***

Profiles from Experiments C01 and C02 – (*Sill and Open End*)

The first three profiles from experiments C01 and C02 describe the properties of the saline fluid as it spills from the plane of the opening down to the impingement region at the base of the sill. These profiles show that since there was no entrainment occurring on the sill side of the spilling fluid, the saline in this region had near uniform density across its depth. Profile 4 shows a thin layer of dense saline fluid beneath a layer of low density saline. This is the jet like layer that exited the impingement region and flowed underneath the nose of the hydraulic jump. A comparison of profile four with profile five then shows that the turbulent hydraulic jump broke down the jet-like layer of saline as it flowed downstream. Profiles 6 through to 8 show how the turbulent mixing in the hydraulic jump increased the depth of the saline layer. Unfortunately, due to the fictitious boundary layer that is present in the experimental results (refer Section 6.1.1), it is not possible to quantify the decay in the density of the fluid adjacent to the model surface.

NOTE:

A small section of both the second and third profile from experiment C01 has been distorted. The profiles are distorted locally as during the experiment a small group of bubbles adhered to the transparent wall of the model. The bubbles partially obscured the video camera view of the fluorescent saline flow in the region of the sill. Figure 6-15 shows the regions of the second and third profiles, where the bubbles have influenced the normalised density difference measurement. Given the similarity in shape of the C01 profiles when compared to the C02 profiles, it is reasonable to interpolate across the sections of the C01 profiles that have been distorted.

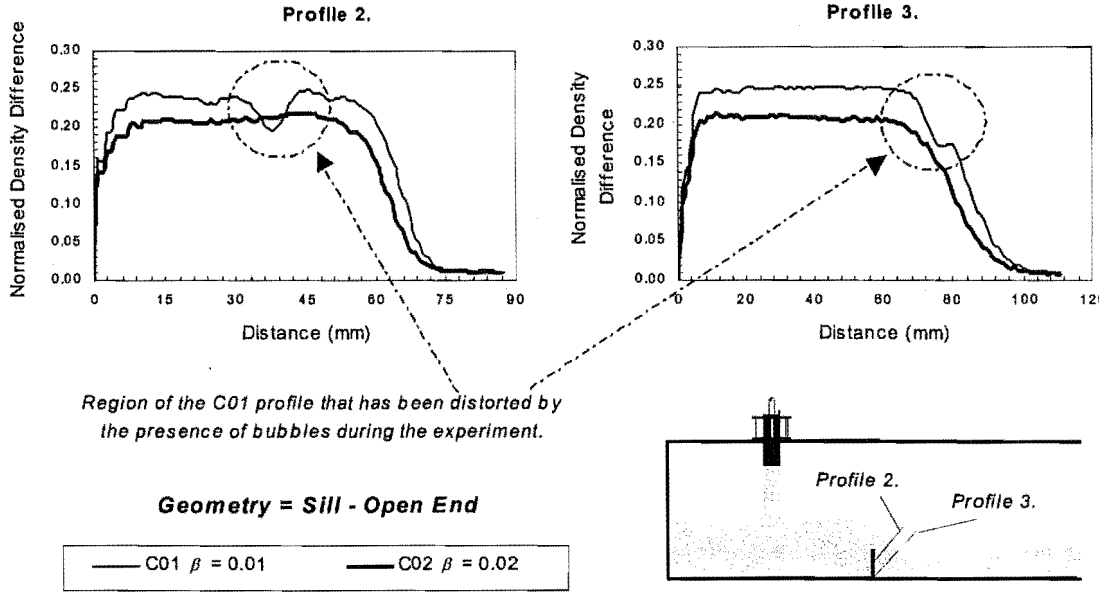

Figure 6-15 Profiles two and three from experiments C01 and C02, showing the errors within the initial profiles of experiment C01.

Profiles from Experiments C03 and C06 – (*Doorway and Open End*)

The first profile from experiments C03 and C06 (or C09) shows that there was a mixing layer on top of the saline fluid that spilt from the vent (that is, the density interface was not sharp). The mixing between the saline and freshwater fluid streams is caused by the destabilising shear along the interface between the flows. The mixing layer is more prominent in this geometry than the last (*Sill - Open End*), because the fluid velocities through the contracted opening in this geometry are greater than the fluid velocities over the sill.

The second and third profiles from experiments C03 and C06 clearly show the presence of the roller region on the underside of the detached spilling plume. The steep kink in the second profile marks the interface between the roller region and the underside of the spilling vent flow. The profiles clearly show that the fluid in the roller region is of a lower density than the fluid in the spilling from the vent. The peak on the left side of profile 3 shows the density of the fluid that has exited the impingement region of the plume and is being drawn up into the recirculation region. Figure 6-16 shows the second and third profiles from experiments C03, C06 and C09, to illustrate the discussion of the roller region. Profiles four through to eight show the hydraulic jump that forms downstream of the vent flow impingement point.

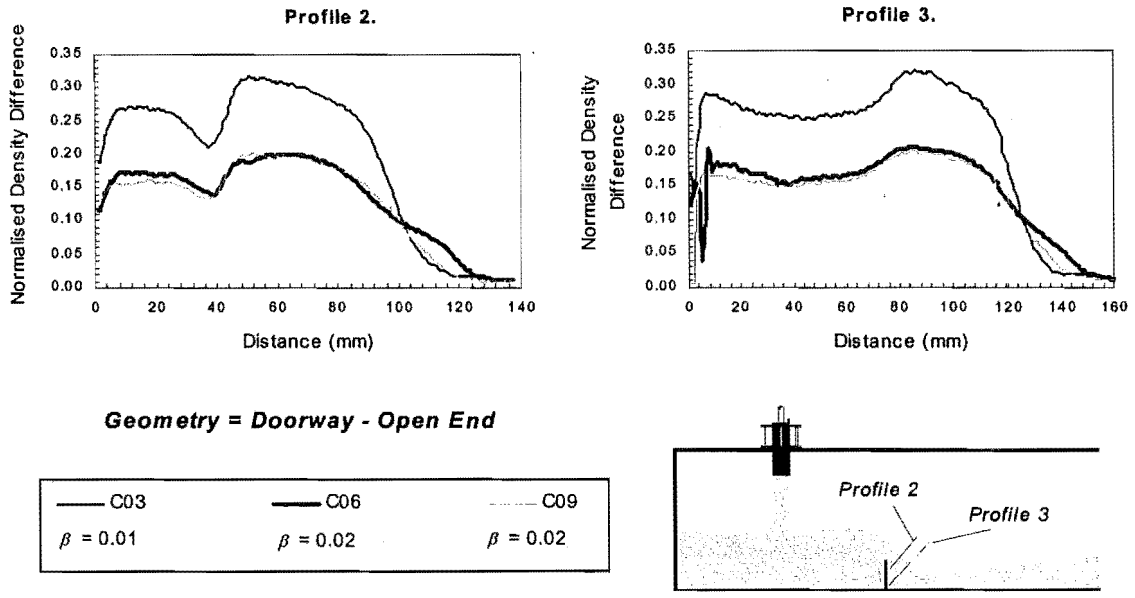

Figure 6-16 Second and third profiles from experiments C03, C06 and C09, showing the recirculation region that formed beneath the spilling vent flow.

Note: The sharp spikes at the beginning of the third profile from experiment C06 are not real. The spikes were created during the image processing because there was a small bubble present at the base of the sill when the background image of the flow was captured. The bubble was washed away by the initial saline flow during the experiment, so that it was not present in the flow images.

Profiles from Experiments C04 and C07 – (*Doorway and Sill*)

The first profile from experiments C04 and C07 shows a mixing layer on the interface of the vent flow (as described in the last geometry). The second and third profiles from these experiments show the existence of a roller region on the underside of the spilling vent flow. Although the roller region is not as well defined in profiles 2 and 3 from this geometry as it was in Figure 6-16, the flow structure is still clearly visible, due to the lower density of the fluid that is being recirculated in the region.

Profiles four, five and six from experiment C04 and C07 show the pocket of low-density saline that was observed around the location where the vent flow plunged into the saline layer. The gradual flattening out of the density profile between profiles five and six shows that the low-density fluid is mixed into the saline layer as it flows downstream toward the sill. Figure 6-17 shows the fifth and sixth profiles from experiments C04 and C07 to illustrate this discussion. Profiles 7 and 8 show that downstream of where the vent flow plunges into the saline layer the layer, has a near uniform density.

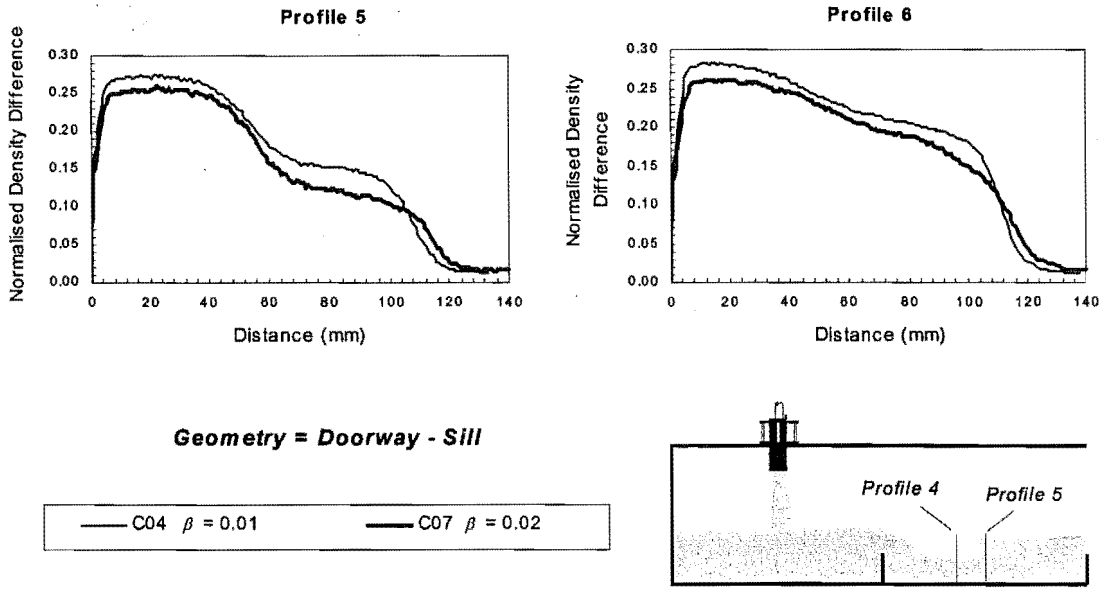

Figure 6-17 ***Profiles five and six from experiments C04 and C07, showing the low-density saline fluid that surrounded the area where the vent flow plunged into the saline layer.***

Note: The small sharp spikes at the beginning of the third profile from experiment C04 are not real; see the note in "Profiles from Experiments C03 and C06" for the explanation.

Profiles from Experiments C05 and C08 – (*Doorway and Doorway*)

All the profiles from experiments C05 and C08 show that the layer in the second compartment has an almost uniform density that is very close to that of the fluid spilling from the source compartment. Figure 6-18 illustrates this point by showing that there is very little dilution that occurs between profiles one and profiles eight in either experiment. Profile 1 is taken just outside the plane of the vent that divides the two compartments, and profile 8 is taken in the saline layer well downstream in the second compartment.

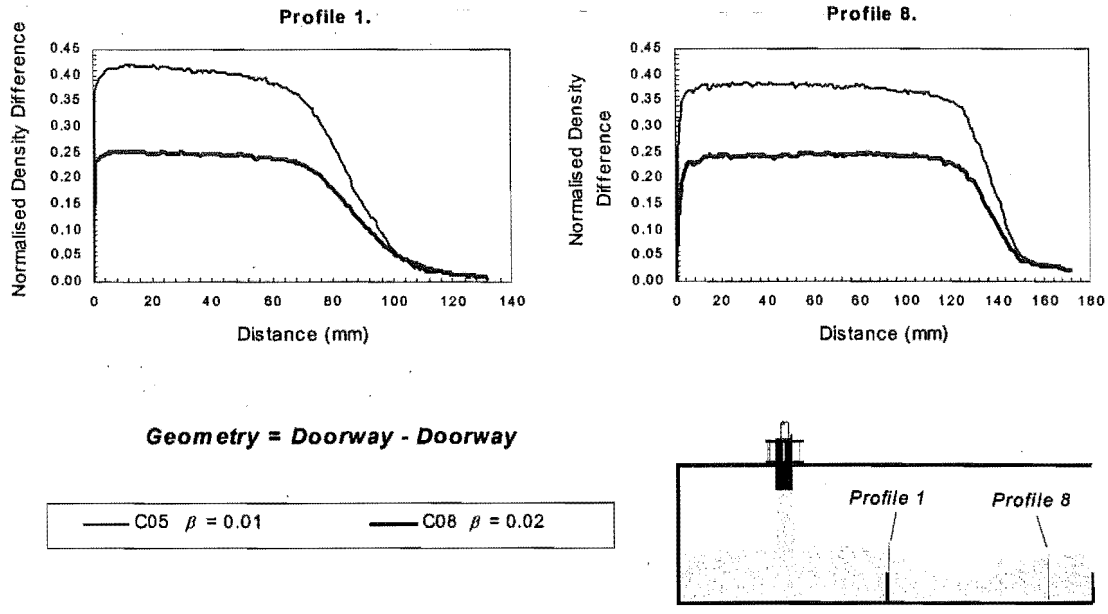

Figure 6-18 ***Profiles one and eight from experiments C05 and C08, showing the minimal entrainment that occurs into the saline between the source compartment and the second compartment.***

6.4.3 Flow Field Development

Experimental measurements were made of the time interval between the occurrences of each of the events used to describe the development of the flow field; Figure 5-13 illustrates the events that were marked in time. The time intervals were measured from development of the flow field in four different model geometries, for two different source plumes. For each source plume, there is good agreement in the time interval between any two events (regardless of the model geometry).

For plume P01 (β = 0.01), the time interval between when the ceiling jet impacted on the back wall of the model and when the saline layer started to spill continuously from the source compartment ($\Delta t_{2\text{-}4}$) was 28 seconds ($\pm 1s$). For plume P06 (β = 0.02), the same time interval ($\Delta t_{2\text{-}4}$) was 21 seconds ($\pm 1s$).

For plume P01 (β = 0.01), the time interval between when the saline layer started to spill continuously from the source compartment and when the return wave in the second compartment touched the spilling vent flow ($\Delta t_{4\text{-}5}$) was 76 seconds ($\pm 2s$). For plume P06 (β = 0.02), the same time interval ($\Delta t_{4\text{-}5}$) was 60 seconds ($\pm 1s$). Thus the flow field development in the C-Series model geometries can be described by the following time intervals:

Source Plume P01 (β = 0.01)		Source Plume P06 (β = 0.02)	
Δt_1	= 5s	Δt_1	= *not measured*
$\Delta t_{1\text{-}2}$	= 10s	$\Delta t_{1\text{-}2}$	= *not measured*
$\Delta t_{2\text{-}3}$	= 14s	$\Delta t_{2\text{-}3}$	= *not measured*
$\Delta t_{2\text{-}4}$	= 28s	$\Delta t_{2\text{-}4}$	= 21s
$\Delta t_{4\text{-}5}$	= 76s	$\Delta t_{4\text{-}5}$	= 60s

Table 5-3 also lists an estimated time for the flow to achieve steady state conditions in each experiment. In reality, the development of the saline density field is an asymptotic process that tends toward a steady state condition, where there is absolutely no change in the mean flow field over time. The steady state time listed in Table 5-3 has been estimated visually from the development of the density field in the centreline plane of the model. This is a crude method of estimation that is unable to gauge very small changes in the mean density field. Thus, the time listed in Table 5-3 for the steady state conditions is perhaps better described as the time to achieve quasi-steady conditions, where the flow field does not change significantly over long time intervals. The time intervals listed in Table 5-3 show that within any C-Series model geometry, the time that it took to achieve quasi-steady conditions was less for source plume P06 (β = 0.02) than it was for source plume P01 (β = 0.01). This implies that the stronger the buoyancy of the source is, the sooner quasi-steady conditions will be achieved in the flow field.

6.4.4 Repeatability

Experiment C09 was a repeat of experiment C06; the comparison of profiles from these experiments is shown in Figure 5-16. This was the only repeatability analysis conducted for the C-Series work. The analysis was undertaken because in experiment C06 a layer of low-density saline fluid was observed on top of the spilling vent flow. The low-density fluid appeared as though it would be drawn away from the vent flow if given sufficient time. Volume restrictions on the source fluid however, meant that images of the flow had to be captured while the low-density saline layer was still present. Experiment C09 was therefore conducted to determine if the low-density fluid was a real steady state feature of the flow. It was not present in experiment C09. The comparison of profile 1 from these two experiments shows the presence of the low-density saline fluid on top of the main vent flow in experiment C06. The profiles downstream of the vent show very good agreement.

6.4.5 *Uncertainty of C-Series Profiles*

Unlike the T-Series and P-Series experiments, there is no way of knowing if the normalised density difference profiles from the C-Series experiment are correct. Both the T-Series and P-Series flows contained a potential core region where the density of the saline fluid was known. Thus, the results given by the LIF analysis for these experiments could be checked (and scaled if necessary). The C-Series flow field however, contains no region where the density of the saline fluid can be determined just from the shape of the profiles. Thus, there is no means of checking the LIF results.

The P-Series experiments used the LIF technique to quantify the density field of the two source plumes used in the C-Series experiments. The results of the P-Series analysis showed that the normalised density difference profiles across the source plumes required scaling to correct them. It is believed that the P-Series profiles required scaling because the foam inside the flow source extracted some tracer dye from the source solution. The same source plumes and flow source as were used in the P-Series experiments were used in the C-Series experiments. Thus, it is expected that the C-Series profiles would require scaling to a similar degree. The exact amount of scaling is indeterminable, however it is expected it would be in the range of 1.1 to 1.3 (refer Table 6-2).

6.5 Conclusions

The salt-water experiments that have been conducted in the first part of this research map the time averaged density field of a natural transitional flow. The transitional flow takes the form of a buoyant spilling saline plume. Six variations of the transitional flow are studied, where the density and volumetric flow rate at the flow source are altered. Eight density difference measurements are made across each transitional flow at different locations, to map the density field. The density difference profiles have been obtained using the Laser Induced dye Fluorescence technique. The repeatability of these density profiles is assessed and found to be excellent. The existence of a potential core region near the flow source has provided a means of quantitatively correcting these profiles for any experimental measurement error.

The frequency of eddies on the perimeter of the transitional flows has also been determined. Turbulent eddies are seen to form continuously on the under side of the spilling plume, while on the upper surface of the plume, the onset of eddy formation is delayed. The degree to which the onset of eddy formation is delayed is dependent upon the source conditions of the flow. Thus, accurately predicting the natural onset of turbulent eddy formation (and consequently turbulent mixing) on the perimeter of these flows would provide a high degree of confidence in a hydrodynamic model.

In addition to the transitional flows, a series of salt water experiments have been conducted that generate a buoyant flow field that resembles the thermal flow field induced by a fire within a building. These fire similar experiments have been broken into two parts, P-Series and C-Series experiments. The P-Series experiments quantify the time averaged density field of the salt water

source plumes used in the C-Series experiments. Eight different density difference profiles are taken across the source plume at different locations. The repeatability of the source conditions was assessed and found to be excellent. The density profiles across the plume show the gradual development toward self-similar Gaussian density distributions, and the transition from jet-like behaviour near the source to buoyancy-dominated behaviour. The height of fall for the buoyant fluid however is too small for the buoyant jet to fully develop into a buoyant plume. As with the transitional flow, the existence of a potential core region in the flow provides a means for correcting the density difference profiles for experimental measurement error. Thus, the source plumes are well quantified for the C-Series experiments.

The C-Series experiments study the buoyant flow field that develops in a room that is connected to another room containing a buoyant plume. The geometry of the opening between the two rooms is varied, as is the geometry of the opening into the ambient environment. Four different model geometries are used, with two different source plumes, to create eight different flow fields. The temporal development of the flow field is recorded. Density difference profiles have been collected of the steady state flow field in the second room. The density profiles have the correct shape, however it is expected that these profiles would require some universal scaling. The degree of scaling is unknown, but it is expected to be of the order of 1.1 to 1.3. That is, the normalised density difference values are expected to be between 10% and 30% larger than the experimental measurements. In combination with the time-line record of the flow field development, the C-Series profile data still provides a good means of assessing the performance of the CFD hydrodynamic code.

6.6 References

1. Steckler, K.D., Baum, H.R. and Quintiere J.G. (1986) Salt Water Modelling of Fire Induced Flows in Multicompartment Enclosures, Proceedings of the 21st International Symposium on Combustions, The Combustion Institute, 1986, pp142-149.

2. Wood, I.R., Bell, R.G and Wilkinson, D.L. (1993) *Ocean Disposal of Wastewater,* Advanced Series on Ocean Engineering – Volume 8, World Scientific Publishing Co. Pte. Ltd, P O Box 128, Farrer Road, Singapore 9128.

3. Farmer, D.M. and Armi, L. (1986) Maximal Two-Layer Exchange Flow over a Sill and through the combination of a Sill and Contraction with Barotropic Flow, *Journal of Fluid Mechanics*, **164**, 53-76.

4. Armi, L. (1986) The Hydraulics of Two Flowing Layers with Different Densities, *Journal of Fluid Mechanics*, **163**, 27-58.

5. Dalziel, S.B. (1991) Two-Layer Hydraulics: A Functional Approach, *Journal of Fluid Mechanics*, **223**, 135-163.

6. Dalziel, S.B. and Lane-Serff, G. (1991) The Hydraulics of Doorway Exchange Flows, *Building and Environment*, **26**, 121-135.

7. Papps, David A. (1995) Merging Buoyant Jets in Stationary and Flowing Ambient Fluids. PhD Thesis, Civil Engineering, University of Canterbury, Christchurch, New Zealand.

8. Papanicolaou, P.N. (1984) Mass and Momentum Transport in a Turbulent Buoyant Axisymmetric Jet, Ph.D. Thesis, W.M. Keck Laboratory of Hydraulic and Water Resources, California Institute of Technology, Pasadena, California, U.S.A.

9. Rodi, W. (1982) *Turbulent Buoyant Jets and Plumes*, The Science & Applications of Heat and Mass Transfer - Reports, Reviews & Computer Programs, Volume 6, Pergamon Press Ltd, Headington Hill Hall, Oxford OX3 0BW, England.

10. Fisher, T.S (1995) Dilution of Axisymmetric Buoyant Jets and Surface Spreading Fields. Masters Thesis, Civil Engineering Department, University of Canterbury, Christchurch, New Zealand.

11. Wood, I.R. and Knudsen, M. (1990) The Interaction between a Boundary and a Horizontal Buoyant Jet, *Journal of Hydraulic Research*, **28** No.3, 375-396.

12. Sharp, J.J. and Vyas, B.D. (1977) The Buoyant Wall Jet, *Proceedings of the Institution of Civil Engineers*, **63** Part 2, 593-611.

13. Wilkinson, D.L. and Wood, I.R. (1971) A Rapidly Varied Flow Phenomenon in a Two-Layer Flow, *Journal of Fluid Mechanics*, **47**, 241-256.

14. Wilkinson, D.L. and Wood, I.R. (1968) The Entraining Hydraulic Jump, *Conference on Hydraulic and Fluid Mechanics*, The Institute of Engineers, Australia, pp.5-9

15. Wood, I.R. and Simpson, J.E. (1984) Jumps in Layered and Miscible Fluids, *Journal of Fluid Mechanics*, **140**, 329-342.

Chapter 7 - SIMULATION OF TRANSITIONAL FLOWS

7.1 Introduction

The Fire Dynamics Simulator (FDS) has been specifically designed to compute smoke movement induced by fire. However the hydrodynamic code that is contained within the FDS is equally applicable to the simulation of buoyant, low Froude number liquid flows. This means it is possible to use the computational fire model to simulate buoyant saline fluid movement within a quiescent freshwater environment[1][2]. The research documented in this chapter assesses how well the FDS is able to compute the T-Series salt water experiments that are described from Chapter 3 through to Chapter 6. The buoyant T-Series flows contain a well defined laminar-turbulent transition. The transition occurs naturally in the flow, rather than being mechanically forced or triggered. This type of transitional flow is extremely difficult to compute correctly[3]. Computational Fluid Dynamics (CFD) publications show that attempts to simulate these natural transitional flows with the Large Eddy Simulation (LES) technique have only been conducted since approximately the mid 1980s[4][5]. The simulation of the complex T-Series flows with the FDS is designed to provide insight into the weaknesses of the hydrodynamic model and the numerical methods that are contained in the model. Information is also sought on the dependence of the computational results on the resolution of the computational grid, and on the selection of the sub-grid scale (SGS) model.

In this research, the T-Series salt water experiments have been simulated using four different grid resolutions and two different SGS models. Grid resolutions of 10.4, 8.0, 5.0 and 4.0*mm* have been used in the computations. These resolutions equate to the discretization of the vertical extent of the domain into 40, 50, 80 and 100 divisions respectively. Finer resolutions were not achievable due to computational hardware constraints. Simulations have been conducted at each resolution using both the Smagorinsky SGS model and a constant viscosity SGS model.

This chapter documents the issues that have been identified and addressed in simulating the T-Series experiments, the results of the most accurate simulations and a discussion of the insight that has been gained from simulating the transitional flows. In the documentation of the research, a large amount of time is spent detailing the issues and assumptions that are utilised in the final simulations. This preliminary work is thoroughly detailed within Section 7.2. The results of the final simulations, which use the findings of all the preliminary work, are detailed in Section 7.3. A discussion of the hydrodynamic model performance, including the grid dependence, and the SGS model dependence of the computational results, is given in Section 7.4. The chapter is completed with Section 7.5, which details a series of conclusions that can be drawn from the exercise.

7.2 Preliminary Determinations

7.2.1 Time Averaging

In the simulation of the T-Series flows, it was necessary to determine the earliest point in time at which averaging could be initiated, and the shortest time averaging interval that could be used to satisfactorily capture the mean properties of the steady state flow field. Together these time intervals determine the minimum duration of the simulations.

Time to Achieve Steady State Conditions

The earliest time at which time averaging could be initiated was determined visually from Smokeview[6] animations of the density field development. These animations of the fluid density in the centreline plane of the model were used to determine when the saline layer had settled at a steady state depth, and when the density distribution within the saline layer was approximately steady. Once these conditions were achieved the time averaging of the spilling saline flow was initiated.

Animations of the density field showed that in the early stage of the flow development, the inflow of saline caused an interfacial wave to set up between the saline layer and the freshwater in the source compartment. The wave propagated backwards and forwards along the surface of the saline layer. The back wall of the model and the sill of the opening reflected the wave at either end of the compartment. The presence of the wave caused the vent flow to pulse, rather than spill continuously. Gradually the amplitude of the wave dissipated and the layer settled at a steady state depth, to provide a continuous vent flow. In simulations of experiment T02, it took approximately 165*s* for the interfacial wave to completely dissipate and leave an established saline layer in the source compartment.

In an attempt to circumvent the time it took the saline inflow to fill the volume of the source compartment beneath the sill level of the opening, a layer of saline fluid was prescribed into the source compartment as an initial condition. The inflow of saline into this layer still created the interfacial wave that had been observed in simulations without the initial layer. However in these simulations, the interfacial wave was still present after 250*s*, rather than being completely dissipated after 165*s*. No explanation was determined for why the presence of the initial saline layer caused the interfacial wave to exist for a longer period than if the entire source compartment had originally only contained ambient fluid. Also, no noticeable reduction could be made to the time taken for the wave to dissipate, by ramping up the volumetric inflow of the saline, rather than injecting it as an abrupt step function.

In the final T-Series simulations, finer grid resolutions were achieved by only computing the flow in the region of the model that immediately surrounded the spilling plume. In these reduced domain simulations, only 100*mm* of the source compartment length (the 100*mm* adjacent to the opening) was included in the computations; refer Section 7.2.5 on reduced length simulations. When

experiment T02 was simulated with these reduced length domains, the interfacial wave dissipated to leave an established saline layer after a period of 45*s* (regardless of whether an initial layer was prescribed or not). Table 7-1 shows the time that it took to achieve steady state conditions in the source compartment, in the reduced length simulations of each T-Series experiment. This time was always governed by the dissipation of the interfacial wave.

Time Averaging Duration

The duration of the time averaging interval for steady state flows is dependent on a velocity scale and a length scale that are representative of the fluid motion. The velocity scale for buoyant convective velocities is given by Equation (7-1)[7]; where *H* is the height of the enclosure in which the buoyancy source is contained.

$$U = \sqrt{\frac{\Delta\rho}{\rho} gH} \qquad \text{Equation (7-1)}$$

The length scale for the steady state time-averaging interval is related to the size of the fluid structures that are seen in the flow. In a fire plume the largest eddy structures are generally of the same order as the diameter of the plume[8]. Thus, the order of time that it takes for a single large-scale eddy to move past a fixed point is given by Equation (7-2). This formulation is not appropriate for the entire saltwater flow field, because the velocity scale given by Equation (7-1) assumes that the fluid motion is driven purely by buoyancy. In salt water flows, the fluid motion near the flow source is primarily driven by the initial momentum with which the fluid is injected into the freshwater. In regions of the flow that are distant from the flow source however, buoyancy is the sole driving force and Equation (7-2) is applicable.

$$t_e = \frac{d_o}{\sqrt{\frac{\Delta\rho}{\rho} gH}} \qquad \text{Equation (7-2)}$$

For the T-Series flows, the diameter of the flow source has been approximated using Equation (7-3), which gives an equivalent source diameter for the spilling plume by assuming that the saline flow occupies half the depth of the opening.

$$d_o = \sqrt{\frac{2W_{door}H_{door}}{\pi}} \qquad \text{Equation (7-3)}$$

We expect that the minimum time averaging interval can be described by Equation (7-4), that simply states that a minimum number of large-scale structures must be included in the averaging to adequately capture the mean properties of the flow.

$$\Delta t_{avg} = k t_e \qquad \text{Equation (7-4)}$$

For the averaging of LES computational results, there may be some argument for the use of a variable length scale that incorporates the resolution of the grid. This premise is based upon the knowledge that a finer degree of detail is resolved in the flow as the LES computational grid is refined. The length of the averaging interval could therefore increase and converge toward the time interval described by Equation (7-4) as the grid resolution is refined. Any dependence upon computational resolution has been left as a possible avenue for further research. In the time averaging analysis detailed in this section a constant grid resolution of 5*mm* has been used.

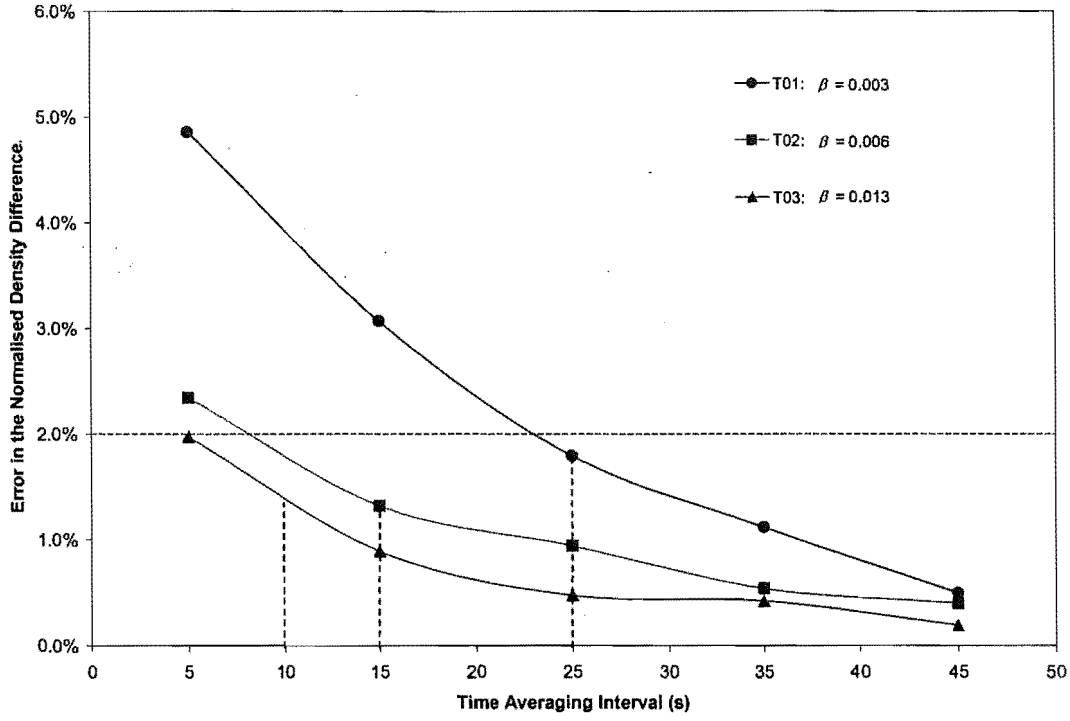

Figure 7-1 ***Results of analysis to determine the duration of time averaging required to satisfactorily capture the mean steady state properties of the flow.***

To determine a value for the parameter *k* in Equation (7-4), time averaging analysis has been conducted on the results of simulations of experiments T01, T02 and T03. These three salt water experiments have the three different buoyancies that were used in the T-Series work. For each experiment, the analysis has examined how the normalised density difference profiles converge as a function of the duration of time averaging. Time averaging durations of 55, 45, 35, 25, 15 and 5*s* have been used. It is assumed that the profiles from the 55*s* time average of the computed flow are the most accurate approximation of the steady state mean density. Using this assumption, the accuracy of the time-averaging interval has been quantified by calculating the average difference

between the density profiles from the 55*s* average and the other time-averaging intervals. The results of this analysis are shown in Figure 7-1.

Figure 7-1 shows the mean difference between the 55*s* time averaged density difference profile and the profiles given by time averaging intervals of a shorter duration. The mean difference is expressed as a percentage of the density difference between the fluids at the source of the flow. A 2% difference can be achieved by using averaging durations of 25*s*, 15*s* and 10*s* for experiments T01, T02 and T03 respectively. These durations equate to an approximate value of 25 for the parameter *k* in Equation (7-4); this value has been used in Equation (7-4) to predict the duration of time averaging for the T-Series computational results. Table 7-1 shows the time averaging parameters that were used to determine the mean density difference profiles from the T-Series simulations.

$$\Delta t_{avg} = \frac{25 d_o}{\sqrt{\frac{\Delta\rho}{\rho} gH}} \qquad \text{Equation (7-5)}$$

Exp	Time to Steady State (s)	Duration of Time Averaging (s)	Duration of Simulation (s)
T01	55	25	80
T02	45	15	60
T03	35	10	45
T04	35	25	60
T05	30	15	45
T06	25	10	35

Table 7-1 ***Time averaging parameters that were used to determine the mean density difference profiles from the T-Series computational results.***

7.2.2 Symmetry

It is common practice in CFD, to use a plane of symmetry in the geometry of an enclosure, to half the physical size of the region in which the fluid flow is computed. This practice, assumes that symmetry in the domain description, boundary conditions and initial conditions, produces a symmetrical flow field. The assumption of symmetry allows finer grid resolutions to be used in simulations, through the application of the entire computational resources to computing only half the flow field. Early simulations conducted with the FDS hydrodynamic algorithm showed that symmetry existed in the computed flow field when the computations were conducted under symmetrical conditions [9][10]. In real fluid flow however, although the enclosure geometry may be symmetrical, the turbulent flows that are generated within that geometry are not symmetrical at any instant in time (although the mean properties of the flow may be symmetrical). Therefore, to better reflect the chaotic instantaneous appearance of real turbulent flows, a small inert cube can be

specified in the FDS domain that will break the symmetry of the computations. The cube is often referred to as a symmetry breaker, and this technique has been used previously in the simulation of fire plumes with the FDS, refer Section 2.2.3 – Isolated Fire Plumes.

The T-Series salt water model possesses all the necessary conditions to make use of the plane of symmetry in the computations. To assess the impact of using the symmetry assumption, analysis was undertaken to compare the results of symmetrical simulations with the results of simulations that used a symmetry breaker. In the analysis, seven simulations were conducted of the T-Series experiment T02. In the simulations, a reduced domain was used that was 400*mm* long, 250*mm* wide and 500*mm* high, (refer Section 7.2.5 for a discussion of the reduced domain simulations). The grid resolution was 5*mm*. Five of the simulations were conducted with a symmetry breaker that was located in one of the positions shown in Figure 7-2. The final two simulations were both conducted without breaking the symmetry of the domain. The first of these simulations computed the flow throughout the entire domain, while in the second simulation the flow was only computed on one side of the plane of symmetry, i.e., the assumption of symmetry was employed in the computations. Figure 7-4 shows a comparison of the time averaged density profiles from all seven simulations.

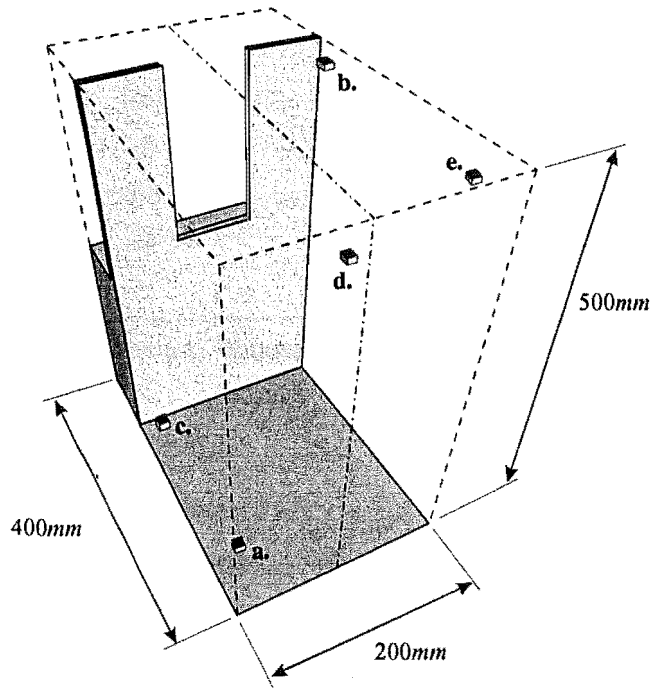

Location of Symmetry Breaker

(a.) XB=0.350, 0.360, 0.020, 0.030, 0.060, 0.070
(b.) XB=0.110, 0.120, 0.240, 0.250, 0.470, 0.480
(c.) XB=0.110, 0.120, 0.020, 0.030, 0.020, 0.030
(d.) XB=0.370, 0.380, 0.115, 0.125, 0.420, 0.430
(e.) XB=0.360, 0.370, 0.200, 0.210, 0.460, 0.470

Figure 7-2 Location of the symmetry breakers within the reduced domain that was used in the analysis of the symmetry assumption.

The normalised density difference profiles in Figure 7-4 show that the location of the symmetry breaker within the domain has negligible effect on the time averaged properties of the flow field. This finding is conditional on the symmetry breaker being sensibly located away from the region of

the flow that is being studied (in this case away from the region of the spilling saline). The most interesting aspect of Figure 7-4 however, is that there is a difference between the profiles that come from the simulations where the domain description is symmetrical. In the case where the flow was computed throughout the entire domain, the time averaged density difference profiles agree well with the profiles from simulations that used a symmetry breaker. In the case where the plane of symmetry was used in the computations, the time averaged density profiles are significantly different from those given by the other simulations; particularly in the highly turbulent region of the flow. Since it has previously been observed that the computed flow field is symmetrical when computations are conducted under symmetrical conditions, the profiles from these last two simulations were expected to agree perfectly. In fact, animations of the simulation results revealed that, in case where the flow was computed throughout the entire domain, the flow field developed an asymmetry without the need for a symmetry breaker. Figure 7-3 shows an instantaneous flow image from three of the different simulations that were conducted in the symmetry analysis. The images are a section through the saline plume just after it spills out of the plane of the opening (that is the plume is spilling out of the page toward the reader). Figure 7-3 clearly shows the asymmetry that developed in the simulation of the full symmetrical domain.

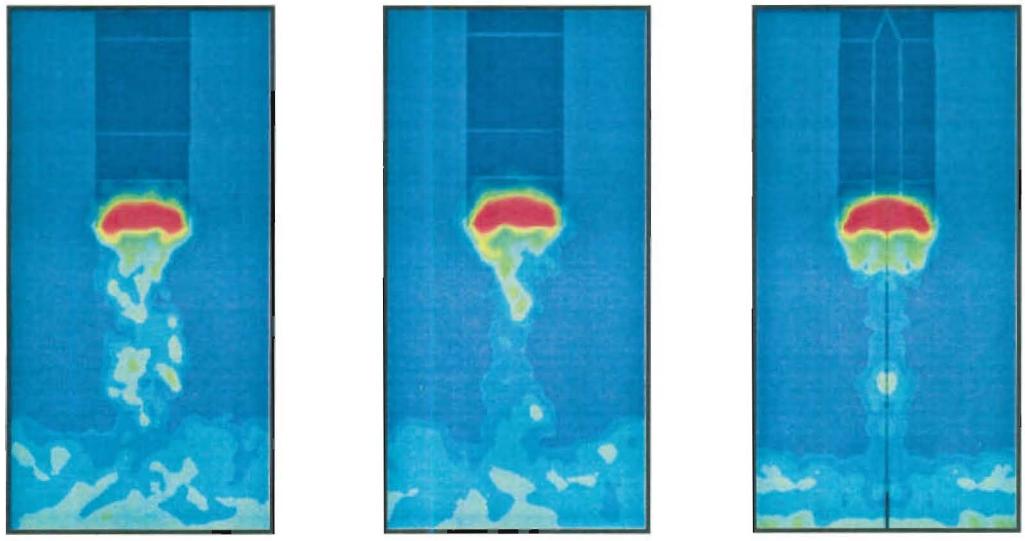

Simulation of Full Domain (Symmetrical)

Simulation of Full Domain with a Symmetry Breaker

Simulation of Half Domain (Assume Symmetry)

Figure 7-3 ***Cross sectional images of the spilling flow showing asymmetry in symmetrical domain computations.***

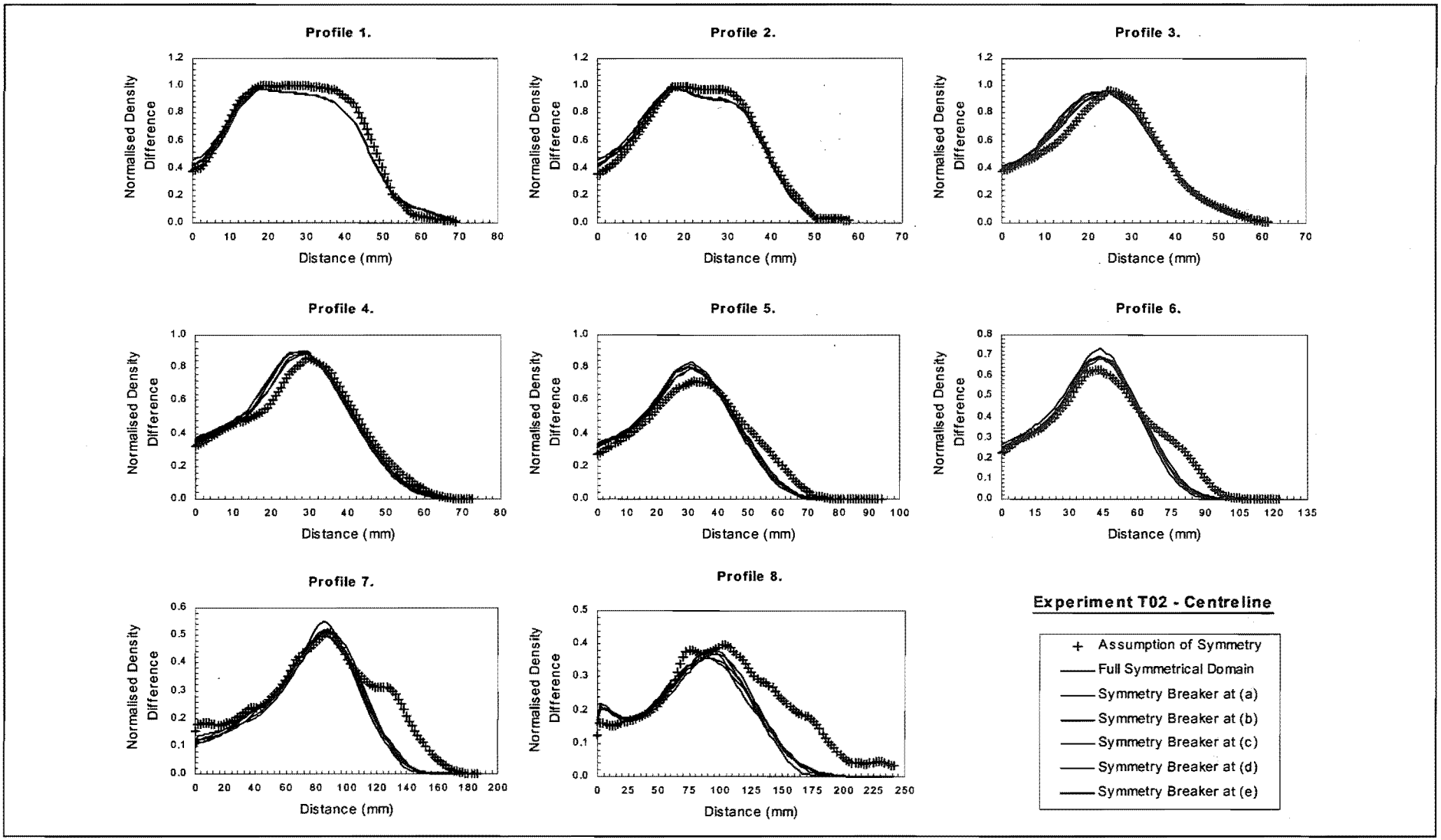

Figure 7-4 ***Density profiles from the centreline plane of the T-Series model, illustrating the dissimilarity of the results from the simulation where symmetry was assumed (resolution=5mm)***

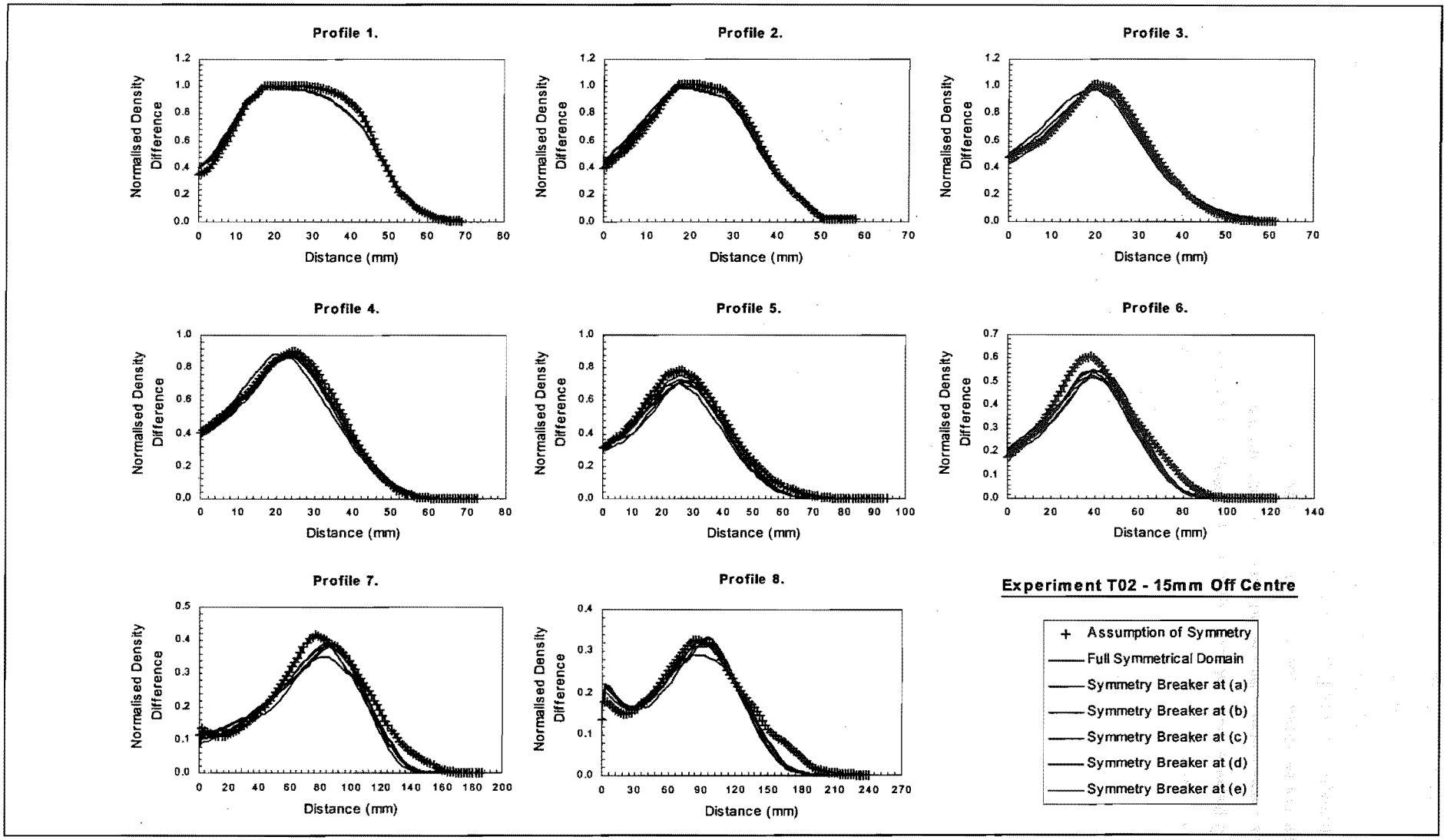

Figure 7-5 ***Density profiles from the vertical plane that was 15mm away from the plane of symmetry. The impact of utilising symmetry in the computations has less influence on the results in this plane than it did on the results in the plane of symmetry.***

It is believed that the symmetry of the full domain computations is broken by an asymmetry forming in the boundary conditions of the domain as the computations progress. In the computational method, cells that represent solid obstructions to the flow are given "ghost" properties to prevent mass transfer occurring between the cell and any adjacent cell that represents fluid. In terms of species conservation, the cell that represents an impermeable boundary is allocated the same species mass fraction as the adjacent cell that represents fluid. This method prevents any gradient forming between the two cells that would result in a transfer of mass. For cells that represent the corner of a solid obstruction (such that they are in contact with more than one cell that represents fluid), the ghost properties of the cell after any time step are the properties of the last adjacent fluid cell that required a boundary condition in computations. Therefore, the order in which the computations are applied throughout the cells in the domain may create an asymmetry in the boundary conditions.

The disagreement between the profiles from the simulation that assumed symmetry and the simulations where the flows were asymmetrical raises questions regarding the appropriateness of assuming symmetry in order to reduce the computational demands. The time averaged density difference profiles that are displayed in Figure 7-4 show the fluid density in the centreline plane of the model, which is the plane of symmetry for the domain. It seems reasonable to expect that the assumption of symmetry will have the strongest influence on the fluid dynamics in the region of the domain that is in close proximity to the plane of symmetry. To verify this, Figure 7-5 shows time averaged density difference profiles from a vertical plane that is offset by 15*mm* from the plane of symmetry. Density profiles from all seven simulations conducted as part of the symmetry analysis are shown in this figure. Figure 7-5 shows that 15*mm* out from the centreline plane of the model, the profiles from the simulation that utilises symmetry agree better with the profiles from the asymmetrical computations than they do on the centreline plane of the model. This results reveals that the impact of assuming the idealised condition of symmetry diminishes with increased distance from the plane of symmetry.

This finding suggests that in simulations where results are being considered from the plane of symmetry, it is not good practice to use the symmetrical assumption to reduce the domain size. Rather, it is better to simulate the entire domain and ensure that the flows become asymmetrical (which is a better reflection of reality). If, on the other hand, results are being taken from regions of the domain that are distant from the plane of symmetry, the influence of the idealised symmetry assumption (on the results) is reduced and hence it may be reasonably employed in computations. This also suggests, that in collecting experimental measurements for the purpose of comparison with computational model predictions, the measurements should be collected away from the plane of symmetry. This way, the assumption of symmetry can be reasonably employed in the computational work to achieve finer grid resolutions with the available computational hardware.

7.2.3 Stability

To maintain computational stability in solving the governing equations of motion, the numerical methods that are used in the FDS require certain parameters to have a value that is within a restricted range. In the FDS, the two parameters that are affected by the stability restrictions are the fluid viscosity and the diffusion parameter. It is difficult to recognise when the FDS computations have become unstable. The computer model does not automatically terminate the computations when they are not stable. Neither is it obvious from time averaged computational results whether the computations were unstable or not. Therefore, this section documents and (where necessary) establishes the range of fluid viscosity and diffusion parameter values that will ensure computational stability in FDS simulations.

Fluid Viscosity

The fluid viscosity is not restricted in any way in FDS computations that use the Smagorinsky SGS model. In these computations, the viscosity of the fluid varies spatially, and the magnitude of the viscosity (in time and space) is automatically determined by the Smagorinsky SGS model; refer Section 2.2.3. Therefore, in Smagorinsky simulations it is only necessary to specify a lower bound for the value of the fluid viscosity, which is generally specified as the real viscosity of the fluid that is being simulated.

In simulations that use the constant viscosity SGS model, the condition of computational stability places a restriction on the viscosity of the fluid. As described earlier in Section 2.1.3, in order for the computations to remain stable, the fluid must be sufficiently viscous to dissipate all the excess kinetic energy passed down from the large-scale structures resolved in the computations. Because the size of the fluid structures that can be directly resolved is dependent on the grid resolution, the minimum viscosity of the fluid is also dependent on the grid resolution.

$$\mathrm{Re} = \frac{\rho_o U H}{\mu} \qquad \text{Equation (7-6)}$$

The relative importance of fluid viscosity in the dynamics of fluid flow is often described via the Reynolds number; refer Equation (7-6). Thus, the relationship between grid resolution and minimum fluid viscosity is often discussed in terms of the maximum resolvable Reynolds number that can be simulated with a computational grid. In LES computations, it is generally accepted that the resolvable Reynolds number is proportional to the number of cells in the characteristic dimension of the domain, squared. For fires inside enclosures the characteristic dimension is generally agreed to be the ceiling height of the enclosure. As such, the resolvable Reynolds number for the LES computations is proportional to the number of grid cells in the vertical extent of the domain, squared; see Equation (7-7).

$$\mathrm{Re} \propto \left(\frac{H}{l}\right)^2 \qquad \text{Equation (7-7)}$$

The velocity scale for buoyant flow in an enclosure of height H has already been given by Equation (7-1). If this velocity scale is substituted into the Reynolds number expression, then Equation (7-7) can be rearranged to give a relationship for the fluid viscosity in terms of the computational grid resolution; see Equation (7-8).

$$\mu \propto \frac{\rho_o l^2}{H^{\frac{1}{2}}} \sqrt{\frac{\Delta\rho}{\rho_o} g} \qquad \text{Equation (7-8)}$$

To complete the relationship given by Equation (7-8), a basic stability investigation was undertaken to determine a constant of proportionality. The investigation involved determining the minimum fluid viscosity at which the simulations of experiments T01, T02 and T05 had stable computations. Four different resolutions were used to simulate each experiment and the minimum viscosity was determined for each simulation.

The stability of the computations was assessed visually from Smokeview[6] animations of the density field in the centreline plane of the T-Series model. When the computations were unstable, the density field of the saline had a discontinuous appearance. This appearance is best described as a stream of high-density saline globules that is mixed in amongst a jagged, disorganized, low-density saline flow. This look is often referred to as a checkerboard appearance; see the instantaneous image in Figure 7-6 for Sc=100 as an example. When the fluid viscosity was large enough to provide stable computations, the computed density field took on a more cohesive continuous appearance in the animations. This method for determining when the computations were unstable was subjective. Ideally in a computational stability assessment, the computed results at a point in the flow field would be compared to a known time dependent solution for the flow at that location. This analytical option was not available for the complex transitional flows that were generated in the T-Series experiments. Although the assessment method is subjective, the high degree of consistency in the constant of proportionality that was determined for each simulation gave confidence in the technique.

From the stability analysis, it was determined that a constant of proportionality equal to 0.52 in Equation (7-9) would provide a minimum fluid viscosity that would ensure computational stability. The constant of proportionality has a precision of 0.13, such that a value of 0.39 was found to give a fluid viscosity that resulted in unstable computations. Further research is required on this relationship to verify its application in simulating fire induced smoke flows (rather than boussinesq salt water flows).

$$\mu_{\min} = 0.52 \frac{\rho_o l^2}{H^{\frac{1}{2}}} \sqrt{\frac{\Delta\rho}{\rho_o} g} \qquad \text{Equation (7-9)}$$

According to Equation (7-9), in order to conduct a true DNS simulation of the T-Series transitional flows, where the real fluid viscosity can be used in the computations, the characteristic dimension of the computations grid must be between 2.1 and 3.1*mm*. This equates to the discretization of the domain height into between 160 and 240 cells (i.e., KBAR = 160 and 240). For the fire similar buoyant flows generated in the P-Series and C-Series salt water experiments, the resolution required for a true DNS is between 1.7 and 2.1*mm*. In this case, this equates to discretization of the domain height into between 190 and 240 cells.

Diffusion

In the FDS, the rate of diffusion is quantified via the specification of a Schmidt number[†] or a diffusion coefficient, depending upon which SGS model is employed in the computations. If the Smagorinsky SGS model is used in simulations, then the rate of diffusion is specified via the Schmidt number. If, on the other hand, the constant viscosity SGS model is employed in the computations, the rate of diffusion is specified via a diffusion coefficient. The nature of the LES approach and the stability conditions of the numerical methods used in the FDS, mean that the real values of these parameters are not appropriate for use in the computations. This section explains why the true values of the diffusion parameters are inappropriate for use in LES, and details the limitations that are imposed on the magnitude of the diffusion variable for computational stability. Throughout the discussion the Schmidt number is used to describe the magnitude of diffusion. For simulations that use the constant viscosity SGS model, the equivalent diffusion behaviour can be obtained by using Equation (7-10) to calculate the appropriate value of the diffusion coefficient D_s from the Schmidt number *Sc*.

$$Sc = \frac{\mu}{\rho D_s} \qquad \text{Equation (7-10)}$$

The large-scale motions that are explicitly calculated in LES are assumed to govern the distribution of mass, momentum and energy. However, in reality small-scale motions make a small contribution to the distribution of these properties as well. Eddies that are too small to be resolved with the computational grid still transport mass and momentum in the flow. In the LES approach, the SGS mass transport is accounted for via an effective diffusion method. In this method an elevated rate of diffusion is specified, to account for the mass transport that occurs via both the molecular process of diffusion and via the small scale eddies that cannot be resolved in the computations. This effective rate of diffusion that is specified for the computations is sometimes referred to as eddy diffusion.

[†] *The Prandtl number is used instead of the Schmidt number in simulations of gas flows.*

The proportion of eddies resolved in computations, and hence the proportion of the mass transport explicitly calculated from first principles, is dependent on the resolution of the computational grid. It follows then, that the amount of mass transport occurring on the SGS will also be grid dependent. As the resolution of the grid is refined, and a greater proportion of the mass transport is calculated explicitly, the amount of mass transport that occurs on the SGS will reduce. Thus, in concept, as the resolution of the computational grid is refined, the value of the Schmidt number that is specified for the LES computations should increase. In reality however, the computational stability of the numerical methods that are used in the FDS restrict the magnitude of the Schmidt number that can be specified.

In using numerical methods to solve the conservation equations, certain terms in the equations have a stabilizing influence on the computations. In the momentum equation, it is the viscous term that plays a stabilizing role (refer Section 2.1.3). The magnitude of the viscous term is described via the Reynolds number. In the conservation of salt mass relationship, it is the diffusion term that is the stabiliser; the magnitude of this term is described via the Péclet number. The Péclet number describes the relative magnitude of advection and diffusion in the flow; it is therefore calculated as the product of the Reynolds number and the Schmidt number. Since the conservation of momentum and species equations are both solved using the same discretised grid, it is not unexpected to find that the stabilizing terms in both equations are required to be of the same order of magnitude to ensure computational stability. When this computational stability requirement is combined with the definition of the Péclet number, it means that the Schmidt number specified for computations is required to be of the order unity.

The real Schmidt number for the diffusion of salt in freshwater is 721[11]. For the LES computations conducted in this research, a value of 0.721 has been specified for the Schmidt in the computations. The precision of this number is misleading; a value of 0.7 would have been entirely sufficient to achieve the same results. The value of 0.721 was used simply because it was equal to the real Schmidt number divided by one thousand. In simulations where the constant viscosity SGS model was employed in the computations, the equivalent diffusion behaviour was given by a diffusion coefficient of the value $1.581 \times 10^{-6} m^2/s$. In this research, a diffusion coefficient of this value was specified in the constant viscosity SGS model simulations.

To illustrate the appearance of computational instabilities in the animations of the computed density field, Figure 7-6 shows an instantaneous image from four simulations that were conducted with different Schmidt numbers (5*mm* grid resolution). The discontinuous checkerboard appearance of the density field can be seen in the images where the computations have had a Schmidt number equal to 10 or 100. The image from the computations where the Schmidt number was equal to 0.1 has a smoothed appearance showing excessive diffusion. It should be noted that computations also become unstable when the Schmidt number has a value much less than unity.

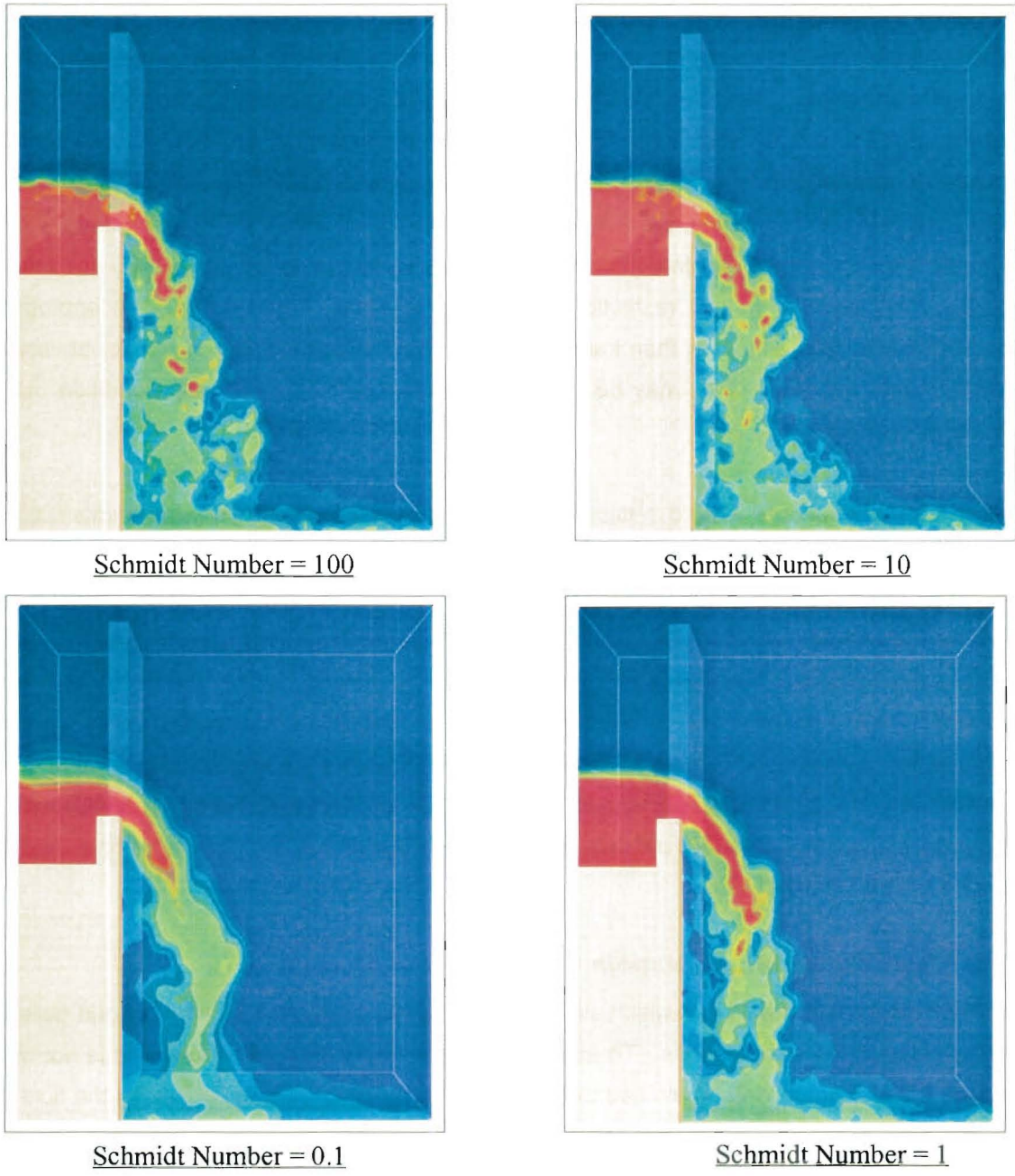

Figure 7-6 ***Instantaneous images of the computed T-Series flow for different Schmidt number values.***

For the simulation of fire induced thermal gas flows, the Prandtl number (representing thermal diffusion) is used in place of the Schmidt number. The Prandtl number for air is of the order of 0.7, such that the real value can be used in simulations without stability problems.

7.2.4 Boundary Conditions

The thermal boundary condition for the simulation of the salt water flows was set, as required, as adiabatic. The tangential velocity boundary condition could vary between a no-slip condition (VBC

= -1) and a full slip condition (VBC=1); refer to Section 2.4.3 for discussion of this parameter. The choice of appropriate boundary condition is dependent on the resolution of the computational grid, and some knowledge of what the real boundary layer depth would be along the surfaces of solid obstructions. The retarding influence that the velocity boundary condition has on the computed fluid velocity extends a number of grid cells into the fluid from a solid boundary. Thus, the larger the grid cells are, the further into the flow the retardation of the velocity along the boundary is felt. To counter this, the degree of retardation at the boundary can be adjusted, so that it is not a no-slip condition. At very coarse grid resolutions, a full-slip boundary condition may be appropriate, because the grid cells are larger than the depth of the real boundary layer. However, at very fine resolutions, the boundary layer may be resolvable, such that the real no-slip condition can be reasonably specified.

For the salt water flows generated in this research, there were no velocity measurements collected in experiments, and there was no simple analytical means of estimating the boundary layer depth at any point in the flow. The grid cell size used in the T-Series computations varied between 4*mm* and 10*mm*. At these resolutions, it was felt that a boundary layer in the salt water flows would not be accurately resolved; however some retardation of the velocity in the cells adjacent to the boundaries could be expected. For this reason, a tangential velocity boundary condition intermediate to no slip and full slip was selected. The VBC parameter was set at a value of 0.5 for all simulations. A simple assessment of the impact of the velocity boundary condition of the computed time averaged density difference profiles determined that the parameter had negligible influence for the T-Series results.

7.2.5 Use of a Reduced Domain

The RAM capacity of the PC on which simulations were run limited the number of grid cells that could be used in the computations. To achieve finer grid resolutions with the available hardware, the size of the computation domain had to be reduced. Thus, rather than simulating the fluid flow throughout the entire T-Series model, the computations were focussed on one particular region of the flow. For the T-Series flows, this meant only simulating the region of the flow that was in the immediate vicinity of the spilling saline plume. This approach has been referred to as using a reduced domain.

This section demonstrates that the flow outside the boundaries of the reduced domain has negligible influence on the spilling saline plume within the domain. To demonstrate this, comparisons have been made of time averaged density difference profiles, from simulations of the complete domain, and from simulations of the reduced domains. The comparisons are only possible at grid resolutions of 10.4*mm* and 7.9*mm*, because hardware limitations prevented finer resolutions being obtained for the complete domain simulations.

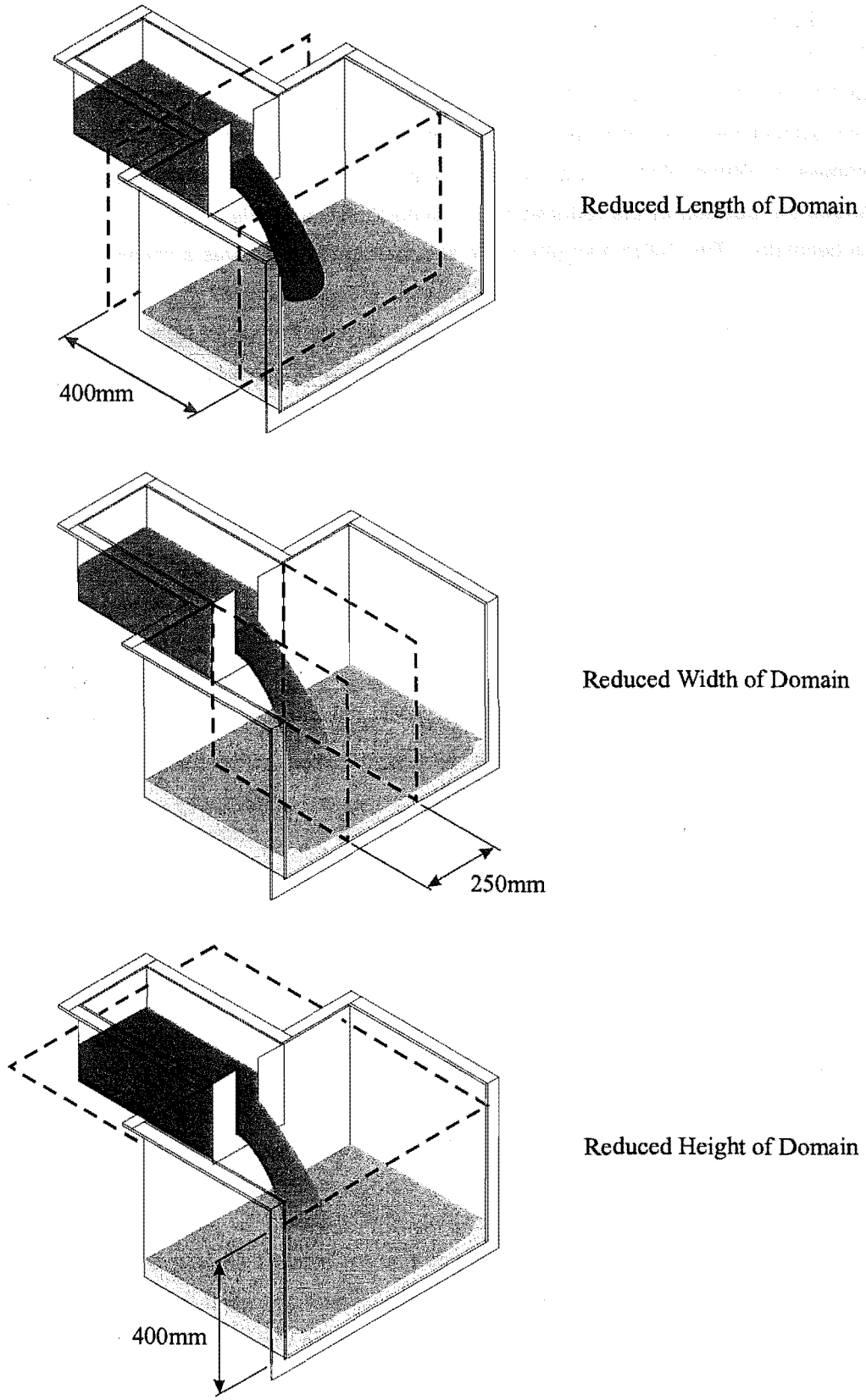

Figure 7-7 ***Boundaries of the reduced domain simulations within the complete geometry of the T-Series model.***

Reduced Length

The internal geometry of the T-Series model was one meter long, although the source structure completely occupied the rear 150*mm* of the source compartment; refer to Figure 3-2. In reduced domain simulations, only 400*mm* of the model length was simulated. The reduced length encompassed 100*mm* of the source compartment and 300*mm* of the second compartment; Figure 7-7 shows the position of the reduced length simulation boundaries within the complete T-Series model geometry. The 100*mm* length of the source compartment was sufficient to capture the full curvature of the density interface between the saline and freshwater fluid streams. The 300*mm* length of the second compartment was sufficient to capture the entire trajectory and impingement region of the spilling saline plume. Downstream of the impingement region, the saline flow was supercritical, so that it had no influence on upstream flow.

Figure 7-8 compares three time averaged density difference profiles from experiment T02 with the computational results from both a complete domain simulation and a reduced length domain simulation. The computational results for each domain are presented for three different grid resolutions. In actual fact, it was not possible to simulate the complete domain with the 5*mm* resolution. Therefore, the results for the 5*mm* resolution are taken from a computational domain where the full length of the T-Series model was simulated, but a reduced width was used. Thus the profiles for this resolution are labelled "full length domain (5*mm*)" rather than "complete domain (5*mm*)". The impact of reducing the domain width is discussed later in this section.

In the comparison of Profile 1 in Figure 7-8, there is a notable difference between the computational results from the reduced length simulations, and the complete domain simulations; the difference does however diminish with increased grid resolution. The concerning aspect of this comparison is that the reduced length simulations provide better results than the complete domain simulations (at the same resolution). The profiles from the reduced length simulations have a peak normalised density difference value of one, which implies there was no mixing occurring in the source compartment. This is correct. The profiles from the complete domain simulations, on the other hand, imply that the saline was diluted in the source compartment, which is incorrect. Although the reduced length simulations appear to perform better than the complete domain simulations, the performance of the complete domain simulations does improve as the grid resolution is refined. This behaviour shows that, although the flow domain may be correctly and completely described in the input data for the simulation (as was the case with the complete domain simulations), the results of the computations can be highly inaccurate at coarse grid resolutions. At fine grid resolutions however the same input description can provide an excellent solution.

The comparison of the computational results at Profile 8 shows better agreement between the reduced length simulations and complete domain simulations for all grid resolutions. This is likely to be because the flow is completely turbulent in these locations, so that there are no sharp density gradients.

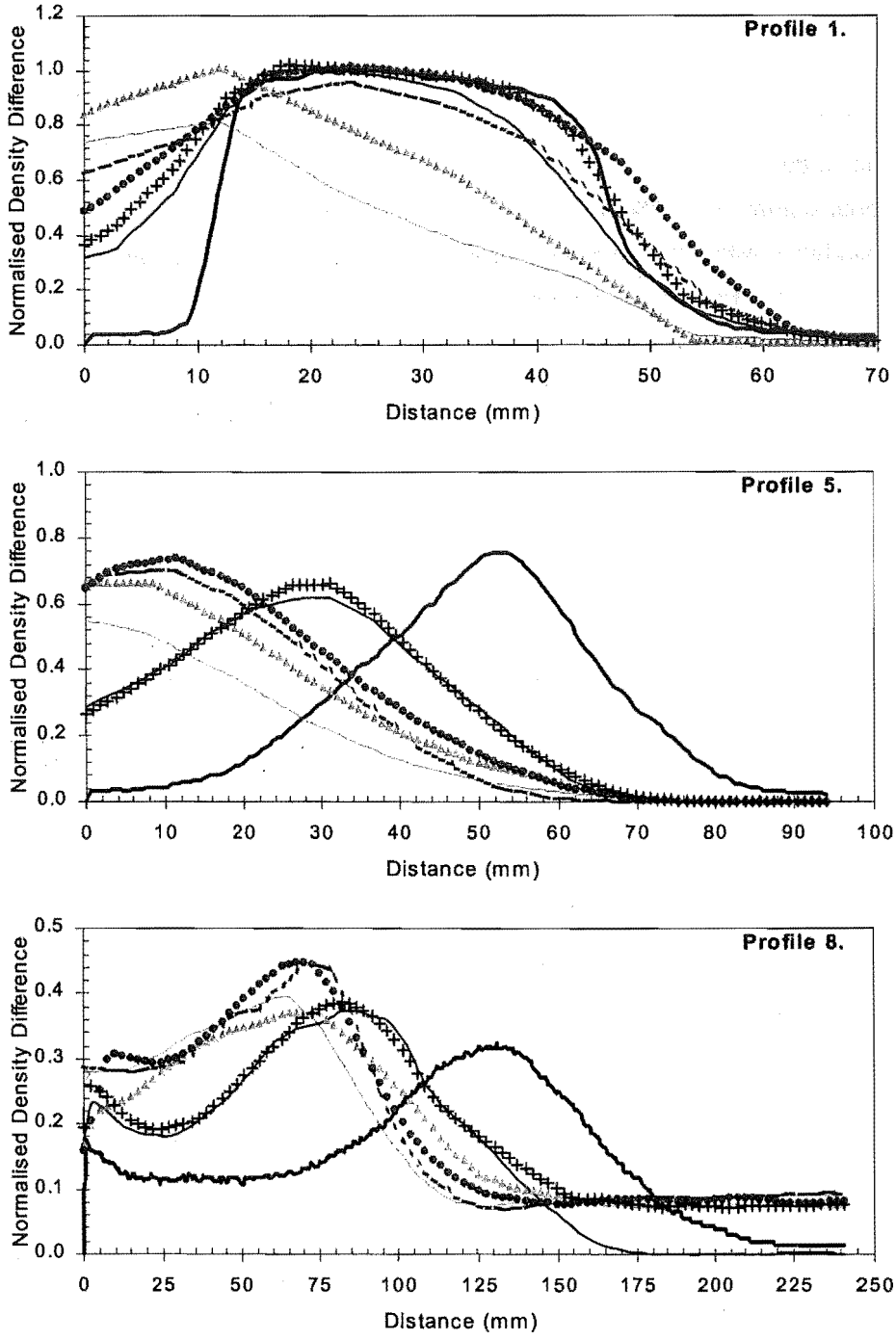

Figure 7-8 ***Comparison of computational results from a simulation where the entire length of the T-Series domain is modelled and a simulation where only 400mm of the domain length is modelled.***

Reduced Width

The T-Series model consisted of two rectangular compartments. The smaller source compartment had an internal width of 250*mm*, while the second compartment had an internal width of 750*mm*. In the reduced domain simulations, the portions of the second compartment that projected out beyond the width of the source compartment were ignored. This meant that the entire computational domain was 250*mm* wide. Figure 7-7 shows the location of the reduced width domain boundaries within the complete T-Series model geometry. By default, the boundaries of the FDS domain are treated as impermeable surfaces. Therefore, in the reduced width domain simulations, it was necessary to specify the domain boundaries on the sides of the second compartment as open passive vents. This specification enabled saline fluid to flow out radially from the impingement region of the plume without any obstruction. However, it also meant that ambient fluid could be drawn into the plume region from the sides of the domain, rather than just from the downstream open end of the model. Thus, any channelling influence that the sidewalls of the second compartment had had on the freshwater flow was not captured in the computational modelling.

Figure 7-9 compares three time averaged density difference profiles from experiment T02 with the computational results from both a complete domain simulation and a reduced width domain simulation. The computational results for each domain are presented for two different grid resolutions, 10*mm* and 8*mm*. In the comparisons at Profile 1 and Profile 5 there is very little difference between the computational results from the complete domain simulations, and the computational results from the reduced width simulations. The agreement was similar for all of the first seven of the eight profiles that were taken across the T-Series plume. This implies that the presence of the sidewalls on the second compartment had very little influence on the saline flow that was spilling from the opening. If the sidewalls of the second compartment were closer to the spilling flow, it would be reasonable to expect that they would have a greater influence on the properties of the plume (due to the restricted flow path they create for the ambient fluid).

The comparison of Profile 8 however, shows a notable and consistent disagreement on the right hand side of the profile. The profiles from the complete domain simulations plateau out at a normalised density difference value of approximately 0.1. The profiles from the reduced width domain and the experimental results plateau out at a value of zero. This implies that in the complete domain simulations, a saline flow at least 50*mm* deep exists around the impingement region of the plume. Given that this layer is not seen in the experimental results (where the model has sidewalls), or the reduced width simulations (where the grid resolution is the same), it would seem that the presence of the layer in the complete domain simulations must be a consequence of the increased floor width. This would suggest that the velocity boundary condition is sufficiently severe (when combined with sufficient floor width) to cause a hydraulic jump structure to form on the ceiling jet, which flows out radially from the impingement region. The complete domain profiles would then suggest that, in the computations, the hydraulic jump must drown out the ceiling jet to form a layer around the impingement region of the plume.

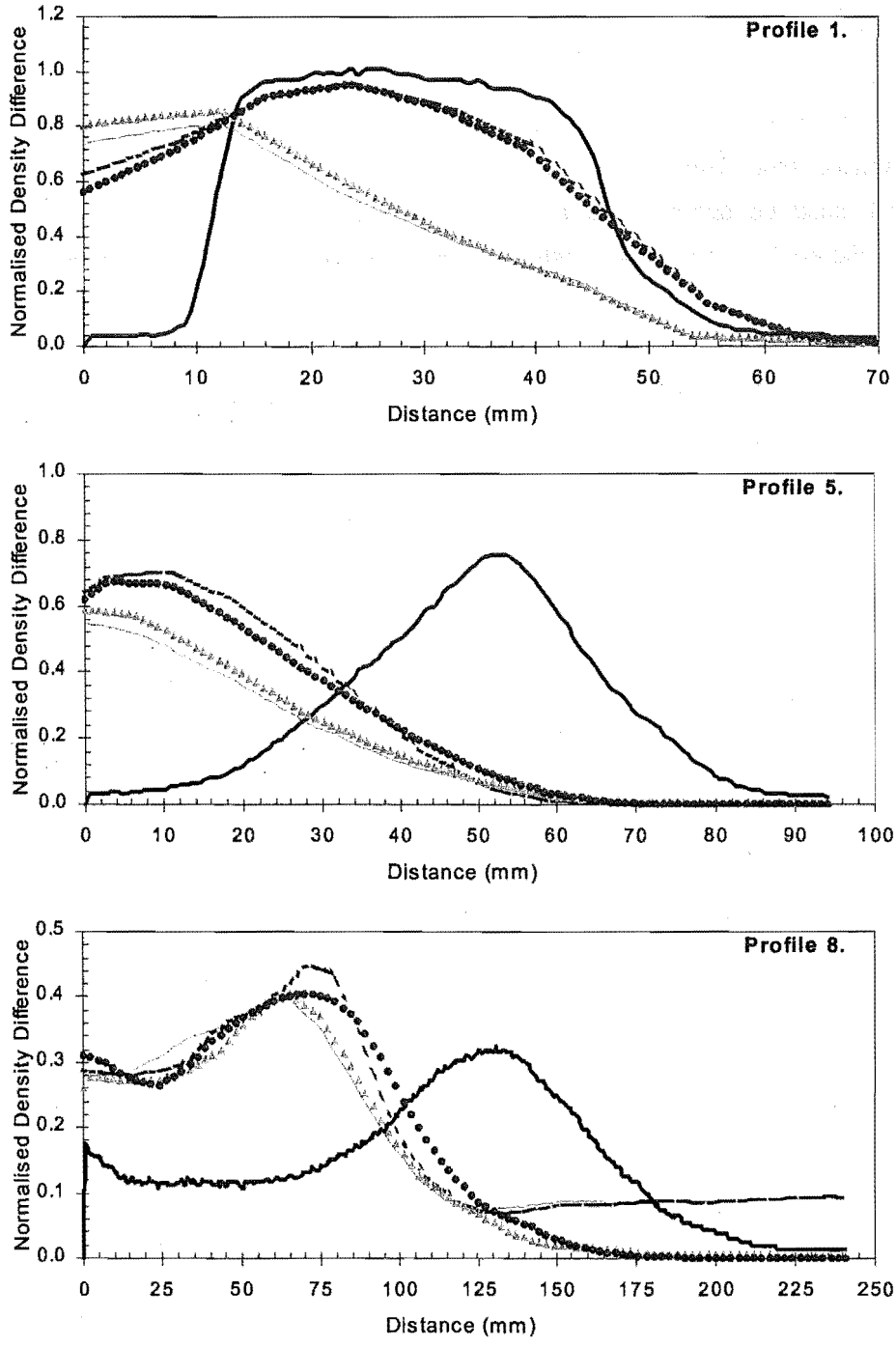

Figure 7-9 ***Comparison of computational results from a simulation where the entire width of the T-Series domain is modelled and a simulation where only the central 250mm of the domain width is modelled.***

Reduced Height

The T-Series model was 500*mm* high. In reduced domain simulations, only the fluid flow in the lower 400*mm* of the model was computed[†]. This approach assumed that the streamlines in the upper 100*mm* of the flow were horizontal, so that there was no vertical mass transfer in this portion of the freshwater flow. Thus, in the reduced height simulations the ceiling of the domain (at height of 400*mm*) could be specified as an impermeable surface with a full-slip velocity boundary condition. Figure 7-7 shows the location of the upper boundary of the reduced height domain within the complete T-Series model geometry.

To account for the flow in the top 100*mm* of the T-Series model, a reduced volume flux of freshwater was specified at the flow source in reduced height domain computations. The reduced volume flux was estimated by assuming that the total volumetric flow rate of freshwater was uniformly distributed over the area the freshwater flow stream occupied in the plane of the vent. From the depth of freshwater in the vent, an estimate could then be made of the freshwater volume flow below the 400*mm* level. In simple terms, this approach merely ensured that within the plane of the vent, the bulk velocity of the freshwater flow was the same in the complete domain simulations as it was in the reduced height simulations. In hindsight, a better approach may have been to choose a reduced volume flux that would match the Froude number of the freshwater layer in the plane of the opening. Thus, the composite Froude number of the exchange flow would remain unchanged, and the dynamics of the saline layer would still dictate the behaviour of the exchange flow[12][13]; refer Section 6.2.4. Having said this, with the approach employed to estimate a reduced volume flux, the Froude number for the freshwater fluid stream was still much smaller than the Froude number of the saline stream in the plane of the vent. Therefore, the saline layer was still the dominant layer in the vent flow. The only exception to this was experiment T04, where in the reduced height simulations, the Froude number of the freshwater layer was greater than the Froude number of the saline layer; see Table 7-2.

Exp	Complete Vent Flow					Reduced Vent Flow		
	h_s	h_∞	$\dot{V}_\infty$	Fr_s	Fr_∞	h_∞	$\dot{V}_\infty$	Fr_∞
	(mm)	(mm)	(l/min)	-	-	(mm)	(l/min)	-
T01	50	155	8.02	0.58	0.02	55	2.84	0.06
T02	38	217	8.03	0.58	0.01	117	3.22	0.02
T03	30	175	8.04	0.56	0.00	75	3.45	0.01
T04	83	122	16.89	0.57	0.18	32	3.05	0.89
T05	68	137	17.30	0.46	0.06	37	4.67	0.21
T06	51	154	17.14	0.53	0.02	54	6.01	0.06

Table 7-2 Characteristics of the freshwater vent flow in the complete domain simulations and the reduced height domain simulations.

[†] *For the simulation of experiment T04 the reduced height was actually 410mm.*

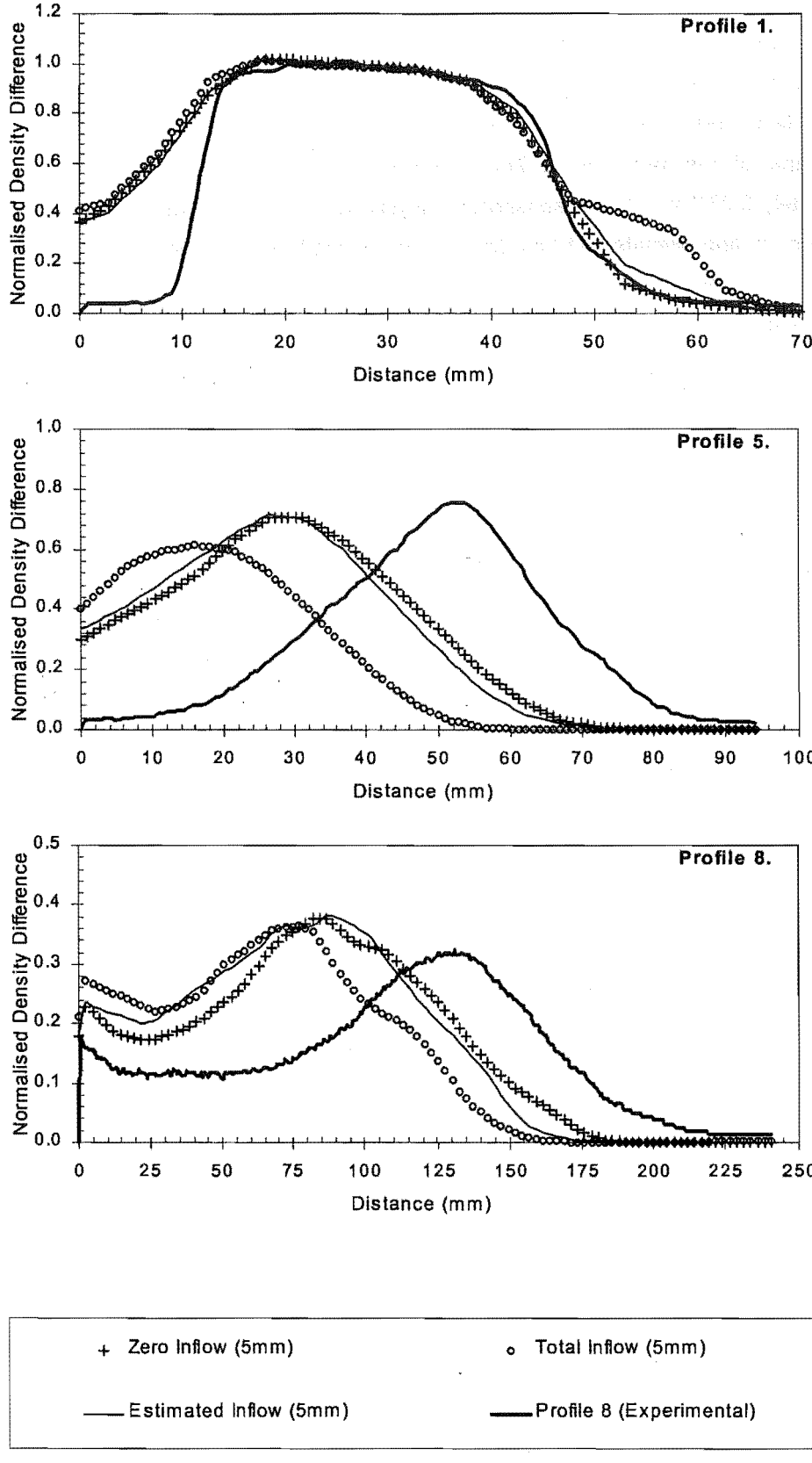

Figure 7-10 ***Comparison of computational results from simulations where the T-Series domain had a reduced height of 400mm and the volumetric flow rate of freshwater through the opening was varied.***

To determine what influence the volumetric flow rate of the freshwater layer had on the time averaged density profiles of the spilling saline plume, a sensitivity analysis was undertaken. In this analysis, experiment T02 was simulated using a reduced height domain and three different volumetric flow rates of freshwater. In reality, for experiment T02, the depth of the freshwater layer in the plane of the vent was 217*mm,* and the volumetric flow rate within this layer was approximately 8.03*l/min.* In the sensitivity analysis simulations, the depth of the freshwater layer was reduced to approximately 117*mm* (due to the reduced height of the domain). Three volumetric flow rates were specified for this fluid stream; 0*l/min*, 3.22*l/min* and 8.03*l/min*. The flow rate of 3.22*l/min* is the flow rate that was given by the estimation method detailed on the last page. The three flow rates gave a Froude number for the freshwater layer in the plane of the opening of zero, 0.02 and 0.11. The freshwater Froude number for the experimental layer was 0.01. Figure 7-10 shows three different density profiles across the plume for the three different freshwater flow rates that were used in the sensitivity analysis.

The comparison of Profile 1 in Figure 7-10 shows that depth of the spilling plume in the plane of the opening was insensitive to the volumetric flow rate of the freshwater layer. On the right hand side of Profile 1 however, there is some difference between the computational results. The profile from the simulation that used the total volumetric flow rate of 8.03*l/min* deviates from the other results. The deviation is evidence of the high shear between the fluid streams, causing dilute saline fluid to peel off the main body of the saline flow and be drawn back into the source compartment in the freshwater fluid stream. As shown in the comparison of Profile 1, this behaviour was only seen in the simulation where the maximum freshwater flow rate was used in the reduced height simulation.

The comparison of Profile 5 in Figure 7-10 shows a significant difference between the computational results. There is little difference between the profiles from the two simulations that had the smaller freshwater volumetric flow rates of 0*l/min* and 3.22*l/min*. However the profile from the simulation that used the total flow rate of 8.02*l/min* is significantly different from the other two. The fact that the peak density difference occurs closer to the source compartment in this latter simulation, implies that the trajectory of the spilling plume has been affected by the volumetric flow rate of the freshwater layer. It seems likely that the higher momentum of the freshwater fluid stream (which is being drawn into the source compartment) has pushed the spilling saline plume closer to the upstream wall that divides the two compartments.

The comparison of Profile 8 in Figure 7-10 shows that there is very little difference between the computational results near the impingement region of the plume, regardless of the flow rate specified for the freshwater layer. The variation between the locations of the peak density difference along this profile is only approximately 15*mm*.

7.2.6 *Format of the Final Simulations*

This section details the format of the final simulations that were used to model the saline plume in the T-Series salt water experiments. The critical content of the input file for each T-Series simulation is detailed in Table 7-3. The input file for the simulation of experiment T02 with a constant viscosity environment is shown below as an example.

In the final simulations of each T-Series experiment, a reduced domain was used in the computations. The domain was 400*mm* long, 250*mm* wide and 400*mm* high. The reduction in the domain height required the specification of a reduced volume flow of freshwater at the flow source; refer Section 7.2.5 – Reduced Height. A symmetry breaker was not used, as the flows naturally become asymmetrical; refer Section 7.2.2. The height of the vent through which saline fluid was injected into the source compartment was specified to match the depth of the steady state saline layer that formed in the source compartment. This approach minimised any mixing that could occur between the fluid streams because of the source representation. The base of the vent through which freshwater was drawn out of the source compartment, lay 10*mm* or 20*mm* above the interface of the steady state saline layer.

```
&HEAD CHID='T02-DNS',TITLE='Salt Water Experiment T02' /
&GRID IBAR=100,JBAR=64,KBAR=100 /
&PDIM XBAR0=0.000,XBAR=0.400,YBAR0=0.000,YBAR=0.250,ZBAR0=0.000,
      ZBAR=0.400 /
&TIME DT=0.1,TWFIN=60. /
&MISC ISOTHERMAL=.TRUE.,DNS=.TRUE.,INCOMPRESSIBLE=.TRUE.,
      BACKGROUND_SPECIES='FRESH_WATER',DENSITY=999.23,
      VISCOSITY=0.00322,SURF_DEFAULT='HALF'  /
&SPEC ID='SALINE',DENSITY=1005.70,VISCOSITY=0.00322,
      DIFFUSION_COEFFICIENT=1.581E-6,
      XB=0.000,0.080,0.000,0.250,0.250,0.340 /
&SURF ID='HALF',VBC=0.5 /
&SURF ID='FULL',VBC=1.0 /
&SURF ID='SALT',MASS_FRACTION(1)=1.,VOLUME_FLUX=-0.0001334 /
&SURF ID='OUT',VOLUME_FLUX=0.0000537 /
&OBST XB=0.000,0.400,0.000,0.250,0.400,0.400, SURF_ID='FULL' /
&OBST XB=0.000,0.100,0.000,0.250,0.000,0.250 /
&OBST XB=0.080,0.100,0.000,0.078,0.250,0.400 /
&OBST XB=0.080,0.100,0.172,0.250,0.250,0.400 /
&OBST XB=0.080,0.100,0.078,0.172,0.250,0.295 /
&VENT CB='XBAR',SURF_ID='OPEN' /
&VENT XB=0.100,0.400,0.250,0.250,0.000,0.400,SURF_ID='OPEN' /
&VENT XB=0.100,0.400,0.000,0.000,0.000,0.400,SURF_ID='OPEN' /
&VENT XB=0.000,0.000,0.000,0.250,0.250,0.340,SURF_ID='SALT' /
&VENT XB=0.000,0.000,0.000,0.250,0.360,0.400,SURF_ID='OUT' /
&SLCF XB=0.000,0.400,0.125,0.125,0.000,0.400,QUANTITY='DENSITY' /
&SLCF XB=0.000,0.400,0.140,0.140,0.000,0.400,QUANTITY='DENSITY' /
&SLCF XB=0.000,0.400,0.110,0.110,0.000,0.400,QUANTITY='DENSITY' /
&SLCF XB=0.110,0.110,0.000,0.250,0.000,0.400,QUANTITY='DENSITY' /
&SLCF XB=0.100,0.100,0.078,0.172,0.295,0.400,QUANTITY='U-VELOCITY' /
&PL3D DTSAM=1000. /
```

Exp	Domain Dimensions			Domain Discretisation			Velocity	Vent Height		Volumetric Flow Rate		Time
	XBAR	YBAR	ZBAR	IBAR	JBAR	KBAR	BC	Saline	Fresh	Saline	Fresh	TWFIN
	(m)	(m)	(m)	(cells)	(cells)	(cells)	(-)	(m)	(m)	(m^3/s)	(m^3/s)	(s)
T01	0.400	0.250	0.400	100	64	100	0.5	0.250-0.350	0.370-0.400	0.00001334	0.0000474	80
T02	0.400	0.250	0.400	100	64	100	0.5	0.250-0.340	0.360-0.400	0.00001334	0.0000537	60
T03	0.400	0.250	0.400	100	64	100	0.5	0.250-0.330	0.350-0.400	0.00001334	0.0000574	45
T04	0.400	0.250	0.410	100	64	100	0.5	0.250-0.385	0.395-0.410	0.00002851	0.0000508	60
T05	0.400	0.250	0.400	100	64	100	0.5	0.250-0.365	0.375-0.400	0.00002851	0.0000779	45
T06	0.400	0.250	0.400	100	64	100	0.5	0.250-0.355	0.365-0.400	0.00002851	0.0001002	35

Table 7-3 Summary of the parameter settings used in the final simulations of the T-Series salt water experiments.

Smagorinsky SGS model Simulations

Schmidt Number	$Sc = 0.721$
Smagorinsky Constant	$C_S = 0.14$
Freshwater Viscosity	$\mu = 0.00114$
Saline Viscosity	$\mu = 0.00114$

Constant Viscosity SGS model Simulations

Diffusion Coefficient	$D_s = 1.581E\text{-}6\ m^2/s$
Freshwater Viscosity	μ = As given by Equation 7-10 (to 5dp)
Saline Viscosity	μ = As given by Equation 7-10 (to 5dp)

7.3 Results

7.3.1 Normalised Density Difference Profiles

All six of the different T-Series experiments were simulated using the FDS. The comparison of the time averaged density difference profiles showed varying degrees of agreement between the experimental measurements and the computational results. To avoid repetition, and to keep this section concise, the comparison is only shown in this chapter for the simulations that gave the best and worst agreement. Figure 7-11 compares the computational profiles and the experimental profiles for experiment T04, which show the best agreement of all the T-Series experiments. Figure 7-12 shows the same comparison for experiment T03, which have the worst agreement. The balance of the comparisons, for all the T-Series experiments, are displayed in Appendix 5.

Functional Analysis

Peacock *et al* [14] proposed a quantitative method for evaluating the comparison of experimental measurements with computer model predictions. The proposed method has been used in this research to provide a defined measure of the model accuracy, so that improvements in the model performance may be assessed in the future. For the T-Series salt water flows, the functional analysis has only been used to measure the comparison of computational results with the scaled experimental profiles; refer Section 7.3.1. The analysis is conducted for the computational profiles that result from a simulation with the Smagorinsky SGS model and a simulation with the constant viscosity SGS model. The domain description for these simulations is detailed in Table 7-3.

The theory behind the functional analysis technique has been well documented and will not be covered again here, readers are referred to the original paper for details[14]. The weakness of the functional analysis method, is that the measure of comparison is not quantified with a single parameter; rather, a series of parameters are used to describe the agreement between the two curves. The need to display and consider multiple parameters for each comparison means it is difficult to quickly interpret the results of the analysis. For this reason, the results of the functional analysis have not been used to describe the comparison of the FDS profiles with the experimental profiles. However, for future verification work on the FDS, where it may be desirable to use the functional analysis method to measure any improvements that have been made in simulating the T-Series transitional flows, the functional analysis results from these simulations have been tabulated in Appendix 6. The formulae that were used in the analysis are also given in Appendix 6.

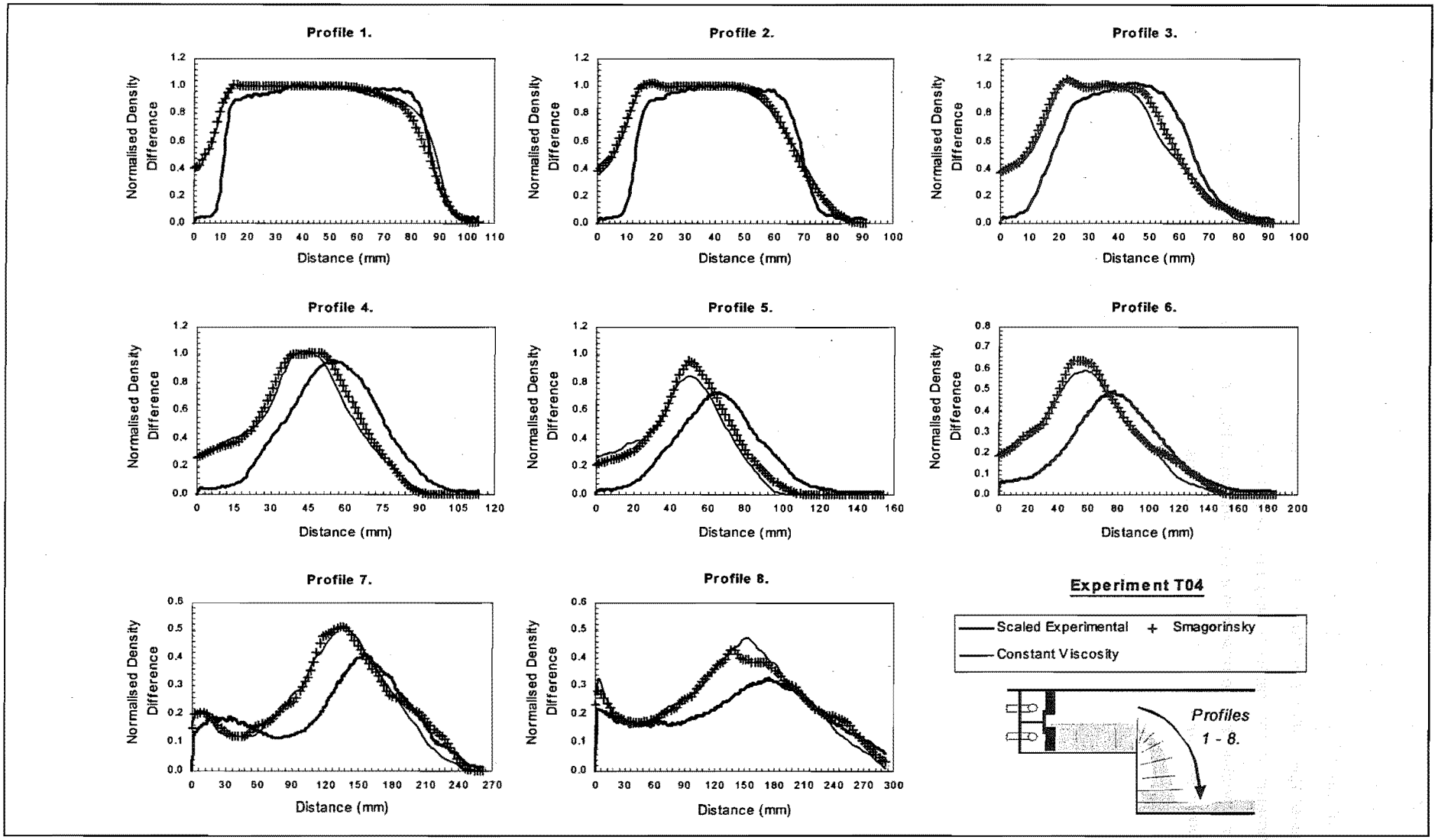

Figure 7-11 The best agreement between the experimental and computational normalised density difference profiles for the T-Series experiments.

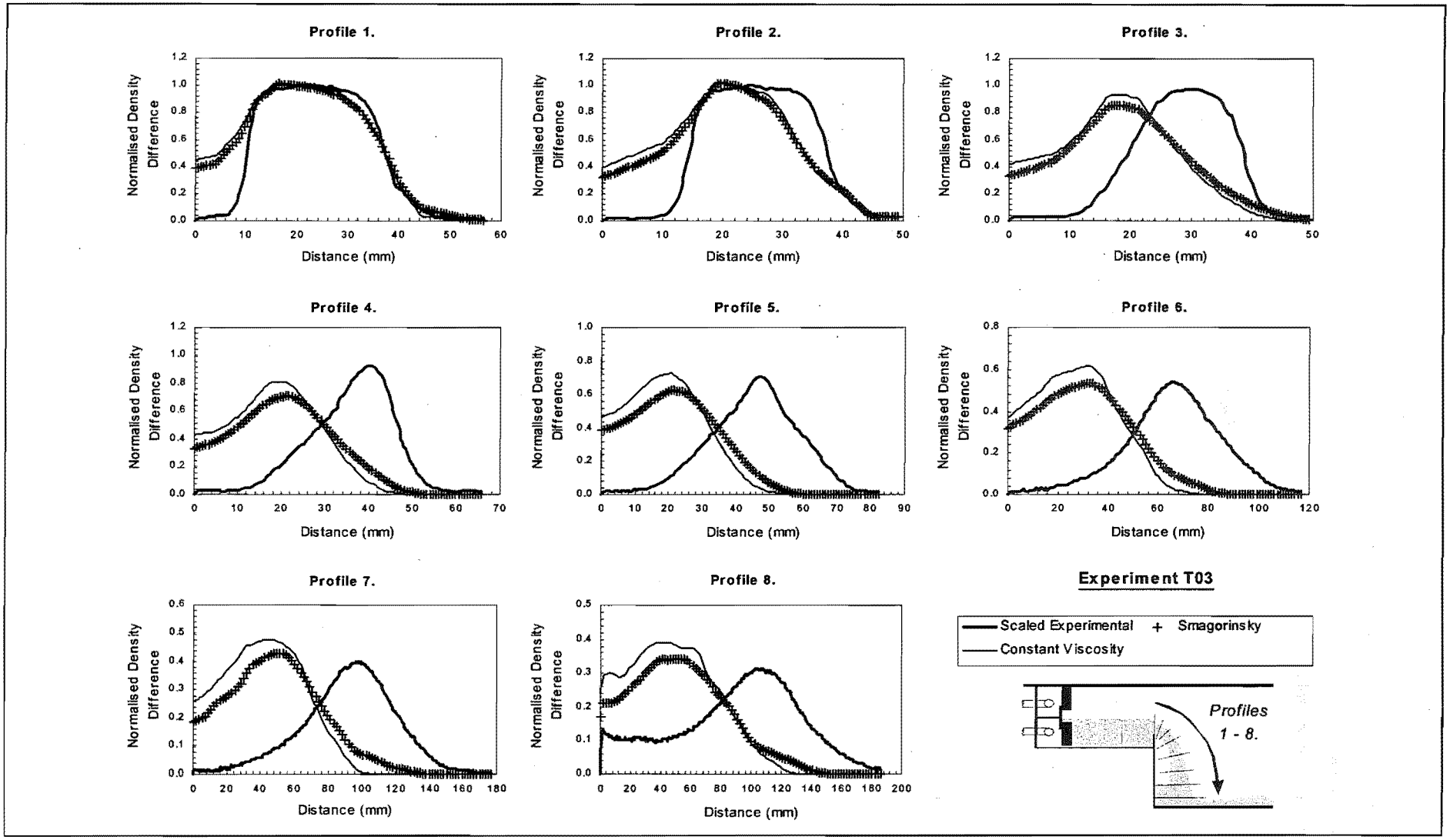

Figure 7-12 The poorest agreement between the experimental and computational normalised density difference profiles for the T-Series experiments

Impact of Spatial Uncertainty

The uncertainty of the coordinates that describe the location of the experimental measurements within the T-Series flow field was evaluated in Section 4.3. For the T-Series experimental measurements, the absolute uncertainty of each component in the Cartesian coordinates was determined to be as follows:

$$\delta x = \pm 4mm$$

$$\delta y = \pm 15mm$$

$$\delta z = \pm 4mm$$

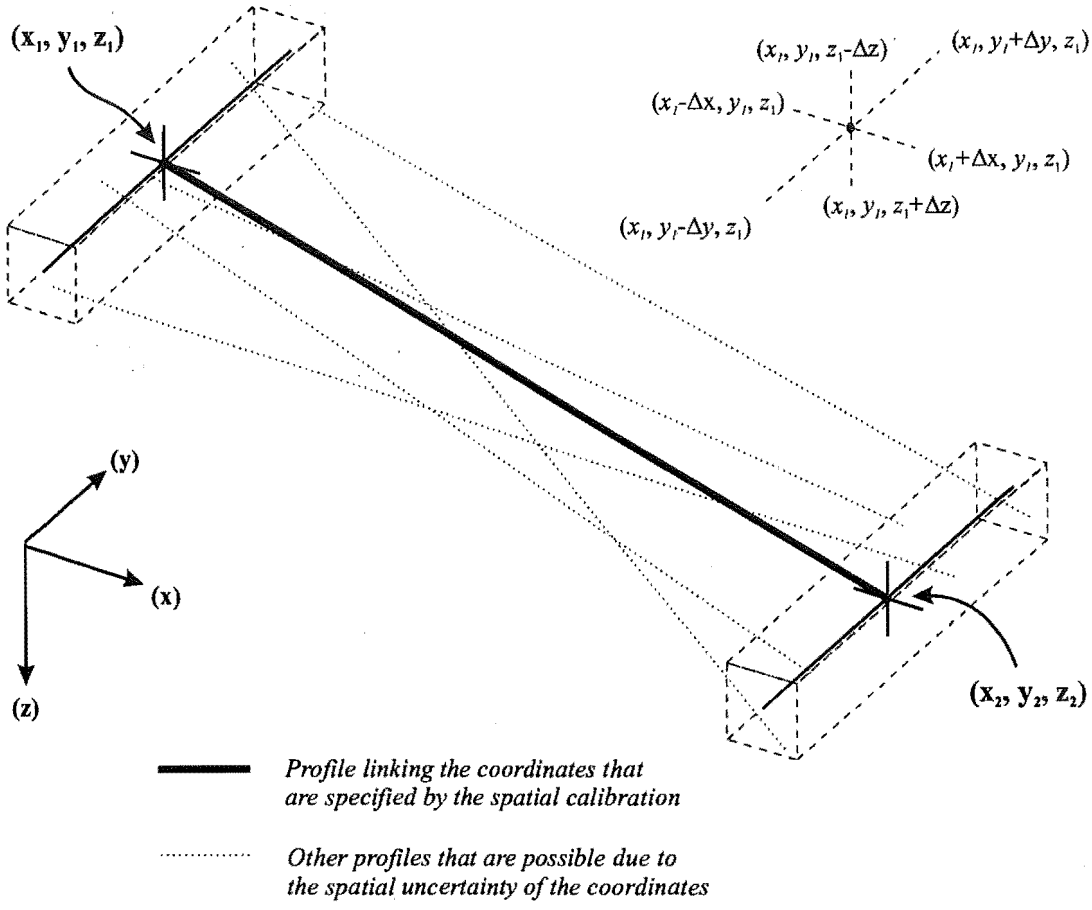

Figure 7-13 Schematic diagram illustrating the uncertainty envelope for the normalised density difference profiles, in terms of the spatial uncertainty of the components in the Cartesian coordinates that describe the profile location.

Figure 7-13 illustrates how the uncertainty in the location of the profile coordinates creates an uncertainty in the length and the location of the profile specified from the calibration of the LIF images. The envelope of uncertainty for each profile could be evaluated using a Monte-Carlo simulation technique. This would be done from computational results, by collecting a sample of the profiles that lie within the uncertainty limits of the specified coordinates, and then scaling the length of those profiles to match the length given by the specified coordinates. This would be a time

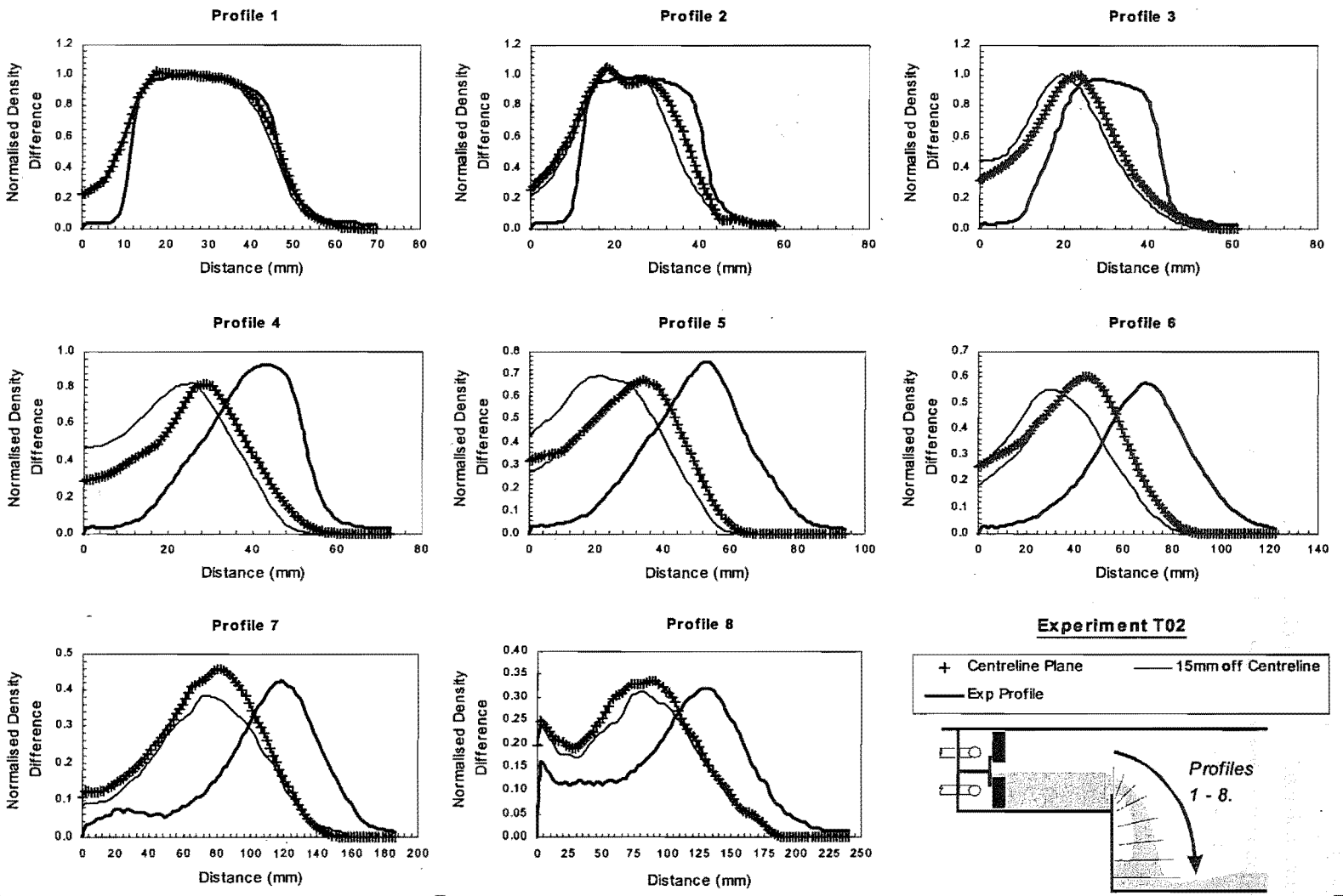

Figure 7-14 ***Comparison of profiles taken from the centreline plane of the domain with profiles taken from the plane that is offset from the centreline by 15mm.***

consuming process and has not been conducted in this research. Instead, to gauge some idea of the uncertainty in the density difference measurements, profiles have been collected from the vertical planes that are offset from the centreline of the T-Series model by the containment width of the laser sheet (that is the planes that lie a distance Δy out from the centreline). The profiles that have been collected from these planes have the x and z coordinates that are listed in Appendix 1. The comparison of these profiles with the profile taken from the centreline of the model geometry is shown in Figure 7-14.

7.3.2 Eddy Frequency

The finest resolution that was used in the computations of the T-Series salt water flows was 4*mm*. At this resolution, it was not possible to evaluate the frequency of the eddy structures on the perimeter of the spilling saline plume. In the analysis that was conducted of the salt water experiments, the eddies were of the order of 15 to 20*mm* in diameter before they were counted. At a 4*mm* resolution, the computations were not able to resolve structures of this size. This comparison is left for future research. The computational resources that will be required to conduct this analysis will probably need to be capable of resolving the T-Series domain, to a level where the cell size is comparable to the pixel size in the video images of the LIF experiments; that is 1.0*mm* to 1.5*mm*.

7.3.3 Dilution Contours

Figure 7-15 and Figure 7-16 compare the experimental and computational time averaged dilution contours for the T-Series experiments. Figure 7-15 shows the comparison for experiments T01 (β = 0.003), T02 (β = 0.006) and T03 (β = 0.013), which all had a volumetric flow rate of 8.0*l/min*. Figure 7-16 shows the comparison for experiments T04 (β = 0.003), T05 (β = 0.006) and T06 (β = 0.013), which all had a volumetric flow rate of 17.1*l/min*.

7.4 Discussion

7.4.1 General Observations of the Flow

Smokeview[6] animations of the computed density field in the centreline plane of the model have been compared to video footage of the real salt water experimental flows. At 10*mm* and 8*mm* grid resolutions, the animated computational results do not compare well with the video footage. At these resolutions, it is difficult to see the structure in the flow, because the saline fluid has a very diffuse appearance. The finest resolution used in the simulations of the T-Series flows is 4*mm*. At this resolution, the instantaneous images of the computed density field show some of the turbulent structures that have been seen in the real salt water flows. In the computations, small turbulent structures are present on the underside of the plume, immediately downstream of the sill. Similarly, large turbulent structures are present on the upper boundary of the plume. The diffuse nature of the density interface in the computational results however, means that it is not possible to

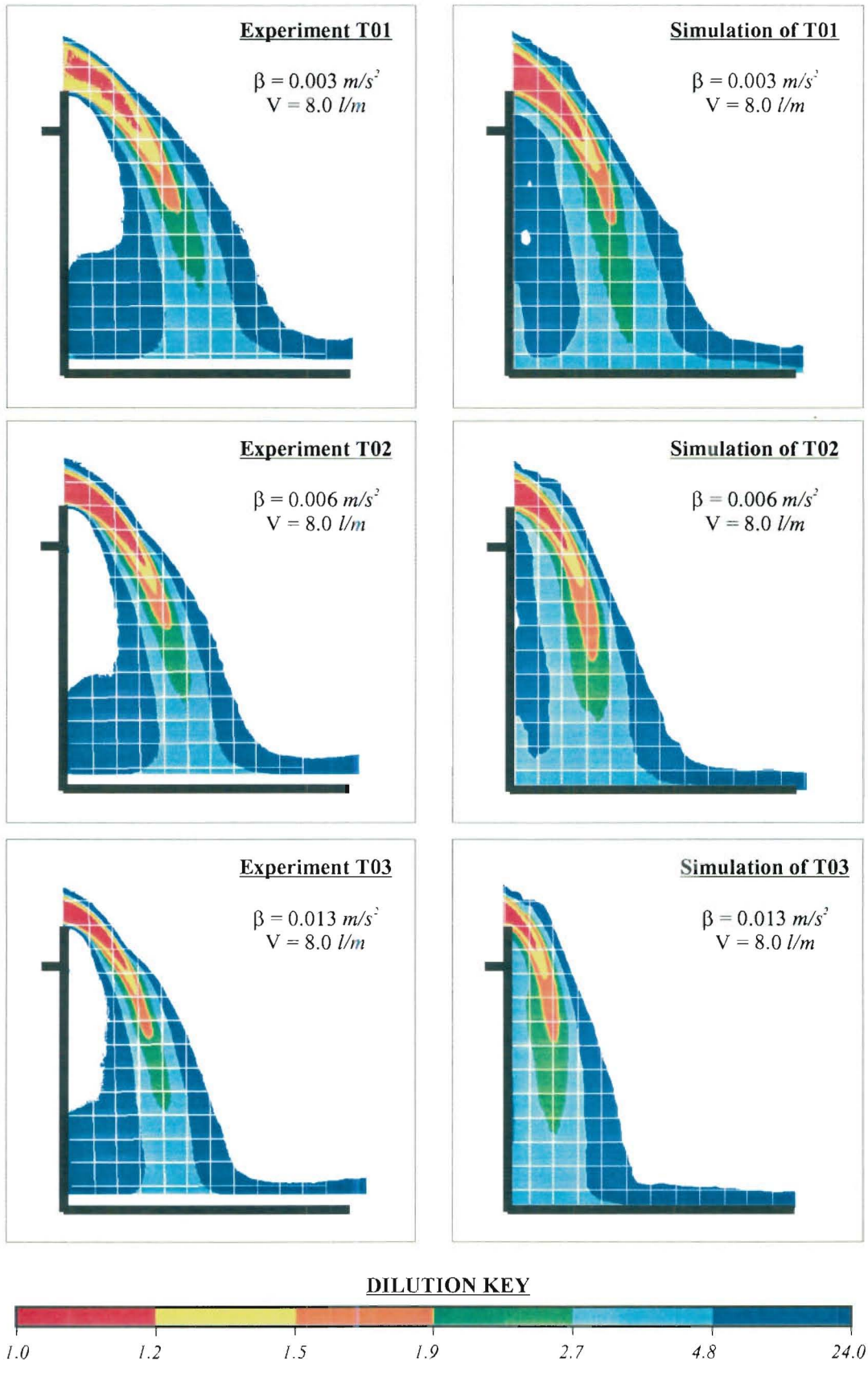

Figure 7-15 ***Comparison of the experimental and computational time averaged dilution contours for experiments T01, T02 and T03.***

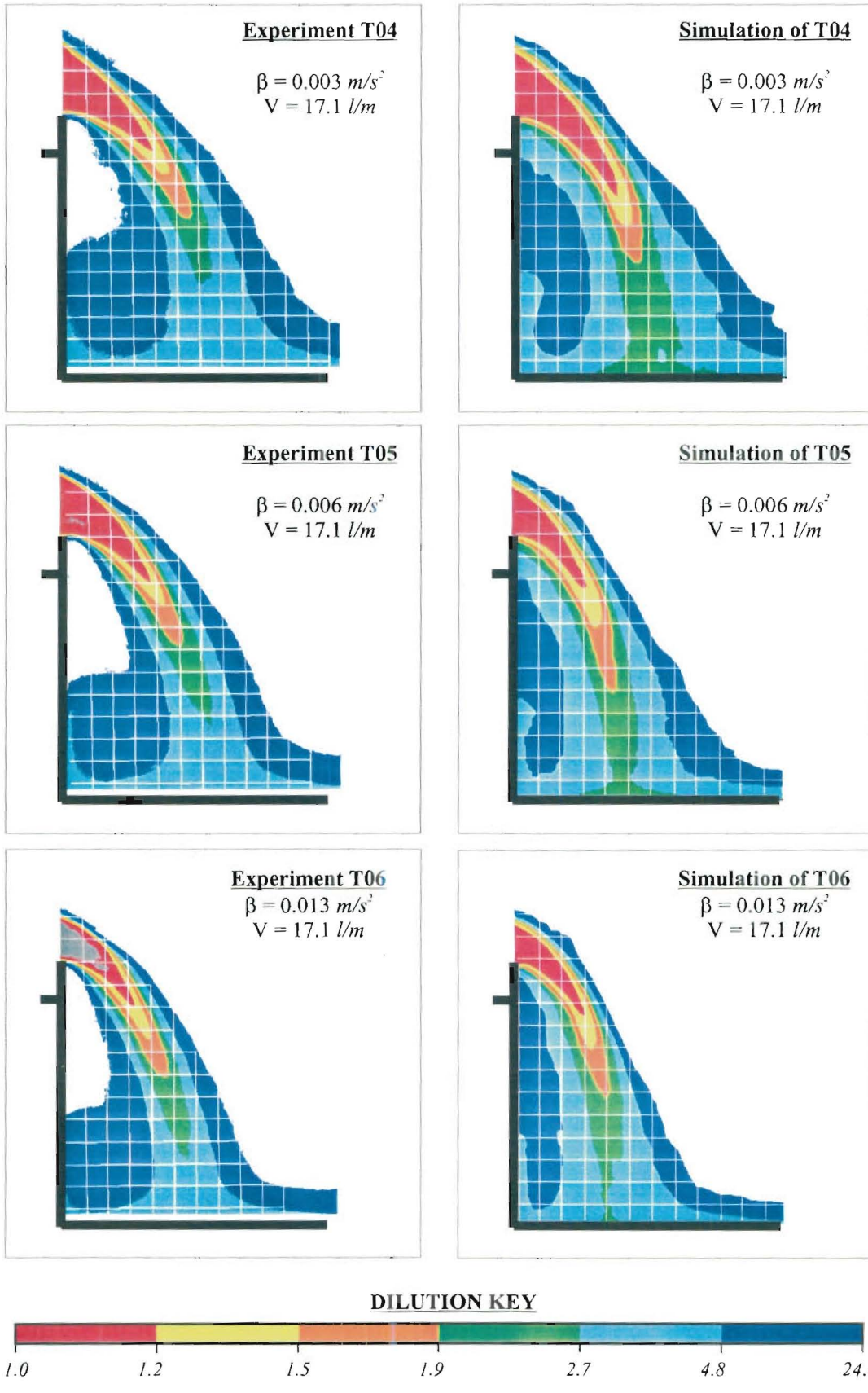

Figure 7-16 ***Comparison of the experimental and computational time averaged dilution contours for experiments T04, T05 and T06.***

see the internal structure of eddies, as had been possible in the salt water experiments. Rather, in the Smokeview animations, the computed eddy structures appear as large lumps on the boundary of the saline flow. The inability of the computations to resolve the internal structure of the turbulent eddies is not a criticism of the FDS model, as numerical methods are not good at resolving sharp interfaces, and the high diffusivity is a necessity of the LES technique; refer Section 7.2.3. In order to reproduce density interfaces as sharp as those seen in experiments, the FDS will require a grid resolution of less than 1 *mm*. This is well beyond the computational hardware abilities available for this research.

Shedding of Saline

The animations of the computed density field show one very obvious difference to the real salt water flows; in the computed flow field, some of the saline appears to detach from the plume and fall toward the floor of the model (beneath the underside of the spilling flow). This behaviour means that, rather than having ambient freshwater beneath the underside of the plume, there is diluted saline fluid. Figure 7-17 shows an instantaneous image of the computed density field from the simulation of experiment T02; the turbulent, diluted saline fluid, can be clearly seen beneath the main body of the spilling saline. A photograph of the real salt water flow is included in the figure, to show that in the real flow, the region beneath the spilling plume is only occupied by the ambient freshwater.

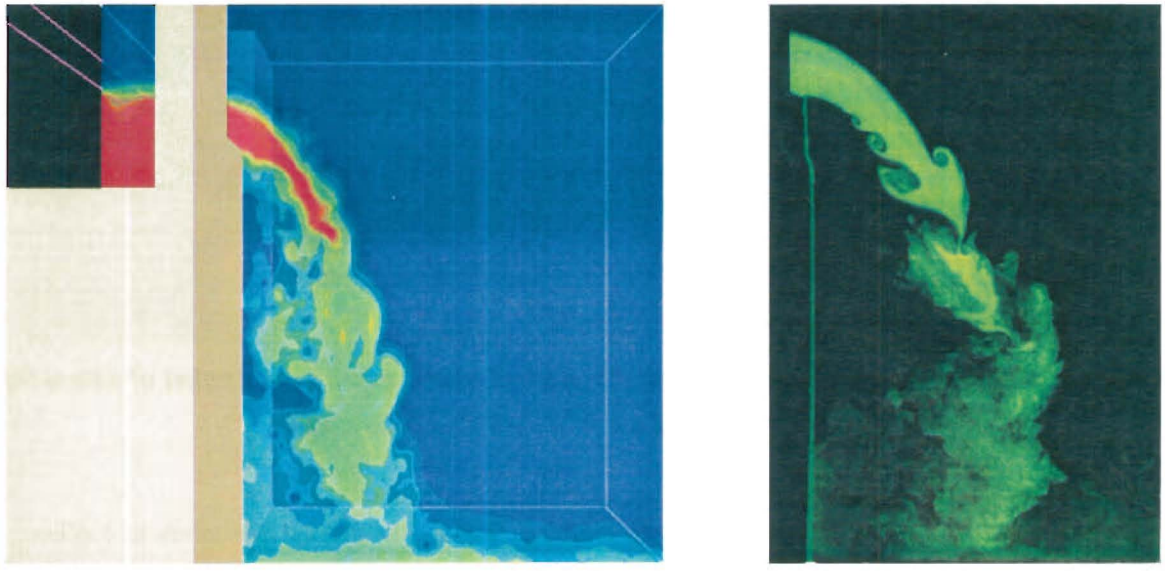

Figure 7-17 Comparison of a photograph of the real salt water flow with an instantaneous image of the computed density field in the simulation of experiment T02.

Animations of the computed density field in the centreline plane of the model show that the saline fluid, which detaches from the main body of the spilling plume, has a three-dimensional flow path.

That is, it does not descend toward the model floor with only a vertical velocity component. Rather, the detached saline fluid has a varying degree of horizontal velocity, and is drawn in and out of the centreline plane (of the model geometry), as it descends. This behaviour gives the computed plume, in the centreline plane of the domain, a very messy appearance, without any distinct boundary to the underside of the spilling flow.

To determine why saline fluid detaches from the main body of the plume in the computations, animations have been studied of the density field in a vertical plane that sections the plume 10*mm* out from the plane of the opening. These animations show that saline fluid is detaching from the sides of the main spilling flow, and being dragged around the perimeter of the plume, toward the underside. The saline fluid, that detaches from the main body of the flow, then falls toward the floor of the model, within a region that is close to the centreline. Figure 7-18 shows a series of instantaneous images from the vertical plane that was viewed in the animations. A black circle is used in each image to track the progress of a pocket of saline fluid that is detaching from the main body of the flow.

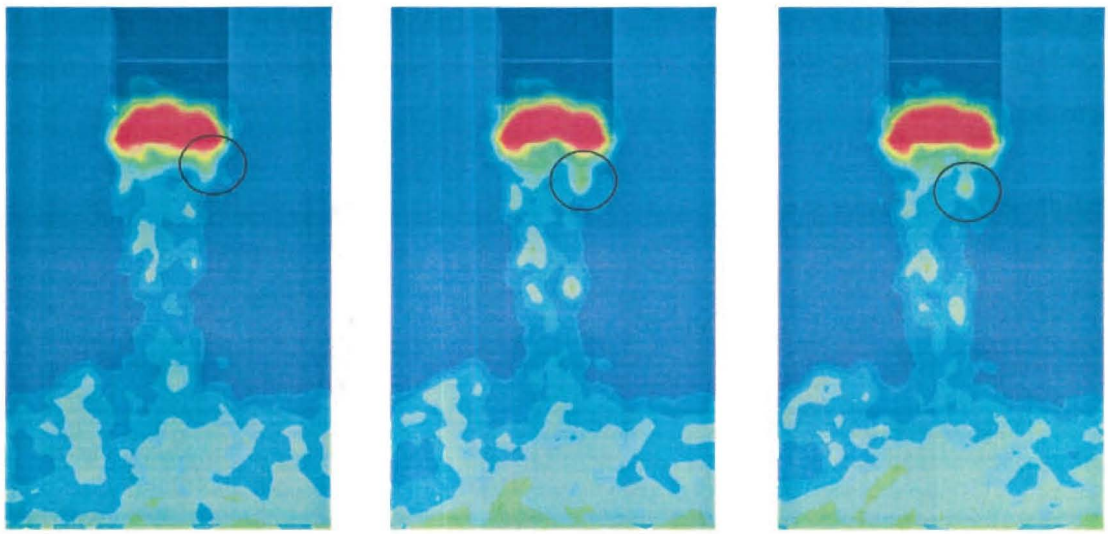

Figure 7-18 A vertical section through the spilling plume showing a pocket of saline fluid being detaching from the main body of the saline flow.

Figure 7-18 shows that the region, within which the detached saline fluid descends to the floor of the model, is thinner than the width of the spilling plume. This congregation of the detached saline fluid near the centreline of the model, is evidence of the velocity field that is induced in the ambient freshwater, by the entrainment demand of the spilling plume. The solid wall beneath the opening prevents ambient fluid being drawn into the region beneath the spilling flow, from anywhere but the sides of the domain. Thus in Figure 7-18, beneath the level of the sill, the ambient fluid is flowing from both sides of the domain, in toward the centreline of the model. Once the ambient fluid is in the region beneath the spilling flow, it is then entrained into the underside of the plume. Thus, the

saline fluid that detaches from the main body of the plume is transported toward the centreline of the model, by the velocity field that is induced in the ambient fluid.

This does not however, explain why the saline is detaching from the main body of the plume, in the computations, but not in the real experiments. This can be explained by considering the shear layer that forms on the perimeter of the plume, and the boundary layer that exists on the saline flow as it exits the opening. The fluid in both the simulations and the experiments is viscous. Viscous action tends toward equalising the momentum of different fluid particles[15]. Thus as the saline flows through the freshwater, the fluid viscosity gradually smears out the velocity gradient between the saline and the ambient. This means that on the perimeter of the spilling plume, there is a shear layer, within which the velocity of the saline is reduced. Additionally, as the saline fluid flows through the opening between the two compartments, the viscosity of the fluid causes a boundary layer to form between the fluid and the solid walls of the opening. Within this boundary layer, the velocity of the saline is less, than the velocity of the main saline body. Thus, as the saline exits the plane of the opening, the fluid around the perimeter of the plume (that is, within the boundary layer and the shear layer) has a reduced horizontal velocity. The reduced horizontal velocity of the fluid means that the buoyancy of the fluid becomes a more dominant component in the trajectory. Therefore, the saline fluid on the perimeter of the plume descends toward the floor of the model earlier, than the main body of the saline flow.

The volume of saline fluid that detaches from the main body of the plume, and descends early, is dependent on the depth of the shear layer and the boundary layer, in the horizontal section of the plume. In the computational modelling, the wall that divides the two compartments is 20*mm* thick. In the real salt water model, however, this wall is only 3*mm* thick[†]. The fact that the internal wall, which contains the opening, is thicker in the simulations than it is in reality, combined with the coarse grid resolutions used in this research (4*mm* – 10*mm*), means that in the computational modelling, the saline flow has a deeper boundary layer at the plane of the opening, than the real salt water flows. Hence in the simulations, a greater volume of the saline fluid has a reduced horizontal velocity, than occurs in the real experimental flows. Additionally, given the coarse grid resolutions used in the simulations, it is likely that immediately outside the plane of the opening, the depth of the shear layer on the perimeter of the plume (that is, the velocity transition) is governed by the grid resolution, rather than the fluid properties and the flow conditions. Hence in the simulations, the volume of saline fluid in the shear region, which has a reduced horizontal velocity, is dependent on the size of the grid cells. Thus, the reason that the detached saline fluid is seen in the computations, and not seen in the real salt water flows, is because in the computational modelling, the boundary layer and the shear layer (near the opening) are thicker than they are in reality. In the computations, the depth of the boundary layer and the shear layer is dependent on

---

[†] *The sill was 20mm thick in all the T-Series simulations to ensure that the sill was always, at least, two grid cells thick for each resolution (4mm – 10mm) used in the research.*

the resolution of the computational grid. Thus, the volume of detached saline fluid is expected to diminish, as the grid resolution is refined. This agrees with computational results, where it was observed that at coarse grid resolutions, larger quantities of saline detach from the plume, than at fine resolutions. Therefore, the anomaly of saline fluid detaching from the main body of the spilling plume is likely to become less significant as the grid resolution is refined. Ultimately however, a grid resolution of $1mm$ or less is likely to be required, in order to completely eliminate the fluid behaviour that is caused by the numerical methods employed in the FDS.

7.4.2 Comparison of the Normalised Density Difference Profiles

The comparisons of the experimental and computational profiles for all the T-Series experiments are shown in Appendix 5. These comparisons show that there is very little difference between the computations that use the Smagorinsky SGS model and the computations that use the constant viscosity SGS model. This implies that in simulating the T-Series transitional flows; the viscosity of the fluid has only a small influence on the results. If the viscosity played a major influencing role in these computations, the different treatment of fluid viscosity, in the Smagorinsky SGS model and the constant viscosity SGS model, would be evident in the comparison of computational results from each simulation. As it is, there is very little difference between the computational results from each SGS model, such that fluid viscosity has only a minor influence on the final computational results.

The best agreement between the computational profiles and the experimental profiles is obtained for experiment T04, which has the higher volumetric flow rate of $17.1l/min$ and the lowest buoyancy of β = 0.003. The worst agreement, between the computational profiles and the experimental profiles, is obtained for experiment T03, which has the lower volumetric flow rate of $8.0l/min$, and the highest buoyancy of β = 0.013. In all of the T-Series simulations however (regardless of source conditions) the peak density difference in the computational profiles is located closer to the plane of the opening than it is in the experimental profiles. Thus the computational spilling plume is not projected out as far from the opening, as the experimental plume is.

The disagreement in the plume trajectory, between the computational flows and the real salt water flows, can be clearly seen in Figure 7-15 and Figure 7-16, which compare the experimental and the computational time averaged dilution contours. Figure 7-15 clearly shows that when the source flow of saline is constant at $8.0l/min$, the agreement between the computational results and the experimental results becomes progressively worse as the buoyancy of the saline is increased. In Figure 7-16, where the source flow of saline is $17.1l/min$, the same relationship can be seen, however to a lesser extent. That is, as the buoyancy of the spilling fluid increases (with a constant volumetric flow rate), the agreement between the computational results and the experimental results gets progressively worse.

The fact that the computational plume descends at a more rapid rate than the real salt water plume, implies that in the computational modelling, the buoyancy of the fluid is a more dominant component in determining the plume trajectory, than it is in the real salt water flows. Given that at the plane of the opening (i.e., Profile 1), the fluid has the correct buoyancy (i.e., a normalised density difference value of one), this finding could imply that the horizontal velocity of the saline is being reduced excessively in the computations. Two options exist, whereby the horizontal velocity of the spilling plume may be reduced, more severely in the computational modelling, than in reality.

One possible means, by which the horizontal velocity may be reduced excessively, is that the computational plume may be entraining more ambient fluid than the real salt water plume. In this case, the initial momentum of the saline fluid is redistributed over a larger mass, thereby lowering the average velocity of the fluid. However, comparison of the peak density difference, between the computational profiles and the experimental profiles, shows that the computational plume is NOT consistently more dilute than the real salt water plume. In fact, the comparisons show, that in general, the computational profiles agree well with the experimental profiles, as to the magnitude of the peak density difference in the plume at any height. Thus the difference in the plume trajectory is not reasoned to be due to incorrect modelling of the entrainment.

A second possibility that exists, for excessive reduction of the horizontal velocity, is associated with the distribution of the shear along the plume boundaries. The numerical methods that are employed in the FDS require smooth transitions in the properties of the flow field. Thus, in the computational modelling, the shear layer that forms along the perimeter of the spilling flow may be distributed over a number of adjacent grid cells. If the grid resolution is sufficiently crude, the shear region could extend across the full width of the plume, retarding the velocity of the entire spilling flow. However, in the computational results displayed in Figure 7-15, Figure 7-16 and Appendix 5, the grid resolution is $4mm$, such that there are 22 grid cells across the width of the opening. It is expected that a transition may occur across a group of five adjacent grid cells (or a number of this order). Thus, in the computational modelling, the velocity in the centreline plane of the flow is initially unaffected by the shear along the plume boundaries. Thus, the grid resolution, and the resulting region of influence for the shear layer, is not responsible for excessively reducing the horizontal velocity of the fluid in the computational plume. It seems therefore, that the disagreement between computations and experiment, as to the plume trajectory, is not primarily due to a difference in the relative size of buoyancy and the initial momentum of the flow.

Another possibility that would explain why the computational plume trajectory does not agree with the real salt water plumes, concerns the spatial distribution of the pressure. Since there is a solid wall beneath the sill of the opening, the entrainment demand for the underside of the spilling plume, must be satisfied by drawing ambient fluid, into the region beneath the plume, from around the sides of the spilling flow. The volume of ambient fluid that is entrained into the underside of the plume is dependent upon the buoyancy of the spilling fluid, and the width of the flow. The solid wall

beneath the opening creates a restricted area through which this volume of ambient fluid can be supplied to the underside of the plume. Thus the ambient fluid velocities beneath the plume are greater than the ambient fluid velocities else where around the plume. The consequence of this is that an under-pressure is created beneath the plume, which draws the plume back onto the wall.

Figure 7-19 illustrates the flow field that creates an under-pressure between the underside of the plume, and the solid wall that is located below the sill of the opening. Figure 7-19(a) shows the geometry of the reduced domain that was used to simulate the T-Series flows. The sidewalls of the domain were specified as open vents, such that ambient fluid could be drawn into the domain, without restraint, through these boundaries. Figure 7-19(b) shows a schematic diagram (not to scale) of the streamlines for the ambient fluid that is entrained into the spilling plume (within the horizontal plane given by the Section A-A). Since the streamlines are congested between the wall and the underside of the plume, the velocity of the ambient fluid in this region, is greater than the velocity of the ambient fluid elsewhere around the plume. The difference in the fluid velocity across the plume creates a pressure difference across the plume, which is illustrated in Figure 7-19(c). The pressure difference can be determined by considering the pressure at sample points A and B, which are marked on the Section A-A in Figure 7-19(b). For each sample point, Bernoulli's equation can be applied to the streamline that links the sample point, to a point that is in a region far from the spilling plume (i.e., where the ambient velocity is zero). Wood and Webby (1980)[16] examine the effects of solid boundaries near turbulent plumes and jets.

The pressure difference described above, and illustrated in Figure 7-19, has an influence on the trajectory of the spilling plume. Therefore, without any evidence to suggest that the difference between the computational plume trajectory, and the experimental plume trajectory, is due to the relative magnitude of buoyancy and inertia, the spatial distribution of the pressure must be considered as a possible cause. Further research is required here to confirm or dismiss this speculation, and to resolve the disagreement in the plume trajectories. Given that previous FDS modelling[17] has resolved the fire plume being blown over in compartment fires, it may be that anomaly described above is only apparent for very small density differences.

Other than the disagreement in the trajectory of the plume, the only other significant difference between the computational profiles and the experimental profiles is that the computational results show the presence of saline fluid on the underside of the plume. That is, the computational density difference profiles all start with a normalised density difference value between 0.2 and 0.4. The experimental profiles, on the other hand, show that on the underside of the plume there is only ambient fluid. The reason for this disagreement has already been explained in Section 7.4.1 – Shedding of Saline.

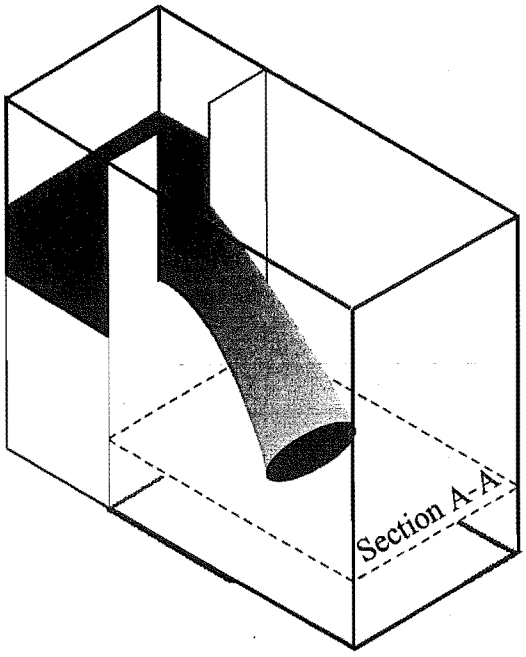

Schematic diagram of the computational domain that was used to simulate the T-Series transitional flows. The side walls of the domain are open vents, which allow ambient fluid to be drawn into the domain to satisfy the entrainment demand of the spilling plume.

Section A-A through the spilling plume, showing the streamlines of the ambient fluid that is entrained into the flow - (not to scale).

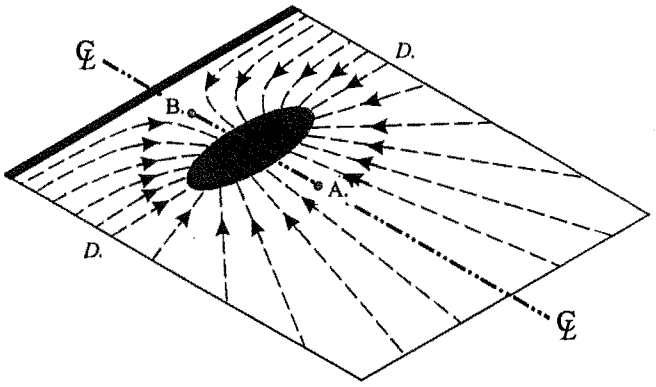

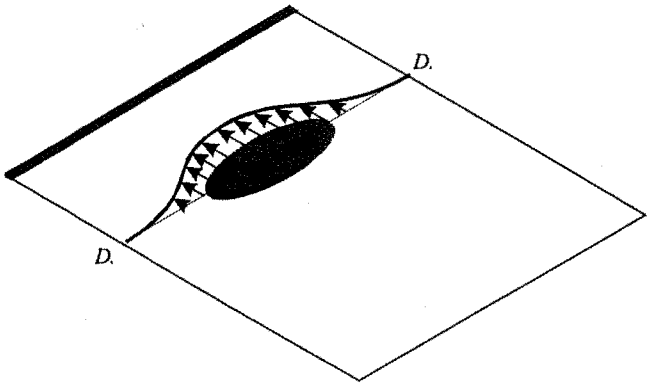

The pressure distribution ΔP on the spilling plume, which draws the plume onto the wall beneath the sill of the opening (not to scale).

Figure 7-19 Schematic diagram illustrating the ambient fluid streamlines in a section through the spilling plume, and the resulting pressure distribution, which can influence the trajectory of the spilling plume.

7.4.3 Impact of the Sub Grid Scale Model

Two SGS models were used in the simulation of the T-Series transitional flows; the Smagorinsky SGS model and the constant viscosity SGS model. The results of these simulations showed no significant difference in the performance of either model for the grid resolutions used in this research. The influences of the different SGS models may however become more apparent at finer grid resolutions.

7.4.4 Grid Dependence

The grid resolutions that have been used in the T-Series simulations range from 10*mm* through to 4*mm*. In terms of the discretization of the domain height, these resolutions equate to 40 through to 100 cells in the vertical dimension (that is KBAR equals 40 through to 100). The resolution range has been limited by the computational hardware that is available for this research; refer Section 2.5.

As expected, the simulation results converge toward the experimental measurements, as the computational grid is refined. At the coarsest resolution (KBAR=40), the performance of the model is very poor. At the finest resolution (KBAR=100), there is some variation as to how well the time averaged density difference profiles from the computations compare to the experimental profiles. The difference in the degree of agreement, depends upon the relative size of the momentum and buoyancy of the saline fluid within the plane of the opening. The best results were obtained in the simulation of the experiments that had the highest source momentum and the lowest fluid buoyancy. The worst results were obtained in simulating the experiments that had the lowest source momentum, and the greatest fluid buoyancy. The principle disagreement, between the computational flow and the experimental flow, is in the trajectory of the plume.

Even at the finest grid resolution (KBAR=100), animations of the computed density field show a significant amount of fluid behaviour occurring solely because of the numerical methods employed in the model. This "artificial" fluid behaviour is caused by the coarseness of the grid resolution. Consequently, as the resolution is refined, the amount of "artificial" fluid behaviour seen in the flow field reduces. This exercise has therefore highlighted, the difficulties in using a numerical model to resolve flow fields where there are sharp/abrupt transitions in the flow field properties (such as thin shear layers along the boundaries of a flow).

Until a resolution is achievable that will enable the sharp density interfaces, and velocity transitions, of the T-Series experiments to be resolved, it will be difficult to determine whether the hydrodynamic model is capable of correctly predicting transitional flows. The most challenging part of computing the T-Series flows is accurately predicting the delay in the onset of turbulent mixing on the upper boundary of the spilling plume. This delay in turbulent mixing produces lopsided density difference profiles across the early sections of the plume; refer Section 6.2.2. In the simulations conducted in this research, it has not been possible to determine if the FDS

hydrodynamic model can correctly resolve the delay in turbulent mixing, because the coarse grid resolutions that were used in the simulations had an overriding influence on the fluid dynamics.

7.5 Conclusions

The simulation of the T-Series transitional flows in this research has been a worthwhile exercise. In general, the research has emphasised the dependence of the hydrodynamic model performance on the resolution of the computational grid. In particular however, the simulations conducted in this research showed that at coarse grid resolutions, the numerical methods employed in the FDS can create fluid behaviour in the computational flow field that does not occur in the real buoyant flows (numerical fluid flow). A number of specific conclusions can be drawn from the results of the T-Series simulations that were conducted in this research.

Computations that are conducted with an initially symmetrical domain and symmetrical initial conditions, will not necessarily generate symmetrical flows, as had been previously observed. It is believed, that in the process of the computations, an asymmetry can form in the boundary conditions of the domain that breaks the symmetry of the computations. This is a consequence of the "ghost properties" approach that is used to mask internal cells in the domain, in order to represent impermeable flow obstructions.

Care must be taken in using a plane of symmetry to reduce the size of the flow field that is computed in simulations. This is of particular importance in situations where the computational results within the plane of symmetry are of interest. Simulations of the T-Series transitional flows showed, that within the plane of symmetry, the computational results from symmetrical simulations differed significantly from computational results where the symmetry of the computations was broken. However, when computational results from locations outside the plane of symmetry were compared, they showed better agreement, regardless of whether the symmetry was broken or not. Thus, the impact of utilising a plane of symmetry in simulations, and thereby imposing an idealised condition on the computed flow field, is most significant on the flow that occurs within the plane of symmetry. The effect of assuming symmetry, on the flow field outside the plane of symmetry, reduces with distance from that plane. All this implies that when experiments are conducted for the purpose of CFD verification, if the experiment is symmetrical, measurements should be taken from outside the plane of symmetry. This then means that the symmetry assumption can be confidently employed in the simulation of the experiments.

The FDS does not automatically terminate simulations when the computations become unstable, nor is it obvious from time averaged results that there were instabilities in the computations. Thus, it is possible to use the FDS in conditions that are numerically unstable. When simulations are conducted with a constant viscosity SGS model, the fluid should be sufficiently viscous to prevent instabilities forming in the computations. In this research, a relationship has been determined for

this minimum fluid viscosity, in terms of the initial buoyancy of the fluid and the resolution of the computational grid. This relationship has not been validated for thermal gas flows, nor for liquid flows outside the density difference ratio range of $0.003 < \beta < 0.013$.

Simulations of the T-Series transitional flows have been conducted at four different uniform grid resolutions, that are described by KBAR = 40, 50, 80 and 100. In these computational grids, the grid cell dimension is practically equal in each of the three component directions. The simulations that computed the flow throughout the entire T-Series model at the coarsest grid resolutions (KBAR = 80 and 100) gave poor results when compared to the experimental measurements. This finding shows that, although the flow field may be described completely and correctly in the input, the computational model can give poor results at coarse grid resolutions.

The T-Series simulations revealed that some artificial fluid behaviour can be created in the computational flow field, by the numerical methods that are employed in the FDS. The requirement for smooth transitions in the properties of the flow means that the region of shear, which forms around the perimeter of the spilling plume, is spread over a number of adjacent grid cells. Due to the coarse grid resolution of the simulations in this research, this requirement meant that the resolution of the grid, rather than the viscosity of the fluids, governs the depth of the shear region. Thus, in the computations, a greater cross sectional area of the spilling plume is influenced by the viscous shear along the plume boundary than occurs in the real salt water plume.

At the grid resolutions used in this research ($40 < KBAR < 100$), there is very little difference in the performance of the two SGS models. However at finer grid resolutions, it is expected that in the simulation of the T-Series transitional flows, the constant viscosity SGS model will perform better than the Smagorinsky SGS model. This is due to the fact that, as the grid resolution is refined in constant viscosity simulations, the viscosity of the fluid in the computations will approach the real viscosity of salt water. In simulations that use Smagorinsky SGS model however, the fluid around the perimeter of the spilling flow will always have a higher viscosity than real salt water. Thus at fine grid resolutions, the constant viscosity SGS model represents the real fluid properties more realistically. Conversely, at fine grid resolutions, the approximations inherent in the Smagorinsky SGS model (i.e., that the fluid viscosity varies spatially) may start to become significant in the fluid dynamics that is resolved.

The principle finding from the T-Series simulations is that, in the simulation of the transitional flows, the trajectory of the computed plume is always steeper than the trajectory of the real salt water plume. The degree of disagreement, between the computed trajectory and the real trajectory, is dependent upon the buoyancy of the spilling flow, and the initial momentum with which the buoyant fluid is discharged (horizontally) from the opening. The best agreement, between experiment and computations, is obtained for the simulation of the experiment where the fluid has the lowest buoyancy and the highest initial momentum. The converse is also true; the worst result comes

from the simulation of the experiment that has the highest buoyancy and lowest initial momentum. From the results of all the T-Series simulations, there is no indication that the horizontal velocity of the spilling flow is being excessively reduced, such that the buoyancy of the flow becomes more dominant. Therefore, it is speculated that, the disagreement between the experimental trajectory and the computational trajectory, may be due to the spatial distribution of pressure in the computational flow field. Further research is required, to confirm or dismiss this speculation, and to resolve the disagreement in the plume trajectories.

This research has been unable to determine if the FDS hydrodynamic model can correctly compute the natural transition to turbulence that occurs in the T-Series experimental flows. The T-Series experiments are difficult to compute correctly due to the differential mixing that occurs around the plume perimeter. On the underside of the plume, there is turbulent mixing for the entire length of the spilling flow. On the upper surface of the spilling plume however, the onset of turbulent mixing is delayed for a distance. The length of this delay is dependent on the source conditions of the plume, which were varied across the six different T-Series experiments. Further simulations are required at finer grid resolutions (KBAR > 100), to determine if the T-Series transitional flow can be correctly computed.

7.6 References

1. Rehm, R.G., McGrattan, K.B., Baum, H.R., and Cassel K.W. (1997) Transport by Gravity Currents in Building Fires, *Fire Safety Science – Proceedings of the Fifth International Symposium*, 391-402.

2. Fleischmann, C.M. and McGrattan, K.B. (1999) Numerical and Experimental Gravity Currents related to Backdrafts, *Fire Safety Journal*, **33**, 21-34.

3. Zang T.A. and Piomelli U. (1993) Large Eddy Simulation of Transitional Flow, In: *Large Eddy Simulation of Complex Engineering and Geophysical Flows*, Ed. Galpin B. and Orszag S. A., Cambridge University Press, pp. 209-227.

4. Dang K.T. and Deschamps V. (1987) Numerical Simulation of Transitional Channel Flow, In: *Numerical Methods in Laminar and Turbulent Flows*, Ed. Taylor C., Habashi W.G. and Hafez M.M., pp. 423-434. Pineridge.

5. Deschamps V. and Dang K.T. (1987) Evaluation of Sub-Grid Scale Models for Large Eddy Simulation of Transitional Channel Flows, *Sixth Symposium of Turbulent Shear Flows*, Toulouse, France.

6. McGrattan K.B. and Forney G.P. (2000) 'Fire Dynamics Simulator – User's Manual' NISTIR 6469, National Institute of Standards and Technology, U.S. Department of Commerce, Gaithersburg, MD 20899.

7. Steckler K.D., Baum H.R. and Quintiere J.G. (1986) Salt Water Modelling of Fire Induced Flows in Multicompartment Enclosures NBSIR 86-3327, National Bureau of Standards, National Engineering Laboratory, Center for Fire Research, Gaithersburg, MD 20899.

8. Baum, H.R. (1999) Large Eddy Simulations of Fires – from Concepts to Computations, *Fire Protection Engineering*, **6**, 36-42.

9. Baum H.R and Rehm R.G (1984) Calculations of Three Dimensional Buoyant Plumes in Enclosures, *Combustion Science and Technology*, **40**, pp. 55-77.

10. Rehm R.G., Baum H.R., Lozier D.W. and Corley D.M. (1988) A Model of Three-Dimensional Buoyant Convection Induced by a Room Fire, Paper Presented at the First National Fluid Dynamics Congress, July 24-28, Cincinnati, Ohio.

11. *CRC Handbook of Chemistry and Physics*, 57th Edition, Ed: R.C. Weast, CRC Press, 18901 Cranwood Parkway, Cleveland, Ohio 44128, U.S.A.

12. Dalziel S.B. and Lane-Serff G. (1991) The Hydraulics of Doorway Exchange Flows, *Building and Environment*, **26**, 121-135.

13. Farmer D.M. and Armi L. (1986) Maximal Two-Layer Exchange Flow over a Sill and through the combination of a Sill and Contraction with Barotropic Flow, *Journal of Fluid Mechanics*, **164**, 53-76.

14. Peacock R.D, Reneke P.A, Davis W.D. and Jones W.W. (1999) Quantifying Fire Model Evaluation using Functional Analysis, *Fire Safety Journal*, **33**, 167-184.

15. Tritton, D.J. (1993) *Physical Fluid Dynamics,* Van Nostrand Reinhold Company Ltd., Molly Millars Lane, Wokingham, Berkshire, England, p 117.

16. Wood I. R. and Webby G. (1980) The effects of Boundaries near Turbulent Plumes and Jets, *Second International Symposium on Stratified Flows*, The Norwegian Institute of Technology, Trondheim, Norway, 24-27 June 1980, pp 128-137.

17. Rehm, R.G., Baum, H.R., Lozier, D.W. and Corley, D.M. (1988) A Model of Three-Dimensional Buoyant Convection Induced by a Room Fire, *Paper Presented at the First National Fluid Dynamics Congress*, July 24-28, Cincinnati, Ohio.

Chapter 8 - SIMULATION OF FIRE SIMILAR BUOYANT FLOWS

8.1 Introduction

This chapter details the simulations of the P-Series ("fire compartment") and C-Series ("adjacent compartment") salt water experiments that are documented in Chapter 3 through Chapter 6. The buoyant saline flows that are produced in these experiments resemble the fire induced smoke flows that develop in the early stages of a building fire. The simulation of these experiments is conducted to assess the performance of the Fire Dynamics Simulator (FDS) hydrodynamic model when it is applied to the simulation of low temperature (boussinesq), adiabatic, non-reacting, fire induced smoke flows.

In this research, the salt water plumes from the P-Series experiments have been simulated prior to any of the C-Series experiments being modelled. The P-Series simulations assess how well the source plume can be modelled and determine how dependent the computational results are on the grid resolution and the choice of Sub-Grid Scale (SGS) model. Five uniform grid resolutions are used in the P-Series simulations, the resolutions are described by KBAR = 40, 50, 64, 72 and 80 (KBAR describes the number of cells in the height of the domain). Two SGS models are used in the P-Series simulations, the Smagorinsky SGS model and a constant viscosity SGS model.

Each C-Series experiment is simulated twice at the same grid resolution (KBAR=50), once with the Smagorinsky SGS model and once with the constant viscosity SGS model. To assess the grid dependence of the C-Series results, one experiment (experiment C04) is simulated at four different grid resolutions. These resolutions are described by KBAR = 20, 40, 50 and 62.

Section 8.2 of this chapter details the preliminary work that was required before the final simulations of each experiment could be conducted. Section 8.3 then presents the comparison of the computational results with the experimental measurements from both the P-Series and C-Series experiments. Section 8.4 discusses these comparisons, with particular focus on the grid dependence of the results and the influence of the SGS model in the simulations. The conclusions that can be drawn from the research detailed in this chapter are presented in Section 8.5.

8.2 Preliminary Determinations

8.2.1 Time Averaging Parameters

P-Series

In order to minimise the duration of the computations, it was necessary to determine the earliest point in time at which time averaging of the flows could begin, and the minimum duration of time-averaging that would adequately capture the steady state mean flow properties. Equation

(7-5) was used to predict the duration of time-averaging. For the source plumes P01 (β = 0.01) and P06 (β = 0.02), Equation (7-5) predicted that time-averaging durations of 7.2*s* and 5.0*s* respectively would be adequate to capture the mean density of the steady state flow field. A ten second time averaging duration was therefore proposed for the analysis of these plumes.

To confirm the proposed 10*s* averaging duration and to determine the earliest point in time at which the time averaging could be initiated, analysis was undertaken on the computational results from a simulation of plume P01 (β = 0.01). The simulation was 180 seconds long and was conducted with a grid resolution of 5.56*mm* (KBAR = 72). In animations of the computed density field, the flow appeared to achieve steady state conditions after approximately 60*s*. Thus, a sixty second time-average of the flow, from 120*s* through to 180*s*, was used to capture the mean steady state conditions. Density profiles, with a ten second time averaging duration, were then compared to the density from this sixty second average, to determine the earliest point in time at which averaging could be initiated. The results of this analysis are shown in Figure 8-1.

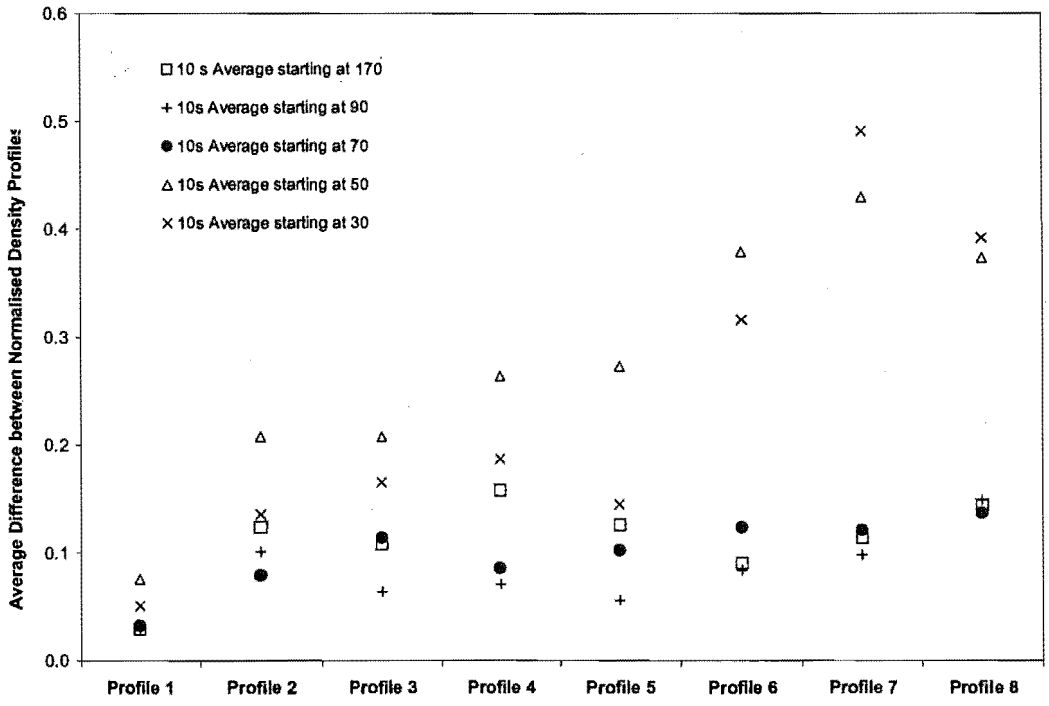

Figure 8-1 ***Determination of the earliest point in time at which time averaging can be initiated to capture the true mean flow field properties in the simulation of plume P01.***

Figure 8-1 shows that once steady state conditions have been achieved in the flow, a ten second time average will provide normalised density difference values that are within 0.16 of the true mean normalised density difference (see data for 10 second average starting at 170 seconds). The

analysis also shows that the earliest point in time at which a ten second time-average of the normalised density difference can be initiated, to obtain normalised density difference values within 0.16 of the true mean values, is after 70 seconds. Thus, the minimum duration of the P-Series simulations was determined to be 80 seconds.

Although this time averaging analysis was conducted on the computational results of a simulation of plume P01 (β = 0.01), the results are also valid for simulations of plume P06 (β = 0.02). The reason for this is that plume P06 has greater buoyancy than plume P01, such that the steady state flow field of plume P06 is achieved at an earlier point in time than it is for plume P01 (see the data in Table 5-3 for an example). Thus, in the analysis of the simulation data for both the P-Series source plumes, the density was averaged over a 10*s* time interval that was initiated at 70*s*.

C-Series

There was some question as to whether Equation (7-5) could be used to predict the time averaging duration in the analysis of the C-Series flows. The saline flow field in the second compartment of the C-Series model had buoyancy that was significantly less than the buoyancy of the fluid that was injected at the flow source. Thus, the fluid in the second compartment moved at a slower rate than the saline that was discharged from the source. In order to apply Equation (7-5) correctly, the fluid densities used in the equation have to be representative of the buoyancy conditions that were present in the second compartment. This was achieved by using the density of the saline fluid that entered the compartment through the opening between the two rooms (i.e. the vent flow density). Similarly, the length scale in Equation (7-5) is required to represent the size of the turbulent flow structures that need to be averaged. For the T-Series and P-Series flows, the turbulent eddies on the perimeter of the saline flow could be reasonably described by the diameter of the flow source. For the C-Series flows, however, the correct choice of the length scale was less obvious, as the turbulent eddy structures in the flow were not clearly discernible. If an equivalent diameter (based upon the area the saline flow occupied in the plane of the opening) was used in Equation (7-5) the relationship predicted a time averaging duration of between 16 and 28 seconds for the various C-Series flows.

To confirm the durations given by Equation (7-5), time averaging analysis (similar to that which was undertaken for the P-Series simulations) was conducted, using computational density data from simulations of experiments C01 (Sill - Open End), C03 (Doorway -Open End) and C05 (Doorway – Doorway). This analysis clearly showed that a ten second time averaging interval would be adequate to capture the mean flow properties for all the C-Series simulations. The required duration of time-averaging is less than the durations predicted by Equation (7-5) as the highly turbulent nature of the C-Series flows means the saline density is well mixed and fairly uniformly distributed in space. Unlike the T-Series and P-Series flows, there are no large-scale eddy structures that have a distinct contrast with the ambient fluid on the interface of the saline layer.

Although a 10*s* time averaging duration was shown to be adequate, a 30*s* average was finally used in the analysis of the C-Series simulation data. The 30s time-averaging interval was used because the total simulation time (estimated prior to the simulations being run) significantly exceeded the time it took to achieve steady state conditions in the computational results. A ten second average could have been used just as well.

The time-averaging duration, combined with the earliest point in time at which the time averaging could be initiated, would determine the minimum duration of the C-Series simulations. According to Table 5-2 and Table 5-3, the time required to achieve steady state flows in the C-Series salt water experiments varied between 170*s* and 360*s*. These times meant that the C-Series simulations would take approximately two days to compute (at the grid resolution given by KBAR = 50). It was therefore decided that preliminary simulations would not be conducted for each C-Series experiment. Rather, each C-Series experiment would be simulated for a duration that would exceed the time to steady state that was given by the experimental data. After the simulations had been run, the animations of the computed density field were studied to estimate the time to steady state in the computational results. Table 8-1 shows the estimated time that it took to achieve steady state conditions in both the experimental and the computations density field, the time at which the time averaging was initiated, and the total time that was simulated for each of the C-Series experiments.

Exp	Estimated $t_{Steady\ State}$		Initiation of Averaging	Duration of Simulation
	Exp (s)	Sim (s)	(s)	(s)
C01	195	160	190	220
C02	165	130	170	200
C03	225	150	220	250
C04	285	260	270	300
C05	405	340	420	450
C06	195	130	195	225
C07	255	230	270	300
C08	345	280	370	400

Table 8-1 ***Estimated time to achieve steady state in the experimental and computational density field, and the time averaging parameters that were used in the analysis of the C-Series computational results.***

8.2.2 Symmetry

A symmetry breaker was not required in the simulations of either the P-Series or the C-Series experiments as it was observed that the computed flows naturally became asymmetrical about the centreline plane of the model; refer Section 7.2.2.

8.2.3 Stability

Equation (7-10) was used to determine the viscosity of the fluid for the simulations that used a constant viscosity SGS model; refer Section 7.2.3. Smokeview[1] animations of the density field in the P-Series simulations showed fluid behaviour that was realistic in appearance, although more viscous than real salt water flows. The accuracy of the constant (0.52) in Equation (7-10) was confirmed by conducting simulations of plume P01 ($\beta = 0.01$), where the viscosity of the fluid was given by Equation (7-10) with the constant reduced to a value of 0.39. Smokeview animations of these simulations showed that regions of the density field in the computed plume had a discontinuous checkerboard appearance, which implied computational instability. A Schmidt number of 0.721 or a diffusion coefficient of $1.581 \times 10^{-6} m^2/s$ was specified in the P-Series and C-Series computations; refer Section 7.2.3.

8.2.4 Boundary Conditions

All of the P-Series and C-Series simulations were conducted with a tangential velocity boundary condition given by VBC = 0.5, refer Section 2.4.3. This condition was intermediate to the full slip and no slip conditions given by VBC = 1 and VBC = -1 respectively. The impact of the velocity boundary condition on the temporal development of the flow field was investigated. The results of this investigation are detailed in Sections 8.3.2 and 8.4.3.

8.2.5 Format of Simulations

P-Series

The P-Series source plumes were simulated using five different grid resolutions. The characteristic dimension of the computational grid used in these simulations was 10.00*mm*, 8.00*mm*, 6.25*mm*, 5.56*mm* and 5.00*mm*. These resolutions equate to the discretisation of the domain height (given by KBAR) into 40, 50, 64, 72 and 80 cells respectively.

The entire length of the P-Series model was not included in the P-Series simulations. Rather, a reduced length domain was used that was only 600*mm* long. The use of a reduced length domain enabled finer grid resolutions to be achieved in the P-Series simulations than would have been possible if the entire P-Series model length was simulated. Time averaged density profiles from the reduced length simulations were compared to density profiles from a simulation where the full length of the model was included (at 8*mm* resolution). The difference between the profiles was negligible. Therefore, dimensions of the domain that was used in the P-Series simulations were 600*mm* long, 400*mm* high and 400*mm* wide.

C-Series

The eight different C-Series experiments were all simulated using a grid resolution of approximately 8*mm*. This resolution equates to the vertical discretisation of the compartment height into 50 cells, (i.e., KBAR = 50). Experiment C04 was also simulated using three other resolutions of 6.4*mm*, 10.1*mm* and 20.0*mm*. These resolutions equate to the vertical discretisation of the compartment height into 62, 40 and 20 cells respectively. Finer resolutions were beyond the computational capacity of the hardware.

The height of the computational domain in the C-Series simulations was greater than the height of the C-Series model. This was because an impermeable roof and a floor of finite thickness were specified for the computations. This would not normally be necessary, as the boundaries of the computational domain are by default impermeable surfaces. However, the spatial uncertainty of the coordinates that describe the location C-Series normalised density difference profiles meant that some profile coordinates were located below the floor level of the model (see profile 4 of experiment C05 for an example). Thus, in order to use the profile coordinates that are specified in Appendix 1, it was necessary to specify a floor and ceiling of finite thickness in the computational representation of the C-Series model.

The specifications that were made in the C-Series simulation input files to give the domain an impermeable floor and ceiling are listed in Table 8-2. The discretisation parameter KBAR that is shown in Table 8-2 was selected as an integer value that satisfied the relationship $2^l3^m5^n$, which assisted computational efficiency[1]. The domain height was then selected to ensure that in the discretised representation of the C-Series model, the internal height of the model would be 400*mm*. This required varying the overall height of the domain until the vertical dimension of the computational grid cells (l_z) factored neatly into 400*mm*. Thus, in some C-Series simulations the overall height of the domain was as much as 480*mm*, however a number of grid cell layers on the floor and ceiling of the domain were then specified as impermeable surfaces to create a 400*mm* height for the fluid flow. Table 8-2 details how thick the impermeable floor and ceiling layers were in each of the C-Series simulations (in terms of grid cells).

Simulation	Domain Height ZBAR (mm)	Discretisation KBAR (cells)	l_z (mm)	Thickness		Flow Depth (mm)
				Ceiling	Floor	
C01 – C08	432	54	8.00	2 cells	2 cells	400.00
C04	480	24	20.00	2 cells	2 cells	400.00
C04	480	48	10.00	4 cells	4 cells	400.00
C04	413	64	6.45	1 cell	1 cell	400.09

Table 8-2 ***Specifications showing how the vertical extent of the C-Series domain was dimensioned and discretised to ensure a 400mm height for the fluid flow.***

In the input file for the C-Series simulations, it was necessary to specify the internal wall that separated the two compartments in the model. In the FDS, impermeable obstacles within the flow field, such as the C-Series model internal wall, must be at least two grid cells thick[1]. Thus, in simulations with a 8*mm* resolution (KBAR = 50), the internal wall was required to be 16*mm* thick, rather than the true 3*mm*. Additionally, to facilitate the accurate comparison of the saline flow transit times (that are detailed in Table 5-3), it was desirable to achieve discretised compartment lengths as near as possible to the as-built 600*mm* lengths. This objective, combined with the minimum internal wall thickness requirement, meant that in the simulations the overall C-Series model length was greater than the as-built 1200*mm*. Table 8-3 details how the length of the C-Series domain was discretised to meet these objectives. The overall dimension and discretisation of the domain length, the length of the grid cells, and the discretised length of both compartments in the C-Series model are given in Table 8-3 for each resolution that was used in the C-Series simulations.

Simulation	Domain Length XBAR (mm)	Discretisation IBAR (cells)	l_X (mm)	Compartment Length (mm)	
				Source	Second
C01, C02, C03, C06	1215	150	8.10	599.40	599.40
C04, C05, C07, C08	1235	150	8.23	601.03	601.03
C04	1280	64	20.00	600.00	600.00
C04	1240	120	10.33	599.33	599.33
C04	1225	192	6.38	599.74	599.74

Table 8-3 ***Specifications showing how the length of the C-Series domain was dimensioned and discretised to obtain compartment lengths that were as near as possible to 600mm.***

The fact that the internal wall of the C-Series model was thicker in the simulations than it was in the real model meant that the coordinates of the C-Series profiles had to be adjusted to account for the extra distance that the second compartment was located away from the plume source. Therefore, in the analysis of the C-Series simulations, the thickness of the internal wall in the simulations was added onto the x-coordinates of the profiles listed in Appendix 1.

Shift of the Coordinate Origin due to Discretisation

In the discretised representation of the domain, the location and dimensions of obstructions to the flow may not exactly match the locations specified in the input file. This is because each cell in the computational domain must wholly represent either fluid or an obstruction. If the size and location of the obstruction that is specified in the input file is not exactly divisible by the appropriate cell dimension (l_x, l_y and l_z), then the discretised representation of the obstruction will be slightly different from the specifications given in the input file. Thus, in the computational representation of the domain, the dimensions and the locations of obstacles and vents can differ slightly from the dimensions and the locations specified in the simulation input file.

The origin for the coordinate system that describes the location of the P-Series and C-Series density profiles is at the centre of the plume source port. In the experimental model this was located on the centreline plane of the model, 300*mm* out from the back wall and 333*mm* above the floor. In the discretised representation of the domain however, the centre of the group of cells that represent the plume source port did not always have this exact location (for the reason detailed in the previous paragraph).

Simulation	*l* (*mm*)	Location of Origin (mm)			Z_{Floor} (*mm*)	Source Dimensions (mm)	
		x	*y*	*z*		Δx	Δy
P01, P06	10.00	305.00	205.00	330.00	330.00	50.00	50.00
P01, P06	8.00	300.00	200.00	336.00	336.00	56.00	48.00
P01, P06	6.25	300.00	200.00	331.25	331.25	50.00	50.00
P01, P06	5.56	302.78	200.00	333.33	333.33	50.00	55.56
P01, P06	5.00	300.00	200.00	335.00	335.00	50.00	50.00
C01, C02, C03, C06	8.03	299.70	200.00	352.00	336.00	48.60	48.00
C04, C05, C07, C08	8.08	296.40	200.00	352.00	336.00	49.40	48.00
C04	20.00	300.00	200.00	380.00	340.00	40.00	40.00
C04	10.11	299.67	205.00	370.00	330.00	41.33	50.00
C04	6.36	299.87	200.00	342.01	335.56	51.04	50.00

Table 8-4 ***Location of the coordinate system origin and the dimensions of the flow source in the discretised representation of the P-Series and C-Series models***

The location of the coordinate system origin and the dimensions of the plume source port in the discretised representation of the P-Series and C-Series domains are listed in Table 8-4 for each grid resolution. The distances *x*, *y* and *z* shown in Table 8-4 are measured from the location of the point (XBAR0, YBAR0, ZBAR0) in the input file description of the domain[1]. As it was necessary in the C-Series simulations to specify an impermeable floor of finite thickness for the model, the parameter Z_{Floor} is also included in Table 8-4, to describe the height that the discharge port of the plume source is located above the floor level of the model.

Location of the Coordinate Origin that was specified for the Profile Program

In using the profile† program to compile the time averaged density profiles from the computational results, it was observed that it was necessary to shift the location of the profile coordinates by half a grid cell dimension in each direction. This shift is due to the way the profile program was written, rather than due to an error in the discretisation of the domain. The location of the coordinate origin that was specified in the profile program is listed in Table 8-5 for each resolution used in the P-Series and C-Series simulations.

Simulation	*l* (*mm*)	Origin Location Specified for Profile Program	
		x (mm)	z (mm)
P01, P06	10.00	310.00	335.00
P01, P06	8.00	304.00	340.00
P01, P06	6.25	303.12	334.38
P01, P06	5.56	305.56	336.11
P01, P06	5.00	302.50	337.50
C01, C02, C03, C06	8.03	303.75	356.00
C04, C05, C07, C08	8.08	300.52	356.00
C04	20.00	310.00	390.00
C04	10.11	303.06	375.00
C04	6.36	304.83	345.24

Table 8-5 ***Coordinate origin location specified in the profile program that was used to analyse the computational results.***

8.3 Results

8.3.1 Normalised Density Difference Profiles

P-Series

Plume P01 (β = 0.01) has been simulated using five different grid resolutions that have a characteristic dimension of 10.00, 8.00, 6.25, 5.56, and 5.00*mm*. These resolutions equate to the discretisation of the vertical extent of the domain into 40, 50, 64, 72 and 80 cells respectively. Figure 8-2 compares the experimental normalised density difference profiles from plume P01 with the profiles given by the simulation of this plume at the five different grid resolutions. In the comparison, the experimental profiles have been scaled, so that the fluid in the potential core region of the plume has a normalised density difference value of one; refer Section 6.3.2. The computational results presented in Figure 8-2 have been obtained by employing the Smagorinsky SGS model in the computations. Figure 8-3 shows the same comparison of profiles for plume P01 (β = 0.01), where the computations have been conducted with the constant viscosity SGS model (and the same five grid resolutions).

P06 (β = 0.02) was simulated at only one grid resolution that is described by KBAR = 80. At this resolution, the plume was simulated using both SGS models; that is, the Smagorinsky SGS model and the constant viscosity SGS model. To avoid repetition in the presentation, the comparisons of the experimental normalised density difference profiles with the computational profiles for plume P06 have been presented in Appendix 5.

---

† *The Fortran code that is the Profile program is appended as Appendix A8*

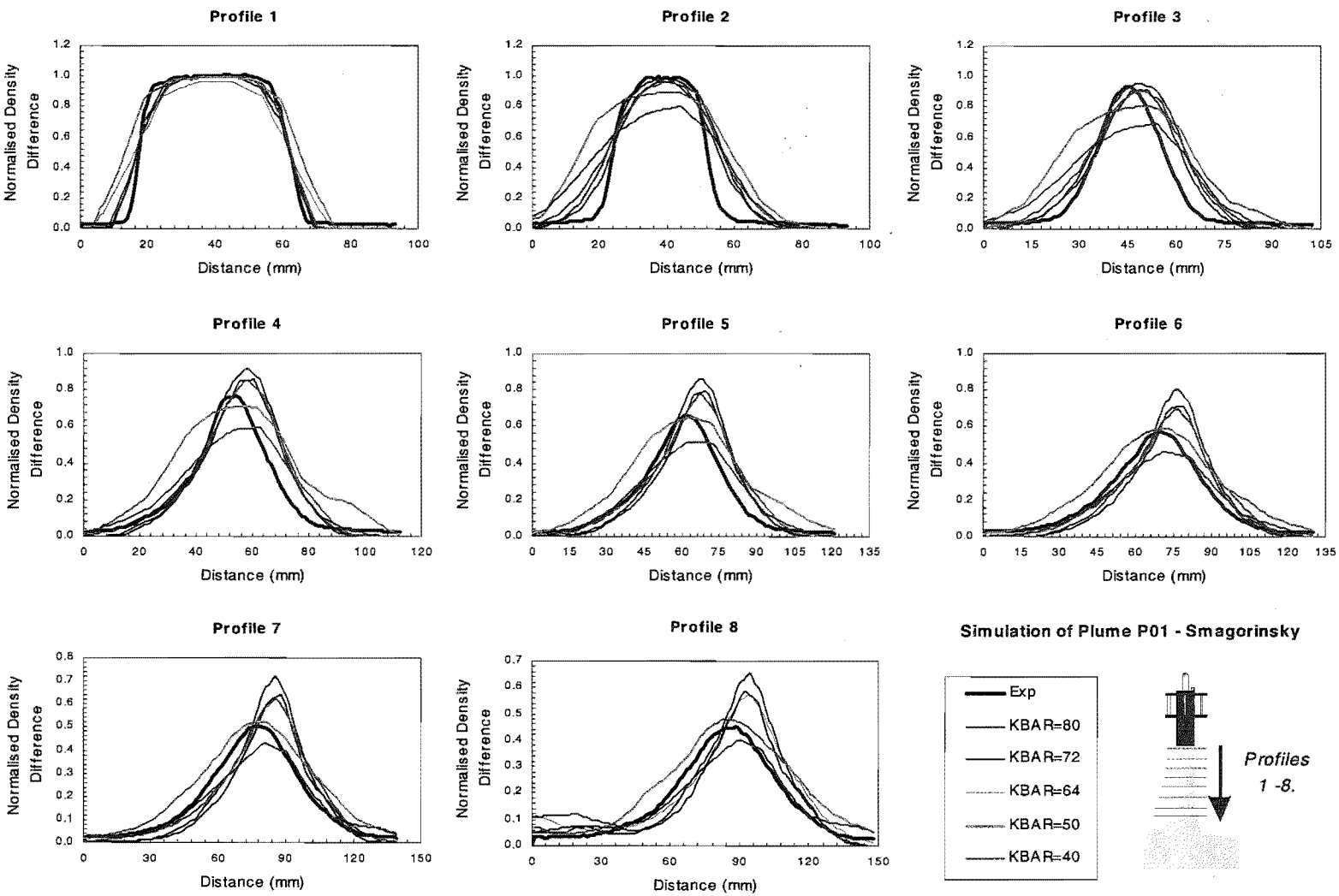

Figure 8-2 ***Comparison of experimental density profiles with computational results from the simulation of plume P01 with the Smagorinsky sub-grid scale (SGS) model at five different grid resolutions.***

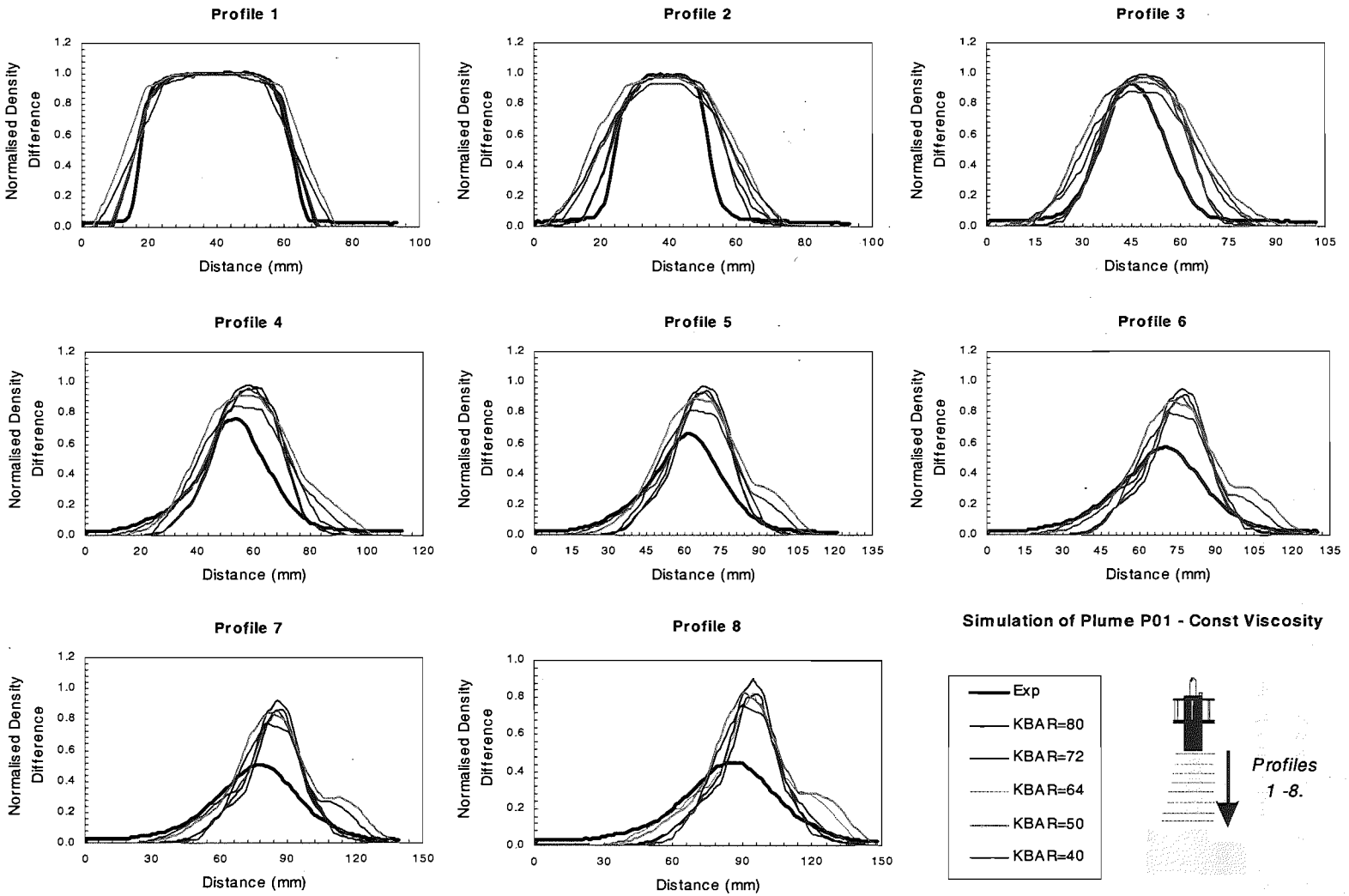

Figure 8-3 ***Comparison of experimental density profiles with computational results from the simulation of plume P01 with the constant viscosity sub-grid scale (SGS) model at five different grid resolutions.***

C-Series

The eight C-Series experiments were each simulated at one grid resolution described by KBAR = 54. At this resolution, each experiment was simulated twice, once with the Smagorinsky SGS model and once with the constant viscosity SGS model. To avoid repetition in the presentation of the results, the normalised density difference profiles from each simulation are compared to the experimental profiles in Appendix 5. Examples of how the experimental profiles compare with the computational profiles are presented in Figure 8-4 and Figure 8-5, which are discussed below.

To determine the grid dependence of the C-Series computational results experiment C04 (Doorway – Sill, β = 0.01) was simulated using four different grid resolutions that had a characteristic dimension of 20.00, 10.11, 8.08 and 6.36*mm*. These resolutions equate to the discretisation of the vertical extent of the domain into 24, 48, 54 and 64 cells respectively. Figure 8-4 compares the experimental normalised density difference profiles from experiment C04 with the profiles given by the simulation of this experiment at the four different grid resolutions. The computational results presented in Figure 8-4 have been obtained by employing the Smagorinsky SGS model in the computations. Figure 8-5 shows the same comparison of profiles for experiment C04 where the computations have been conducted with the constant viscosity SGS model (and the same four grid resolutions). Unlike the comparison of experimental and computational profiles from the T-Series and P-Series experiments, the profiles from the C-Series experiments have not been scaled, although it is expected that some degree of scaling is required; refer Section 6.4.5.

Functional Analysis

As with the T-Series simulations (refer Section 7.3.3), functional analysis has been used to quantify the comparison of the computational and experimental normalised density difference profiles for the P-Series simulations. The P-Series experimental profiles have been scaled for the analysis; refer Section 6.3.2. The functional analysis has only been conducted on the results of the finest grid resolution simulations that used the Smagorinsky SGS model and the constant viscosity SGS model. The results of the analysis are listed in Appendix 6.

Functional analysis has not been conducted on the results of the C-Series simulations. This is due to the fact that although the C-Series experimental profiles have the correct shape, they are likely to require some universal scaling, refer Section 6.4.5. Unfortunately however, the exact scale factor is undeterminable, because there is no region in the flow field where the real density difference is known, such that the experimental measurement could be corrected.

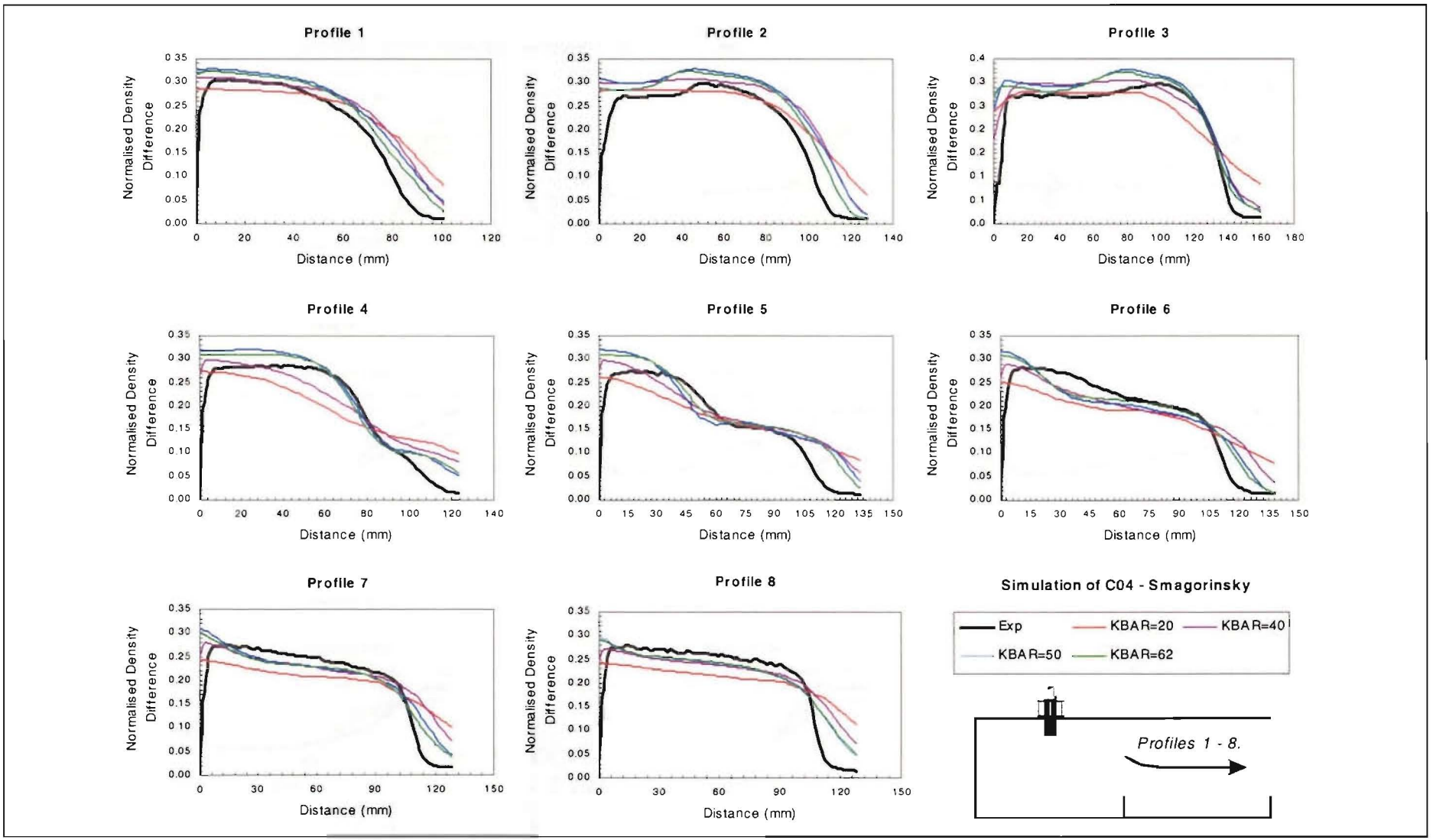

Figure 8-4 ***Comparison of experimental density profiles with computational results from the simulation of experiment C04 with the Smagorinsky sub-grid scale (SGS) model at four different grid resolutions.***

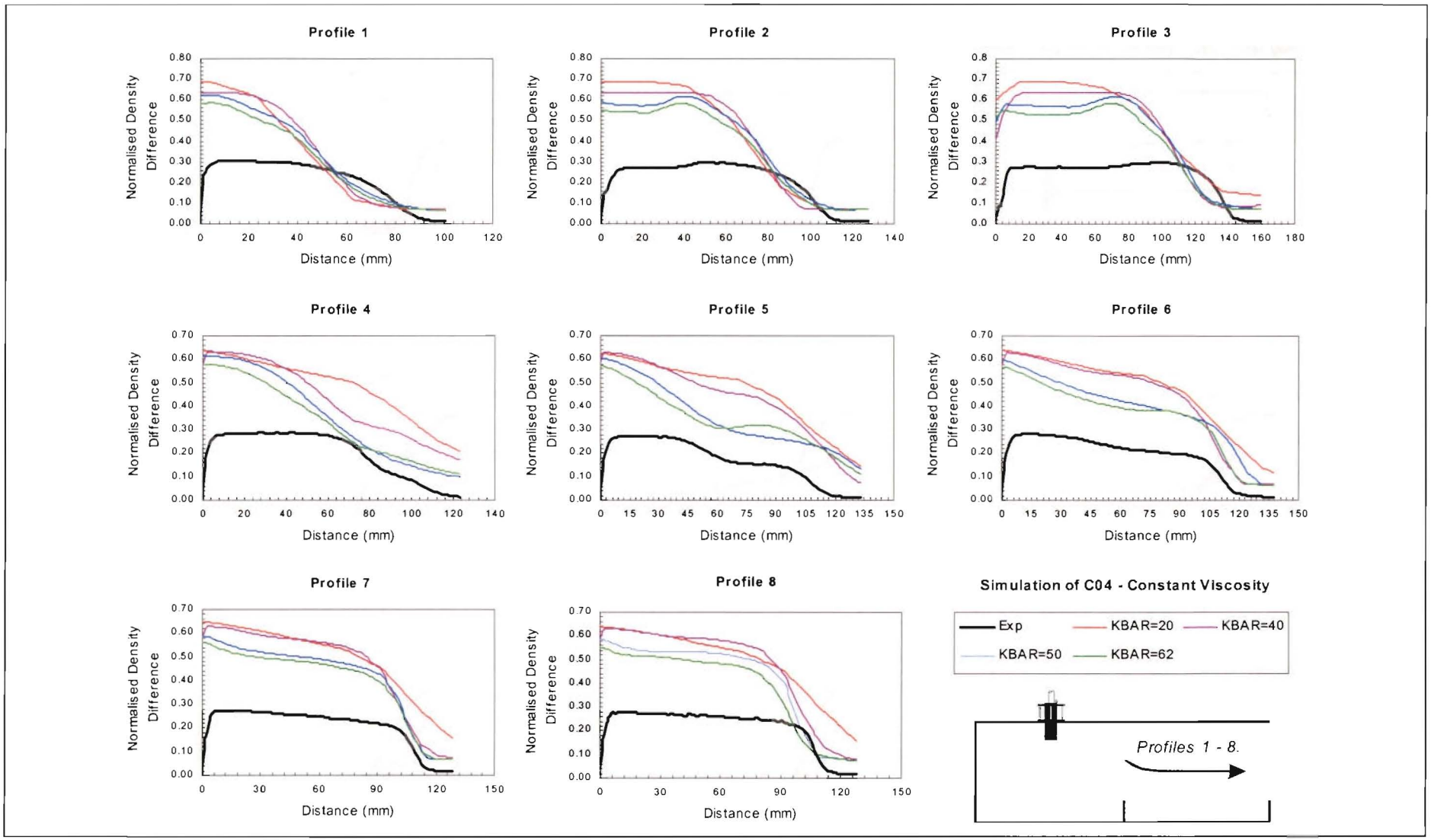

Figure 8-5 ***Comparison of experimental density profiles with computational results from the simulation of experiment C04 with the constant viscosity sub-grid scale (SGS) model at four different grid resolutions.***

Impact of Spatial Uncertainty

The uncertainty of the coordinates that describe the location of the experimental measurements within the flow field was evaluated in Section 4.3. For the P-Series and C-Series experimental measurements, the absolute uncertainty of each component in the Cartesian coordinates was determined to be as follows:

P-Series	C-Series
$\delta x = 2mm$	$\delta x = 5mm$
$\delta y = 15mm$	$\delta y = 20mm$
$\delta z = 2mm$	$\delta z = 5mm$

Figure 7-13 illustrated how the uncertainty in the location of the profile coordinates creates an uncertainty in the length and the location of the experimental profile, which is specified in Appendix 1. Section 7.3.1 then proposed a method for determining the uncertainty envelopes of the normalised density difference profiles from the spatial uncertainty of the profile coordinates. The uncertainty envelopes for the profiles, however, have not been evaluated in this research due to the time consuming nature of the proposed analysis method. Rather, to give some indication of the impact that spatial uncertainty has on the normalised density difference profiles, computational results have been used to compare density difference profiles from the centreline plane of the model geometry with profiles from the vertical planes that are offset from the centreline by the containment width of the laser sheet (that is the planes that lie a distance Δy out from the centreline). The profiles that have been collected from these planes have the x and z coordinates that are listed in Appendix 1.

For the P-Series flow field (source plume), Figure 8-6 shows the comparison of density difference profiles from the centreline plane of the model geometry with the density difference profiles from the vertical planes that are $15mm$ either side of the model centreline. This assessment has been conducted using the computational results from a simulation of plume P01 ($\beta = 0.01$)

In the C-Series experiments, four different model geometries were used, such that four different flow fields were studied. Thus, the spatial uncertainty of the C-Series normalised density difference profiles has not been estimated for each of the eight different C-Series experiments, but rather just once for each of the four different model geometries. Thus, the spatial uncertainty of the density difference profiles has been estimated for experiments C01 (sill – nothing), C03 (door – nothing), C04 (door – sill) and C05 (door – door). Figure 8-7 shows the comparison of density difference profiles from the centreline plane of the C04 model geometry (door – sill) with the density difference profiles from the vertical planes that are $20mm$ either side of the model centreline. The same comparisons, which estimate the spatial uncertainty of the density difference profiles, for experiments C01, C03 and C05 have been appended to this report as Appendix 7.

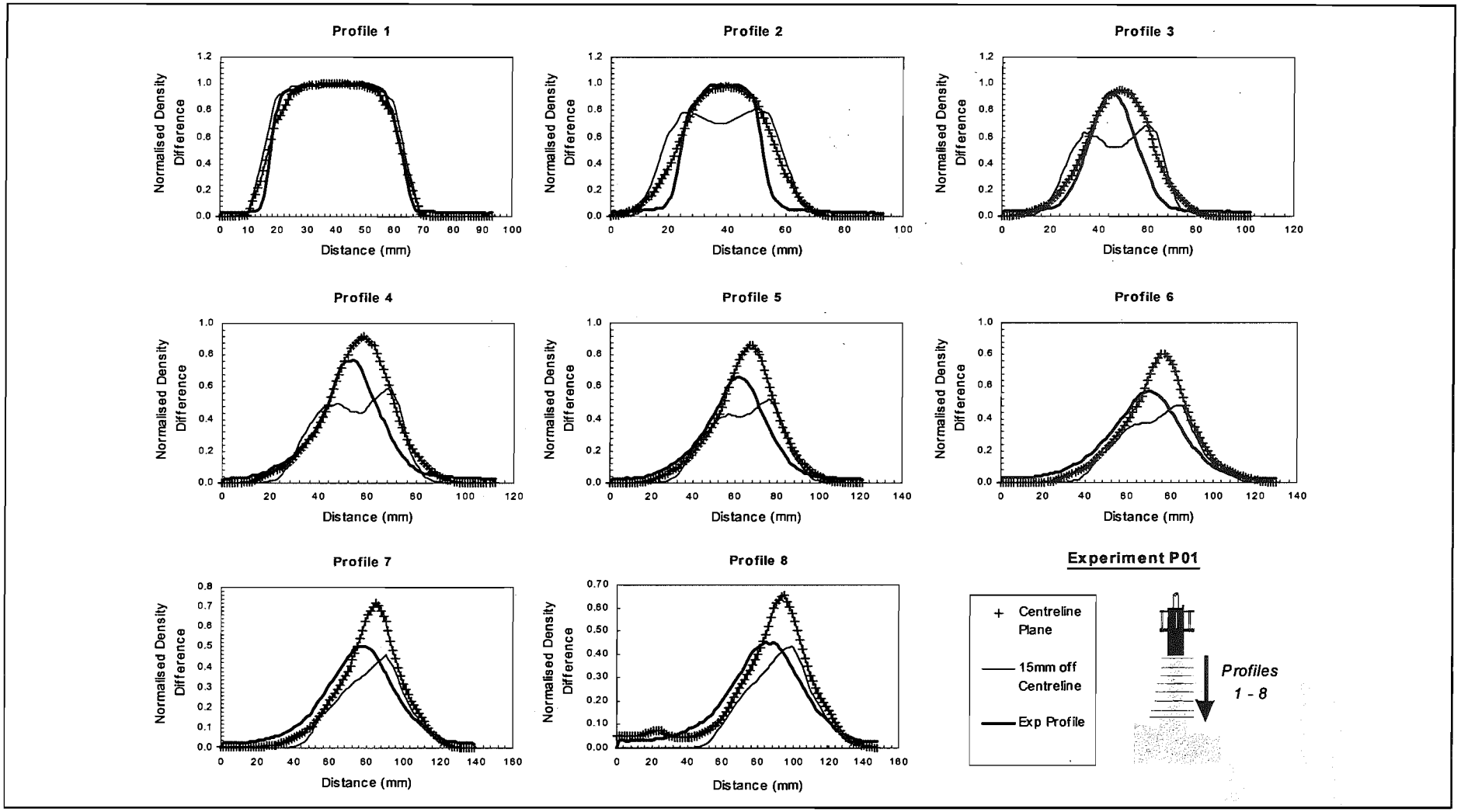

Figure 8-6 ***Comparison of the normalised density difference profiles from the centreline plane of the computations with profiles taken from the vertical planes that are located 15mm off the model centreline. This comparison provides an estimate of how the spatial uncertainty in the experimental profile coordinates affects the normalised density difference profiles of plume P01.***

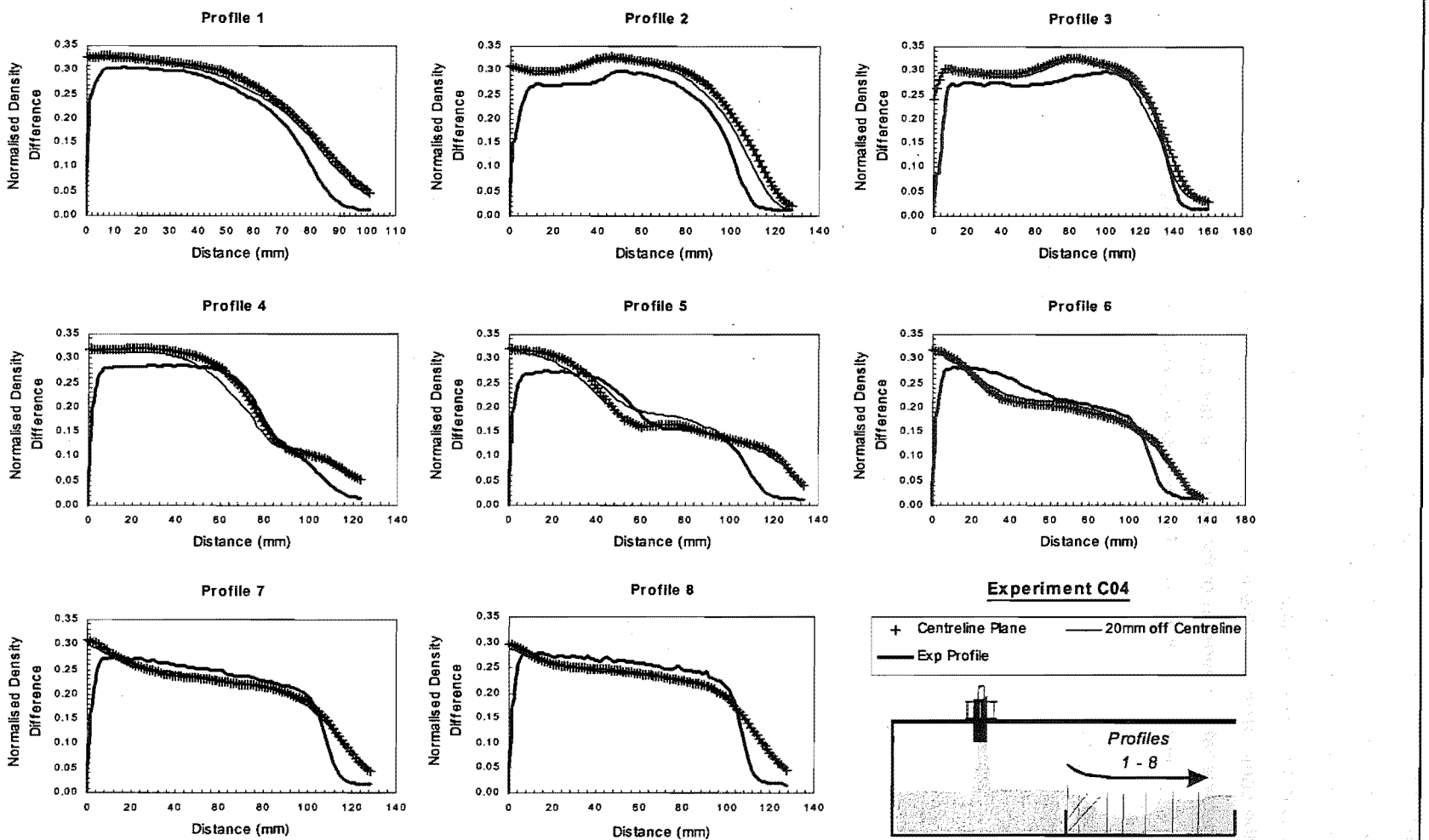

Figure 8-7 ***Comparison of the normalised density difference profiles from the centreline plane of the computations with profiles taken from the vertical planes that are located 20mm off the model centreline. This comparison provides an estimate of how the spatial uncertainty in the experimental profile coordinates affects the normalised density difference profiles of plume C04.***

8.3.2 *Temporal Development of the Flow Field*

In the P-Series simulations, plume P01 (β = 0.01) was simulated using five different grid resolutions and two different SGS models. The temporal development of the flow field from each simulation was analysed and has been detailed in Table 8-6. The first two columns of Table 8-6 give the resolution of the computations as the number of cells in the vertical dimension of the domain, and then as the characteristic dimension of the grid. The last three columns in Table 8-6 list the time intervals Δt_1, $\Delta t_{1\text{-}2}$, and $\Delta t_{2\text{-}3}$ that describe the development of the flow field in the source compartment; refer Figure 4-13. Within each column, a time interval is presented from the Smagorinsky simulation, the constant viscosity simulation, and the real experimental saline flow. The time intervals in Table 8-6 are presented as follows:

Smagorinsky / Constant Viscosity / (Experimental)

Resolution		Δt_1	$\Delta t_{1\text{-}2}$	$\Delta t_{2\text{-}3}$
KBAR (cells)	*l* (mm)	(s)	(s)	(s)
40	10.00	6 / 6 / (5)	5 / 7 / (10)	16 / 15 / (14)
50	8.00	6 / 6 / (5)	5 / 6 / (10)	17 / 15 / (14)
64	6.25	7 / 6 / (5)	3 / 4 / (10)	17 / 15 / (14)
72	5.56	6 / 6 / (5)	4 / 4 / (10)	17 / 18 / (14)
80	5.00	6 / 6 / (5)	4 / 3 / (10)	17 / 16 / (14)

Table 8-6 ***Time intervals that describe the development of the flow field in the source compartment for source plume P01 (β = 0.01).***

In all the finest resolution simulations of the P-Series and C-Series experiments, the velocity boundary condition was specified as VBC = 0.5. To assess the influence that this boundary condition has on the flow field development, simulations were conducted of plume P01 (β = 0.01) where the velocity boundary condition was varied between a full slip condition (VBC = 1) and a no slip condition (VBC = -1). These simulations employed the Smagorinsky SGS model. The dependence of the flow field development on the velocity boundary condition in these simulations is shown in Table 8-7, which lists the three time intervals Δt_1, $\Delta t_{1\text{-}2}$, and $\Delta t_{2\text{-}3}$ for each of the velocity boundary conditions VBC = -1.0, 0.0, 0.5 and 1.0.

Boundary Condition	VBC (-)	Δt_1	$\Delta t_{1\text{-}2}$	$\Delta t_{2\text{-}3}$
		(s)	(s)	(s)
Full Slip	1.0	7 (5)	3 (10)	18 (14)
Intermediate	0.5	7 (5)	3 (10)	17 (14)
Intermediate	0.0	7 (5)	4 (10)	16 (14)
No Slip	-1.0	7 (5)	6 (10)	16 (14)

Table 8-7 ***Influence of the velocity boundary condition on the time intervals that describe the development of the source compartment flow field.***

The eight different C-Series experiments were simulated using a grid resolution described by KBAR = 62. Two simulations were run of each experiment, one that used the Smagorinsky SGS model and a second that used the constant viscosity SGS model. Table 8-8 lists the time intervals that describe the development of the flow field in each simulation.

The last five columns in Table 8-8 list the time intervals Δt_1, $\Delta t_{1\text{-}2}$, $\Delta t_{2\text{-}3}$, $\Delta t_{2\text{-}4}$, and $\Delta t_{4\text{-}5}$ that describe the development of the flow field throughout the two compartments in the C-Series model; refer Figure 5-13. Within each column, a time interval is presented from the Smagorinsky simulation, the constant viscosity simulation, and the real experimental saline flow. The time intervals in Table 8-6 are presented as follows:

Smagorinsky / Constant Viscosity / (Experimental)

During experiments no measurements were taken of the flow field development in the source compartment for plume P06 (β = 0.02). Therefore, within Table 8-8, the lack of this experimental data is marked with a dash, i.e., (-).

Exp	Transit Times (s)				
	t_1	$\Delta t_{1\text{-}2}$	$\Delta t_{2\text{-}3}$	$\Delta t_{2\text{-}4}$	$\Delta t_{4\text{-}5}$
C01	6 / 6 / (5)	5 / 6 / (10)	15 / 14 / (14)	29 / 32 / (27)	-
C02	5 / 5 / (-)	3 / 4 / (-)	13 / 12 / (-)	23 / 25 / (21)	-
C03	6 / 6 / (5)	4 / 6 / (10)	17 / 14 / (14)	28 / 30 / (29)	-
C04	6 / 6 / (5)	4 / 6 / (10)	16 / 14 / (14)	28 / 32 / (27)	73 / 76 / (78)
C05	6 / 6 / (5)	4 / 6 / (10)	17 / 14 / (14)	28 / 31 / (28)	75 / 73 / (74)
C06	5 / 5 / (-)	3 / 4 / (-)	12 / 12 / (-)	23 / 24 / (22)	-
C07	5 / 5 / (-)	3 / 5 / (-)	12 / 10 / (-)	22 / 25 / (21)	56 / 59 / (61)
C08	5 / 5 / (-)	3 / 5 / (-)	13 / 11 / (-)	24 / 25 / (21)	52 / 58 / (60)

Table 8-8 ***Time intervals that describe the development of the computational and experimental flow field in the C-Series model.***

8.4 Discussion

8.4.1 General Observations of the Flow

The computational density field was compared to the experimental density field in the centreline plane of the model by viewing Smokeview[1] animations of the simulations results and then viewing the video record of the real salt water experiments. The following discussion details a number of anomalies that were observed in the comparison.

P-Series

After the plume impacted on the floor of the model, the saline flow spread out radially as a ceiling jet. From the video record of the experiments it was observed that as the saline ceiling jet spread out from the point of impact, the nose of the flow would often lift off the floor of the model and curl up to form an eddy. As this nose of the ceiling jet lifted off the floor of the model, saline fluid would flow underneath this fluid and form a new nose on the ceiling jet. The whole process would then repeat itself over again, such that in the real salt water experiments the ceiling jet lifted off the floor of the model (to curl up as an eddy structure) approximately three times, before the flow impacted on the rear wall of the source compartment.

This phenomenon was not observed in any of the finest grid resolution simulations (KBAR = 80) that were conducted with either the Smagorinsky SGS model or the constant viscosity SGS model. In these simulations, the saline fluid spread out from the plume as a layer that remained attached to the floor of the model until the flow impacted on the wall of the compartment. However, in investigating the influence on the tangential velocity boundary condition (VBC) at a cruder grid resolution (KBAR = 64), some evidence of this fluid behaviour was seen in the computational results when the velocity boundary condition was set as a no-slip condition, rather than the intermediate slip condition of VBC = 0.5. This simulation was conducted with the Smagorinsky SGS model.

This observation tends to suggest that a no-slip tangential velocity boundary condition (given by VBC=-1) is required to accurately capture the dynamics of the ceiling jet at finer grid resolutions,, rather than an intermediate slip condition, as was used (given by VBC=0.5). This would agree with the concept employed in FDS to model the influence of boundary layers on the flow near solid surfaces (refer Section 2.4.3), which contends that at finer grid resolutions it is more appropriate to push the value of the VBC parameter towards a value of -1. Since thermal detector activation within the ceiling jet flow is heavily dependent on the local fluid velocity, and previous research has already shown that the three dimensional structures in the flow can have a large influence on the convective heat transfer [2], this observation should be investigated further. If the no-slip boundary condition is required in order to accurately capture the fluid dynamics of the ceiling jet in computations, then the grid resolution will need to be refined in the regions of the flow domain adjacent to the bounding surfaces. The fine grid resolution is required next to the solid surfaces to prevent the formation of an unrealistically deep boundary layer (due to the velocity retarding influence of the boundary condition being distributed over a number of adjacent cells).

C-Series

In C-Series experiments C01, C02, C03 and C06, there was no obstruction on the end of the second compartment (i.e., the model had a completely open end). In these experiments a hydraulic jump formed downstream of where the vent flow impinged on the floor of the model. With time the hydraulic jump moved upstream in the second compartment, so that the front of the jump

sat very near the impingement point for the vent flow. In the simulations that were conducted with the constant viscosity SGS model, it was observed that the hydraulic jump was located further downstream from the vent that it was in the real salt water flows. This is believed to be due to the high fluid viscosity that was required in these computations for computational stability. Figure 8-8 is an instantaneous image from the smokeview animation of the C01 simulation, which shows the presence of the hydraulic jump structure during steady state flow. The presence of the jump can also be clearly seen in a comparison of profiles four and five from the simulation experiment C01 with a constant viscosity SGS model; see Appendix 5.

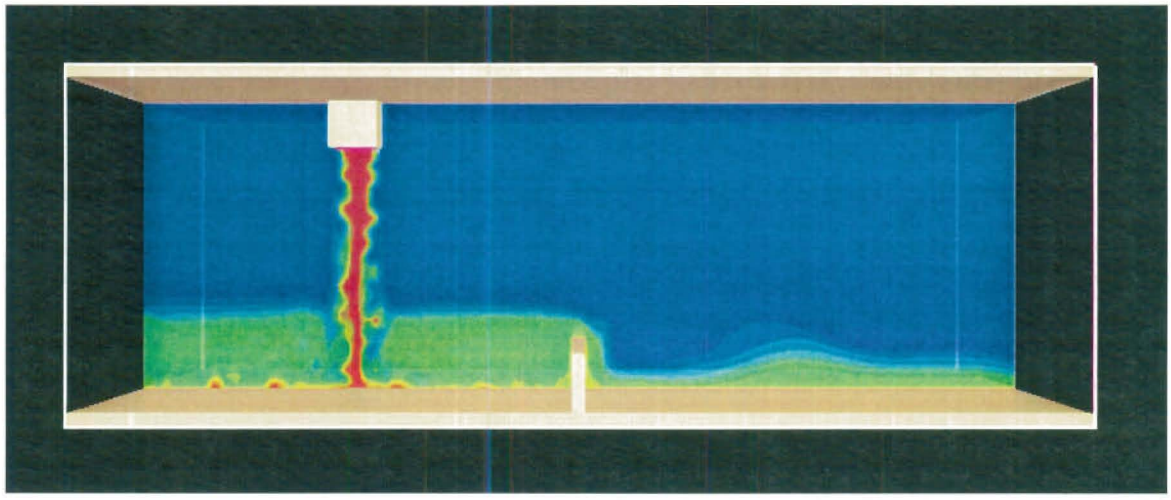

Figure 8-8 ***Instantaneous image of the computed density field in the simulation of experiment C01, showing the hydraulic jump structure that formed in the simulations where there was a free overfall on the end of the C-Series model.***

8.4.2 Interpretation of Normalised Density Difference Profiles

P-Series

The results of the spatial uncertainty analysis show that the peak density difference within the source plume is highly sensitive to the y-coordinate; refer Section 8.3.1. That is, the density decays rapidly with distance away from the centreline plane of the plume. The high dependence of the peak density difference on the accuracy of the y coordinate demonstrates the importance of having a planar laser sheet that is as thin as possible in LIF research on plumes.

In all the P-Series simulations, the comparison of the computational results with the salt water measurement of the density difference at Profile 1 was very good. This implied that the plume source was well quantified and represented in the computations. One apparent discrepancy that was noted in the comparison of computational results from different grid resolutions was that the density difference profiles from the 8*mm* resolution simulations (KBAR = 50) were constantly wider than the density difference profiles from the 10*mm* simulations (KBAR = 40); refer Figure 8-2 and Figure 8-3. This seemed counter-intuitive as generally speaking the cruder the grid resolution is, the more smeared out and diffuse the saline flows appear; hence it was expected that the 10*mm* resolution computations would give wider profiles than the 8*mm* resolution computations. The

explanation for this anomaly is that the discretised representation of the plume source in the 8*mm* simulations was longer (x-dimension) than the discretised representation of the plume source in the 10*mm* simulations. In the 8*mm* simulations, the discretised source for the flow was 56*mm* long by 48*mm* wide (7 cells by 6 cells); while in the 10*mm* simulations the source was only 50*mm* long by 50*mm* wide (5 cells by 5 cells); refer Table 8-4. This anomaly in the presentation of the results could have been avoided by non-dimensionalising the distance axis of the profiles with the dimension of the plume source. This was not done however, as it would have hidden a feature of the FDS that users of the model should be aware of (that is the distortion of domain features due to the discretised representation of the domain).

Another anomaly that was noted in Figure 8-2 and Figure 8-3 was that the profiles from the 10*mm* resolution simulations consistently had a lower peak density difference than the other computational profiles, which generally agree well at the peak density difference. All the computational profiles that are shown in Figure 8-2 and Figure 8-3 are taken from the centreline plan of the model geometry. In the discretised representation of the domain at a 10*mm* resolution (KBAR = 40) however, the centre of the plume source is offset from the centreline plane of the model by 5*mm;* refer Table 8-4. Hence, the profiles that are shown for the 10*mm* resolution simulations are actually taken from the plane that is offset from the plume source centre by 5*mm*.

In all the P-Series simulations (regardless of resolution), the agreement between the experimental profiles and the computational profiles as to the location of the peak density difference gets progressively worse with distance from the plume source. At Profile 1 (9*mm* below the discharge port), the agreement between experiment and computational results is very good. However at Profile 8 (240*mm* below the discharge port) the peak density difference in the experimental profile is significantly closer to the back wall of the source model than it is in the computational profile; refer Figure 8-2 and Figure 8-3. To illustrate this point Figure 8-9 shows a plot of the normalised density difference at different heights beneath the discharge port for both the experimental and computational flow field of plume P01 (β = 0.01). The normalised density difference profiles in Figure 8-9 show the location of the peak density difference (relative to the centreline plane of the plume source) for both the experimental and computational results. The computational profiles clearly show that there is no horizontal shift in the location of the peak density difference in the computational plume; that is, the peak density difference always occurs on the centreline axis of the plume source. In contrast however, the experimental profiles show that the peak density difference in the real salt water plume moves toward the back wall of the model as the distance below the plume source increases.

To ensure that the drift in the experimental results was not due to different rates of turbulent mixing occurring on either side of the plume, the symmetry of the experimental profiles about the peak density difference was assessed. This was accomplished by reflecting the left side of each experimental profile about the peak density difference value to create a symmetrical profile. The symmetrical profile was then compared to the real experimental profile; this comparison is shown in

Figure 8-10. The comparison of profiles in Figure 8-10 showed that the experimental profiles were very nearly symmetrical, such that there was no apparent difference in the rate of turbulent mixing on either side of the plume. This agreed with experimental observations that did not detect any extended delay in turbulent mixing on either side of the plume. Hence, the drift in the peak is reasoned to be due to drift in the plume trajectory, which was not predicted in the simulations. Like the T-Series simulations, the disagreement of the experimental plume trajectory with the computational plume trajectory, raises questions about the spatial distribution of pressure in the computational flow field; refer Section 7.4.2.

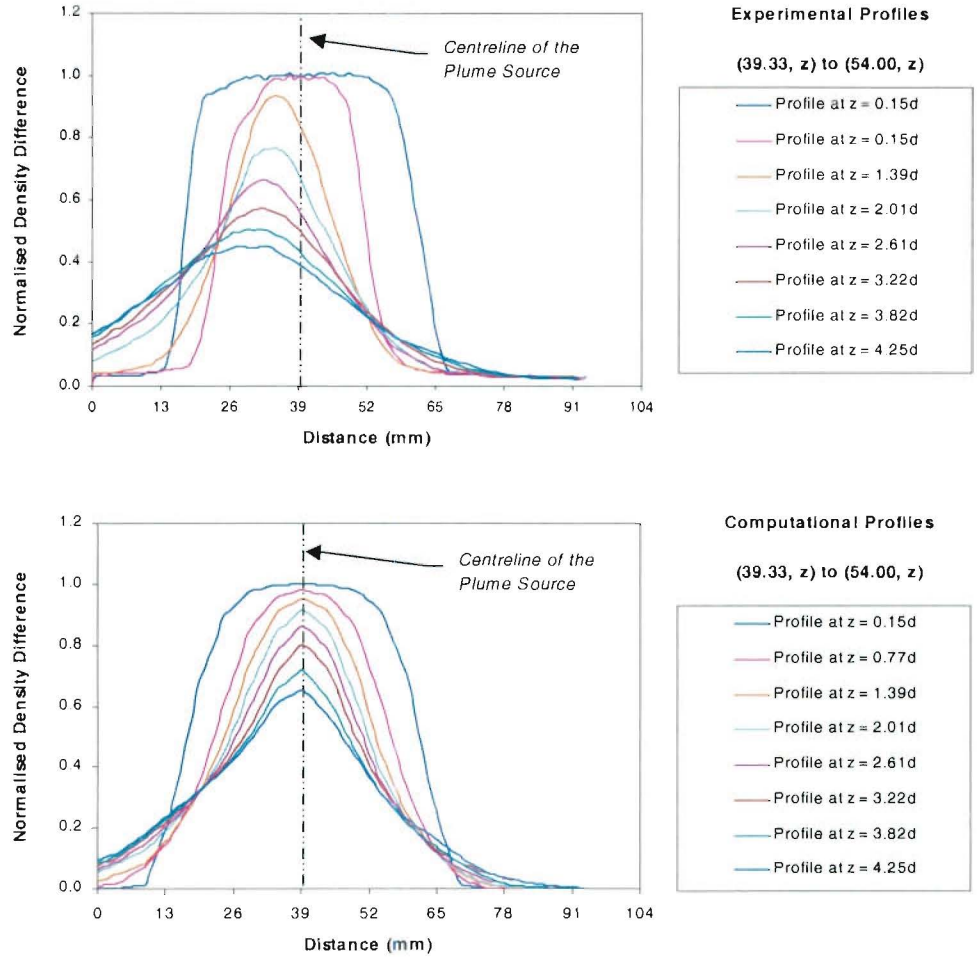

Figure 8-9 ***Density profiles across the plume P01 that show the drift in location of the peak density difference in the experimental measurements, but not in the computational results.***

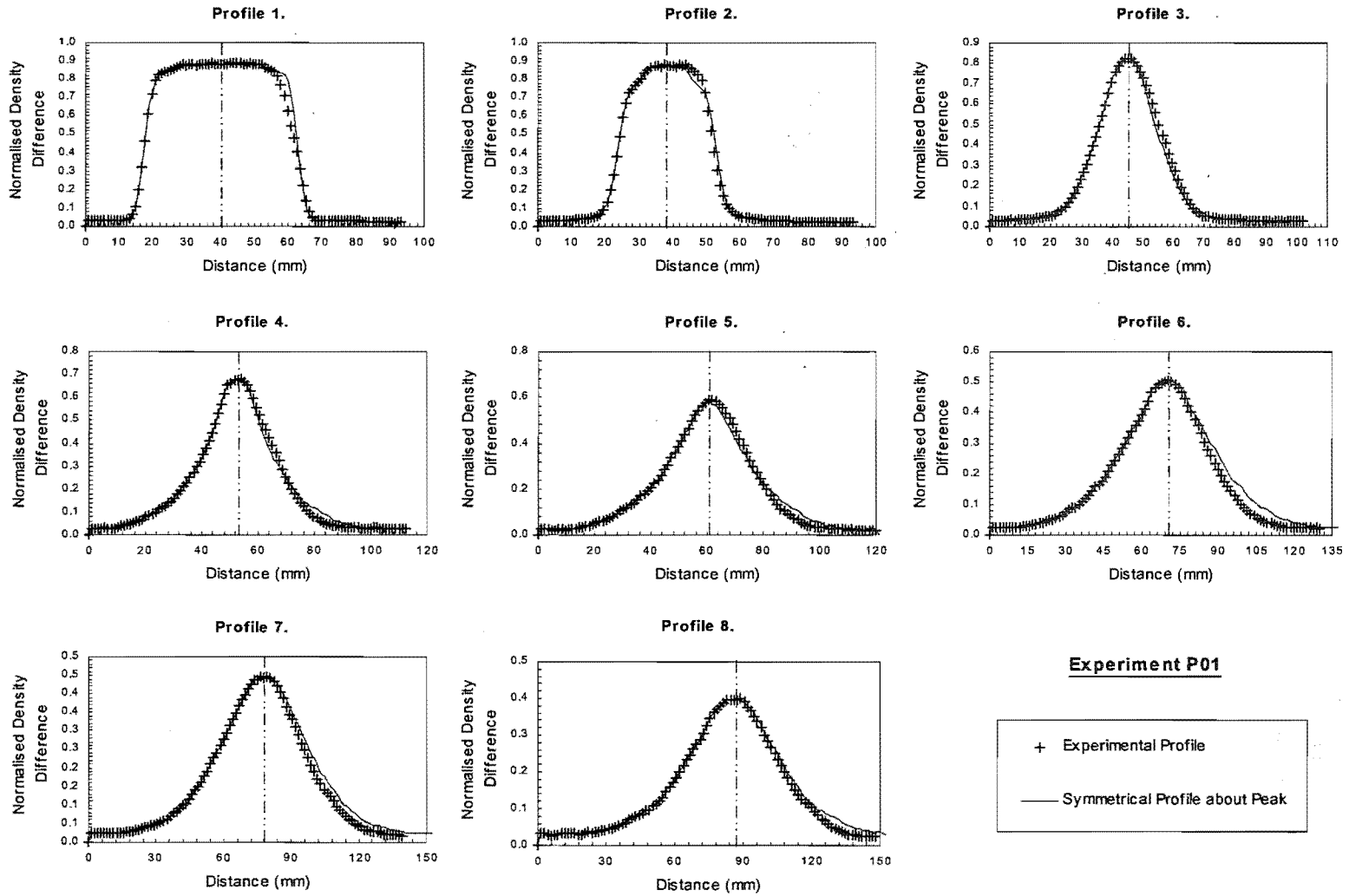

Figure 8-10 ***Comparison of experimental density profiles from plume P01 with symmetrical profiles to determine if there was differential rates of turbulent mixing across the plume.***

Figure 8-2 and Figure 8-3 compare the computational normalised density difference profiles to the experimental profiles for plume P01 (β = 0.01). These figures show that as the grid resolution is refined, the computational results converge slightly toward profiles that have a peak density difference greater than the experimental peak. It is difficult to conclude from these comparisons however if the computational model is underestimating entrainment in the plume. The spatial uncertainty analysis showed that the peak density difference in the plume is highly sensitive to the location of the laser sheet across the width of the model. Consequently, the peak density difference in the experimental profile cannot confidently be regarded as the absolute peak density difference within the real salt water plume.

The shape of the experimental normalised density difference profiles for plume P01 (refer Figure 5-10) show that the potential core region of the flow is totally consumed by the elevation of the third profile, which is 79*mm* below the discharge port. Thus, in the experimental profiles the fluid below this height has normalised density difference values that are all less than a value of one. The spatial uncertainty of the experimental results however, means that the experimental profiles could have come from a plane that was offset from the centreline plane of the plume source by as much as 15*mm*, refer Table 4-4. If this were the case, the experimental profiles would show the potential core region of the plume being consumed earlier than it really was on the centreline plane. Thus, it is possible that in the real salt water plume, there was fluid that was further than 79*mm* below the discharge port that still had a time averaged normalised density difference value of one.

In the constant viscosity simulations, the computational plume still contains fluid with a normalised density difference value of one right down to the elevation of approximately the fifth or sixth profile, which are 150-180*mm* below the discharge port. Although it is possible that within the real salt water plume the fluid had a normalised density difference value of one at heights greater than 79*mm* below the discharge port, the large difference between 79*mm* and 150*mm* still implies that the constant viscosity simulation was underestimating the mixing in the computational plume. Additionally, video footage of the experimental flows show that the real salt water plume became considerably more turbulent and well mixed than the animations of the constant viscosity simulations suggest. It would seem therefore that the constant viscosity simulations are underestimating the mixing in the source plumes. This is because of the damping effect that high fluid viscosity (required in the constant viscosity SGS model to ensure computational stability) has on turbulent motion. The consequence of this is that in the simulations that use the constant viscosity SGS model, the saline fluid that flows into the second compartment of the C-Series model has not been diluted as much as it was in reality.

C-Series

The C-Series spatial uncertainty analysis (Section 8.3.1) showed that the curvature in the laser sheet would have had very little impact on the normalised density difference profiles from the second compartment of the C-Series model; refer Figure 8-7 and Appendix 7. That is, the C-Series computational results are not highly sensitive to the uncertainty in the *y* coordinate. The region of the flow where the vent flow impinges onto the model floor, or plunges into the saline layer, is the most sensitive to uncertainty in the *y*-coordinate (see Profile 4 in Figure 8-7). This is because the saline fluid in this region is either spreading out radially as a hydraulic jump, or it is being diluted within the small region of the saline layer that surrounds the plunging vent flow; thus the density of the flow in this region is changing radially.

Simulations conducted with the Smagorinsky SGS model constantly produced better results than the simulations conducted with the constant viscosity SGS model. This is because within the constant viscosity simulations the fluid had a high viscosity, which caused the underestimation of turbulent mixing in the source plume. Thus, in the constant viscosity simulations, the saline fluid that spilt from the source compartment into the second compartment had a much higher density than the real vent flow in the experiments.

One point that did stand out in the simulation of experiments C03 and C06 (Doorway – Open End, β = 0.01 and β = 0.02 respectively) was that the computational density profiles from these simulations (regardless of SGS model), did not show evidence of the roller region that was observed in the experiments. The animations of the computational results from these simulations showed that the region beneath the vent flow was filled with fluid that had a density very close to that of the spilling saline. The experimental profiles from C03 and C06 however, clearly showed that the fluid in the recirculation region had a density that was less than the density of the vent flow; refer Section 6.4.2. What was even more surprising, however, was that the computational density profiles from simulations of experiments C04 and C07 (Doorway – Sill, β = 0.01 and β = 0.02 respectively) did show the presence of a roller region beneath the vent flow when a saline layer had formed in the second compartment. It is not known why the roller region was seen in simulations where a saline layer developed in the second compartment, and yet not seen in simulations where there was an open end on the second compartment. However, it is interesting to note that this discrepancy in the C-Series simulations occurred in a region of the flow that resembled the T-Series experimental flows. That is, a buoyant flow that is discharged horizontally from an opening. If the numerical fluid behaviour that was observed in the T-Series simulations was also occurring in the vent flow of the C-Series simulations (that is, saline fluid detaching from the main body of the vent flow, refer Section 7.4.1), this would explain why the roller region had a higher saline concentration in the simulations than it did in the real experimental flows. Further research is required to investigate this. It is possible however, that the FDS may require fine grid resolutions in regions of flow where the momentum of the fluid and the buoyancy of the fluid are acting in perpendicular directions. That is, within the turning regions of spilling flows such as spill

plumes and vent flows. The fine grid resolution may be required in these regions, to prevent the numerical methods employed in the model, creating "artificial" fluid flow that significantly affects the results.

8.4.3 Temporal Development of the Flow Field

P-Series

In general, the computational results shown in Table 8-6 imply that, over the grid resolution range described by 40 < KBAR < 80, the transit times for the saline flow in the source compartment have very little dependence on the grid resolution of the computations. The exception to this is the time interval that it takes for the ceiling jet to move from the impact point of the plume on the model floor to the rear wall of the source compartment. In simulations that use the constant viscosity SGS model, this time interval did exhibit some resolution dependence. The time dependence of the fluid movement is not surprising for this SGS model however, as the viscosity of the fluid is dependent on the grid resolution. However, what is surprising is that as the viscosity of the fluid in computations approaches the real viscosity of the fluid being simulated, the agreement between the experimental transit time and the computational transit time gets progressively worse. This is believed to be due to the selection of the velocity boundary condition. The results in Table 8-6 are all taken from simulations where the velocity boundary condition was an intermediate slip condition (VBC = 0.5). The results in Table 8-7 show that if a no slip boundary condition (VBC = -1) had been specified, the transit time for the ceiling jet would have been extended, which would agree better with experimental observations. The velocity boundary condition only appears to influence the transit time for saline flows that move along solid surfaces. The transit time for the plume to initially impact on the model floor, and the transit time for the reflected ceiling jet to travel back to the plume impingement region (on top of the saline fluid that is the ceiling jet), were relatively unaffected by the velocity boundary condition. Thus, the largest discrepancy between the computational results and the experimental measurements of transit times was in the comparison of the propagation time for the ceiling jet. It is believed that this transit time would compare more favourably at finer grid resolutions when a full slip boundary condition is specified (as there is also some indication that the smaller eddy disturbances on the nose of the ceiling jet could be resolved at finer resolutions; refer Section 8.4.1).

C-Series

The C-Series computational transit time intervals are all within 20% of the experimental results, with the exception of the transit time for the ceiling jet in the source compartment ($\Delta t_{2\text{-}3}$), which has been discussed above. The disagreement of the time interval $\Delta t_{2\text{-}3}$, and yet the relatively good agreement of the time interval $\Delta t_{4\text{-}5}$, is interesting, because a portion of the time interval $\Delta t_{4\text{-}5}$ involves the propagation of the ceiling jet along the floor of the second compartment in the C-Series model. It was hypothesized above that the disagreement in the transit time $\Delta t_{2\text{-}3}$ was primarily due to the selection of the velocity boundary condition; thus an error is also expected in the transit time $\Delta t_{4\text{-}5}$ for the same reason. However, the time interval $\Delta t_{4\text{-}5}$ involves two stages.

Firstly, the time it takes for the ceiling jet to travel the length of the second compartment, and secondly the time that it takes for the reflected wave to return to the impingement region of the vent flow. These transit times were combined in the experimental analysis because the laser sheet in the experimental LIF work was not long enough to illuminate the entire length of the C-Series model. Thus, in the video footage of the C-Series experiments it was not possible to determine when the ceiling jet in the second compartment had impacted on the sill at the end of the model. This means it is not possible to determine how the 20% relative error in the computational time interval time $\Delta t_{4\text{-}5}$ should be proportioned between the two stages of the flow. It is likely (given the disagreement of transit time $\Delta t_{2\text{-}3}$), that the transit time for the ceiling jet to travel to the end wall of the second compartment is the primary source of the error. The relative error for this transit time could still be beneath the 20% threshold because of the fact that the total time for the two flow stages is significantly larger than the time it took for the ceiling jet to propagate the length of the second compartment. Thus, it is speculated that the computational transit time interval $\Delta t_{4\text{-}5}$ would agree better with experiments if a no slip boundary condition were specified for the computations.

8.4.4 Grid Dependence

P-Series

Previous FDS research has recommended a minimum resolution for the simulation of the fire plume[3]. The recommended resolution has the characteristic dimension of one tenth of the plume structure length scale D_c given by Equation (2-9). For buoyant salt water plumes, the equivalent plume structure length scale is given by Equation (8-1).

$$D_c = \left(\frac{\dot{m}_{salt}}{\rho_\infty \sqrt{g'}} \right)^{\frac{2}{5}} \qquad \text{Equation (8-1)}$$

$$\dot{m}_{salt} = C_{salt} \times \dot{V}_s \qquad \text{Equation (8-2)}$$

Where

$\dot{m}_{salt}$ is the flow rate of salt mass (the buoyancy agent) from the plume source.

C_{salt} is the concentration of salt mass in the saline solution.

$\dot{V}_s$ is the volumetric flow rate of saline solution.

For the salt water plumes P01 (β = 0.01) and P06 (β = 0.02), the concentration of salt mass in solution is approximately 14.1*g/l* and 30.6*g/l* respectively[4]. Thus, using Equation (8-1), the recommended resolution for the simulation of the salt water plumes is of the order of 1*mm* (0.7*mm* for plume P01 and 0.9*mm* for plume P06). This resolution equates to the division of the plume source into approximately 50 cells in each direction, which is well beyond the computational abilities of the hardware available to simulate the P-Series experiments in this research. In simulating fire plumes, the plume length scale D_c should equate roughly with the plume diameter

near the base[3]. Thus in simulating the salt water plumes, if the plume source diameter d_o is used instead of the plume length scale D_c, the recommended resolution of $0.1d_o$ (5.6*mm*) can be achieved in the simulations.

Five resolutions were used in simulating the P-Series plumes; they were 10.00, 8.00, 6.25, 5.56 and 5.00*mm*. These resolutions equate to the division of the vertical extent of the domain into 40, 50, 64, 72 and 80 divisions respectively. Figure 8-2 and Figure 8-3 show the computed density difference profiles from the simulation of plume P01 ($\beta = 0.01$) at the five different grid resolutions. The profiles in Figure 8-2 and Figure 8-3 show that the time averaged density profiles are relatively insensitive to the resolution of the computational grid in the range KBAR=40 to KBAR=80. The simulations conducted with the Smagorinsky SGS model were slightly more sensitive to the grid resolution than the simulations conducted with a constant viscosity SGS model. The low sensitivity of the constant viscosity simulations to grid resolution, and the over estimation of the peak density difference, is a reflection of the inhibiting effect that the high fluid viscosity (required for computational stability) has on the turbulent mixing occurring in the plume.

C-Series

The grid dependence of the C-Series simulation was evaluated by simulating experiment C04 (Doorway – Sill, $\beta = 0.01$) at four different resolutions, which are described by KBAR = 20, 40, 50, 62. All the other C-Series experiments were only simulated using a resolution of KBAR = 50.

The highly turbulent nature of the C-Series flow meant that there were no sharp interfaces in the saline layer. The sharpest interface that was present in the flow field was the density gradient between the saline layer and the ambient freshwater. Accurately resolving the density gradient on the top of the saline layer was one of the greatest sources of disagreement between the computational results and the experimental data. Figure 8-4 and Figure 8-5 show how the computational profiles converge toward the experimental profiles as the grid resolution is refined. There is not a large amount of difference between the profiles from the two simulations where KBAR = 50 and KBAR = 62. Therefore, it remains to be seen whether finer grid resolution simulations (KBAR > 62) will converge much further toward the experimental measurement of the density gradient on the top of the saline layer. In the simulation of fire induced smoke flows, this would equate to resolving the interface between the hot layer and the cool air. In the case of the thermal flows however, radiative heating of the ambient layer would assist in smearing out the thermal interface between the flows. Still, care should be taken in considering FDS results to take into account that sharp interfaces are not resolved well with numerical methods.

Simulations that had a grid resolution equal to, or greater than, KBAR = 50 (that is 8*mm* cell size) generally seemed to resolve the flow features observed in experiments. The exception to this was the simulation of experiments C03 and C06 (Doorway – Open End, $\beta = 0.01$ and $\beta = 0.02$ respectively), where the roller region beneath the vent flow was not resolved; refer Section 8.4.2.

In general however, the shape of the time averaged density profiles from these simulations agreed well with the shape of the experimental profiles. In the grid resolution study, the simulations of experiment C04 (Doorway – Sill, β = 0.01) with resolutions of KBAR = 20 and KBAR = 40 did not produce density profiles that clearly showed the presence of the recirculation region downstream of the point where the vent flow plunged into the saline layer. Thus, it seems that simulations of similar fire flows within residential scale buildings should not be conducted with a uniform grid resolution less than KBAR = 50. It can be expected however, that the finer the grid resolution is, the more accurately the fluid structures will be resolved in the flow field.

8.4.5 SGS Model Dependence

A study of Figure 8-1 through to Figure 8-5 shows that at crude grid resolutions it is better to use the Smagorinsky SGS model rather than the constant viscosity SGS model. The constant viscosity model consistently underestimates the entrainment into the source plume due to the high viscosity of the fluid. Ultimately, this error propagates through into the second compartment, where the buoyancy of the saline layer is then overestimated. Further research is required to determine if the correct application of the constant viscosity SGS model in simulating a fire environment will cause the equivalent over prediction of the smoke layer temperature (due to the underestimation of the mass entrainment into the fire plume).

It is expected that as the grid resolution is refined the performance of the constant viscosity SGS model will improve (as the fluid viscosity in computations approaches the real viscosity of the fluid being simulated). In fact, at finer grid resolutions it is reasonable to expect that the constant viscosity SGS model will perform better than the Smagorinsky SGS model, because the fluid conditions in the constant viscosity model will better reflect reality. At these finer grid resolutions, the use of the Smagorinsky SGS model could cause artificial fluid behaviour, due to the spatial variation in the fluid viscosity. The transition (in terms of grid resolution), between when it is preferable to use the Smagorinsky SGS model, and when it is preferable to use the constant viscosity SGS model for the FDS, will need further research. If the constant viscosity SGS model does in-fact perform better at finer grid resolutions, this causes difficulties in choosing a SGS model for simulations where there is a non-uniform grid resolution. In the coarse regions of the grid, the Smagorinsky SGS model performs better, while in the fine grid regions (like, for example, adjacent to the surfaces that bound the flow) it may be desirable to use the constant viscosity SGS model. One suspects, that the grid resolution in the coarse regions of a non-uniform grid will govern the choice of the SGS model.

In using the Smagorinsky SGS model, care needs to be taken in choosing the velocity boundary condition, because in this SGS model the viscosity of the fluid is distributed according to the distribution of shear in the flow. Thus, a no-slip condition can attract high fluid viscosity to the region of the flow adjacent to the wall; on the other hand, a full slip condition could concentrate fluid viscosity away from the boundaries of the flow. These considerations may be significant if heat

transfer is being evaluated for detector activation. There is also some question as to whether LES can be successfully applied to regions of flow that are adjacent to solid boundaries[†]. This question, along with the choice of appropriate velocity boundary conditions, will require further research for the FDS, particularly as the computational abilities of hardware increase toward a level where grid resolution is no longer the critical restraint in simulations.

8.5 Conclusions

The simulation of the fire similar P-Series ("source compartment") and C-Series ("adjacent compartment") flows has been a worthwhile exercise. The research has shown that due to the highly turbulent nature of the fire similar flows, the computational results are not as highly dependent on the grid resolution as the T-Series transitional flow simulations were. Also, the P-Series and C-Series simulations have emphasised the difference in the performance of the Smagorinsky SGS model and the constant viscosity SGS model. This section details the conclusions that have been drawn from the results of the P-Series and C-Series simulations.

Care should be taken in analysing the FDS results, as the "ghost properties" method that is used to mask cells within the domain can cause the discretised representation of the domain to be slightly different from the specifications given in the input file for the simulations. The size and location of objects and vents can be changed, or shifted, by a distance equal to half the dimension of a grid cell. Thus, in describing the input file, and in considering the FDS computational results, care must be taken to think about how the domain is discretised. This is a minor point, however it is something that users of the FDS should consider when constructing a simulation.

The fire similar buoyant flows have been simulated with uniform grid resolutions that are described by the range $40 < KBAR < 80$. In these computational grids the dimension of the grid cells in each of the coordinate directions has been practically equal. Within the range of grid resolutions, the Smagorinsky SGS model has performed better than the constant viscosity SGS model. The high fluid viscosity that is required by the constant viscosity SGS model (for computational stability at coarse grid resolutions) has meant that the constant viscosity simulations under-predict the turbulent mixing in the source plume. Consequently, the peak density difference in the source plume is over estimated in the constant viscosity simulations. This error then propagates downstream into the second compartment that is attached to the source compartment, such that the buoyancy of the saline layer in this room is over estimated. As the computational grid resolution is refined, the performance of the constant viscosity simulations improves. At coarse grid resolutions of $KBAR < 80$, however, it is preferable to use the Smagorinsky SGS model. The uniform grid resolution, at which it is preferable to use the constant viscosity SGS model over the

---

[†] *This issue is often discussed under the title of "wall bounded flows" in LES literature.*

Smagorinsky SGS model in the simulation of fire similar flows, has not been determined. This is left for future research.

In the simulations of the salt water source plume, with a uniform grid resolution range described by 40 < KBAR < 80, the performance of the Smagorinsky SGS model has not been highly grid dependent. Downstream in the room that is adjacent to the source compartment however, a minimum grid resolution of KBAR = 50 is recommended to resolve the features of the buoyant flow. Thus, in simulations of fire similar flows within residential scale buildings, where the Smagorinsky SGS model is used, it is recommended that the maximum cell dimension, in any direction, should not exceed the compartment height divided by 50. Finer grid resolutions should be used wherever possible.

In the P-Series and C-Series simulations (KBAR = 50), the time intervals that describe the movement of saline fluid throughout the C-Series compartments are within 20% of the experimental values (regardless of SGS model). The only exception to this, is the transit time for the ceiling jet, which would agree better with experiments if the velocity boundary condition had been set at a no-slip condition (VBC = -1), rather than an intermediate-slip condition (VBC = 0.5). This finding means that caution is required in evaluating detector response, where the detector is distant from the smoke source, and the smoke is required to travel along solid surfaces to reach the location of detection. The relative significance of the transit time error will need to be evaluated, by comparing the transit time for smoke to reach the detection location, with the time taken for the detector to activate, given the presence of smoke.

There are indications that a grid resolution finer than KBAR = 80, and a non-slip boundary condition, are required to correctly resolve the dynamics of the ceiling jet, (which has direct impact on thermal detector activation analysis). Further work is therefore required, to investigate the impact of the velocity boundary condition, and the grid resolution, on the transit time for smoke movement along solid flat surfaces, and the modelling of convective heat transfer.

In the simulation of the P-Series salt water source plumes, the computational model does not resolve the drift that is observed in the real experimental plume. The computational results show no drift in the trajectory of the plume, such that the peak concentration in the plume always occurs on the centreline of the plume source. When this finding is considered in conjunction with the trajectory disagreements that were seen in the T-Series transitional flow simulations, it reinforces the speculation that there may be a problem with the spatial distribution of pressure within the computational flow field, for small density difference flows. Further work is therefore required to determine why the computational plume trajectories do not agree with the experimental plume trajectories.

In the simulation of some C-Series experiments, the computations over predict the density of the fluid that is contained in the roller region, which is located underneath a spilling vent flow. The spilling vent flow, in these simulations, resembles the T-Series transitional flows; that is, a buoyant fluid that is discharged horizontally. The T-Series computational flow field contained some "numerical fluid behaviour", where artificial fluid flow was created purely by the numerical methods that were employed in the FDS. If similar "numerical fluid behaviour" were occurring in the C-Series simulations, this would explain why the fluid in the roller region has a higher density than expected. Further research is therefore required, to determine if the FDS requires fine grid resolutions in regions of the flow, where the fluid buoyancy and momentum are orientated in perpendicular directions. In the simulation of fire induced smoke flows, this would mean refining the computational grid in the turning regions of vent flows and spill plumes.

8.6 References

1. McGrattan K.B. and Forney G.P. (2000) Fire Dynamics Simulator – Users manual, NISTIR 6469, national Institute of Standards and Technology, U.S. Department of Commerce, Gaithersburg, MD 20899.

2. Rehm R.G., McGrattan K.B., Baum H.R. and Cassel K.W. (1997) Transport by Gravity Currents in Building Fires, *Fire Safety Science – Proceedings of the Fifth International Symposium*, pp. 391-402.

3. Baum H.R., McGrattan K.B., and Rehm R.G. (1997) Three Dimensional Simulations of Fire Plume Dynamics, *Fire Safety Science – Proceedings of the Fifth International Symposium*, pp. 511-522.

4. *CRC Handbook of Chemistry and Physics*, 57th Edition, Ed: R.C. Weast, CRC Press, 18901 Cranwood Parkway, Cleaveland, Ohio 44128, U.S.A

5. Rehm, R.G., Baum, H.R., Lozier, D.W. and Corley, D.M. (1988) A Model of Three-Dimensional Buoyant Convection Induced by a Room Fire, *Paper Presented at the First National Fluid Dynamics Congress*, July 24-28, Cincinnati, Ohio.

6. Simcox, S., Wilkes, N.S. and Jones, I.P. (1988) 'Fire at Kings Cross Underground Stations, 18th November 1987: Numerical Simulations of the Buoyant Flow and Heat Transfer', Harwell Report AERE-G 4677, May.

Chapter 9 - CONCLUSIONS AND FUTURE RESEARCH

The research that is detailed within this document has been conducted as the first stage of a six year research program, into improving fire safety in New Zealand residential buildings. One of the objectives of the research program is to investigate the potential of smoke detectors to save lives in residential building fires. The Fire Dynamics Simulator (FDS) is to be used to investigate this problem. As preliminary work for this investigation, the research that is detailed within this document assesses the accuracy of the FDS hydrodynamic model (that is, how well the FDS models the fluid dynamics of smoke movement). As part of this work, the dependence of the computational results upon computational settings such as, grid resolution, boundary conditions and sub-grid scale model are investigated. The next stage of research, in the 6 year research program, will carry on from this work, to develop a smoke detection algorithm for the FDS. Thus, from this preliminary research, recommendations are required on how to best model residential building fires with the FDS.

In this research, a series of salt water experiments have been conducted; the experiments have then been simulated with the FDS. The accuracy of the FDS hydrodynamic model has been assessed, by comparing simulation results to the experimental measurements. Two types of buoyant salt water flows have been generated in the experiments; transitional flows, and flows that resemble fire induced smoke flow within a residential building. The simulation of the complex transitional flows, has the objective of exposing weaknesses in the FDS hydrodynamic model. The simulation of the fire similar flows, has the objective of determining the accuracy of the hydrodynamic model, when the FDS is used to model preflashover, residential building fires.

Simulations in this research have used the Fire Dynamics Simulator (FDS), Version 1.0.0.

9.1 Conclusions

9.1.1 Salt Water Experiments

The first section of the salt-water experimental program maps the time averaged density field of a natural transitional flow. The transitional flow, takes the form of a buoyant spilling saline plume. Six variations of the flow are studied, where the density and volumetric flow rate at the source are altered. Eight density difference measurements are made across each transitional flow at different locations, to map the time-averaged density field. The repeatability of the density profiles is assessed and found to be excellent. The existence of a potential core region, near the source of the spilling flow, provides a means of quantitatively correcting the profiles for any experimental measurement error.

The frequency of eddies on the perimeter of the transitional flows has also been determined. Turbulent eddies are seen to form continuously on the under side of the spilling plume, while on the upper surface of the plume, the onset of eddy formation is delayed. The degree to which the onset of eddy formation is delayed is dependent upon the source conditions of the flow. Thus, accurately predicting the natural onset of turbulent eddy formation (and consequently turbulent mixing) on the perimeter of these flows would provide a high degree of confidence in a hydrodynamic model.

In the second section of the experimental work, a series of salt water experiments are conducted that generate a buoyant flow field, which resembles the thermal flow field induced by a fire within a building. These fire similar experiments are broken into two parts, P-Series and C-Series experiments. The P-Series experiments quantify the time averaged density field of the salt water source plumes, which are used in the C-Series experiments. Eight different density difference profiles are taken across the source plume at different locations. The repeatability of the source conditions is assessed and found to be excellent. The density profiles across the plume show the gradual development toward self-similar Gaussian density distributions. The height of fall for the buoyant fluid however, is too small for the buoyant jet to fully develop into a buoyant plume. As with the transitional flow, the existence of a potential core region, adjacent to the source, provides a means for correcting the density difference profiles for experimental measurement error. Thus, the source plumes are well quantified for the C-Series experiments.

The C-Series experiments study the buoyant flow field that develops in a compartment, which is connected to another compartment containing a buoyant plume. The geometry of the opening between the two rooms is varied, as is the geometry of the opening into the ambient environment. Four different model geometries are used, with two different source plumes, to create eight different flow fields. For each experiment, the temporal development of the flow field is recorded. Density difference profiles are collected of the steady state flow in the second room. The density profiles have the correct shape, however it is expected that these profiles require some universal scaling. The degree of scaling is unknown, but it is expected to be of the order of 1.1 to 1.3. That is, the normalised density difference values are expected to be between 10% and 30% larger than the experimental measurements. In combination with the time-line record of the flow field development, the C-Series profile data still provides a good means of assessing the performance of the CFD hydrodynamic code.

In general, the salt water experimental data provides an excellent opportunity to test the hydrodynamic code of a CFD model. The natural transitional flows are particularly challenging to simulate, due to the delayed onset of turbulent mixing around the perimeter of the spilling flow. The frequencies of eddies on the perimeter of the flow will be valuable to field models that use the LES technique. For the fire similar flows, the buoyancy source (that is, the plume) is well defined, and has been well measured in experiments. The density difference profiles from the second compartment (adjacent to the source room) may require some degree of uniform scaling. The time

intervals, that describe the movement of the buoyant flow throughout the geometry of a residential building, will be valuable to field models that simulate thermal detector activation in fire scenarios.

9.1.2 Transitional Flows

In general, the simulations of the transitional flows show that the accuracy of the FDS computations is heavily grid dependent. The main reason for this is that the real salt water transitional flows contain sharp density interfaces and steep velocity gradients, which the numerical model cannot replicate well. As the grid resolution is refined, the computational model is better able to represent these sharp transitions in the properties of the flow field, and consequently, the agreement between the computational results and the experimental data improves. However, the difference in the velocity gradients and density gradients, between the computational model and the real flow, results in different fluid behaviour. This is clearly seen in the transitional flow simulations, because the momentum and the buoyancy of the spilling flow are orientated in perpendicular directions at the source. Thus, it is easy to see that the computational flow field contains fluid behaviour that was not present in the real salt-water flows. The amount, or quantity, of this "artificial" fluid behaviour (or "numerical fluid behaviour" – as it is sometimes referred to within this document) diminishes with refinement of the grid resolution. Thus, the transitional flow simulations are highly grid dependent.

Simulations of the transitional flows are conducted with a uniform grid resolution, where the spatial dimension of the grid cell is approximately equal in each direction. At the coarse grid resolutions, where the grid cell dimension is equal to the domain height divided by forty or fifty, (i.e. KBAR = 40 or 50), the agreement between the experimental measurements and the computational results is poor. At the finest resolution, described by KBAR = 100, the agreement is notably better; however, even at this resolution, the computational flow field contains fluid behaviour that does not occur in the real salt water flows. This "artificial" fluid behaviour is seen in the computed flow, because the depth of the velocity transition, across the perimeter of the spilling flow, is governed by the resolution of the grid rather than the local fluid properties and flow conditions. Thus, the shear region, which contains saline fluid that is moving slower than the main body of the plume, is larger in computational flow field than it is in reality. Since the buoyant saline fluid in the shear layer has a lower horizontal velocity, than the saline in the main plume body, this fluid descends toward the floor of the model with a steeper trajectory. Consequently, in the transitional flow simulations, saline fluid is seen to fall from the underside of the spilling plume, when this does not occur in the real salt water flows. Therefore, in the simulation of the T-Series transitional flows, a grid resolution in excess of KBAR = 100, is required in the turning region of the flow, to minimise artificial fluid behaviour that is created by the numerical methods employed in the model.

The transitional flow simulations conducted in this research, are unable to determine if the FDS hydrodynamic model can correctly compute the natural transition to turbulence, which occurs in the T-Series experimental flows. The transitional flows are difficult to compute correctly, due to the

differential mixing that occurs around the plume perimeter. The coarse grid resolutions that have been used in the T-Series simulations (40 < KBAR < 100) have an overriding affect on the fluid dynamics resolved by the computations, such that it is not possible to determine if the computations can correctly predict the delayed onset of turbulent mixing on the upper boundary of the spilling flow. Further simulations of the T-Series transitional flows are therefore required, at grid resolutions finer than KBAR = 100, to determine if the transition can be correctly computed.

The principle finding from the T-Series simulations is that, in the simulation of the transitional flows, the trajectory of the computed plume is always steeper than the trajectory of the real salt water plume. The degree of disagreement, between the computed trajectory and the real trajectory, is dependent upon the buoyancy of the spilling flow, and the initial momentum with which the buoyant fluid is discharged (horizontally) from the opening. The best agreement, between experiment and computations, is obtained for the simulation of the experiment where the fluid has the lowest buoyancy and the highest initial momentum. The converse is also true; the worst result comes from the simulation of the experiment that has the highest buoyancy and lowest initial momentum. From the results of all the T-Series simulations, there is no indication that the horizontal velocity of the spilling flow is being excessively reduced, such that the buoyancy of the flow becomes more dominant. Therefore, it is speculated, that the disagreement between the experimental trajectory and the computational trajectory, may be due to the spatial distribution of pressure in the computational flow field. Further research is required, to confirm or dismiss this speculation, and to resolve the disagreement in the plume trajectories.

In the simulation of the T-Series transitional flows, there is very little difference in the computational results, regardless of whether the Smagorinsky SGS model or the constant viscosity SGS model is used. In the process of using the constant viscosity SGS model, however, a relationship has been determined for the minimum fluid viscosity that is required for stable computations. The fluid viscosity is determined from the initial buoyancy of the fluid and the resolution of the computational grid. The relationship has not been validated for thermal gas flows, nor for liquid flows outside the density difference ratio range of $0.003 < \beta < 0.013$.

9.1.3 Fire Similar Flows

Generally speaking, in the simulation the fire similar salt water flows, the accuracy of the FDS is very good. Due to the highly turbulent nature of the flow field, the computational results are not as dependent on the grid resolution as the transitional flows were. Still, as the grid resolution is refined, the agreement between the computational results and the experimental measurements improves. Thus, based upon the research in this study, it is recommended that in simulating residential building fires with the FDS, the grid cell dimension (in any direction) should not exceed the compartment height divided by 50, (that is, $l_i < H/50$). At this resolution, the simulations conducted in this research produced time averaged density difference results that were within the

order of uncertainty of the experimental measurements. Finer grid resolutions are recommended wherever possible, particularly within the region of the fire plume, and possibly within the regions of the ceiling jet flows if detector activation is being evaluated.

Simulations of the fire similar buoyant flows also revealed, that at coarse grid resolutions, the computations that use the Smagorinsky SGS model are more accurate than the computations that use the constant viscosity SGS model. Therefore, in residential fire simulations, where the grid cell dimension is greater than the compartment height divided by 50 (i.e., KBAR < 50), the Smagorinsky SGS model should be used. The simulations that employ the constant viscosity SGS model at these coarse grid resolutions, under predict the turbulent mixing in the source plume, due to the high fluid viscosity that is required for computational stability. Consequently, at coarse grid resolutions, the constant viscosity SGS model over-predicts the buoyancy of the fluid in the source plume. This error propagates downstream from the source compartment, where it is accentuated further, due to the inhibiting effect that the high fluid viscosity has on vent flow mixing as well. Thus, in simulating residential fire, where any grid cell dimension is greater than compartment height divided by 50, the Smagorinsky SGS model should be used.

In the simulations of the fire similar flows, at a grid resolution described by KBAR = 50, the time intervals that describe the movement of saline fluid throughout the C-Series compartments are within 20% of the experimental values (regardless of SGS model). The only exception to this is the transit time for the ceiling jet; the computations predict that the ceiling jet moves across the solid boundaries of the model faster than it does in reality. The transit times for the computational ceiling jet however, would agree better with experiments if the tangential velocity boundary condition was set as a no-slip condition (VBC = -1), rather than the intermediate-slip condition (VBC = 0.5) that was used in this research, refer Section 2.4.3. This finding means that caution is required in evaluating detector response times with the FDS, where the detector is distant from the smoke source, and the smoke is required to travel along solid surfaces to reach the location of detection. The relative significance of the transit time error will need to be evaluated, by comparing the transit time for smoke to reach the detection location, with the time taken for the detector to activate, given the presence of smoke.

In the simulation of salt water source plumes, at resolutions described by 20 < KBAR < 80, the computational model does not resolve the drift that is observed in the real experimental plume. The computational results show no drift in the trajectory of the plume, such that the peak concentration occurs on the centreline axis of the plume source. When this finding is considered in conjunction with the trajectory disagreements that were seen in the T-Series transitional flow simulations, it raises questions regarding the spatial distribution of pressures within the computational flow field. Further work is therefore required to determine why the computational plume trajectories do not agree with the experimental plume trajectories.

In the simulation of some C-Series experiments, the computations over predict the density of the fluid that is contained in the roller region, which is located underneath a spilling vent flow. The spilling vent flow, in these simulations, resembles the T-Series transitional flows; that is, a buoyant fluid that is discharged horizontally. The T-Series computational flow field contained some "numerical fluid behaviour", where artificial fluid flow was created purely by the numerical methods that were employed in the FDS, refer Section 9.1.2. If similar "numerical fluid behaviour" were occurring in the C-Series simulations, this would explain why the fluid in the roller region has a higher density than expected. Further research is therefore required, to determine if the FDS requires fine grid resolutions in regions of the flow, where the fluid buoyancy and momentum are orientated in perpendicular directions. In the simulation of fire induced smoke flows, this would mean refining the computational grid in the turning regions of vent flows and spill plumes.

9.2 Future Research

Further simulations can be carried out of the salt water experiments that have been conducted in this research. To extend the transitional flow work that has been detailed in this document, simulations can be conducted of the T-Series experiments, with uniform grid resolutions that have a characteristic dimension of less than $4mm$. The results of these simulations can be directly compared to the results presented in this document. However, to utilise computational resources more sensibly in future transitional flow simulations, a non-uniform grid resolution should be used in these computations. The grid resolution, should be concentrated in the turning region of the plume (that is, close to the plane of the opening), and can be relaxed downstream in the turbulent region of the flow. To minimise the depth of the shear layer that forms on the perimeter of the spilling plume (and consequently, minimise the "numerical fluid behaviour"), the grid resolution should be compressed in the y and z directions. That is, across the width, and through the height of the plume. The objective of these simulations will be, to determine if the FDS hydrodynamic model can correctly predict the delayed onset of turbulent mixing on the upper boundary of the spilling plume. This would be an excellent measure of the hydrodynamic model performance.

Further simulations can also be conducted, of the P-Series and C-Series fire similar flows. Again, finer, uniform grid resolution simulations can be conducted of these experiments, to extend the results that have been presented in this research. However, it seems that efforts may be better focussed in future work, in determining how a non-uniform grid resolution, should be distributed throughout the two compartments of the C-Series model. Previous research has already suggested a minimum grid resolution for the simulation of the fire plume. It seems likely however, that a refined grid resolution is also required along the ceiling of the compartments, to accurately capture the spread, and the fluid dynamics of the ceiling jet. There is also some indication, in this research, that the grid resolution may need to be refined in the turning region of the vent flow. Thus, further simulations can be conducted of the P-Series and C-Series salt water experiments, to investigate, which regions of the flow require fine grid resolution in the FDS. This work should be

accompanied by a description of why the fine resolution is required in each area, (i.e., resolution should be concentrated near the ceiling to accurately model thermal detector activation). Thus, compromises, in how the grid resolution should be distributed in simulations, can be correctly decided in the context of the issue that is being evaluated. Further research is also required (in the simulation of fire similar flows), to document the performance of the SGS models as a function of grid resolution. In particular, it seems desirable to determine the grid resolution conditions, in which it is preferable, to use one SGS model above another.

The simulation of the salt water experiments from this research has provided a degree of verification for the hydrodynamic model in the FDS. However, the range over which this verification work is valid, is limited to the simulation of adiabatic, boussinesq flows. Thus further verification work is required for non-boussinesq flows that involve heat transfer. Therefore, the following experiments and simulations are suggested, for the next stage of the FDS verification.

In simulating fire induced smoke flows within compartments, the FDS has the facility to approximate thermal detector activation times. The activation time is dependent upon the characteristics of the detection device, the local properties of the flow field, and the convective heat transfer model in the FDS. Further salt water experiments would be useful in verifying the computed flow field of the ceiling jet, in particular, the fluid velocities. The simulation of these experiments would be useful in providing information on, grid resolution requirements, and the corresponding selection of the velocity boundary conditions, for ceiling jet flows. It is suggested that useful data could be obtained from experiments, where a salt water plume is discharged onto a flat, or inclined plate. Experimental measurements of the velocities in the ceiling jet should be measured, at different heights above the surface of the plate, and at different radial distances from the axis of the plume. Fluid velocities could be measured using a hot wire anemometer. Time averaged profiles of the fluid velocities in the ceiling jet (including the boundary layer), could then be plotted as a function of distance from the plume axis. A time dependent record of the fluid velocities at a point might also be useful, if the FDS can resolve intermittent structures in the ceiling jet.

Another possible avenue for future FDS verification work, is to simulate unidirectional flow pass a cylinder, which is similar to the ceiling jet flow around the frangible bulb within a sprinkler head. A large amount of research has been done in the fluid mechanics field, on unidirectional flow past a cylinder, and the frequency with which eddies are generated in the wake of the flow. If it were possible to describe the FDS computational domain in cylindrical coordinates, such that a solid cylinder could be described into the model, the eddy frequency from the computational results could be compared to experimental data. The frequency of eddies, as a function of the Reynolds number, could then be used to measure the accuracy of the hydrodynamic model in these simulations.

APPENDICES

Appendix 1 Profile Coordinates

T-Series Profile Coordinates

		X_{Start}	Z_{Start}	X_{Finish}	Z_{Finish}
T01	Profile 1	2.53	9.36	3.40	-63.36
	Profile 2	6.78	11.63	34.56	-46.80
	Profile 3	20.15	26.77	67.09	-21.87
	Profile 4	27.72	51.03	106.67	15.97
	Profile 5	40.10	91.26	141.24	60.74
	Profile 6	41.78	131.54	172.98	108.64
	Profile 7	0.46	184.02	226.14	175.69
	Profile 8	0.49	241.10	257.86	241.38

		X_{Start}	Z_{Start}	X_{Finish}	Z_{Finish}
T02	Profile 1	5.03	10.27	6.04	-59.42
	Profile 2	10.67	13.30	35.59	-39.07
	Profile 3	20.46	25.42	75.64	-0.48
	Profile 4	30.00	55.04	96.68	26.84
	Profile 5	36.71	84.69	129.05	66.39
	Profile 6	34.04	122.76	156.41	133.69
	Profile 7	1.09	183.71	187.26	176.45
	Profile 8	0.27	240.23	241.28	241.06

		X_{Start}	Z_{Start}	X_{Finish}	Z_{Finish}
T03	Profile 1	3.33	9.21	4.59	-47.36
	Profile 2	5.35	14.50	24.12	-30.83
	Profile 3	15.72	28.88	58.28	3.86
	Profile 4	22.34	52.38	82.13	25.05
	Profile 5	26.14	75.18	105.88	55.42
	Profile 6	20.85	121.68	136.54	107.28
	Profile 7	2.51	174.47	179.49	168.69
	Profile 8	0.52	232.15	186.52	232.73

		X_{Start}	Z_{Start}	X_{Finish}	Z_{Finish}
T04	Profile 1	4.31	7.93	6.05	-96.32
	Profile 2	10.68	10.18	50.48	-71.61
	Profile 3	28.30	23.03	86.47	-47.56
	Profile 4	35.75	48.05	129.60	-15.89
	Profile 5	50.28	77.65	198.44	34.83
	Profile 6	68.05	131.70	253.56	119.41
	Profile 7	0.15	170.60	261.70	166.10
	Profile 8	0.51	234.03	292.06	234.46

		X_{Start}	Z_{Start}	X_{Finish}	Z_{Finish}
T05	Profile 1	4.84	8.88	6.54	-80.65
	Profile 2	11.11	14.92	54.23	-53.70
	Profile 3	18.04	24.74	80.92	-36.43
	Profile 4	25.47	45.93	118.10	-3.28
	Profile 5	29.18	77.04	152.40	43.65
	Profile 6	38.99	127.28	193.88	103.01
	Profile 7	0.06	184.54	225.48	169.61
	Profile 8	0.57	232.88	245.03	233.52

		X_{Start}	Z_{Start}	X_{Finish}	Z_{Finish}
T06	Profile 1	3.42	9.99	4.83	-66.81
	Profile 2	9.61	19.04	47.45	-42.14
	Profile 3	18.50	35.66	83.18	-18.09
	Profile 4	28.51	69.74	129.35	31.06
	Profile 5	37.80	106.18	159.26	86.60
	Profile 6	34.21	149.54	187.32	131.71
	Profile 7	0.57	202.76	219.60	196.25
	Profile 8	0.57	241.74	248.65	243.40

		X_{Start}	Z_{Start}	X_{Finish}	Z_{Finish}
T07	Profile 1	4.88	10.00	6.30	-59.21
	Profile 2	10.63	13.08	35.74	-39.20
	Profile 3	20.63	25.38	75.85	-0.71
	Profile 4	29.72	55.37	96.55	26.99
	Profile 5	36.65	84.58	129.42	66.25
	Profile 6	34.09	122.98	156.42	113.96
	Profile 7	0.97	183.56	187.59	176.28
	Profile 8	0.40	240.32	241.20	240.95

		X_{Start}	Z_{Start}	X_{Finish}	Z_{Finish}
T08	Profile 1	4.96	10.29	5.95	-59.49
	Profile 2	10.68	13.35	35.89	-38.76
	Profile 3	20.58	25.60	75.70	-0.49
	Profile 4	30.25	54.72	96.95	27.09
	Profile 5	37.04	84.62	128.87	66.20
	Profile 6	34.34	122.97	156.38	113.79
	Profile 7	1.06	183.56	187.32	176.79
	Profile 8	0.26	240.35	241.43	241.43

		X_{Start}	Z_{Start}	X_{Finish}	Z_{Finish}
T09	Profile 1	4.84	10.30	5.77	-59.13
	Profile 2	10.62	13.40	35.33	-39.01
	Profile 3	20.65	25.76	75.55	-0.38
	Profile 4	29.72	55.10	96.99	26.64
	Profile 5	36.61	84.44	129.15	66.76
	Profile 6	33.92	123.03	156.13	113.79
	Profile 7	1.07	184.07	187.25	176.23
	Profile 8	0.31	240.49	241.52	240.92

		x_{Start}	z_{Start}	x_{Finish}	z_{Finish}
T10	**Profile 1**	5.02	10.52	6.34	-59.79
	Profile 2	10.68	13.54	35.86	-38.76
	Profile 3	20.45	25.66	75.91	-0.25
	Profile 4	29.93	55.30	96.96	27.05
	Profile 5	36.57	85.03	129.40	66.62
	Profile 6	33.76	122.49	156.12	114.04
	Profile 7	1.06	183.86	187.14	176.34
	Profile 8	0.01	240.13	241.57	241.41

P-Series Profile Coordinates

		X_{Start}	Z_{Start}	X_{Finish}	Z_{Finish}
P01	**Profile 1**	-39.33	8.88	54	8.57
	Profile 2	-39.36	44.42	53.8	43.23
	Profile 3	-48.65	78.86	53.61	77.72
	Profile 4	-57.91	113.16	54.34	113.17
	Profile 5	-67.12	147.31	54.15	147.46
	Profile 6	-76.3	181.32	53.95	181.63
	Profile 7	-85.44	215.19	53.76	215.68
	Profile 8	-94.56	239.28	53.62	239.92

		X_{Start}	Z_{Start}	X_{Finish}	Z_{Finish}
P02	**Profile 1**	-39.44	9.18	54.18	8.79
	Profile 2	-39.37	43.88	54.09	43.59
	Profile 3	-48.59	78.47	53.99	78.26
	Profile 4	-57.78	112.92	53.89	112.81
	Profile 5	-66.93	147.23	53.8	147.23
	Profile 6	-76.04	181.39	53.7	181.52
	Profile 7	-85.12	215.41	53.61	215.69
	Profile 8	-94.19	239.62	53.54	240.03

		X_{Start}	Z_{Start}	X_{Finish}	Z_{Finish}
P03	**Profile 1**	-39.1	9.21	54.56	8.8
	Profile 2	-39.07	43.97	54.38	43.68
	Profile 3	-48.33	78.59	54.2	78.41
	Profile 4	-57.54	113.04	54.03	112.98
	Profile 5	-66.71	147.31	53.85	147.41
	Profile 6	-75.83	181.41	53.68	181.68
	Profile 7	-84.9	215.33	53.5	215.8
	Profile 8	-93.97	239.44	53.38	240.08

		X_{Start}	Z_{Start}	X_{Finish}	Z_{Finish}
P04	**Profile 1**	-39.19	9.19	54.39	8.7
	Profile 2	-39.14	43.88	54.26	43.49
	Profile 3	-48.39	78.46	54.14	78.16
	Profile 4	-57.59	112.91	54.02	112.71
	Profile 5	-66.76	147.21	53.9	147.12
	Profile 6	-75.89	181.36	53.77	181.42
	Profile 7	-84.98	215.37	53.65	215.59
	Profile 8	-94.07	239.57	53.57	239.92

		X_{Start}	Z_{Start}	X_{Finish}	Z_{Finish}
P05	**Profile 1**	-39.38	9.17	54.33	8.62
	Profile 2	-39.39	43.84	54.15	43.38
	Profile 3	-48.72	78.43	53.98	78.04
	Profile 4	-58.01	112.88	53.81	112.57
	Profile 5	-67.26	147.2	53.64	146.99
	Profile 6	-76.48	181.38	53.46	181.29
	Profile 7	-84.74	215.44	53.29	215.49
	Profile 8	-93.91	239.68	53.17	239.84

		x_{Start}	z_{Start}	x_{Finish}	z_{Finish}
P06	**Profile 1**	-39.7	8.83	53.92	8.96
	Profile 2	-39.54	43.63	53.91	43.87
	Profile 3	-48.67	78.36	53.9	78.66
	Profile 4	-57.77	112.94	53.89	112.32
	Profile 5	-66.82	147.38	53.87	146.85
	Profile 6	-75.84	181.67	53.86	181.25
	Profile 7	-84.82	215.8	53.85	215.53
	Profile 8	-93.83	240.1	53.84	239.93

C-Series Profile Coordinates

		X_{Start}	Z_{Start}	X_{Finish}	Z_{Finish}
C01	Profile 1	300.48	263.60	300.10	203.17
	Profile 2	300.69	298.59	330.91	216.58
	Profile 3	300.90	332.56	362.61	240.75
	Profile 4	385.85	332.64	385.74	270.72
	Profile 5	450.68	332.49	450.80	273.16
	Profile 6	550.97	332.75	551.56	252.41
	Profile 7	651.84	332.10	652.83	255.15
	Profile 8	751.55	332.33	752.85	261.55

		X_{Start}	Z_{Start}	X_{Finish}	Z_{Finish}
C02	Profile 1	300.76	264.23	300.92	203.63
	Profile 2	301.42	298.06	331.43	216.79
	Profile 3	301.60	332.70	364.60	241.93
	Profile 4	387.39	332.83	387.31	280.71
	Profile 5	452.65	332.72	452.76	263.96
	Profile 6	554.06	333.03	554.51	258.55
	Profile 7	655.15	333.34	656.01	254.03
	Profile 8	755.95	332.73	756.98	265.25

		X_{Start}	Z_{Start}	X_{Finish}	Z_{Finish}
C03	Profile 1	300.72	263.05	300.74	163.32
	Profile 2	300.71	298.27	353.26	180.97
	Profile 3	300.70	333.42	390.25	200.31
	Profile 4	422.50	332.62	422.77	257.66
	Profile 5	474.02	333.05	474.33	273.44
	Profile 6	550.52	332.77	550.95	273.14
	Profile 7	654.65	332.73	655.50	249.48
	Profile 8	749.44	332.59	750.37	260.18

		X_{Start}	Z_{Start}	X_{Finish}	Z_{Finish}
C04	Profile 1	300.80	263.11	300.89	162.22
	Profile 2	300.77	298.10	352.83	181.18
	Profile 3	300.74	333.01	390.26	200.55
	Profile 4	422.09	332.08	422.65	208.83
	Profile 5	474.02	331.55	474.84	198.23
	Profile 6	550.80	332.09	551.98	194.06
	Profile 7	654.38	331.92	655.88	203.61
	Profile 8	749.75	331.69	751.60	204.06

		X_{Start}	Z_{Start}	X_{Finish}	Z_{Finish}
C05	Profile 1	301.48	262.85	301.11	147.63
	Profile 2	300.60	298.01	362.89	160.71
	Profile 3	300.68	333.07	413.62	165.54
	Profile 4	421.76	333.33	422.23	167.41
	Profile 5	474.01	332.93	474.91	153.06
	Profile 6	551.35	332.77	552.79	158.04
	Profile 7	654.08	332.84	656.27	158.57
	Profile 8	748.66	332.84	751.37	169.19

		X_{Start}	Z_{Start}	X_{Finish}	Z_{Finish}
C06	Profile 1	301.31	262.84	301.39	137.57
	Profile 2	301.29	298.04	357.21	172.67
	Profile 3	301.27	333.16	389.84	200.28
	Profile 4	421.96	332.06	422.46	227.89
	Profile 5	474.43	331.85	474.86	268.44
	Profile 6	551.27	331.96	551.92	262.95
	Profile 7	653.66	332.40	654.84	241.27
	Profile 8	748.78	331.83	750.11	250.53

		X_{Start}	Z_{Start}	X_{Finish}	Z_{Finish}
C07	Profile 1	300.82	263.21	301.18	153.53
	Profile 2	300.71	297.83	352.99	181.40
	Profile 3	300.59	333.32	390.14	200.00
	Profile 4	423.14	332.67	423.95	195.70
	Profile 5	474.17	332.24	475.15	191.52
	Profile 6	551.25	332.98	552.50	187.54
	Profile 7	654.54	332.14	655.95	202.13
	Profile 8	749.37	332.12	751.04	202.89

		X_{Start}	Z_{Start}	X_{Finish}	Z_{Finish}
C08	Profile 1	301.29	262.77	301.44	130.83
	Profile 2	301.48	298.19	362.67	159.73
	Profile 3	300.81	332.57	407.14	173.76
	Profile 4	422.69	333.15	422.84	157.31
	Profile 5	473.64	332.49	474.31	145.65
	Profile 6	551.33	331.96	552.72	150.69
	Profile 7	654.82	331.55	657.09	158.63
	Profile 8	748.75	331.10	751.85	159.17

		X_{Start}	Z_{Start}	X_{Finish}	Z_{Finish}
C09	Profile 1	300.80	262.66	300.94	137.60
	Profile 2	300.76	298.46	357.35	173.06
	Profile 3	300.72	333.28	389.72	200.20
	Profile 4	422.31	332.78	422.86	228.19
	Profile 5	474.10	332.95	474.55	267.81
	Profile 6	551.27	333.21	551.95	262.74
	Profile 7	653.74	332.65	654.96	240.79
	Profile 8	749.27	332.97	750.61	251.01

Appendix 2 Derivatives from Uncertainty Evaluation

T-Series and P-Series Uncertainty

$$\Delta\rho^* = C_{Drift}\left[\frac{G_{Flow}-G_{B-Flow}}{G_{Cal}-G_{B-Cal}}\right]$$

Where

$$G = 5.705\times10^{-8}R^4 - 2.292\times10^{-5}R^3 + 3.984\times10^{-3}R^2 + 0.6892R$$

Such that

$$\sigma^2_{\Delta\rho^*} = \left(\frac{\partial\Delta\rho^*}{\partial G_{Flow}}\right)^2\left(0.125\left(\frac{\partial G_{Flow}}{\partial R_{Flow}}\right)^2 + 0.0025G^2_{Flow}\right) +$$
$$\left(\frac{\partial\Delta\rho^*}{\partial G_{B-Flow}}\right)^2\left(0.125\left(\frac{\partial G_{B-Flow}}{\partial R_{B-Flow}}\right)^2 + 0.0025G^2_{B-Flow}\right) +$$
$$\left(\frac{\partial\Delta\rho^*}{\partial G_{Cal}}\right)^2\left(0.125\left(\frac{\partial G_{Cal}}{\partial R_{Cal}}\right)^2 + 0.0025G^2_{Cal}\right) +$$
$$\left(\frac{\partial\Delta\rho^*}{\partial G_{B-Cal}}\right)^2\left(0.125\left(\frac{\partial G_{B-Cal}}{\partial R_{B-Cal}}\right)^2 + 0.0025G^2_{B-Cal}\right) + \left(\frac{\partial\Delta\rho^*}{\partial C_{Drift}}\right)^2\sigma^2_C$$

Where

$$\frac{\partial\Delta\rho^*}{\partial G_{Flow}} = \left[\frac{C_{Drift}}{G_{Cal}-G_{B-Cal}}\right] \qquad \frac{\partial\Delta\rho^*}{\partial G_{B-Cal}} = C_{Drift}\left[\frac{G_{Flow}-G_{B-Flow}}{(G_{Cal}-G_{B-Cal})^2}\right]$$

$$\frac{\partial\Delta\rho^*}{\partial G_{B-Flow}} = \left[\frac{-C_{Drift}}{G_{Cal}-G_{B-Cal}}\right] \qquad \frac{\partial\Delta\rho^*}{\partial C_{Drift}} = \left[\frac{G_{Flow}-G_{B-Flow}}{G_{Cal}-G_{B-Cal}}\right]$$

$$\frac{\partial\Delta\rho^*}{\partial G_{Cal}} = -C_{Drift}\left[\frac{G_{Flow}-G_{B-Flow}}{(G_{Cal}-G_{B-Cal})^2}\right]$$

$$\frac{\partial G_i}{\partial R_i} = 2.282\times10^{-7}R_i^3 - 6.876\times10^{-5}R_i^2 + 7.968\times10^{-3}R_i + 0.6892$$

C-Series Uncertainty

$$\Delta\rho^* = C_{Drift}\left[\frac{F_{Cal}}{F_o}\right]\left[\frac{G_{Flow}-G_{B-Flow}}{G_{Cal}-G_{B-Cal}}\right]$$

Where

$$G = 5.705\times10^{-8}R^4 - 2.292\times10^{-5}R^3 + 3.984\times10^{-3}R^2 + 0.6892R$$

Such that

$$\sigma^2_{\Delta\rho^*} = \left(\frac{\partial\Delta\rho^*}{\partial G_{Flow}}\right)^2\left(0.125\left(\frac{\partial G_{Flow}}{\partial R_{Flow}}\right)^2 + 0.0025G^2_{Flow}\right) +$$
$$\left(\frac{\partial\Delta\rho^*}{\partial G_{B-Flow}}\right)^2\left(0.125\left(\frac{\partial G_{B-Flow}}{\partial R_{B-Flow}}\right)^2 + 0.0025G^2_{B-Flow}\right) +$$
$$\left(\frac{\partial\Delta\rho^*}{\partial G_{Cal}}\right)^2\left(0.125\left(\frac{\partial G_{Cal}}{\partial R_{Cal}}\right)^2 + 0.0025G^2_{Cal}\right) +$$
$$\left(\frac{\partial\Delta\rho^*}{\partial G_{B-Cal}}\right)^2\left(0.125\left(\frac{\partial G_{B-Cal}}{\partial R_{B-Cal}}\right)^2 + 0.0025G^2_{B-Cal}\right) +$$
$$\left(\frac{\partial\Delta\rho^*}{\partial C_{Drift}}\right)^2\sigma^2_C + \left(\frac{\partial\Delta\rho^*}{\partial F_{Calibration}}\right)^2\sigma^2_{F_{Calibration}} + \left(\frac{\partial\Delta\rho^*}{\partial F_o}\right)^2\sigma^2_{F_o}$$

Where

$$\frac{\partial\Delta\rho^*}{\partial G_{Flow}} = C_{Drift}\left[\frac{F_{Cal}}{F_o}\right]\left[\frac{1}{G_{Cal}-G_{B-Cal}}\right]$$

$$\frac{\partial\Delta\rho^*}{\partial G_{B-Flow}} = -C_{Drift}\left[\frac{F_{Cal}}{F_o}\right]\left[\frac{1}{G_{Cal}-G_{B-Cal}}\right]$$

$$\frac{\partial\Delta\rho^*}{\partial G_{Cal}} = -C_{Drift}\left[\frac{F_{Cal}}{F_o}\right]\left[\frac{G_{Flow}-G_{B-Flow}}{(G_{Cal}-G_{B-Cal})^2}\right]$$

$$\frac{\partial\Delta\rho^*}{\partial G_{B-Cal}} = C_{Drift}\left[\frac{F_{Cal}}{F_o}\right]\left[\frac{G_{Flow}-G_{B-Flow}}{(G_{Cal}-G_{B-Cal})^2}\right]$$

$$\frac{\partial \Delta\rho^*}{\partial F_o} = -C_{Drift}\left[\frac{F_{Calibration}}{F_o^2}\right]\left[\frac{G_{Flow}-G_{B-Flow}}{G_{Cal}-G_{B-Cal}}\right]$$

$$\frac{\partial \Delta\rho^*}{\partial F_{Calibration}} = C_{Drift}\left[\frac{1}{F_o}\right]\left[\frac{G_{Flow}-G_{B-Flow}}{G_{Cal}-G_{B-Cal}}\right]$$

$$\frac{\partial \Delta\rho^*}{\partial C_{Drift}} = \left[\frac{F_{Cal}}{F_o}\right]\left[\frac{G_{Flow}-G_{B-Flow}}{G_{Cal}-G_{B-Cal}}\right]$$

$$\frac{\partial G_i}{\partial R_i} = 2.282\times10^{-7}R_i^3 - 6.876\times10^{-5}R_i^2 + 7.968\times10^{-3}R_i + 0.6892$$

Scale Factor

$$C_{Drift} = \frac{G_{AVG}}{G_{AVG} - D_{Decay}\Delta t}$$

Therefore

$$\sigma_C^2 = \left(\frac{\partial C_{Drift}}{\partial D_{Decay}}\right)^2 \sigma_D^2$$

$$\frac{\partial C_{Drift}}{\partial D_{Decay}} = \frac{\Delta t G_{AVG}}{\left(G_{AVG} - D_{Decay}\Delta t\right)^2}$$

Appendix 3 Salt Water Experimental Density Profiles

T-Series Results

Normalised Density Difference Profiles from experiment T01
Normalised Density Difference Profiles from experiment T02
Normalised Density Difference Profiles from experiment T03
Normalised Density Difference Profiles from experiment T04
Normalised Density Difference Profiles from experiment T05
Normalised Density Difference Profiles from experiment T06
Repeatability of experiment T02.

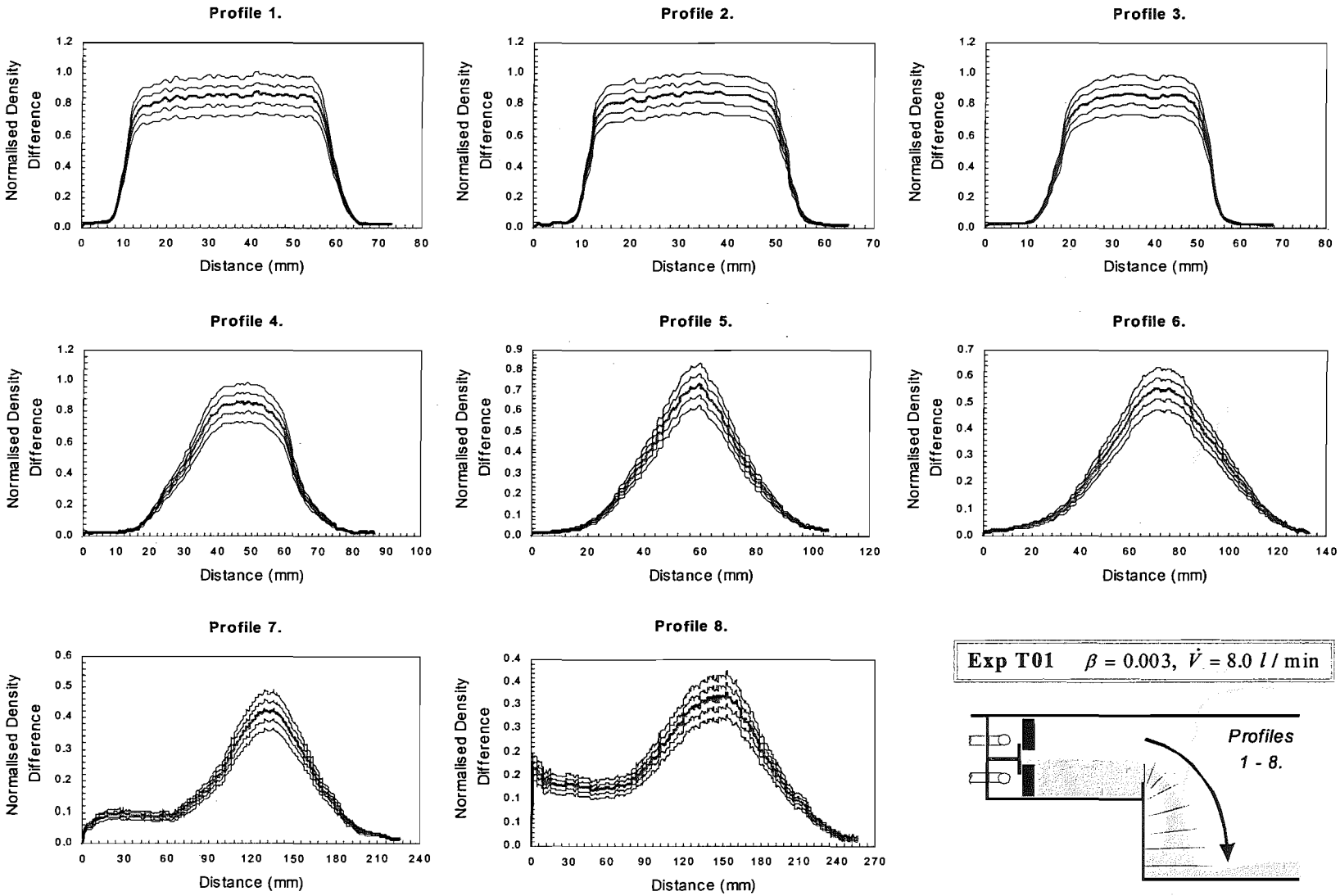
Profile 1.
Profile 2.
Profile 3.
Profile 4.
Profile 5.
Profile 6.
Profile 7.
Profile 8.
Normalised Density Difference
Distance (mm)
Exp T01 β = 0.003, $\dot{V}$ = 8.0 l / min
Profiles 1 - 8.

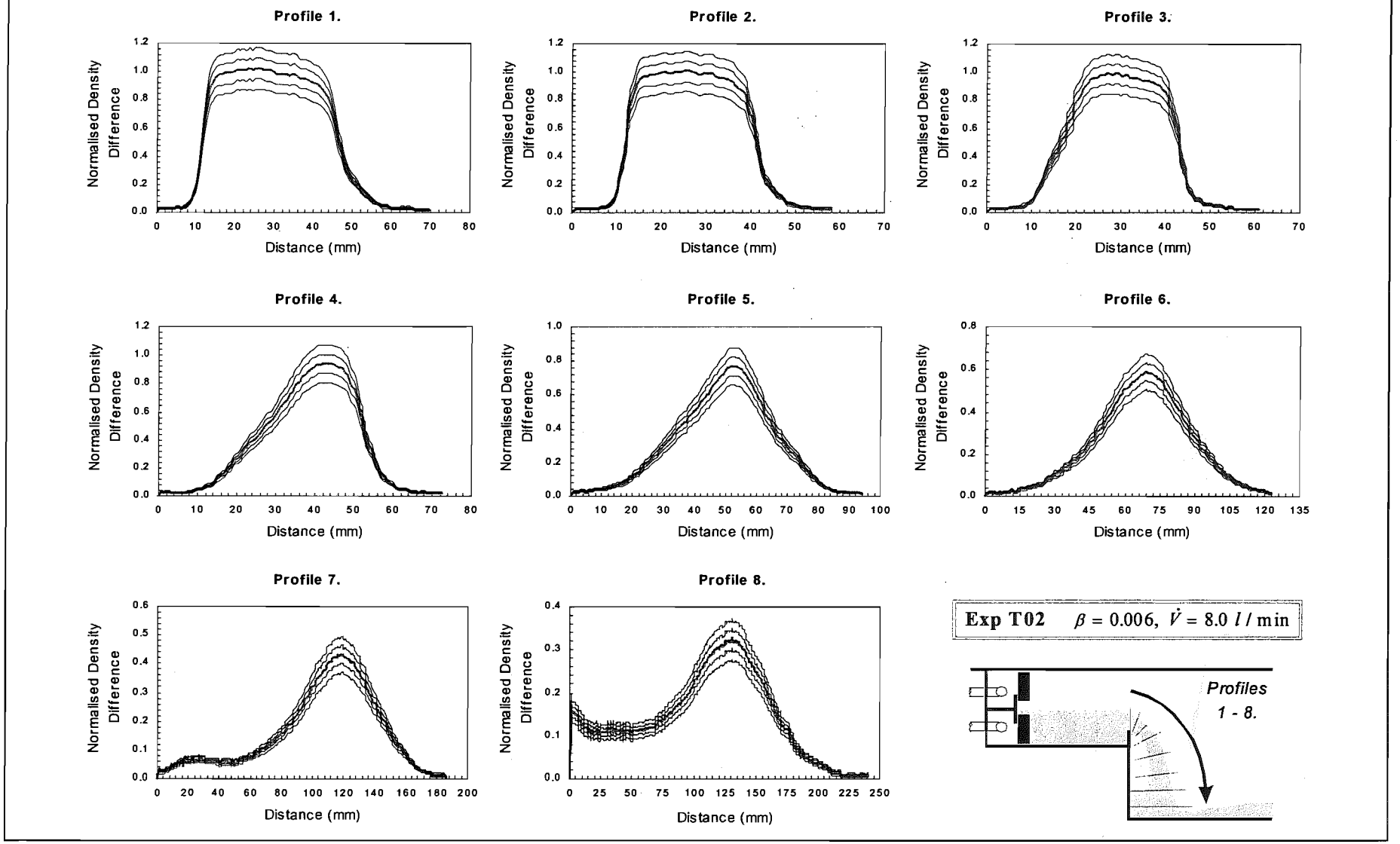
Profile 1.
Profile 2.
Profile 3.
Profile 4.
Profile 5.
Profile 6.
Profile 7.
Profile 8.
Normalised Density Difference
Distance (mm)
Exp T02 $\beta = 0.006$, $\dot{V} = 8.0\ l/\min$
Profiles 1 - 8.

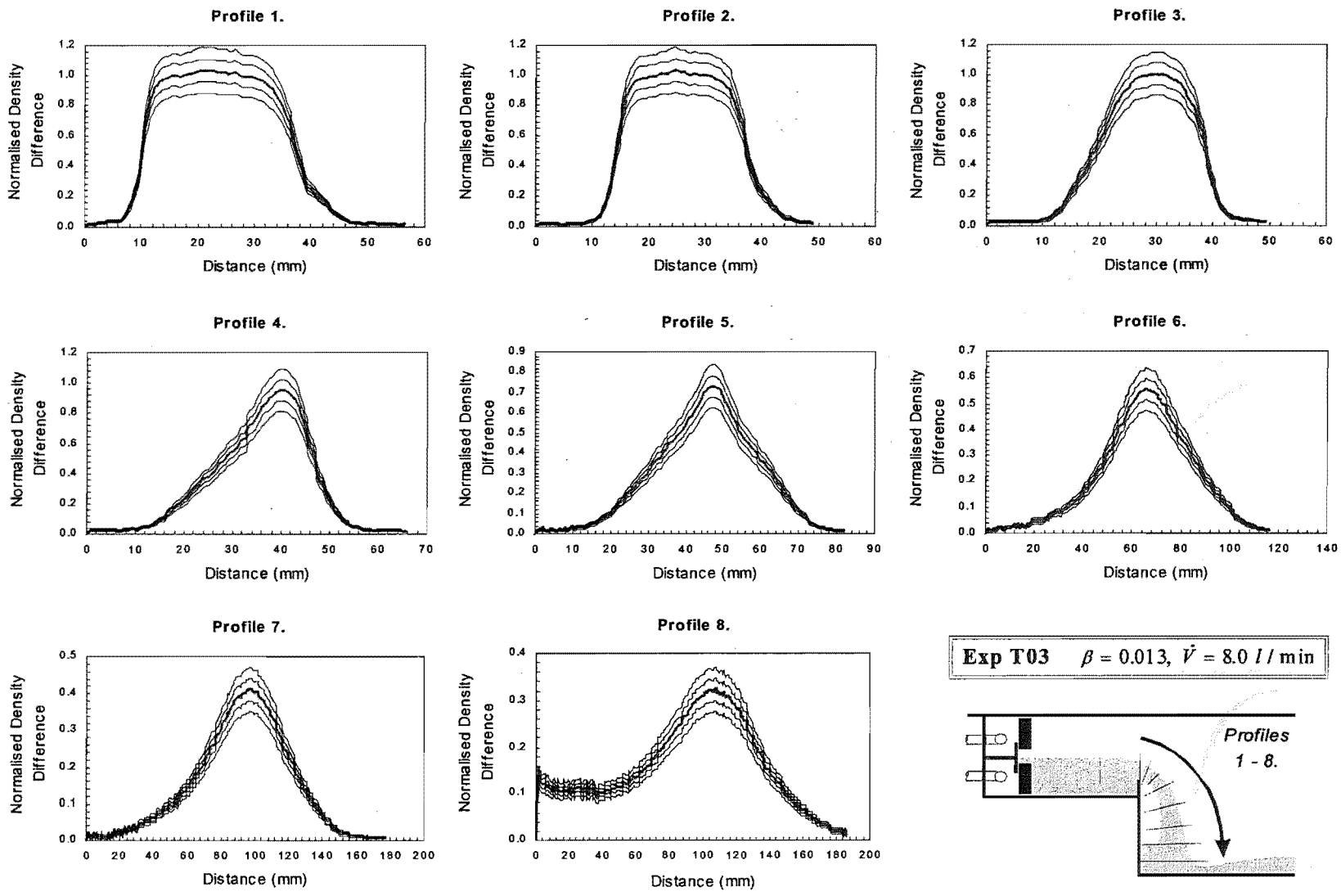
Profile 1.
Profile 2.
Profile 3.
Profile 4.
Profile 5.
Profile 6.
Profile 7.
Profile 8.
Normalised Density Difference
Distance (mm)
Exp T03 $\beta = 0.013$, $\dot{V} = 8.0$ l / min
Profiles 1 - 8.

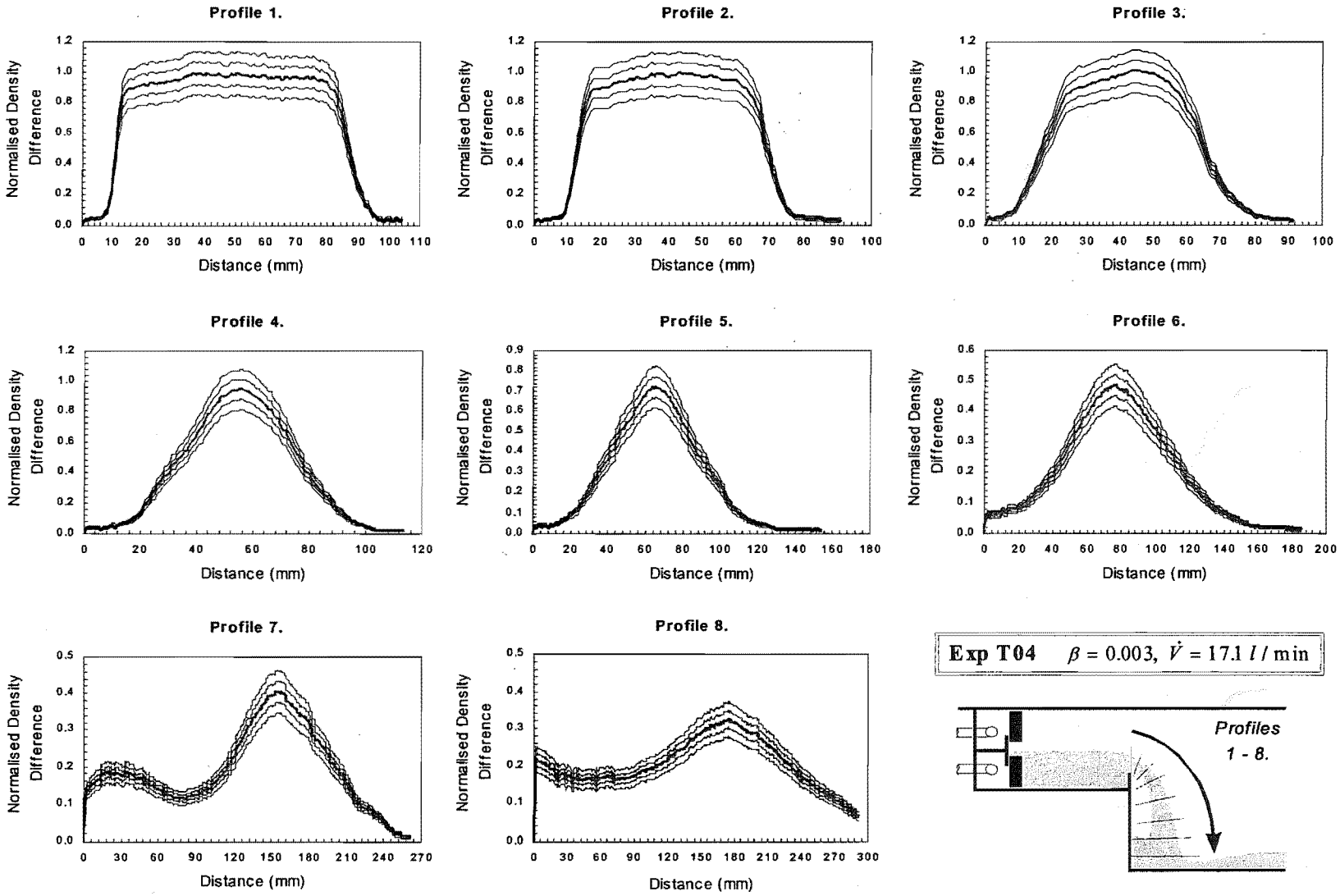
Profile 1.
Profile 2.
Profile 3.
Profile 4.
Profile 5.
Profile 6.
Profile 7.
Profile 8.
Normalised Density Difference
Distance (mm)
Exp T04 $\beta = 0.003$, $\dot{V} = 17.1\ l/\min$
Profiles 1 - 8.

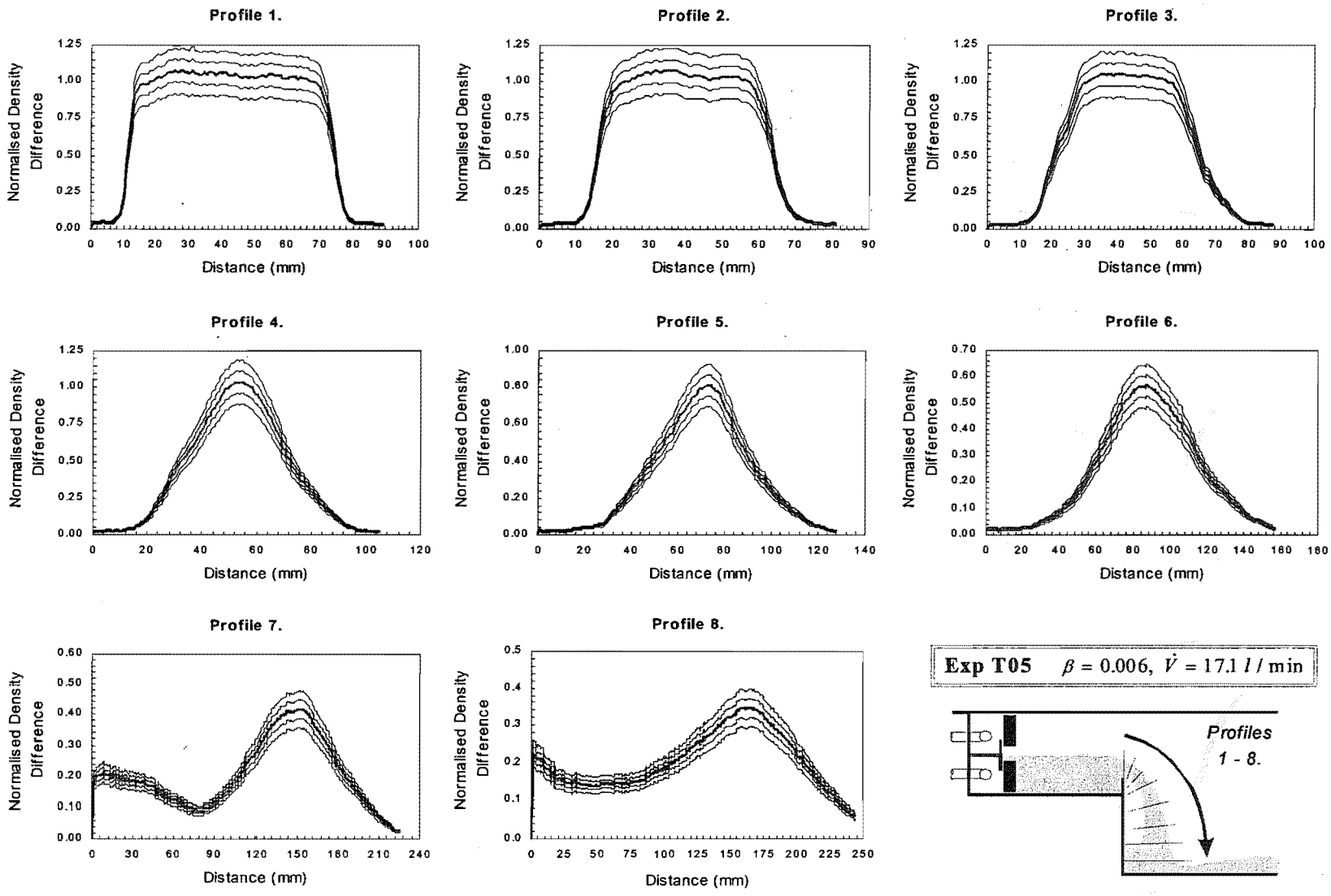
Profile 1.
Normalised Density Difference
Distance (mm)
Profile 2.
Normalised Density Difference
Distance (mm)
Profile 3.
Normalised Density Difference
Distance (mm)
Profile 4.
Normalised Density Difference
Distance (mm)
Profile 5.
Normalised Density Difference
Distance (mm)
Profile 6.
Normalised Density Difference
Distance (mm)
Profile 7.
Normalised Density Difference
Distance (mm)
Profile 8.
Normalised Density Difference
Distance (mm)
Exp T05 $\beta = 0.006$, $\dot{V} = 17.1\ l/\min$
Profiles 1 - 8.

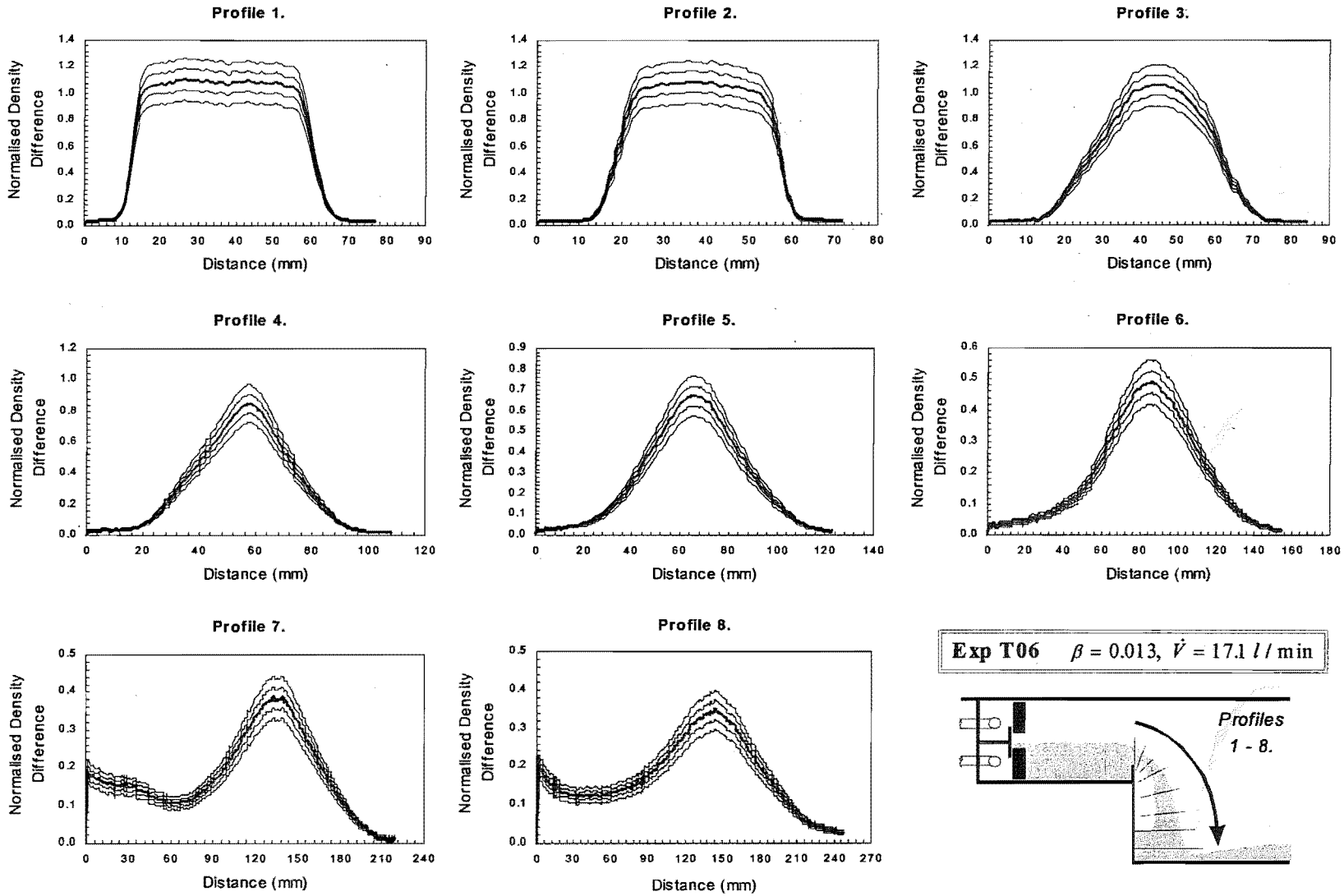
Profile 1.
Profile 2.
Profile 3.
Profile 4.
Profile 5.
Profile 6.
Profile 7.
Profile 8.
Normalised Density Difference
Distance (mm)
Exp T06 $\beta = 0.013$, $\dot{V} = 17.1\ l/\min$
Profiles 1 - 8.

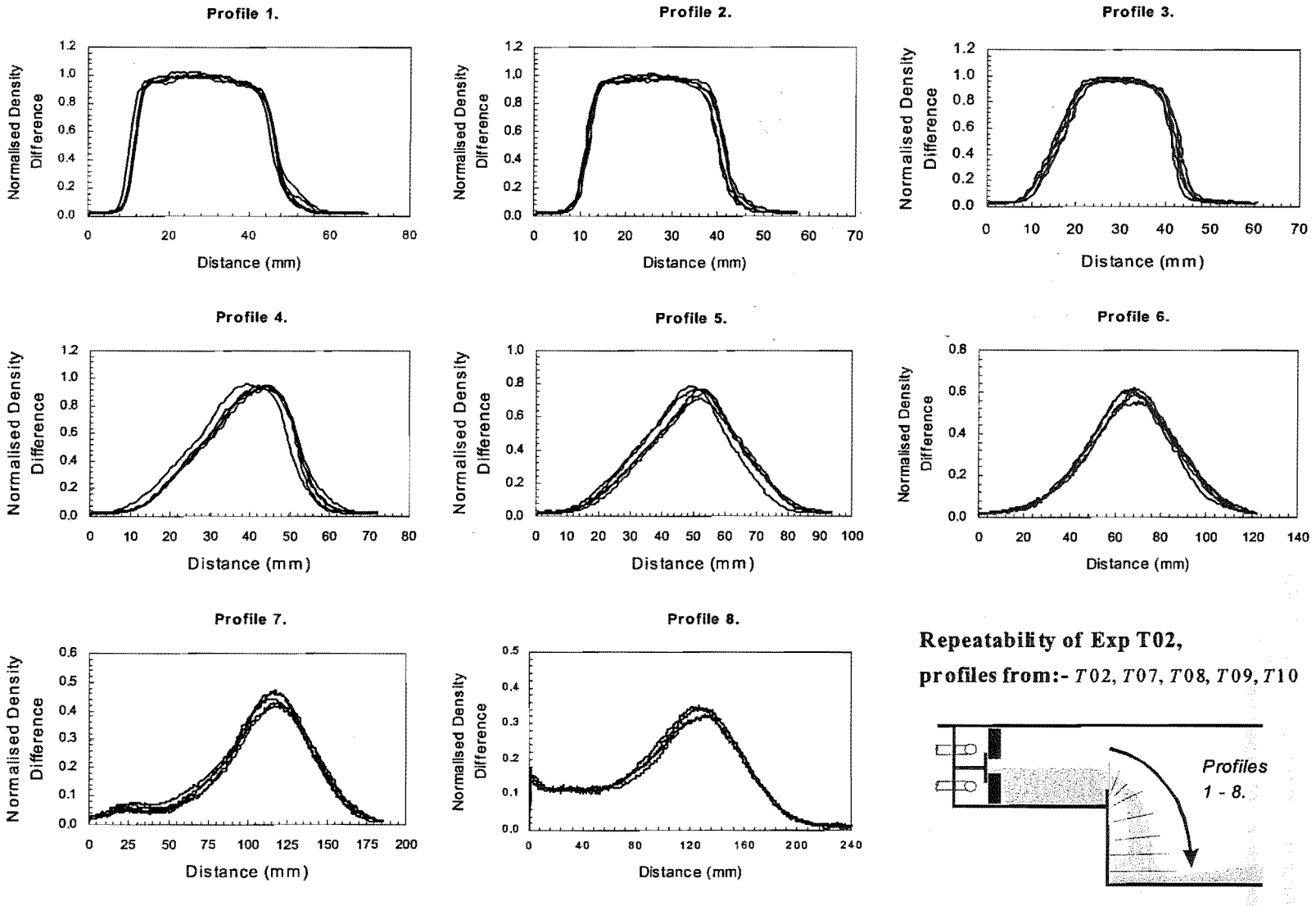
Profile 1.
Normalised Density Difference
Distance (mm)
Profile 2.
Normalised Density Difference
Distance (mm)
Profile 3.
Normalised Density Difference
Distance (mm)
Profile 4.
Normalised Density Difference
Distance (mm)
Profile 5.
Normalised Density Difference
Distance (mm)
Profile 6.
Normalised Density Difference
Distance (mm)
Profile 7.
Normalised Density Difference
Distance (mm)
Profile 8.
Normalised Density Difference
Distance (mm)
Repeatability of Exp T02,
profiles from:- T02, T07, T08, T09, T10
Profiles
1 - 8.

P-Series Simulations

Normalised Density Difference Profiles from experiment P01

Normalised Density Difference Profiles from experiment P06

Repeatability of experiment P01.

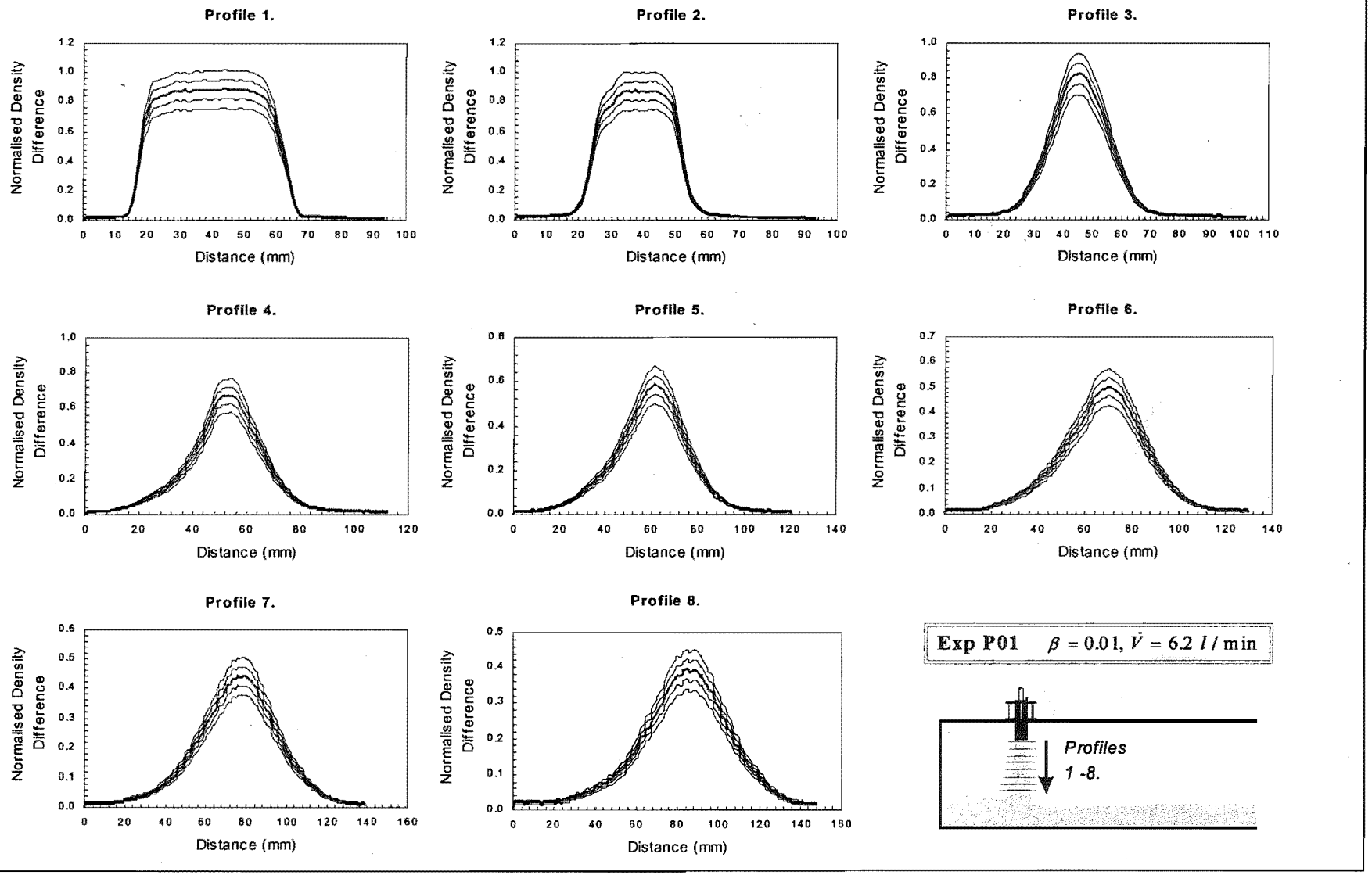
Profile 1.
Profile 2.
Profile 3.
Profile 4.
Profile 5.
Profile 6.
Profile 7.
Profile 8.
Normalised Density Difference
Distance (mm)
Exp P01 $\beta = 0.01$, $\dot{V} = 6.2\ l/\min$
Profiles
1 -8.

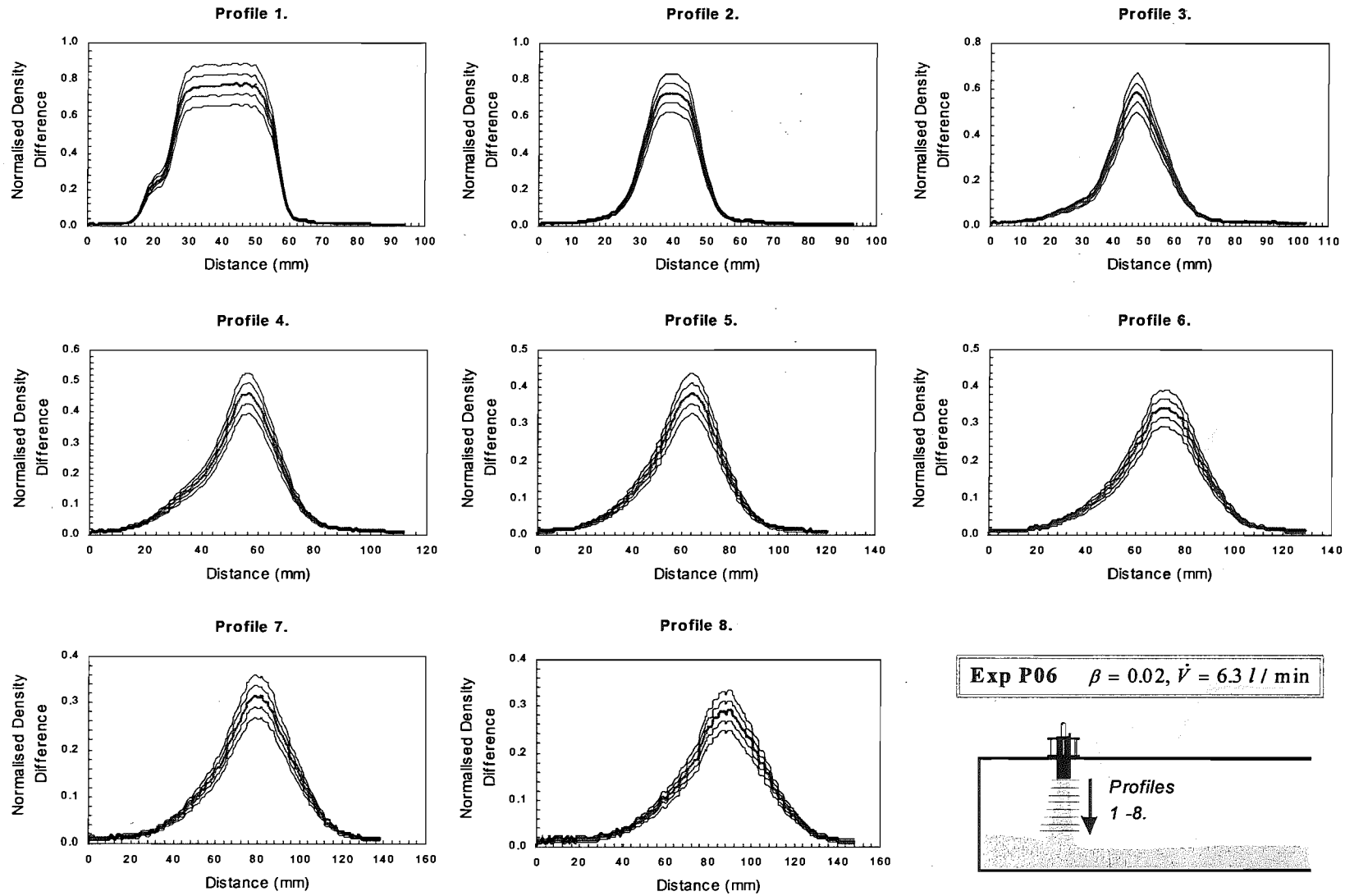
Profile 1.
Profile 2.
Profile 3.
Profile 4.
Profile 5.
Profile 6.
Profile 7.
Profile 8.
Normalised Density Difference
Distance (mm)
Exp P06 $\beta = 0.02$, $\dot{V} = 6.3\ l/\min$
Profiles 1 -8.

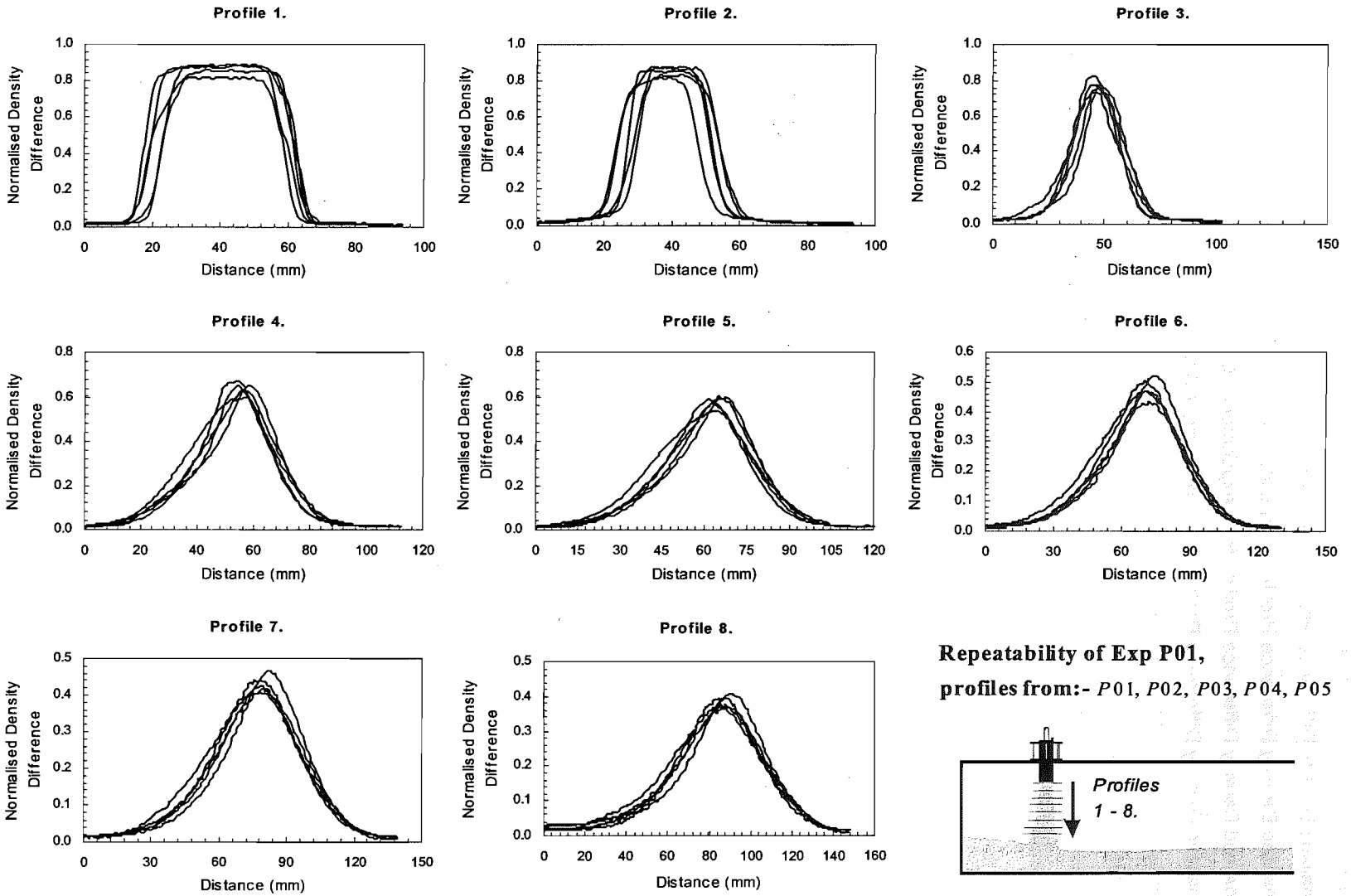
Profile 1.
Profile 2.
Profile 3.
Profile 4.
Profile 5.
Profile 6.
Profile 7.
Profile 8.
Normalised Density Difference
Distance (mm)
Repeatability of Exp P01,
profiles from:- P01, P02, P03, P04, P05
Profiles
1 - 8.

C-Series Simulations

Normalised Density Difference Profiles from experiment C01
Normalised Density Difference Profiles from experiment C02
Normalised Density Difference Profiles from experiment C03
Normalised Density Difference Profiles from experiment C04
Normalised Density Difference Profiles from experiment C05
Normalised Density Difference Profiles from experiment C06
Normalised Density Difference Profiles from experiment C07
Normalised Density Difference Profiles from experiment C08
Repeatability of experiment C06.

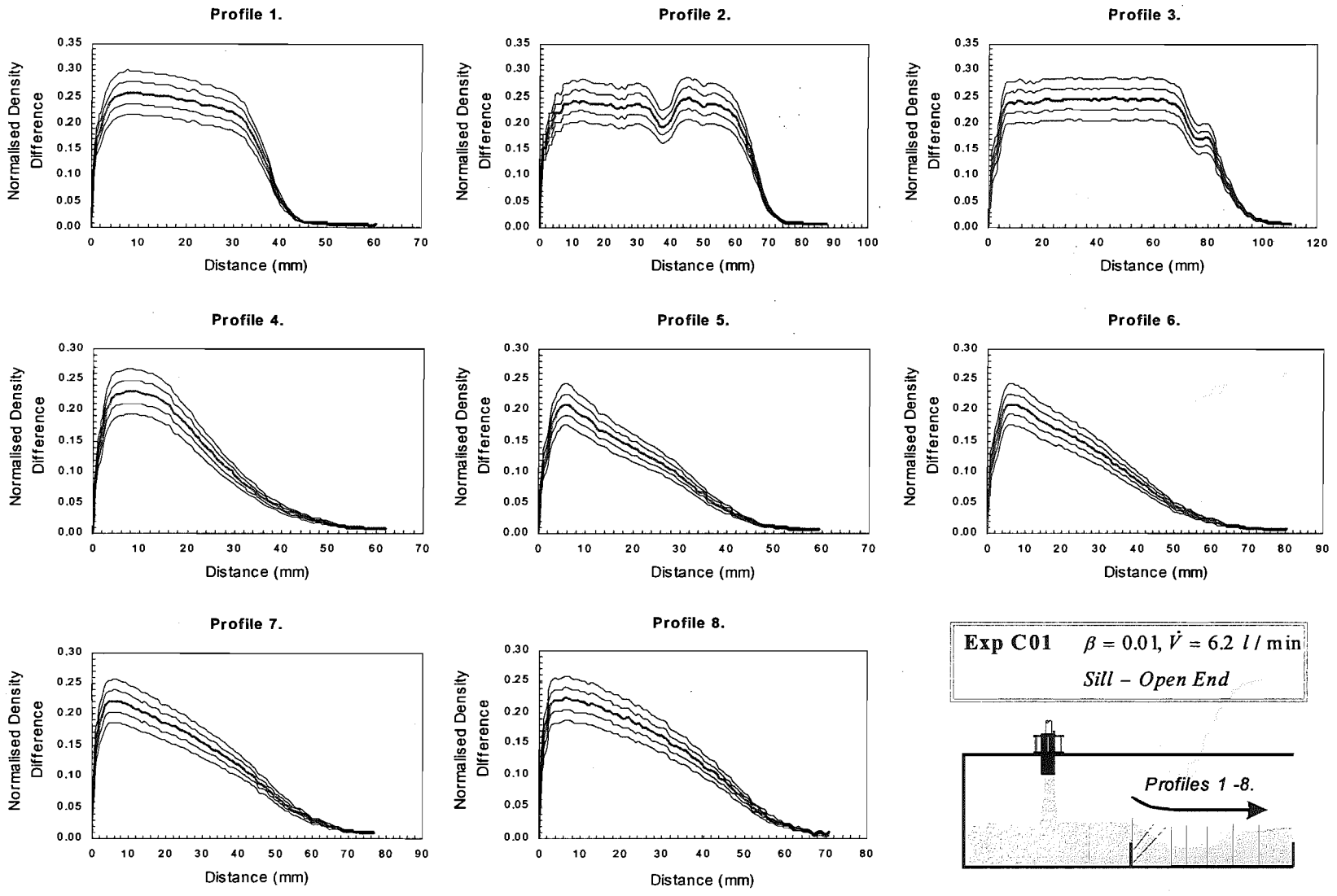
Profile 1.
Profile 2.
Profile 3.
Profile 4.
Profile 5.
Profile 6.
Profile 7.
Profile 8.
Normalised Density Difference
Distance (mm)
Exp C01 $\beta = 0.01, \dot{V} = 6.2\ l/\min$
Sill – Open End
Profiles 1 -8.

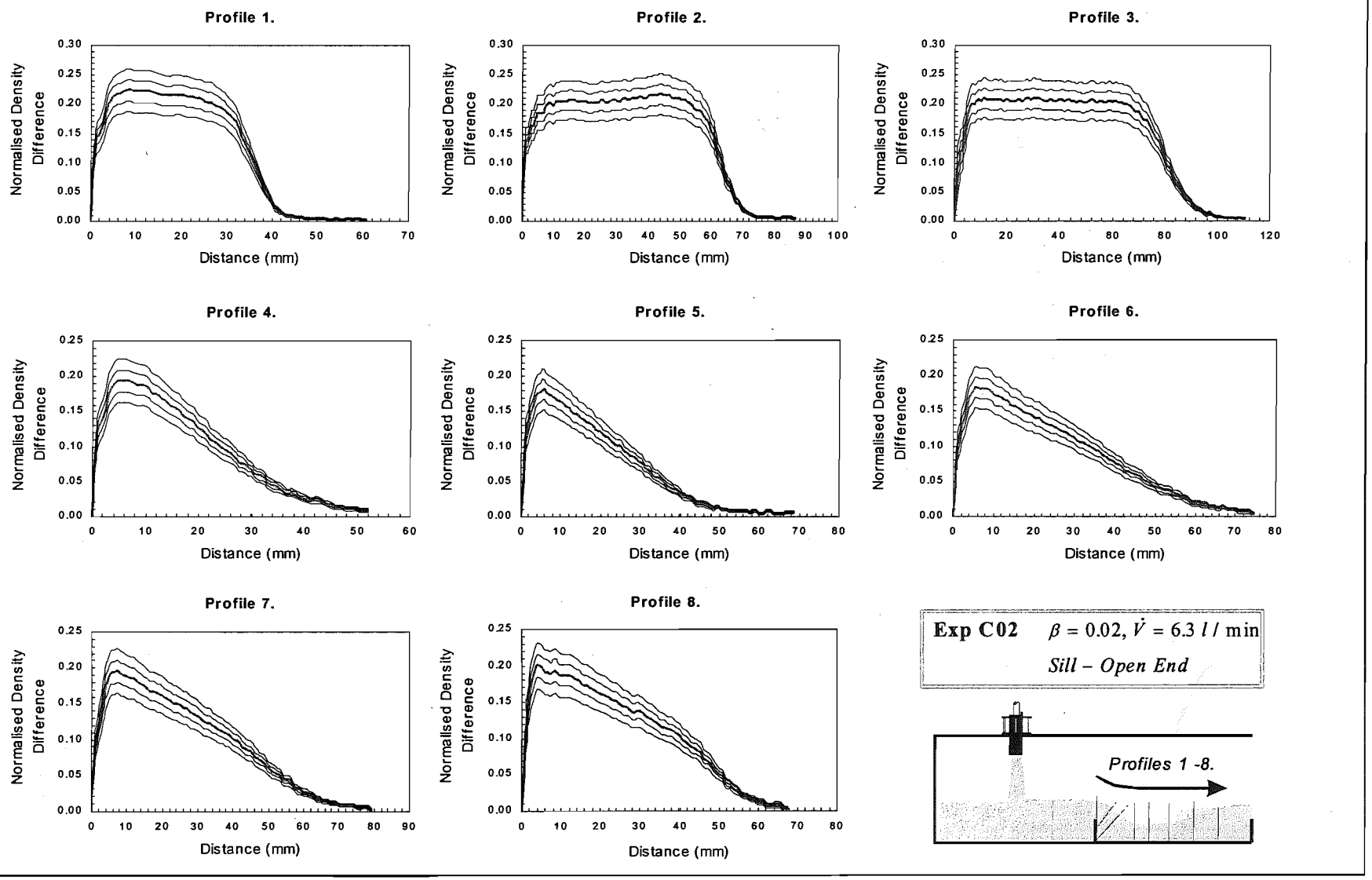
Profile 1.
Profile 2.
Profile 3.
Profile 4.
Profile 5.
Profile 6.
Profile 7.
Profile 8.
Normalised Density Difference
Distance (mm)
Exp C02 $\beta = 0.02, \dot{V} = 6.3\ l/\min$
Sill – Open End
Profiles 1 -8.

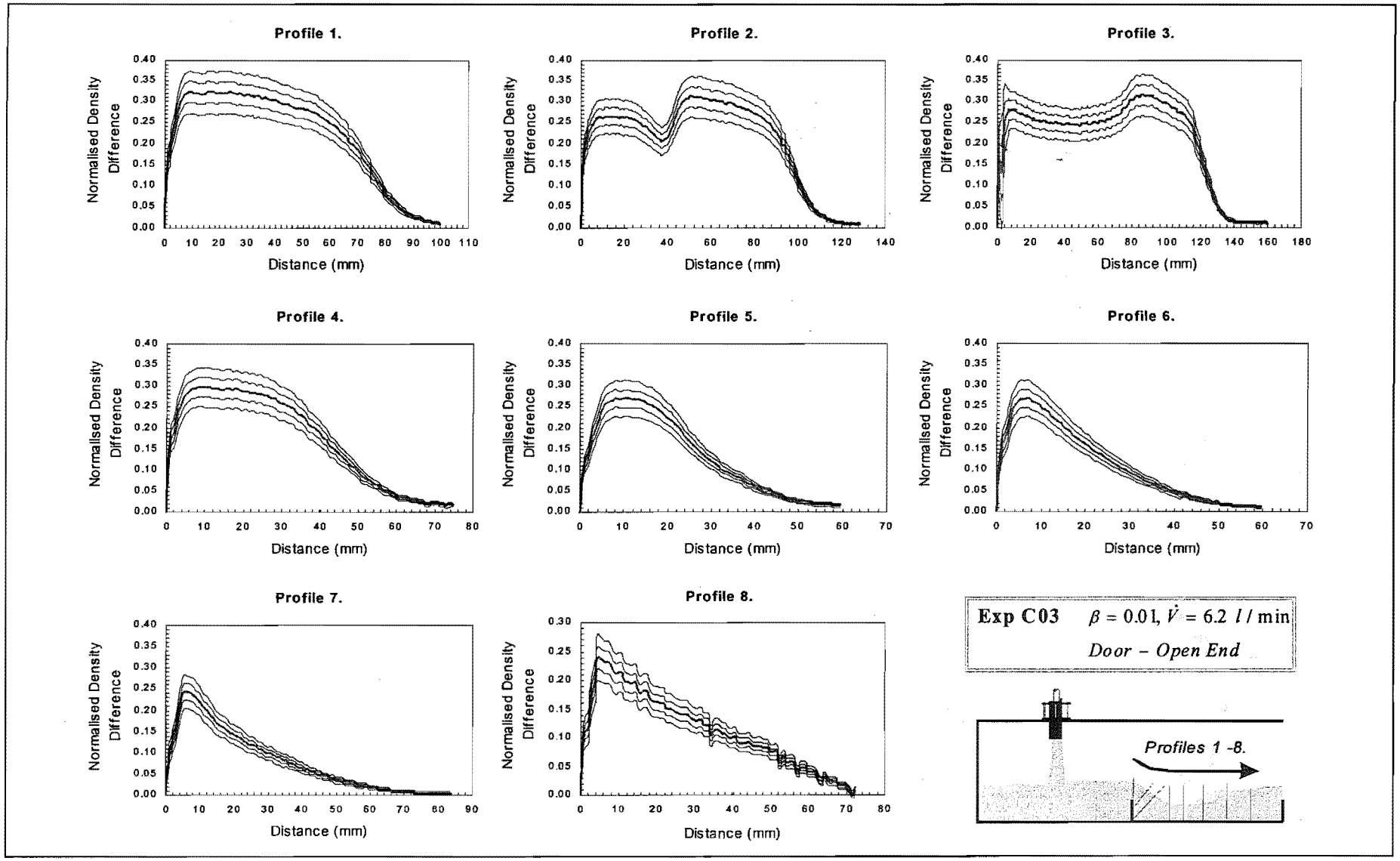
Profile 1.
Profile 2.
Profile 3.
Profile 4.
Profile 5.
Profile 6.
Profile 7.
Profile 8.
Normalised Density Difference
Distance (mm)
Exp C03 $\beta = 0.01$, $\dot{V} = 6.2$ l / min
Door – Open End
Profiles 1 -8.

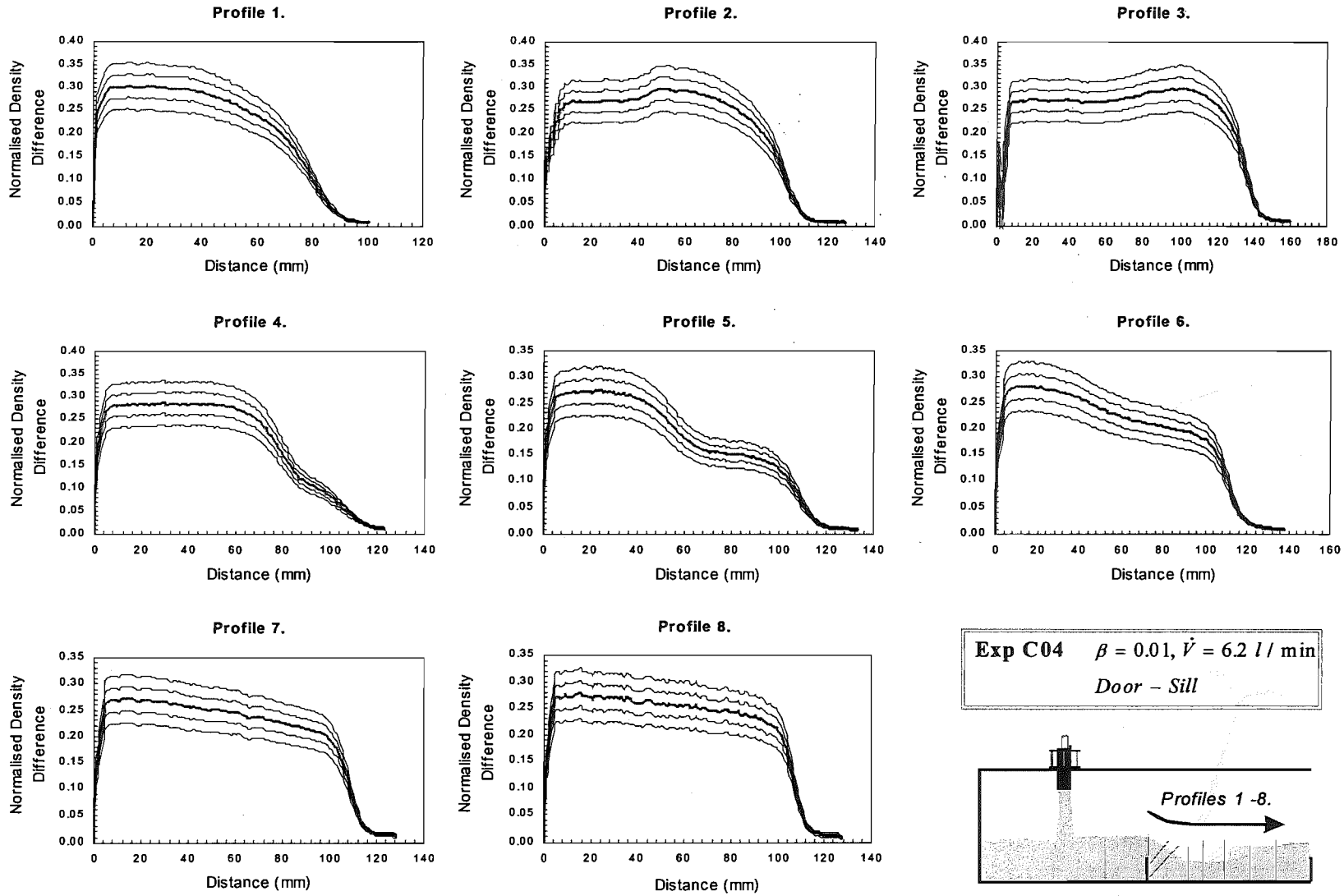
Profile 1.
Profile 2.
Profile 3.
Profile 4.
Profile 5.
Profile 6.
Profile 7.
Profile 8.
Normalised Density Difference
Distance (mm)
Exp C04 $\beta = 0.01, \dot{V} = 6.2\ l/\min$
Door – Sill
Profiles 1 -8.

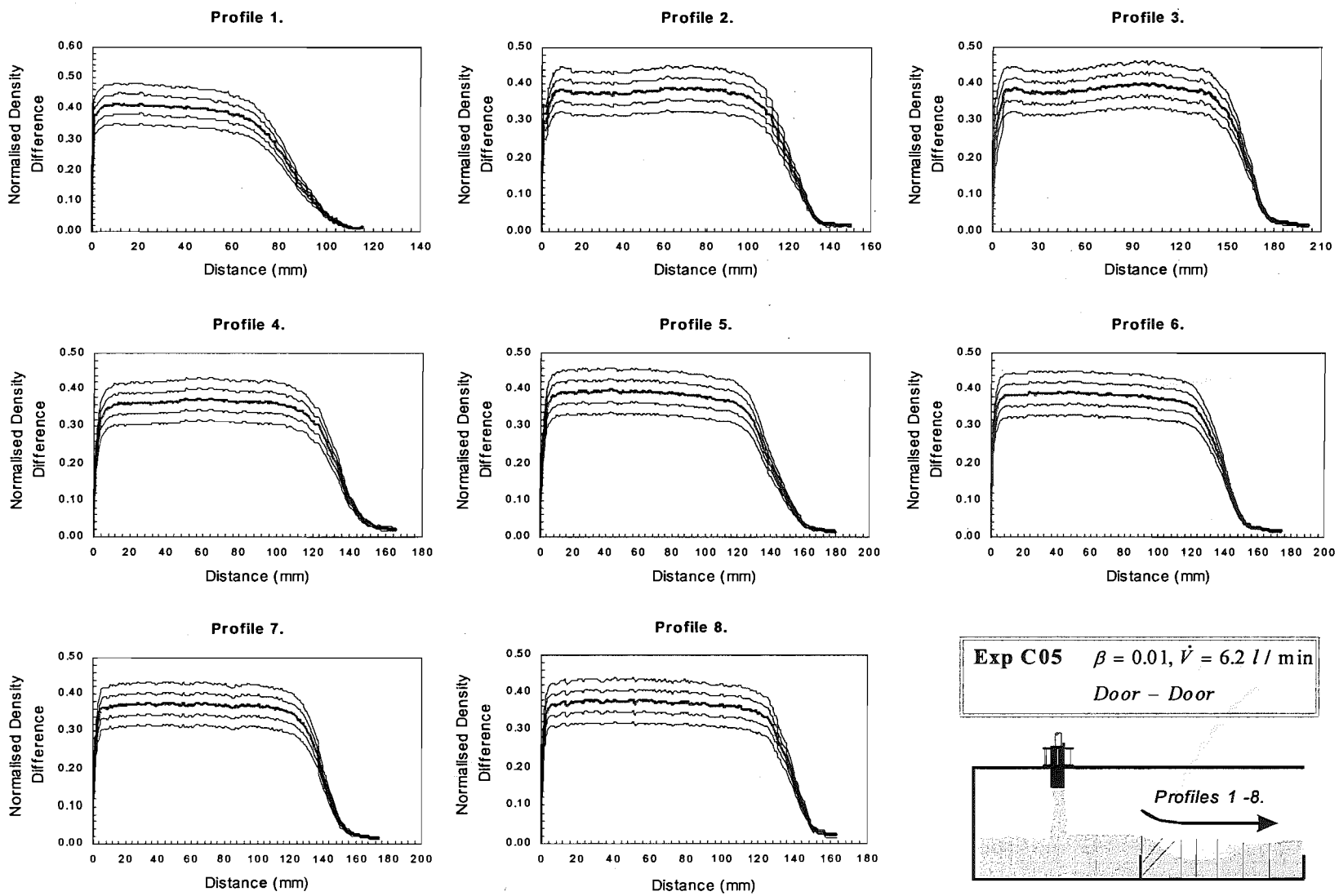
Profile 1.
Profile 2.
Profile 3.
Profile 4.
Profile 5.
Profile 6.
Profile 7.
Profile 8.
Normalised Density Difference
Distance (mm)
Exp C05 $\beta = 0.01, \dot{V} = 6.2\ l/\min$
Door – Door
Profiles 1 -8.

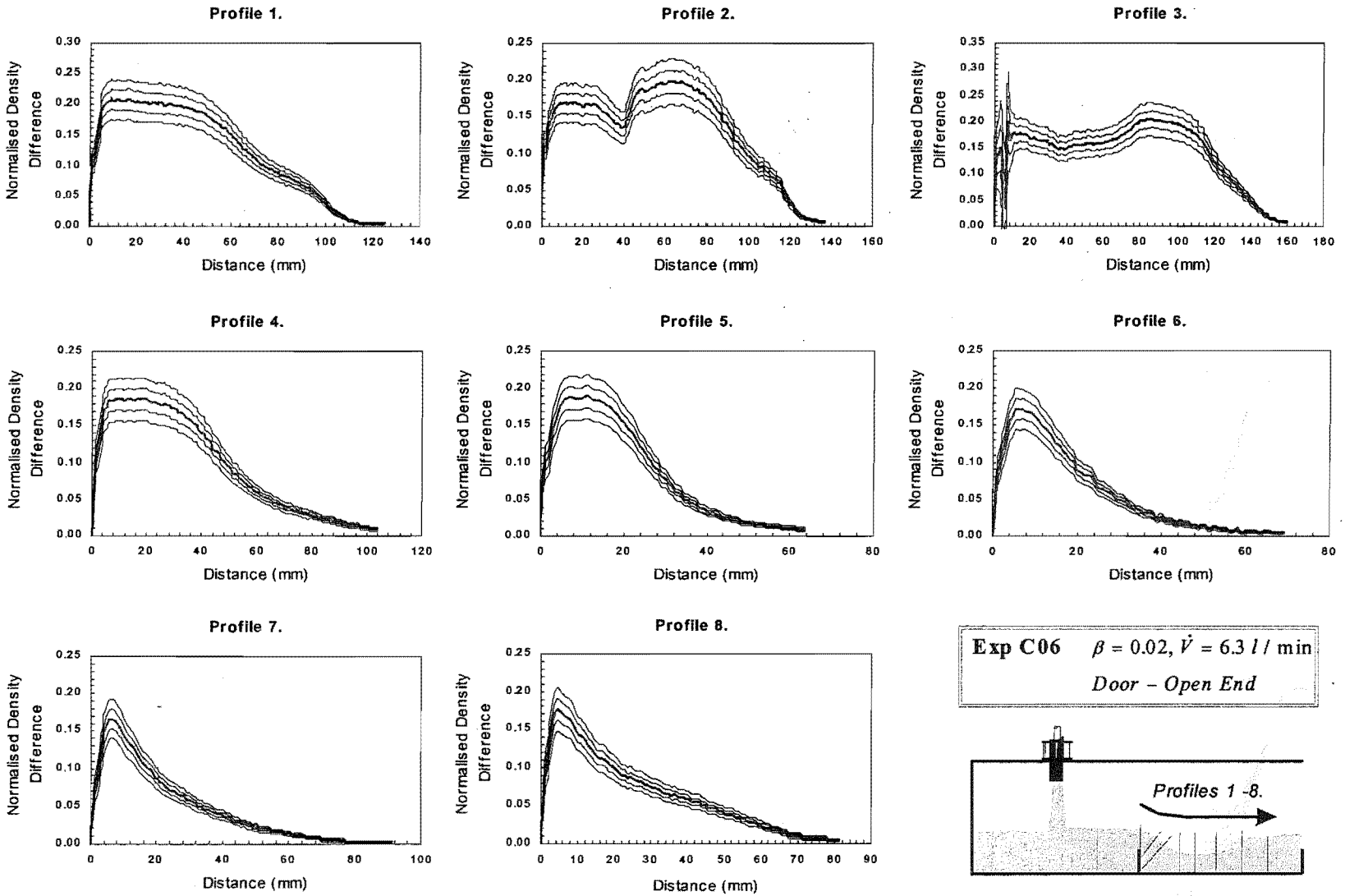
Profile 1.
Profile 2.
Profile 3.
Profile 4.
Profile 5.
Profile 6.
Profile 7.
Profile 8.
Normalised Density Difference
Distance (mm)
Exp C06 $\beta = 0.02, \dot{V} = 6.3\ l/\min$
Door – Open End
Profiles 1 -8.

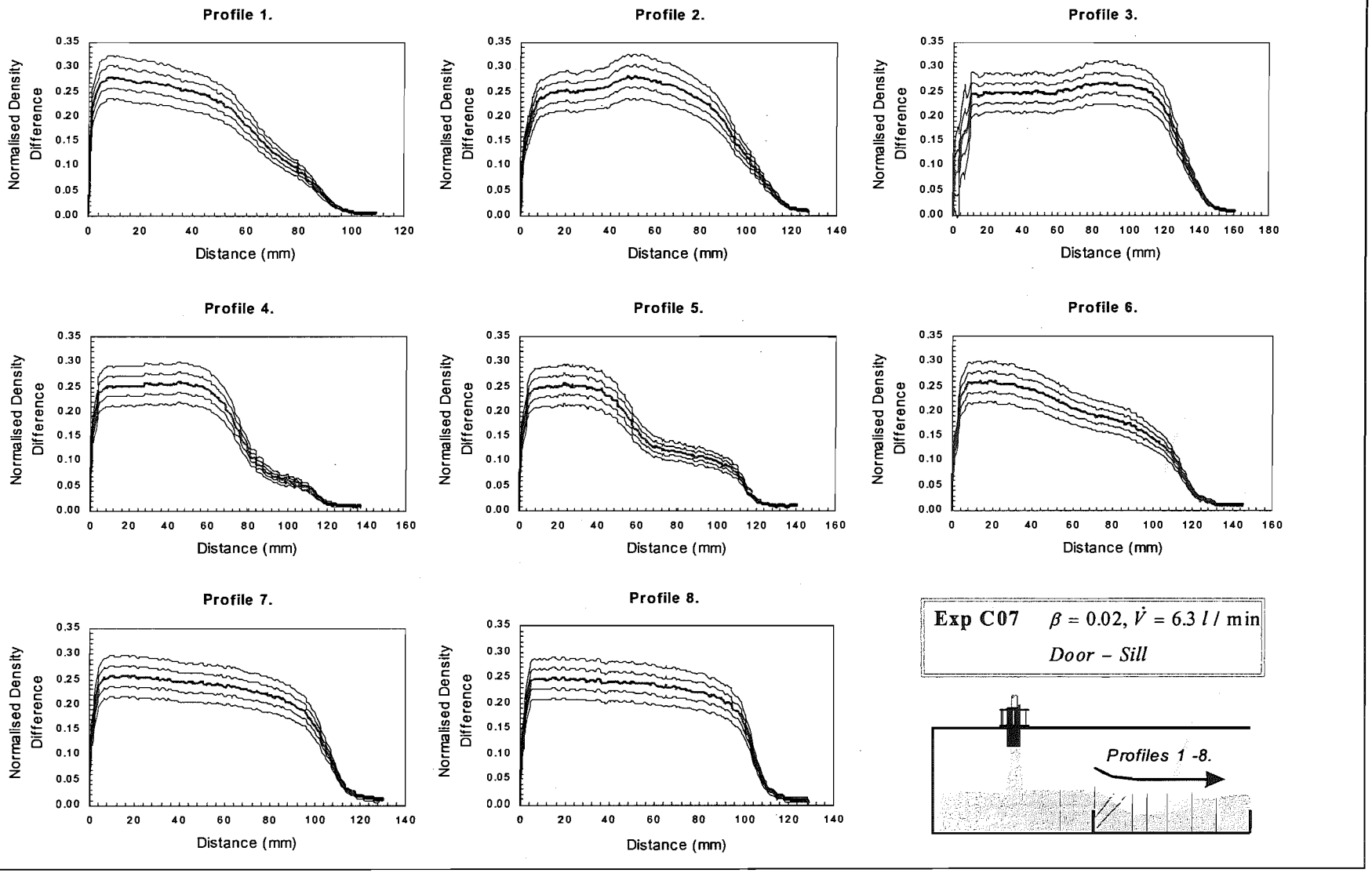
Profile 1.
Profile 2.
Profile 3.
Profile 4.
Profile 5.
Profile 6.
Profile 7.
Profile 8.
Normalised Density Difference
Distance (mm)
Exp C07 $\beta = 0.02, \dot{V} = 6.3\ l$ / min
Door – Sill
Profiles 1 -8.

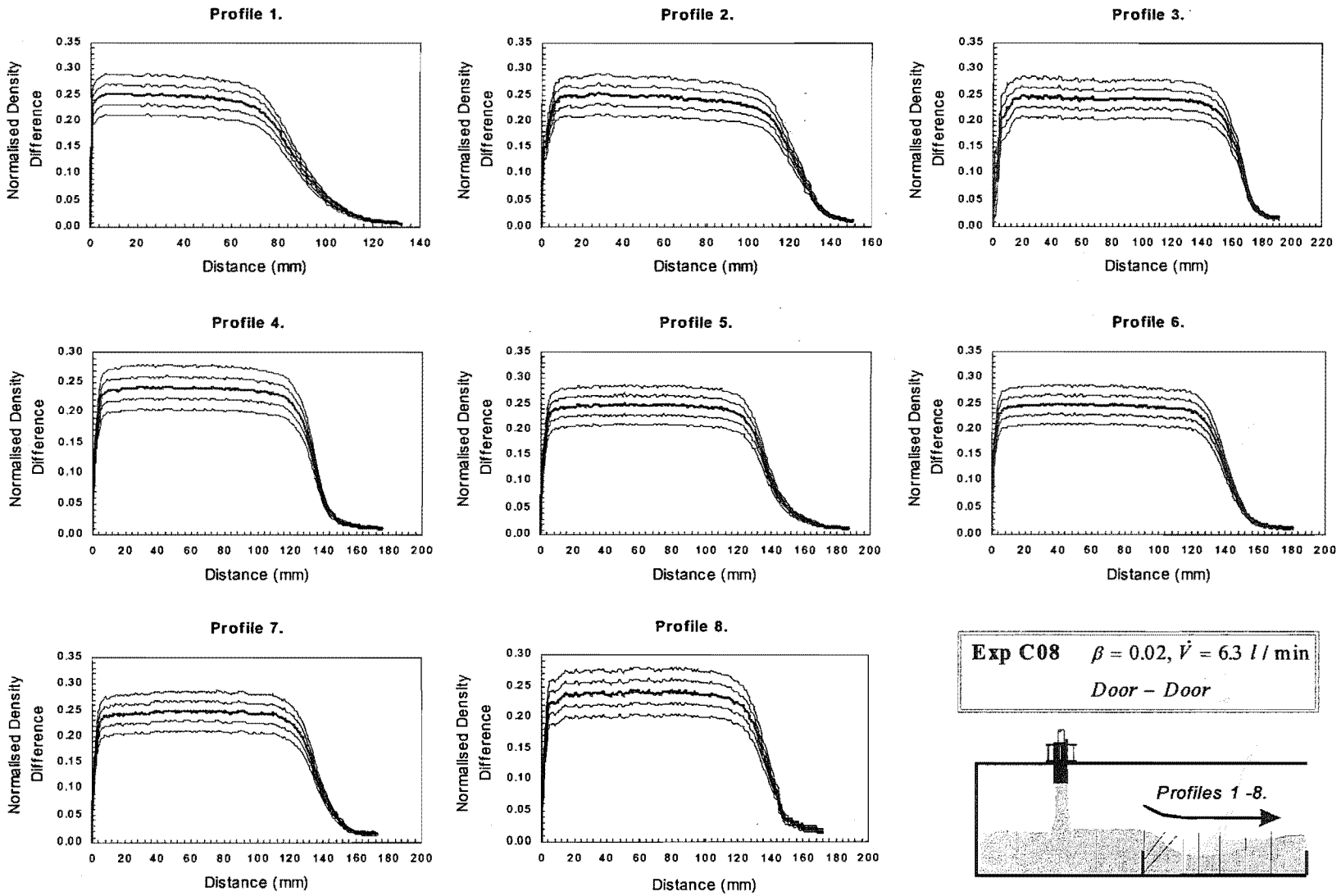
Profile 1.
Profile 2.
Profile 3.
Profile 4.
Profile 5.
Profile 6.
Profile 7.
Profile 8.
Normalised Density Difference
Distance (mm)
Exp C08 $\beta = 0.02, \dot{V} = 6.3\ l/\min$
Door – Door
Profiles 1 -8.

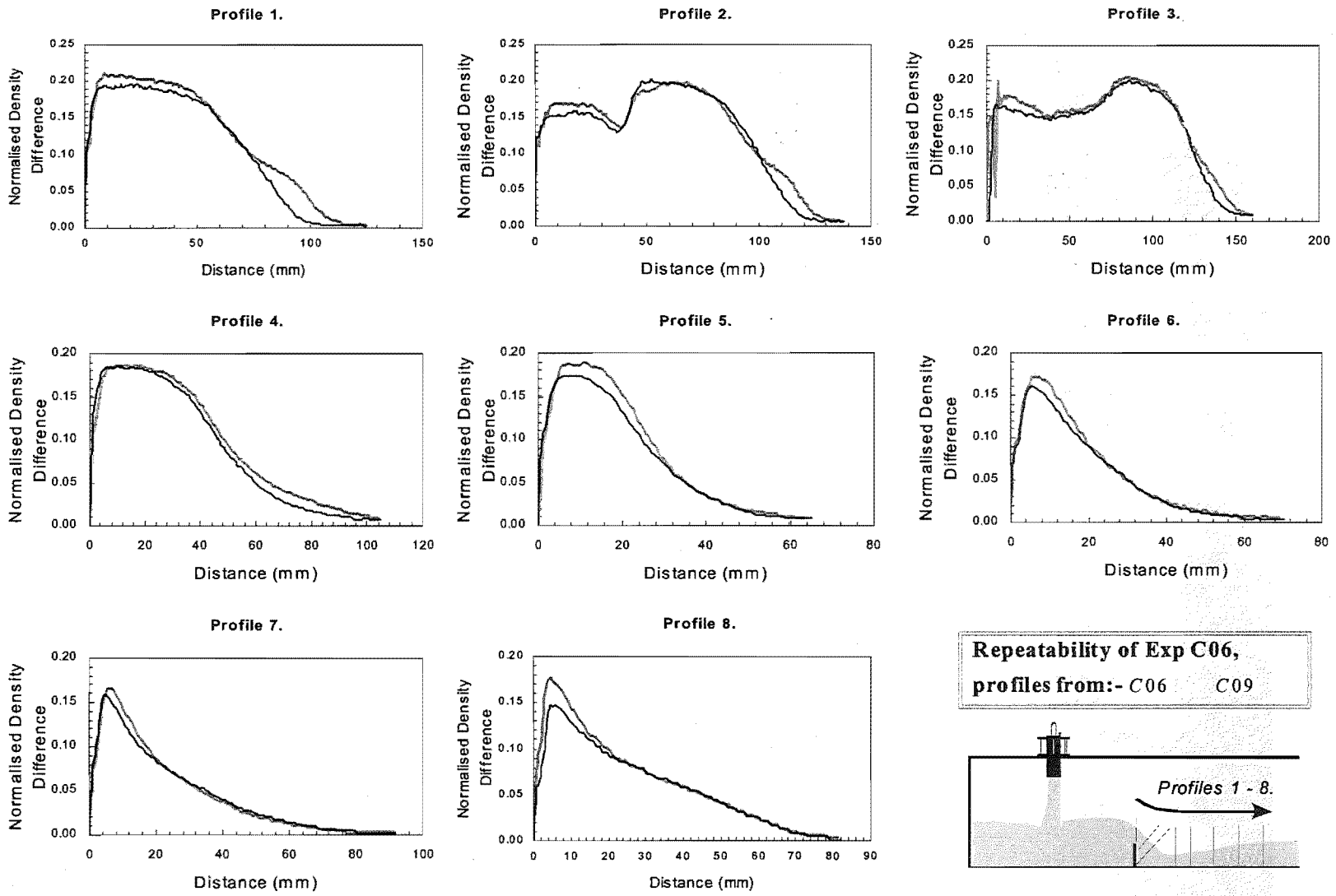
Profile 1.
Profile 2.
Profile 3.
Profile 4.
Profile 5.
Profile 6.
Profile 7.
Profile 8.
Normalised Density Difference
Distance (mm)
Repeatability of Exp C06,
profiles from:- C06 C09
Profiles 1 - 8.

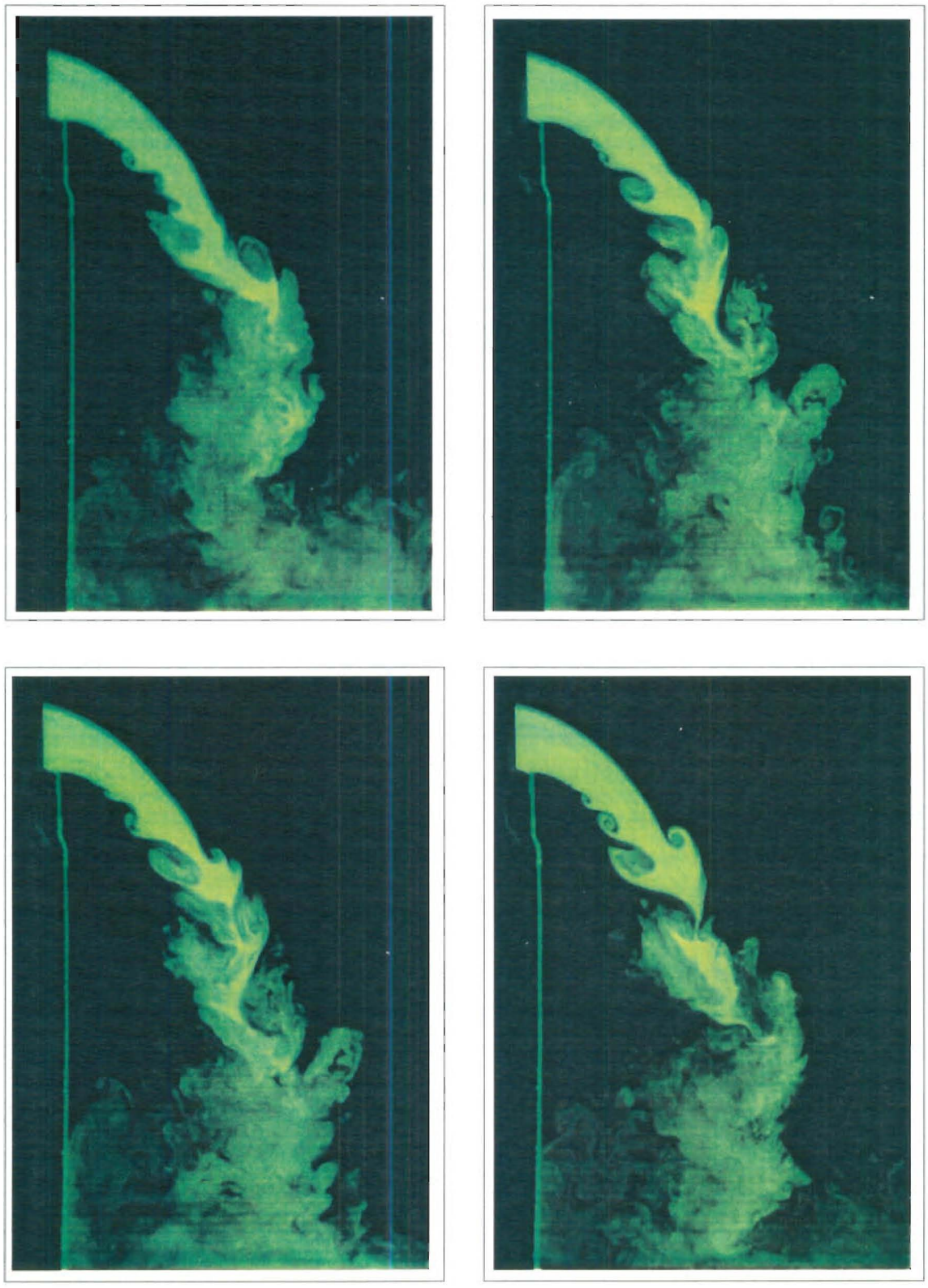

Appendix 5 Computational Density Profiles

T-Series Simulations

Simulations of experiment T01 – against scaled experimental profile.

Simulations of experiment T02 – against scaled experimental profile.

Simulations of experiment T03 – against scaled experimental profile.

Simulations of experiment T04 – against scaled experimental profile.

Simulations of experiment T05 – against scaled experimental profile.

Simulations of experiment T06 – against scaled experimental profile.

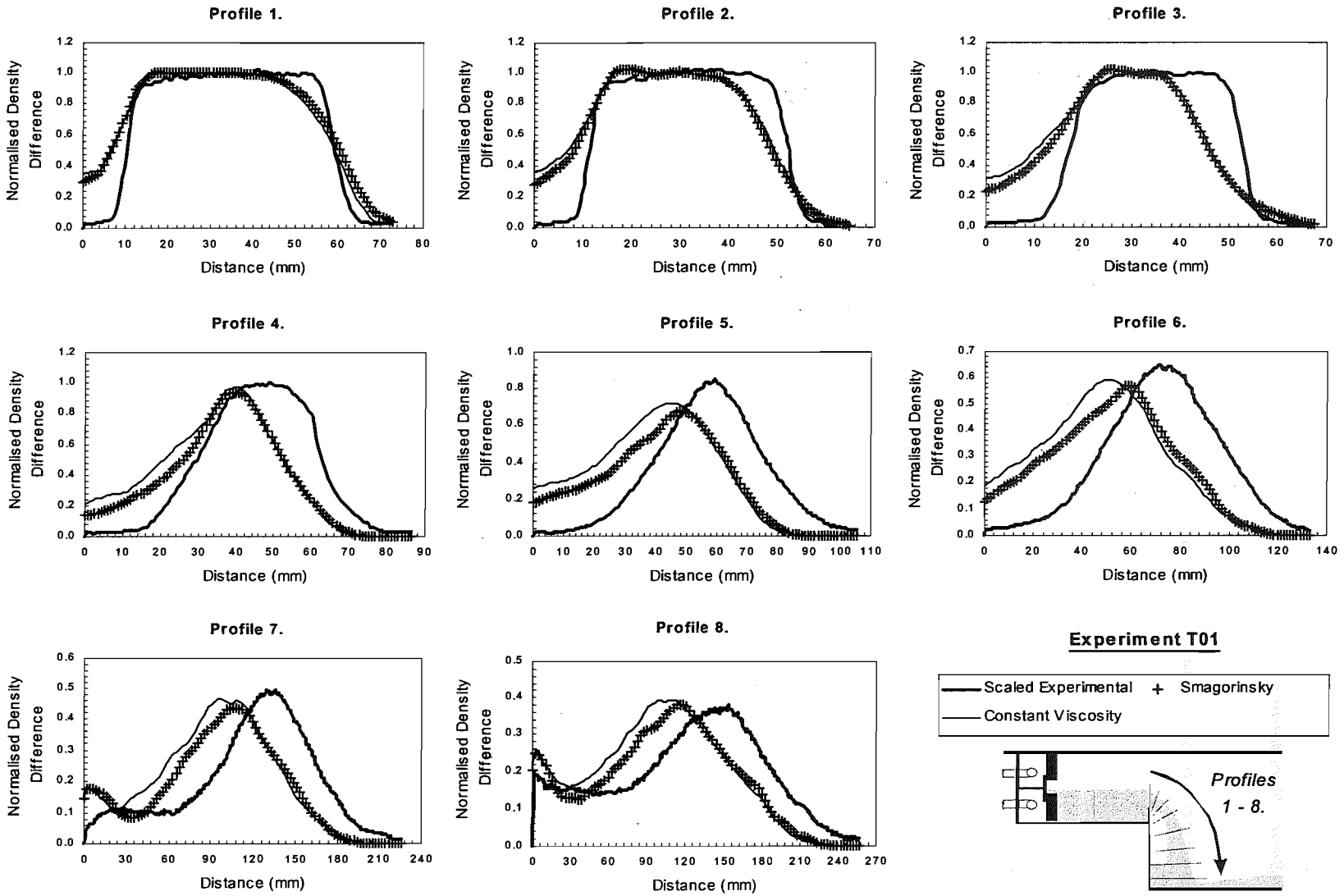
Profile 1.
Profile 2.
Profile 3.
Profile 4.
Profile 5.
Profile 6.
Profile 7.
Profile 8.
Normalised Density Difference
Distance (mm)
Experiment T01
Scaled Experimental
Smagorinsky
Constant Viscosity
Profiles 1 - 8.

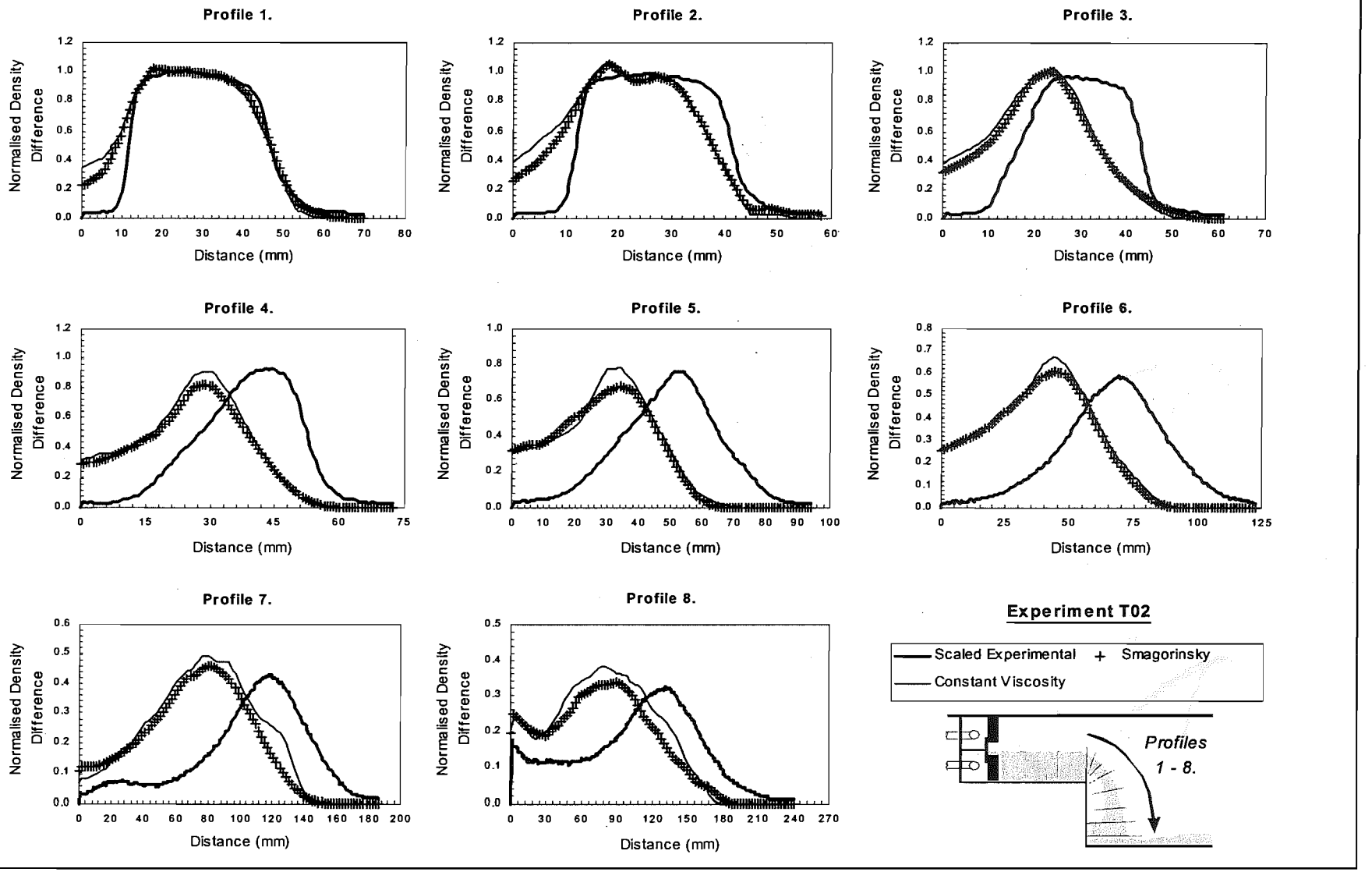
Profile 1.
Profile 2.
Profile 3.
Profile 4.
Profile 5.
Profile 6.
Profile 7.
Profile 8.
Normalised Density Difference
Distance (mm)
Experiment T02
Scaled Experimental
Smagorinsky
Constant Viscosity
Profiles 1 - 8.

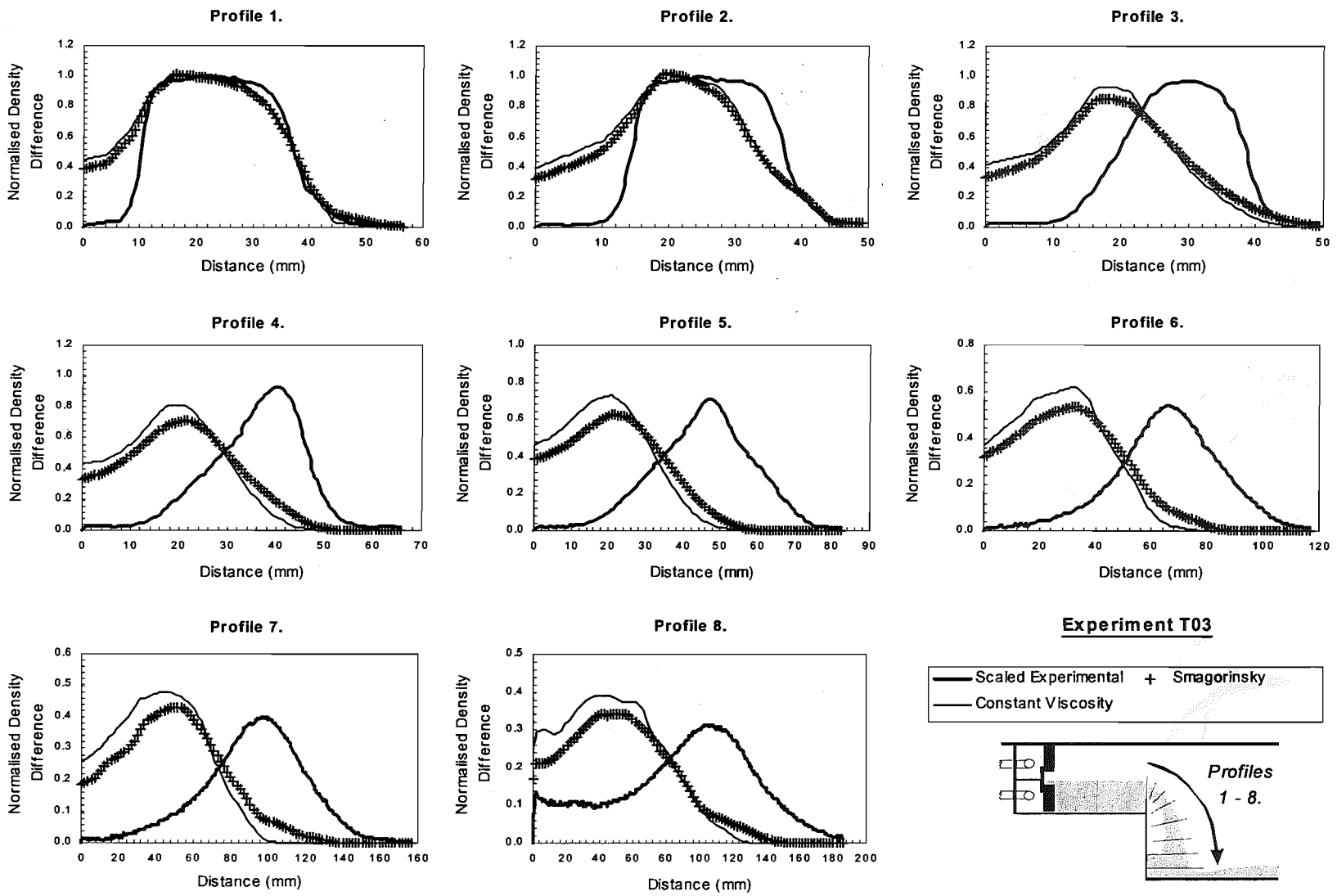
Profile 1.
Profile 2.
Profile 3.
Profile 4.
Profile 5.
Profile 6.
Profile 7.
Profile 8.
Normalised Density Difference
Distance (mm)
Experiment T03
Scaled Experimental
Smagorinsky
Constant Viscosity
Profiles 1 - 8.

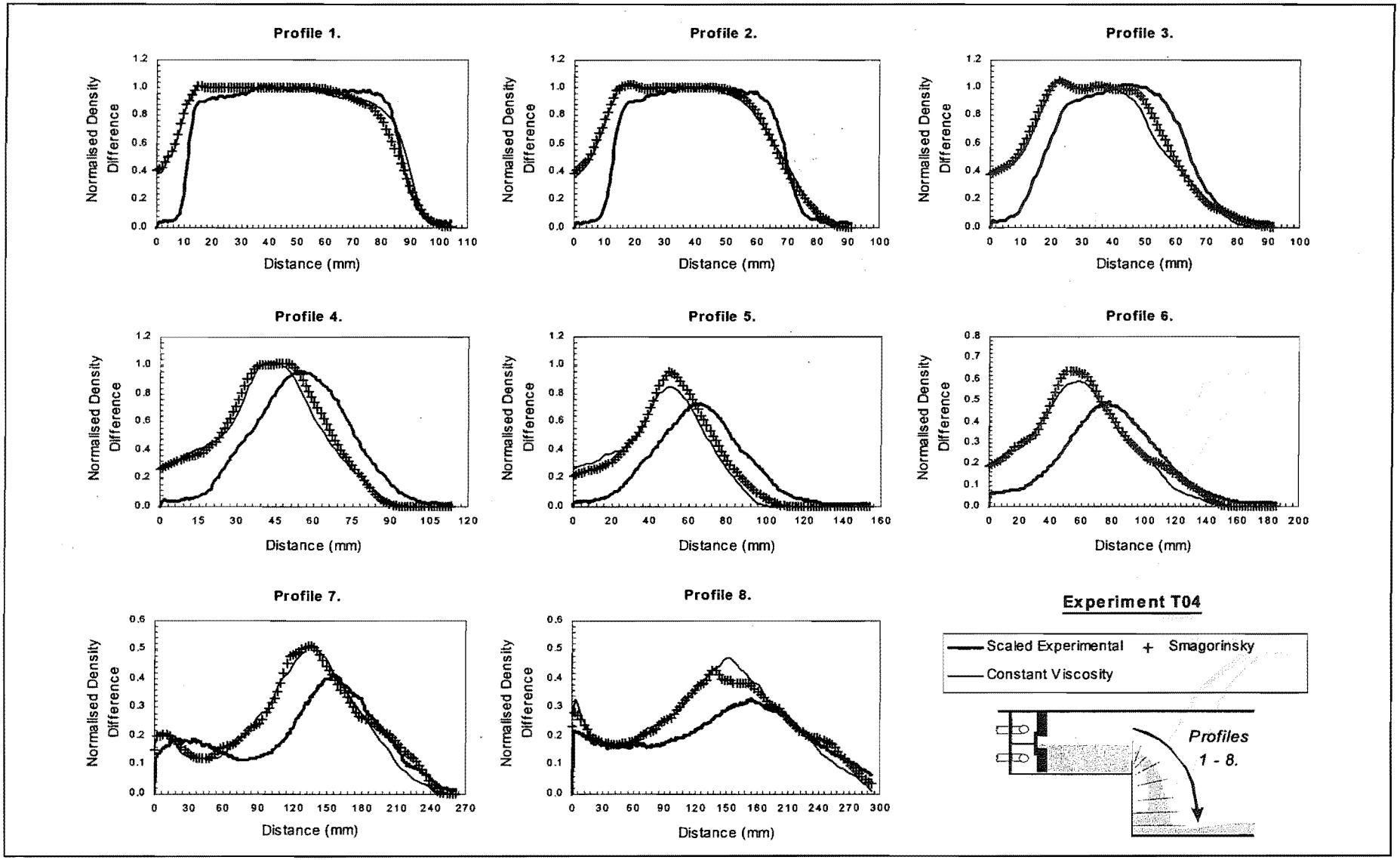
Profile 1.
Profile 2.
Profile 3.
Profile 4.
Profile 5.
Profile 6.
Profile 7.
Profile 8.
Normalised Density Difference
Distance (mm)
Experiment T04
Scaled Experimental
Smagorinsky
Constant Viscosity
Profiles 1 - 8.

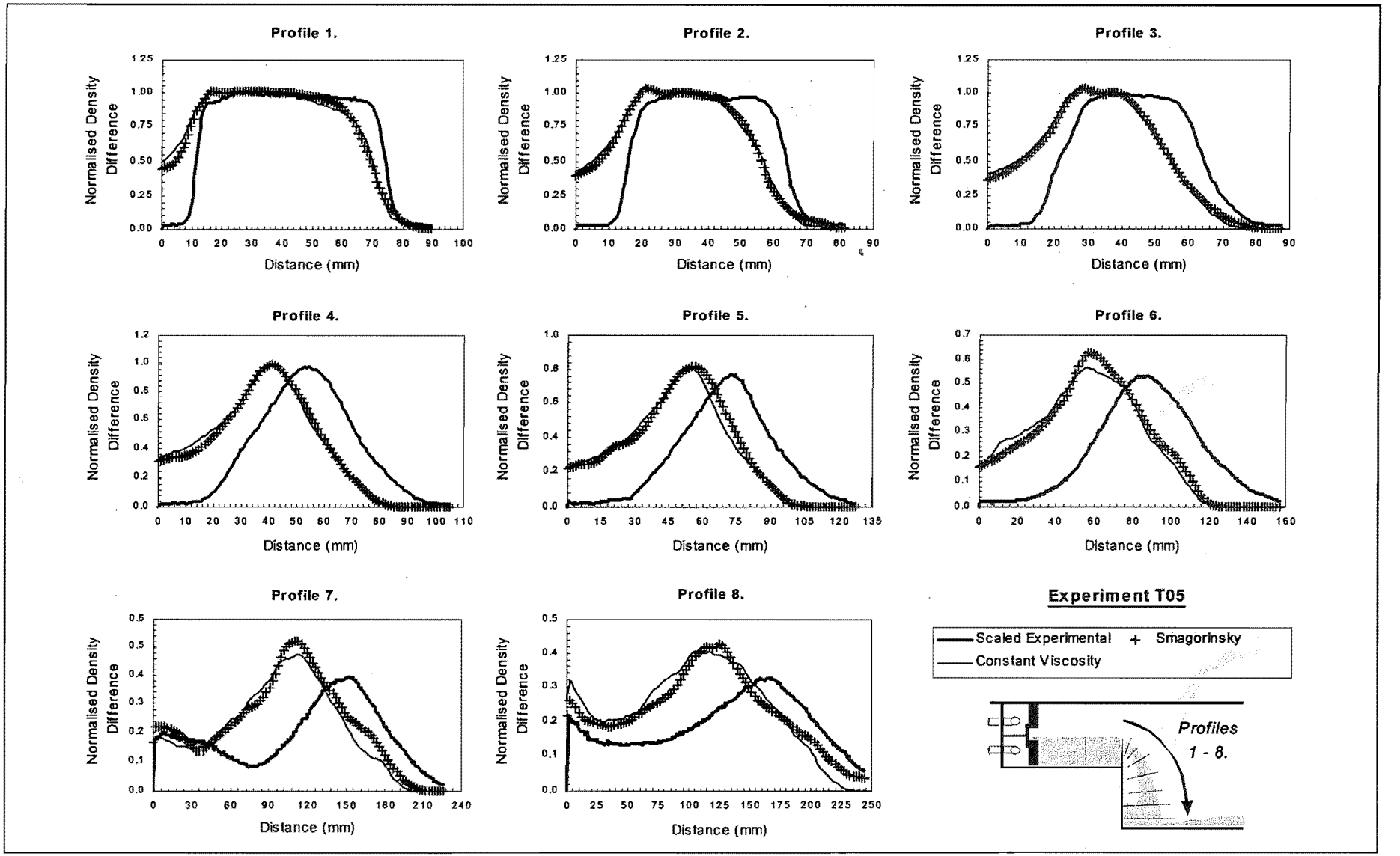
Profile 1.
Profile 2.
Profile 3.
Profile 4.
Profile 5.
Profile 6.
Profile 7.
Profile 8.
Normalised Density Difference
Distance (mm)
Experiment T05
Scaled Experimental
Smagorinsky
Constant Viscosity
Profiles 1 - 8.

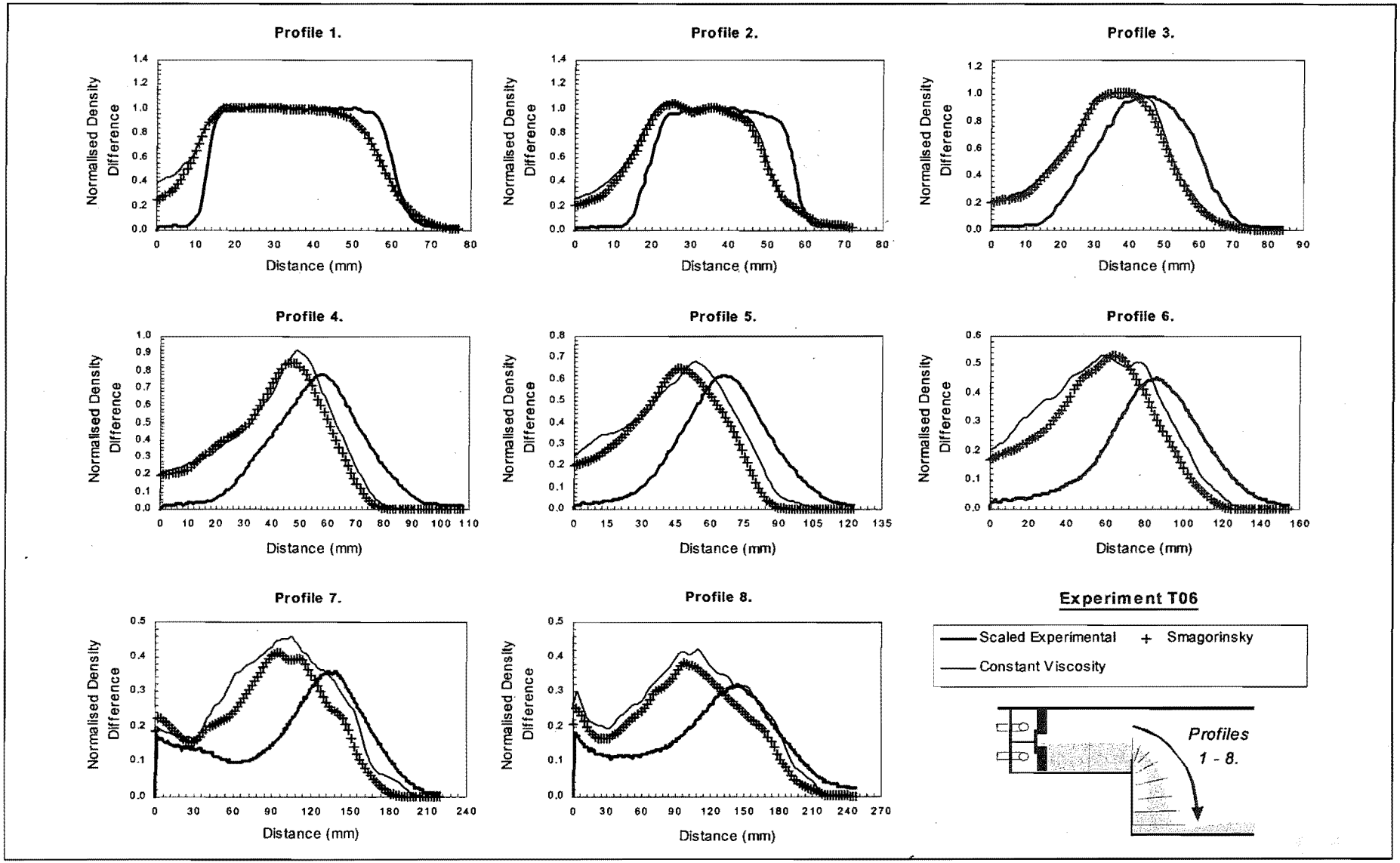
Profile 1.
Profile 2.
Profile 3.
Profile 4.
Profile 5.
Profile 6.
Profile 7.
Profile 8.
Normalised Density Difference
Distance (mm)
Experiment T06
Scaled Experimental
Smagorinsky
Constant Viscosity
Profiles 1 - 8.

P-Series Simulations

Simulations of experiment P01 – against scaled experimental profile.

Simulations of experiment P06 – against scaled experimental profile.

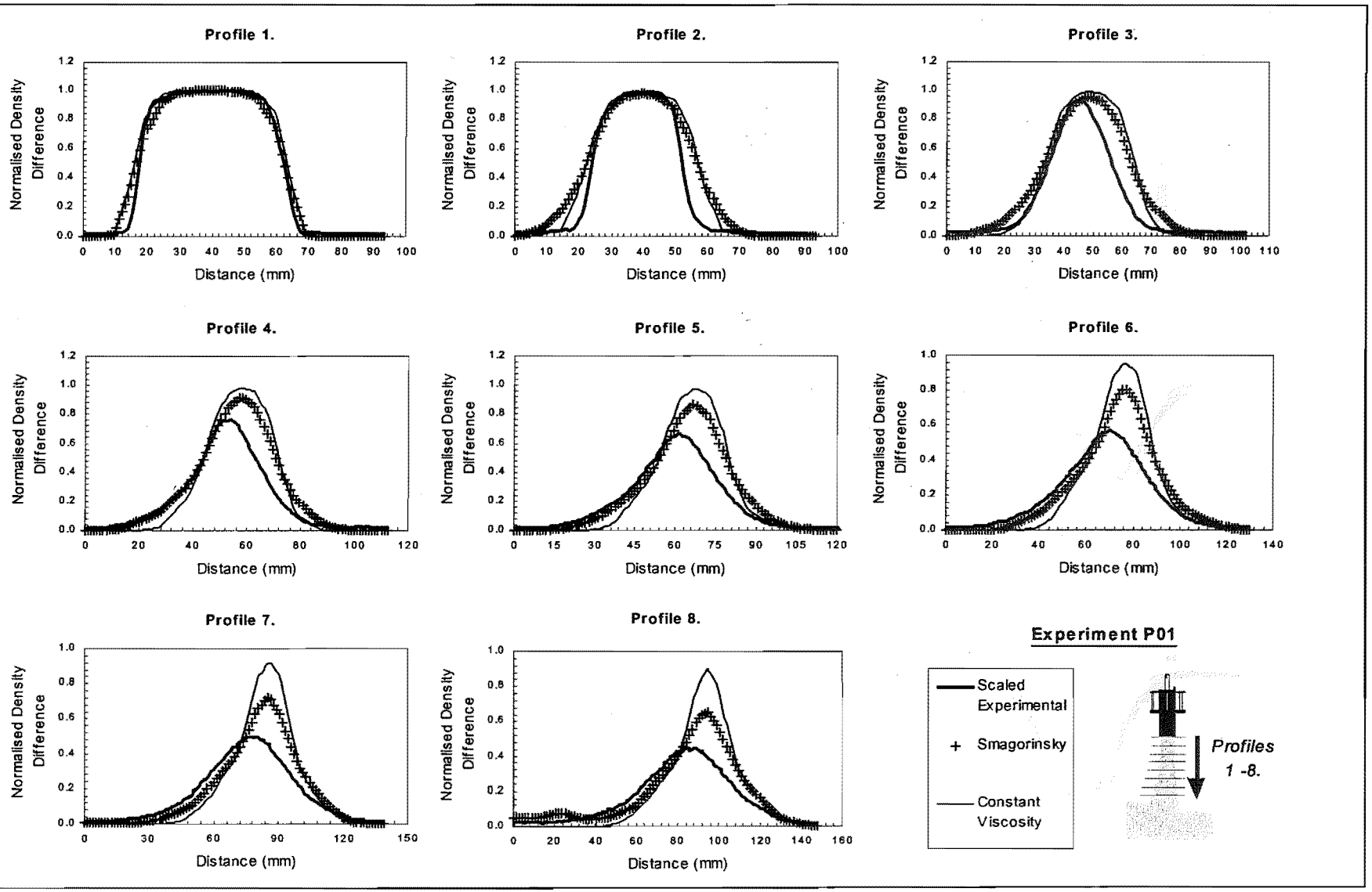
Profile 1.
Profile 2.
Profile 3.
Profile 4.
Profile 5.
Profile 6.
Profile 7.
Profile 8.
Normalised Density Difference
Distance (mm)
Experiment P01
Scaled Experimental
Smagorinsky
Constant Viscosity
Profiles 1 -8.

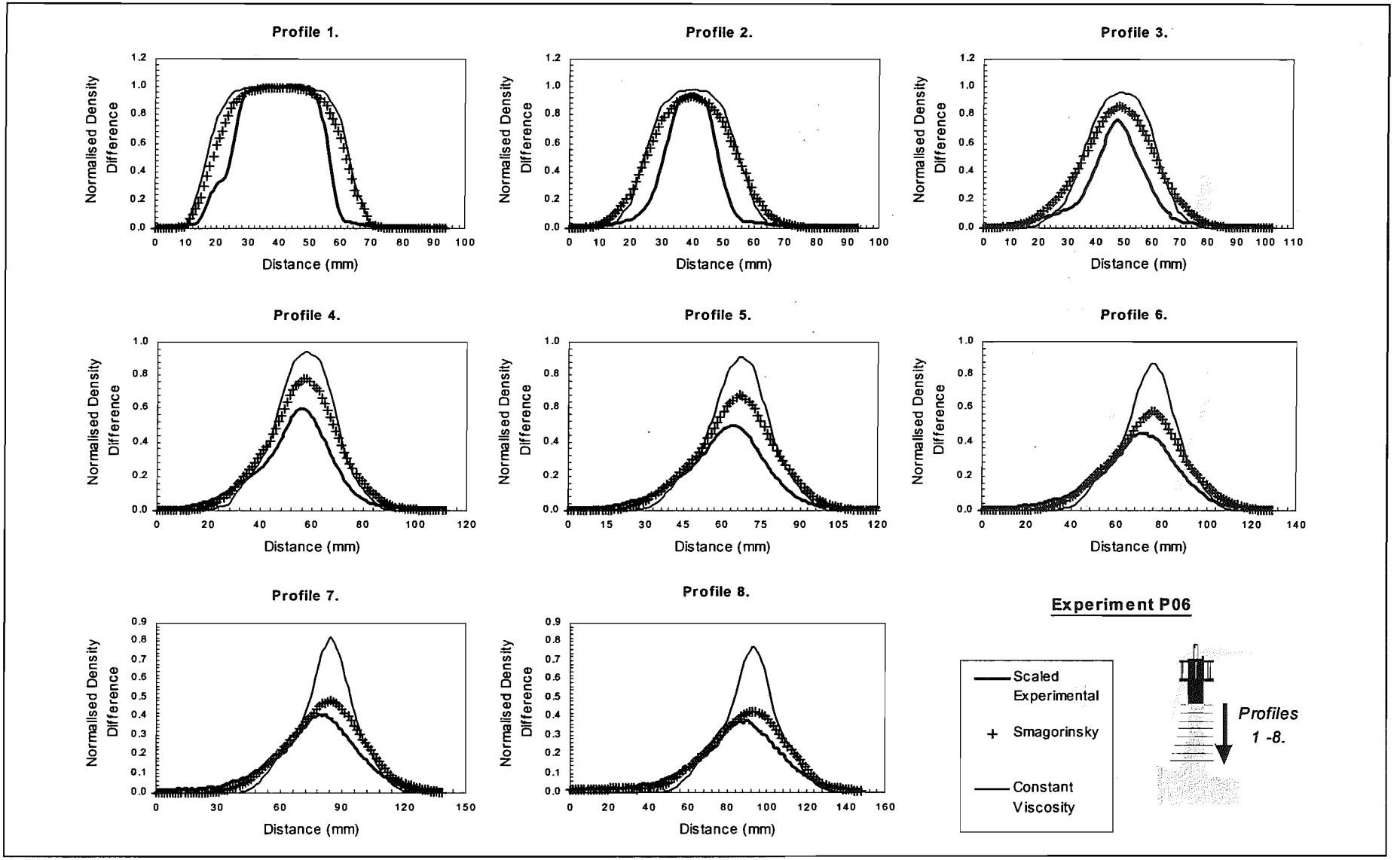
Profile 1.
Profile 2.
Profile 3.
Profile 4.
Profile 5.
Profile 6.
Profile 7.
Profile 8.
Normalised Density Difference
Distance (mm)
Experiment P06
Scaled Experimental
Smagorinsky
Constant Viscosity
Profiles 1 -8.

C-Series Simulations

Simulations of experiment C01 with the Smagorinsky SGS model.
Simulations of experiment C02 with the Smagorinsky SGS model.
Simulations of experiment C03 with the Smagorinsky SGS model.
Simulations of experiment C04 with the Smagorinsky SGS model.
Simulations of experiment C05 with the Smagorinsky SGS model.
Simulations of experiment C06 with the Smagorinsky SGS model.
Simulations of experiment C07 with the Smagorinsky SGS model.
Simulations of experiment C08 with the Smagorinsky SGS model.
Simulations of experiment C01 with the Constant Viscosity SGS model.
Simulations of experiment C02 with the Constant Viscosity SGS model.
Simulations of experiment C03 with the Constant Viscosity SGS model.
Simulations of experiment C04 with the Constant Viscosity SGS model.
Simulations of experiment C05 with the Constant Viscosity SGS model.
Simulations of experiment C06 with the Constant Viscosity SGS model.
Simulations of experiment C07 with the Constant Viscosity SGS model.
Simulations of experiment C08 with the Constant Viscosity SGS model.

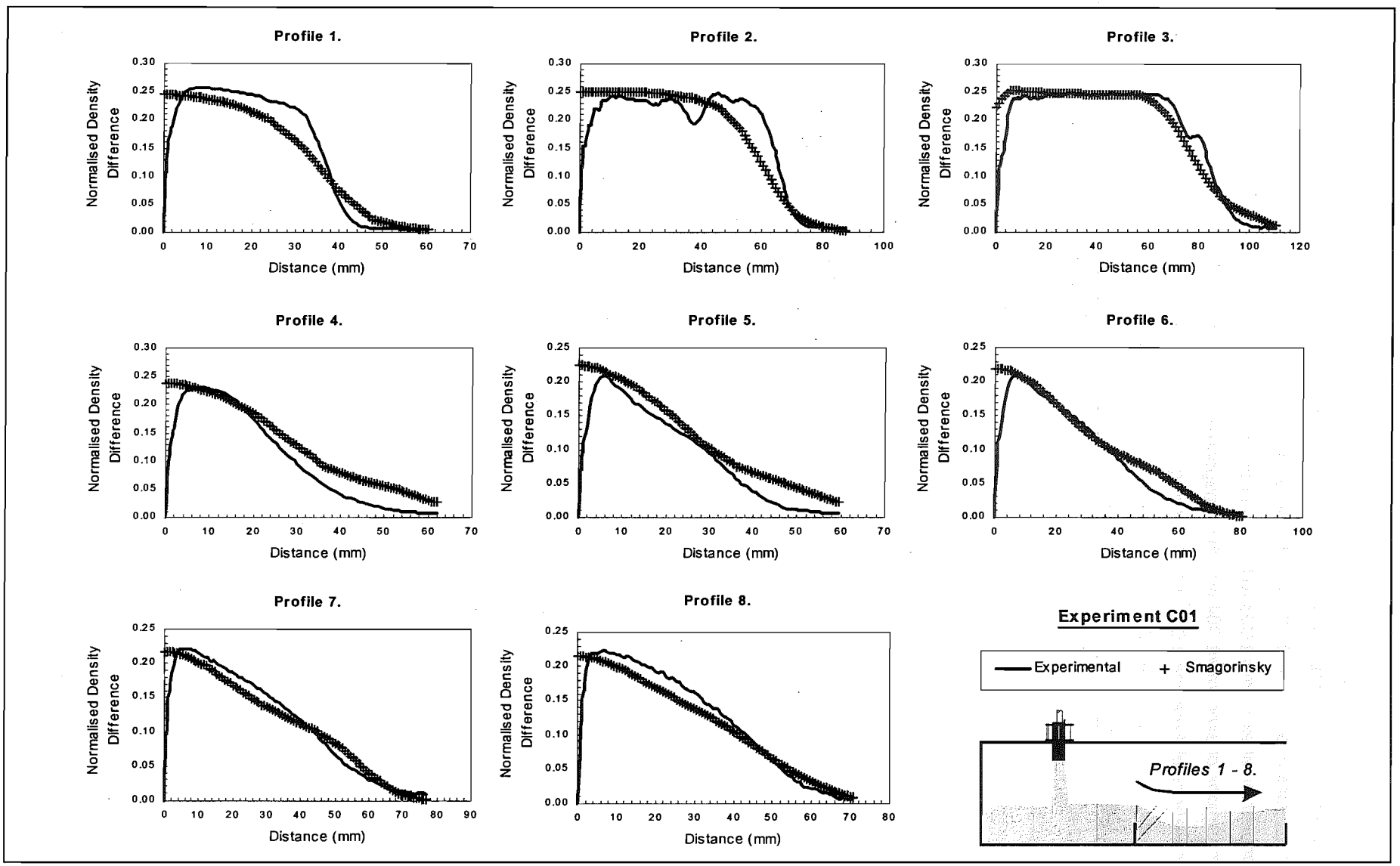
Profile 1.
Profile 2.
Profile 3.
Profile 4.
Profile 5.
Profile 6.
Profile 7.
Profile 8.
Normalised Density Difference
Distance (mm)
Experiment C01
Experimental
Smagorinsky
Profiles 1 - 8.

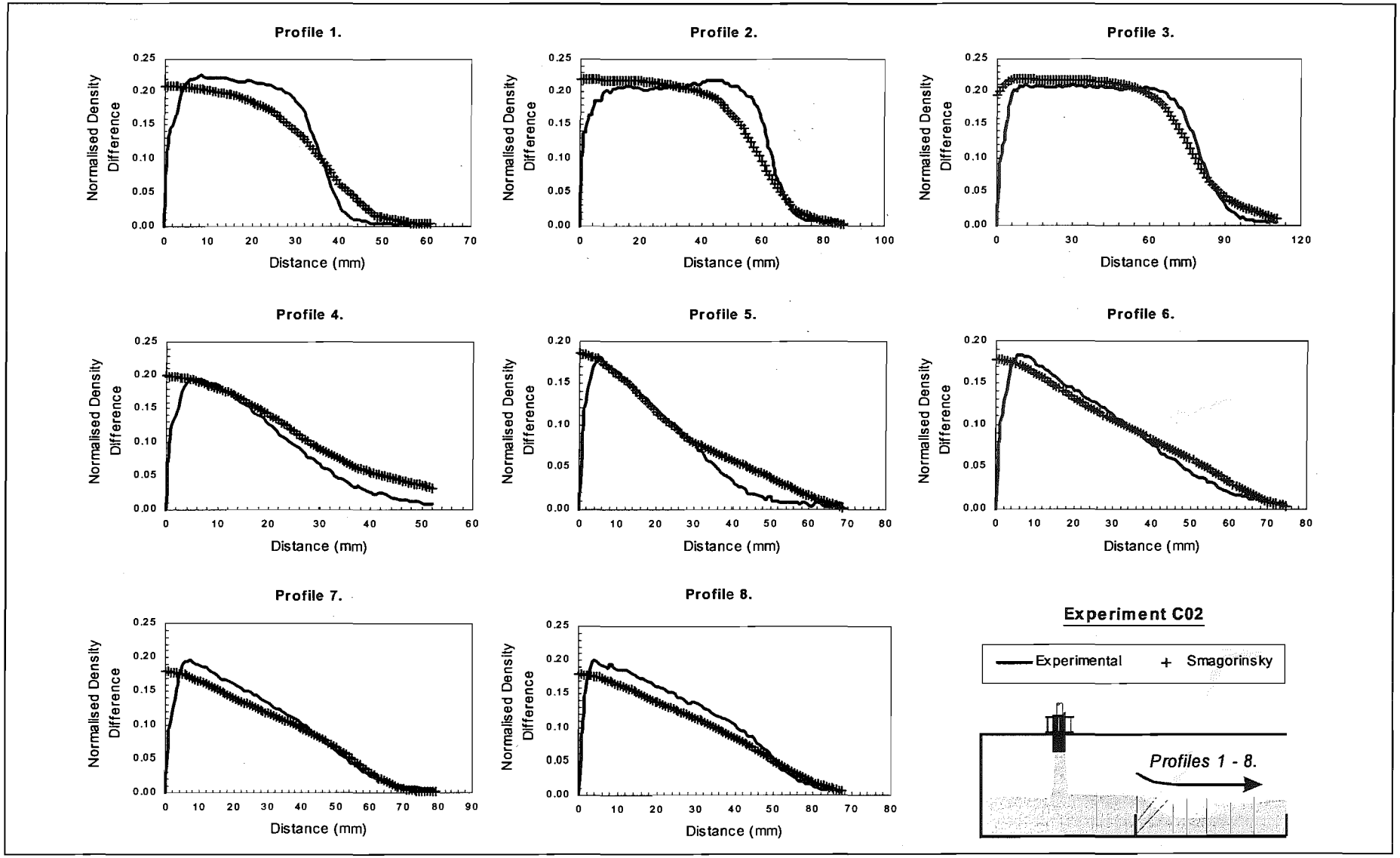
Profile 1.
Profile 2.
Profile 3.
Profile 4.
Profile 5.
Profile 6.
Profile 7.
Profile 8.
Normalised Density Difference
Distance (mm)
Experiment C02
Experimental
Smagorinsky
Profiles 1 - 8.

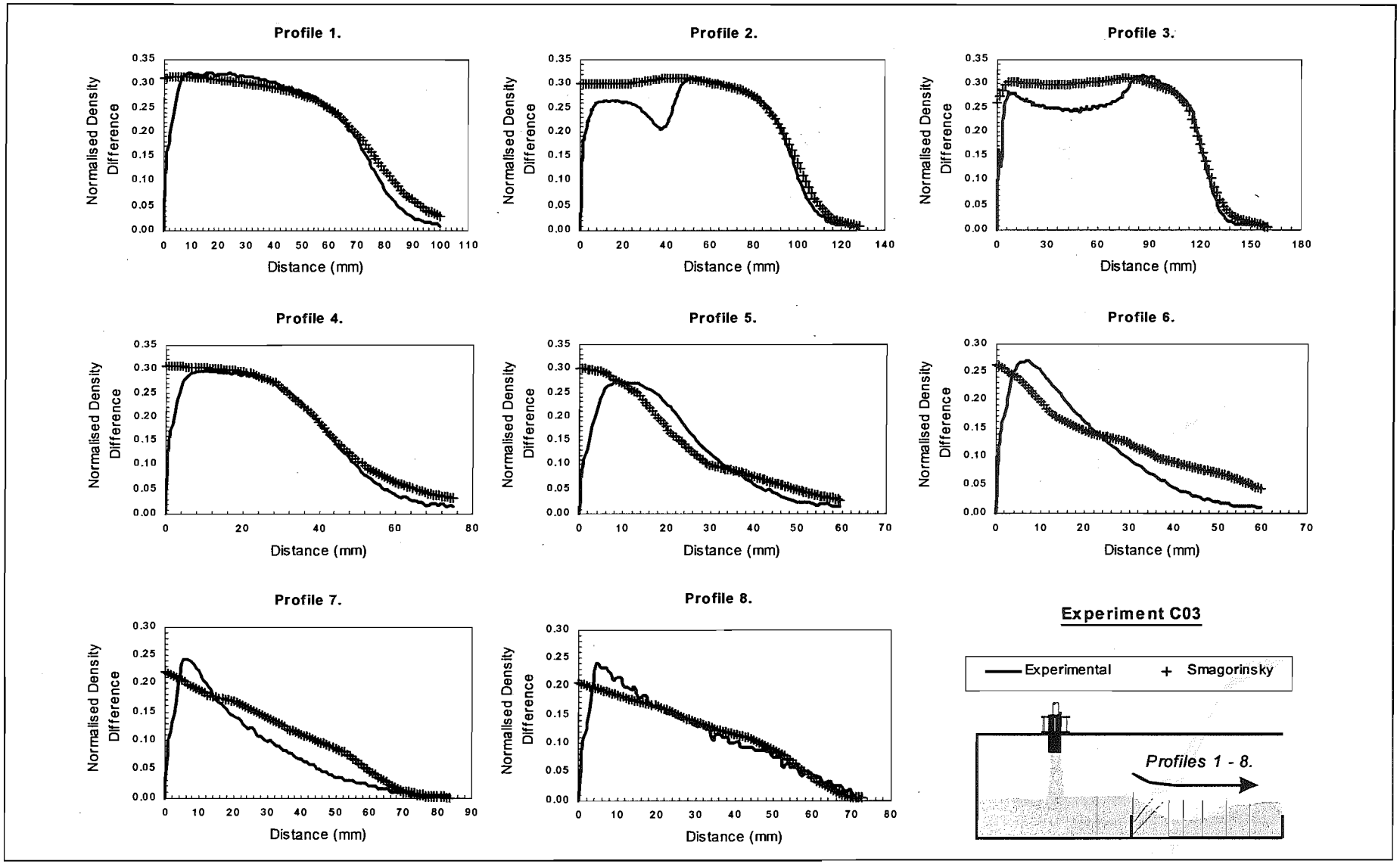
Profile 1.
Profile 2.
Profile 3.
Profile 4.
Profile 5.
Profile 6.
Profile 7.
Profile 8.
Normalised Density Difference
Distance (mm)
Experiment C03
Experimental
Smagorinsky
Profiles 1 - 8.

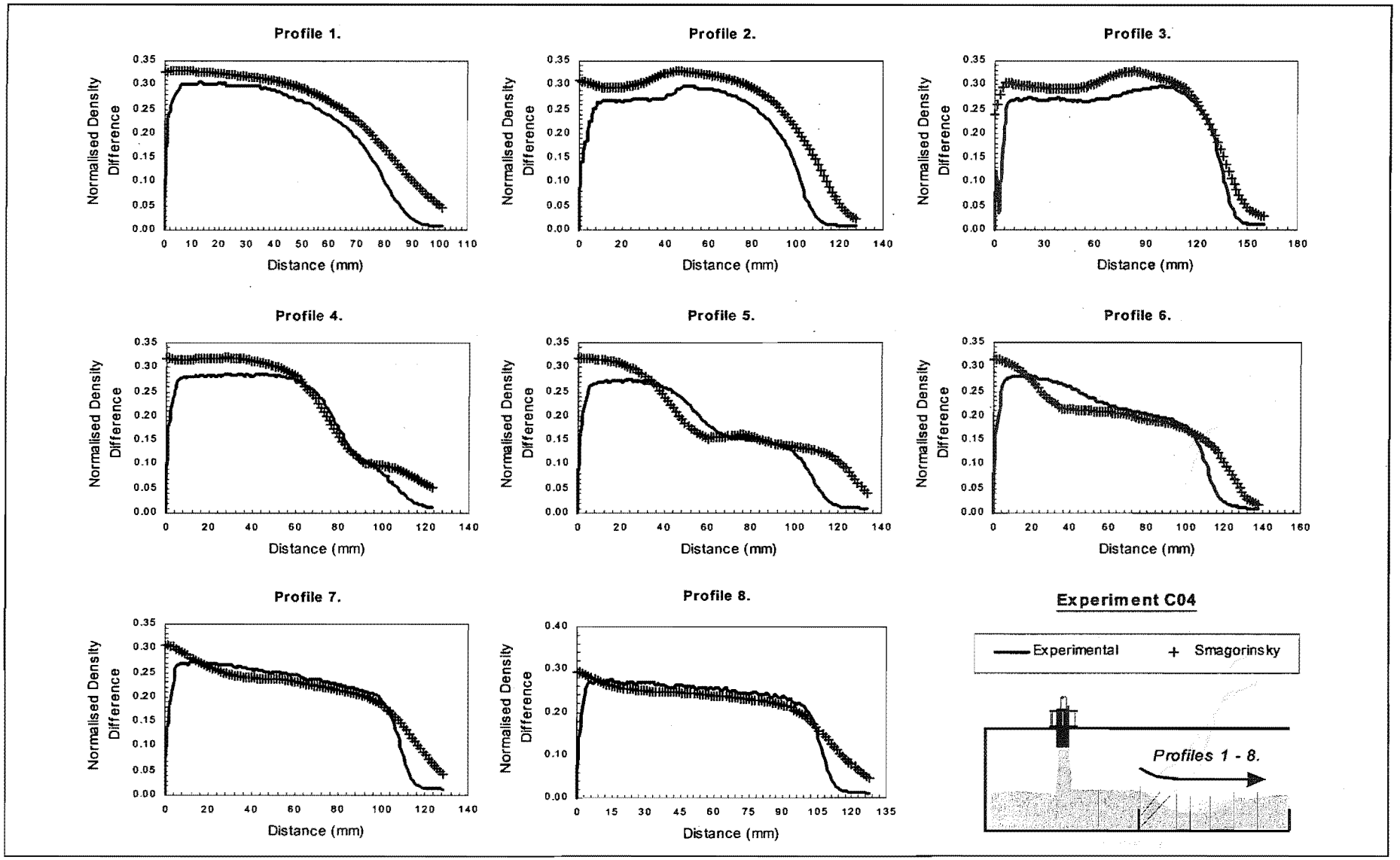
Profile 1.
Profile 2.
Profile 3.
Profile 4.
Profile 5.
Profile 6.
Profile 7.
Profile 8.
Normalised Density Difference
Distance (mm)
Experiment C04
Experimental
Smagorinsky
Profiles 1 - 8.

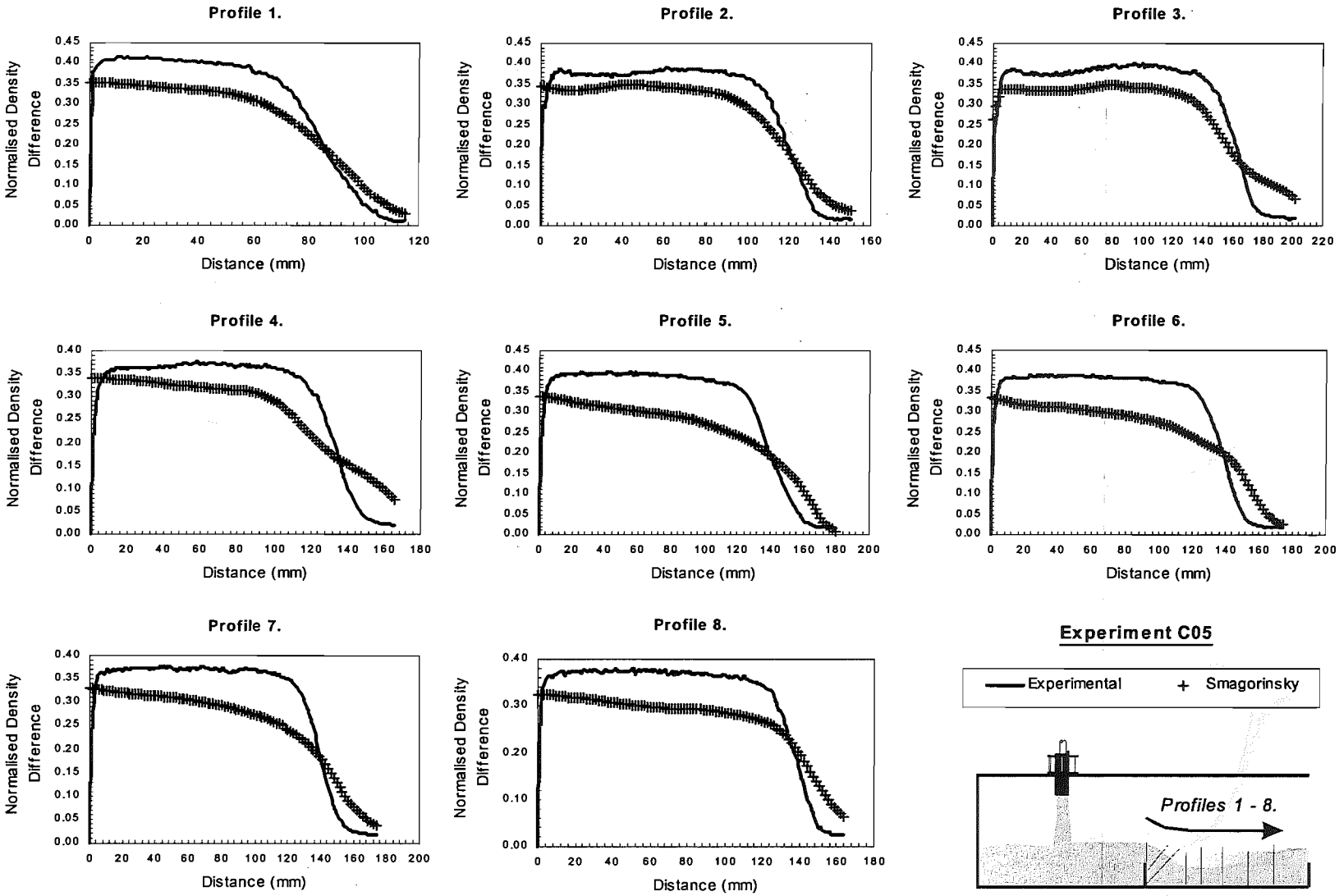
Profile 1.
Profile 2.
Profile 3.
Profile 4.
Profile 5.
Profile 6.
Profile 7.
Profile 8.
Normalised Density Difference
Distance (mm)
Experiment C05
Experimental
Smagorinsky
Profiles 1 - 8.

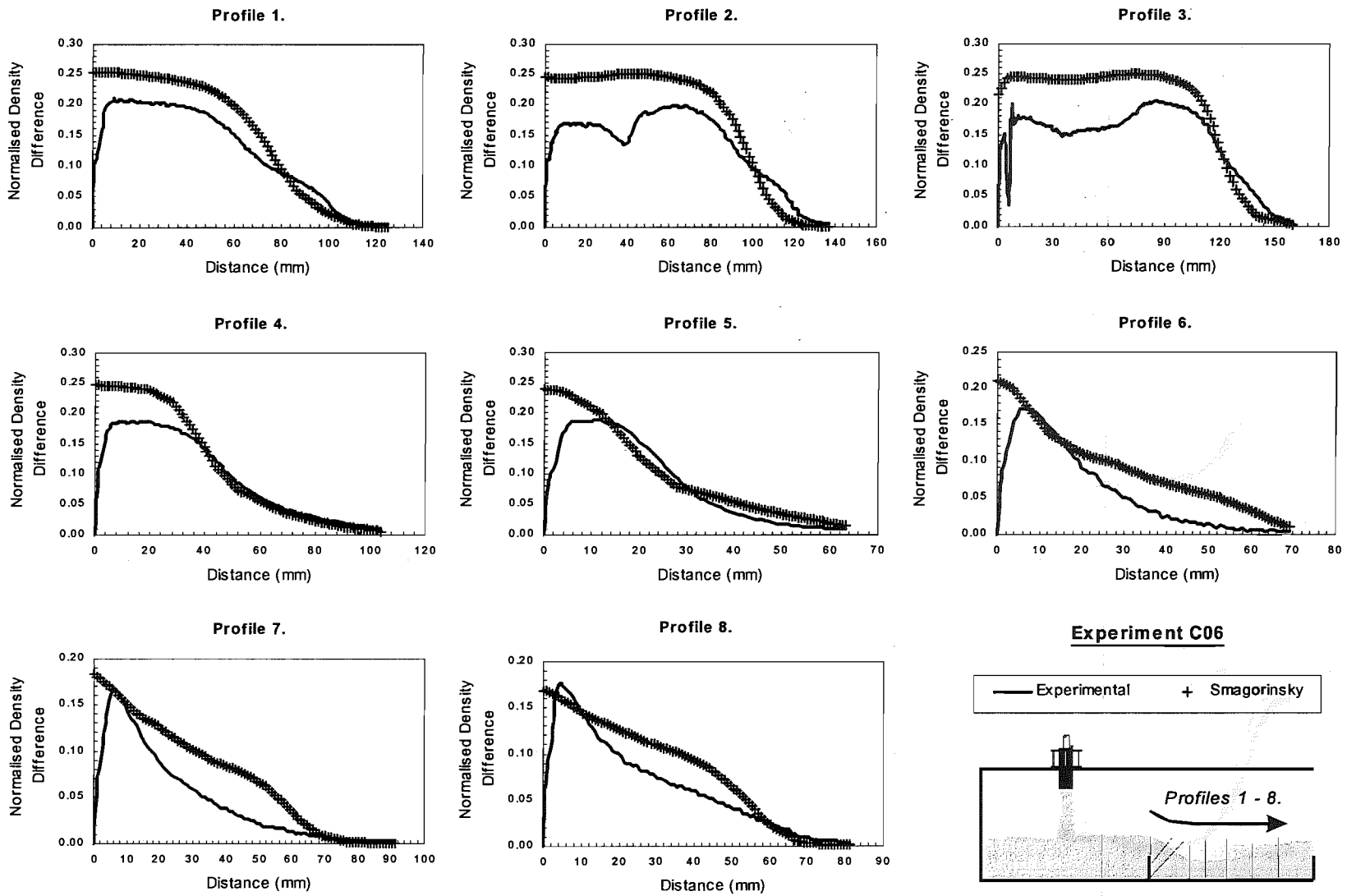
Profile 1.
Profile 2.
Profile 3.
Profile 4.
Profile 5.
Profile 6.
Profile 7.
Profile 8.
Normalised Density Difference
Distance (mm)
Experiment C06
Experimental
Smagorinsky
Profiles 1 - 8.

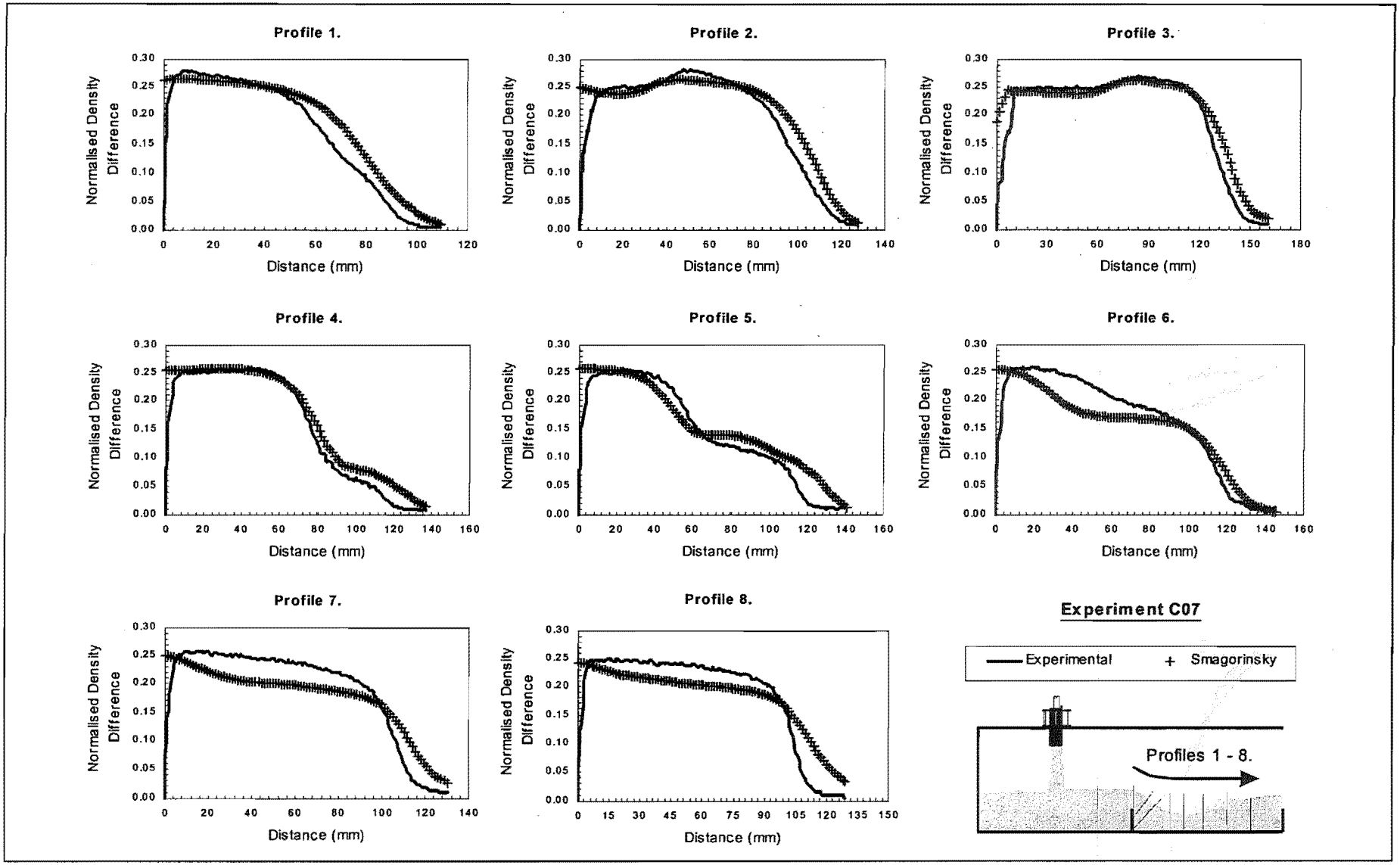
Profile 1.
Profile 2.
Profile 3.
Profile 4.
Profile 5.
Profile 6.
Profile 7.
Profile 8.
Normalised Density Difference
Distance (mm)
Experiment C07
Experimental
Smagorinsky
Profiles 1 - 8.

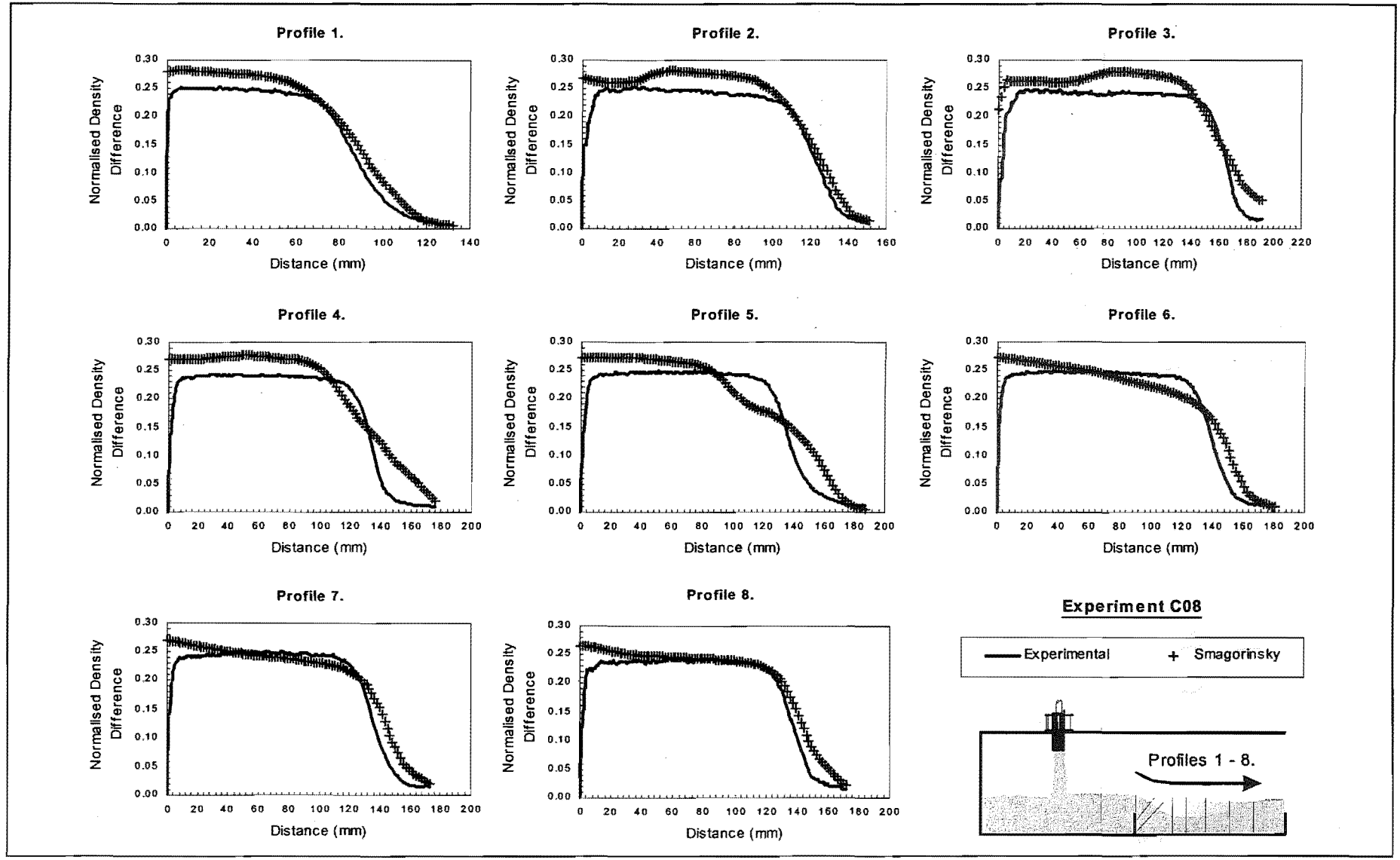
Profile 1.
Profile 2.
Profile 3.
Profile 4.
Profile 5.
Profile 6.
Profile 7.
Profile 8.
Normalised Density Difference
Distance (mm)
Experiment C08
Experimental
Smagorinsky
Profiles 1 - 8.

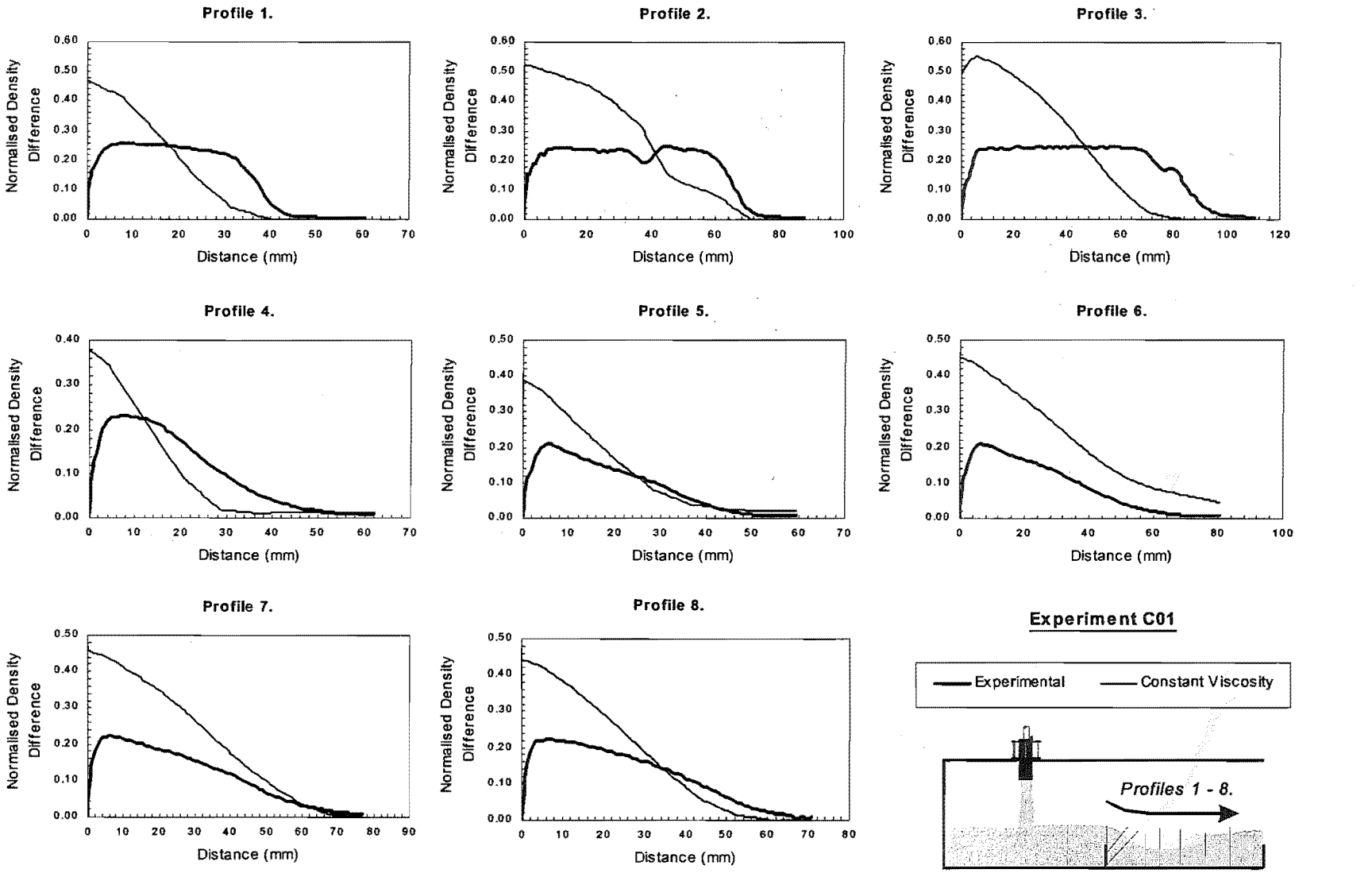
Profile 1.
Profile 2.
Profile 3.
Profile 4.
Profile 5.
Profile 6.
Profile 7.
Profile 8.
Normalised Density Difference
Distance (mm)
Experiment C01
Experimental
Constant Viscosity
Profiles 1 - 8.

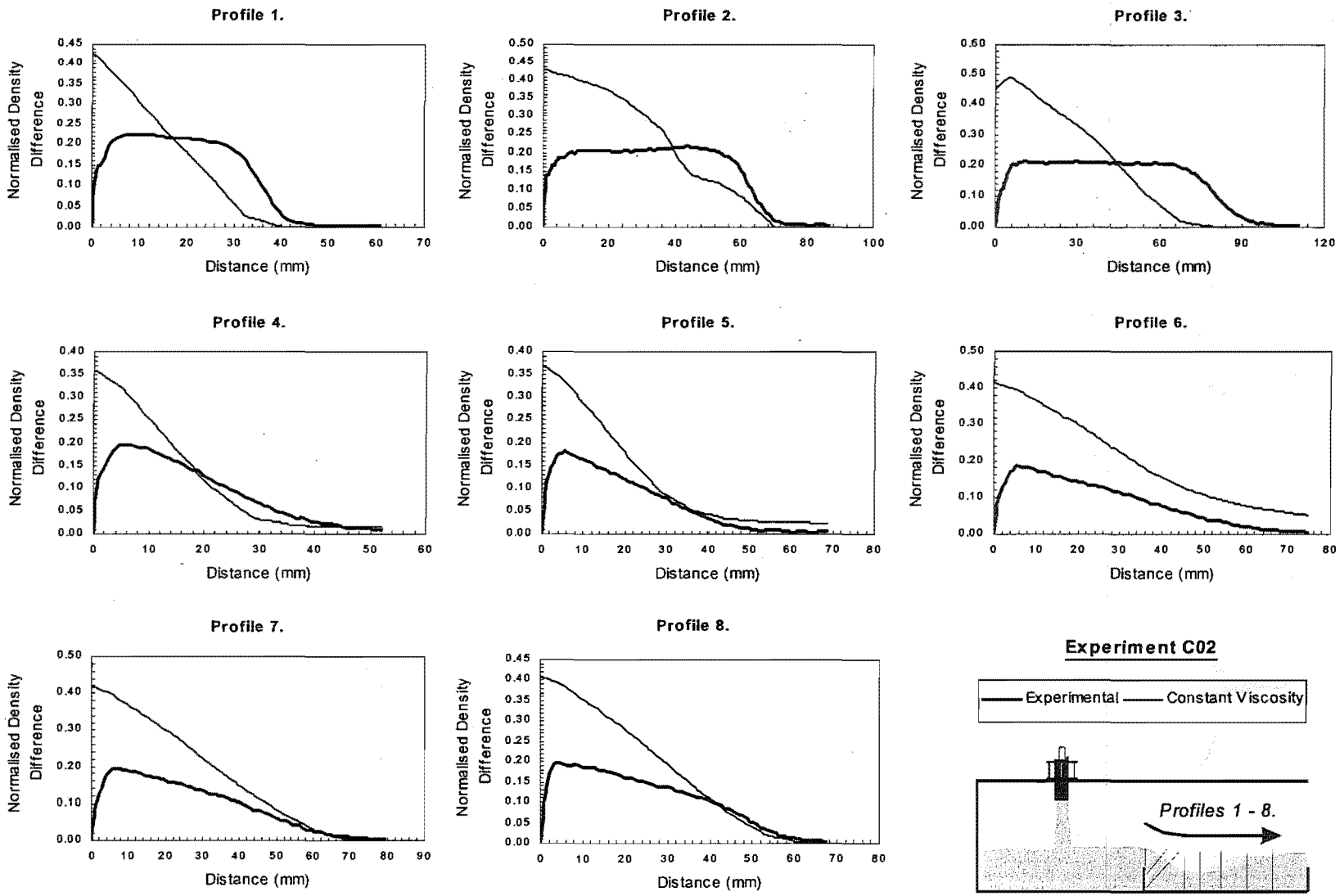
Profile 1.
Profile 2.
Profile 3.
Profile 4.
Profile 5.
Profile 6.
Profile 7.
Profile 8.
Normalised Density Difference
Distance (mm)
Experiment C02
Experimental
Constant Viscosity
Profiles 1 - 8.

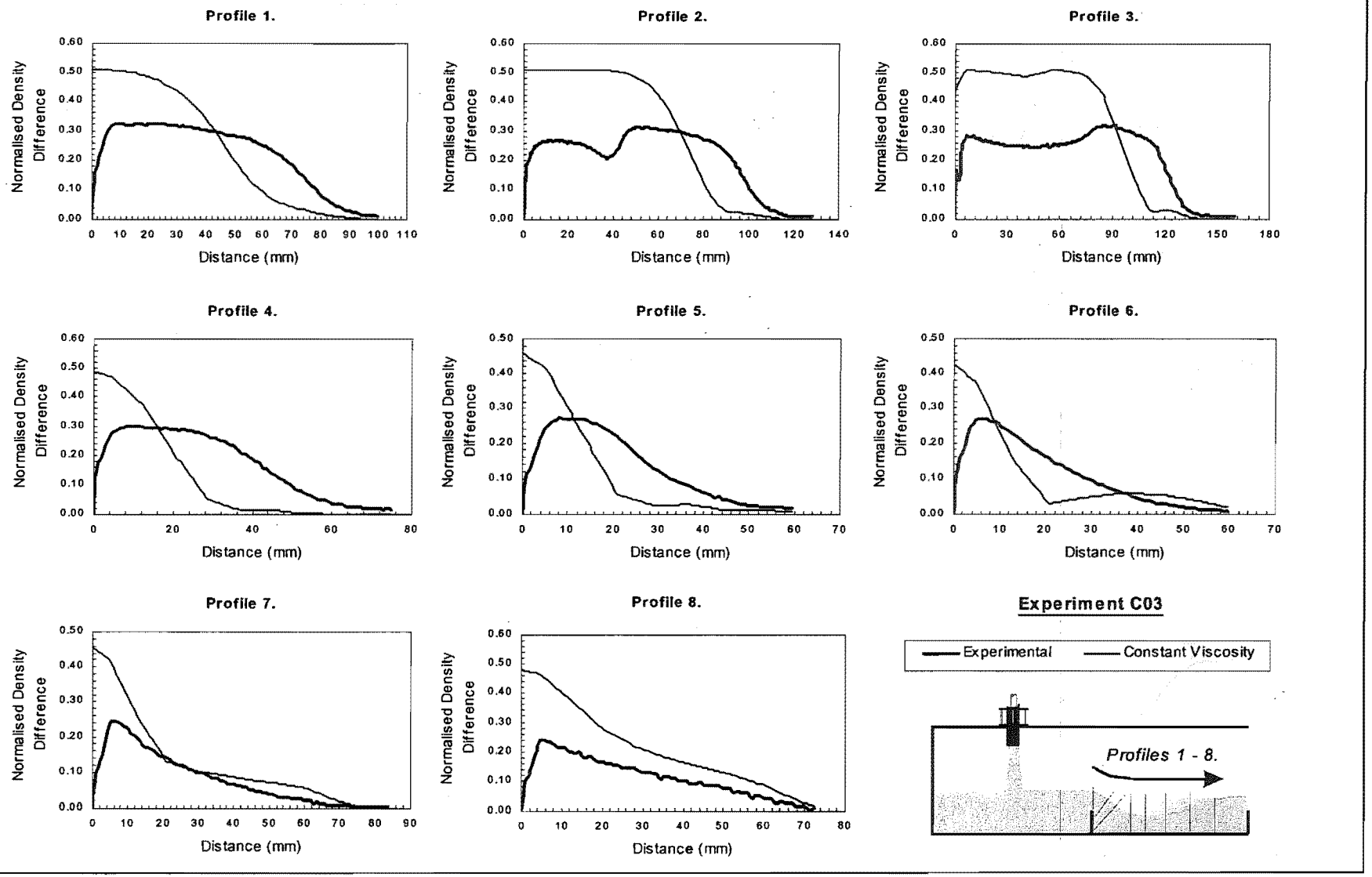
Profile 1.
Profile 2.
Profile 3.
Profile 4.
Profile 5.
Profile 6.
Profile 7.
Profile 8.
Normalised Density Difference
Distance (mm)
Experiment C03
Experimental
Constant Viscosity
Profiles 1 - 8.

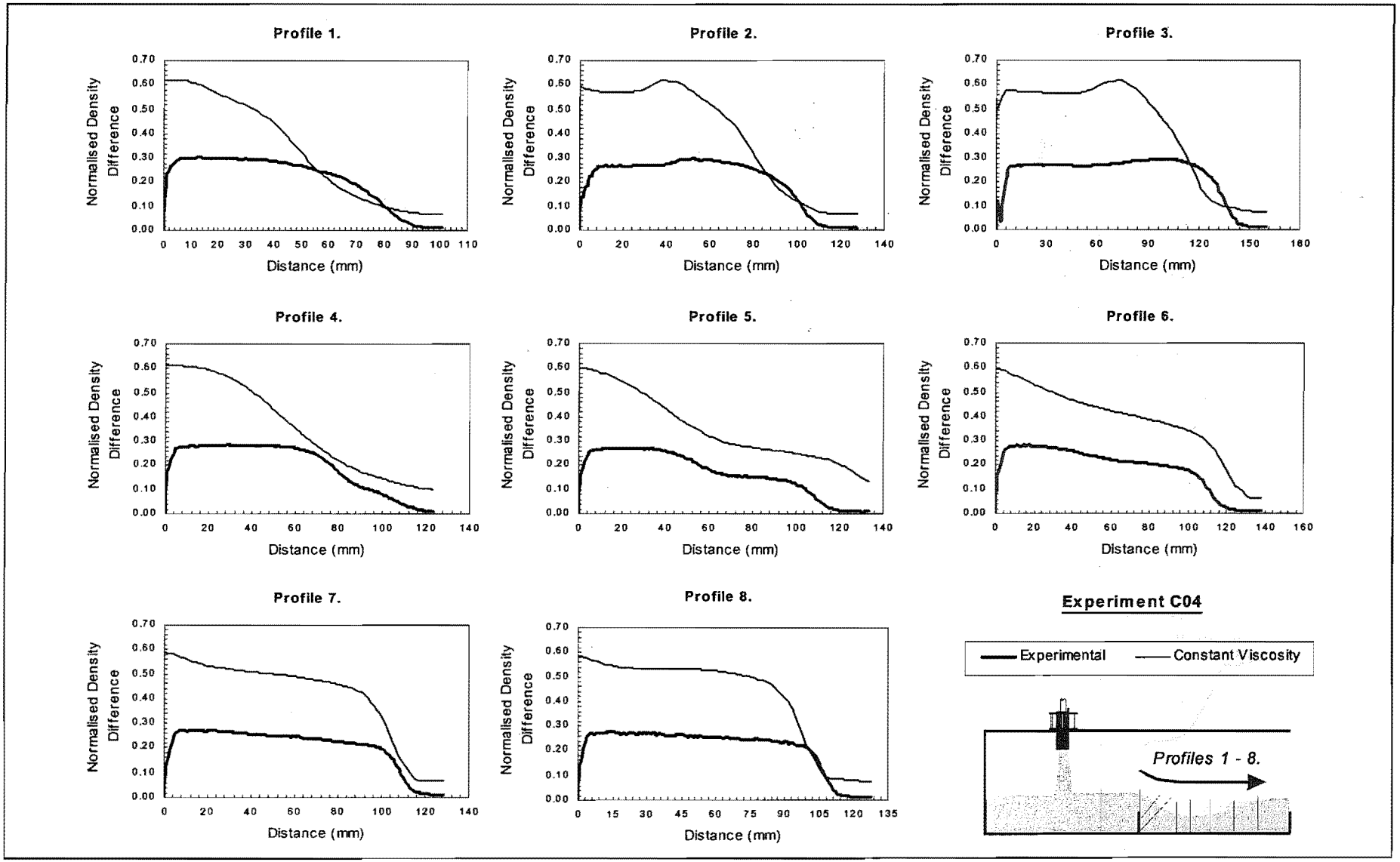
Profile 1.
Profile 2.
Profile 3.
Profile 4.
Profile 5.
Profile 6.
Profile 7.
Profile 8.
Normalised Density Difference
Distance (mm)
Experiment C04
Experimental
Constant Viscosity
Profiles 1 - 8.

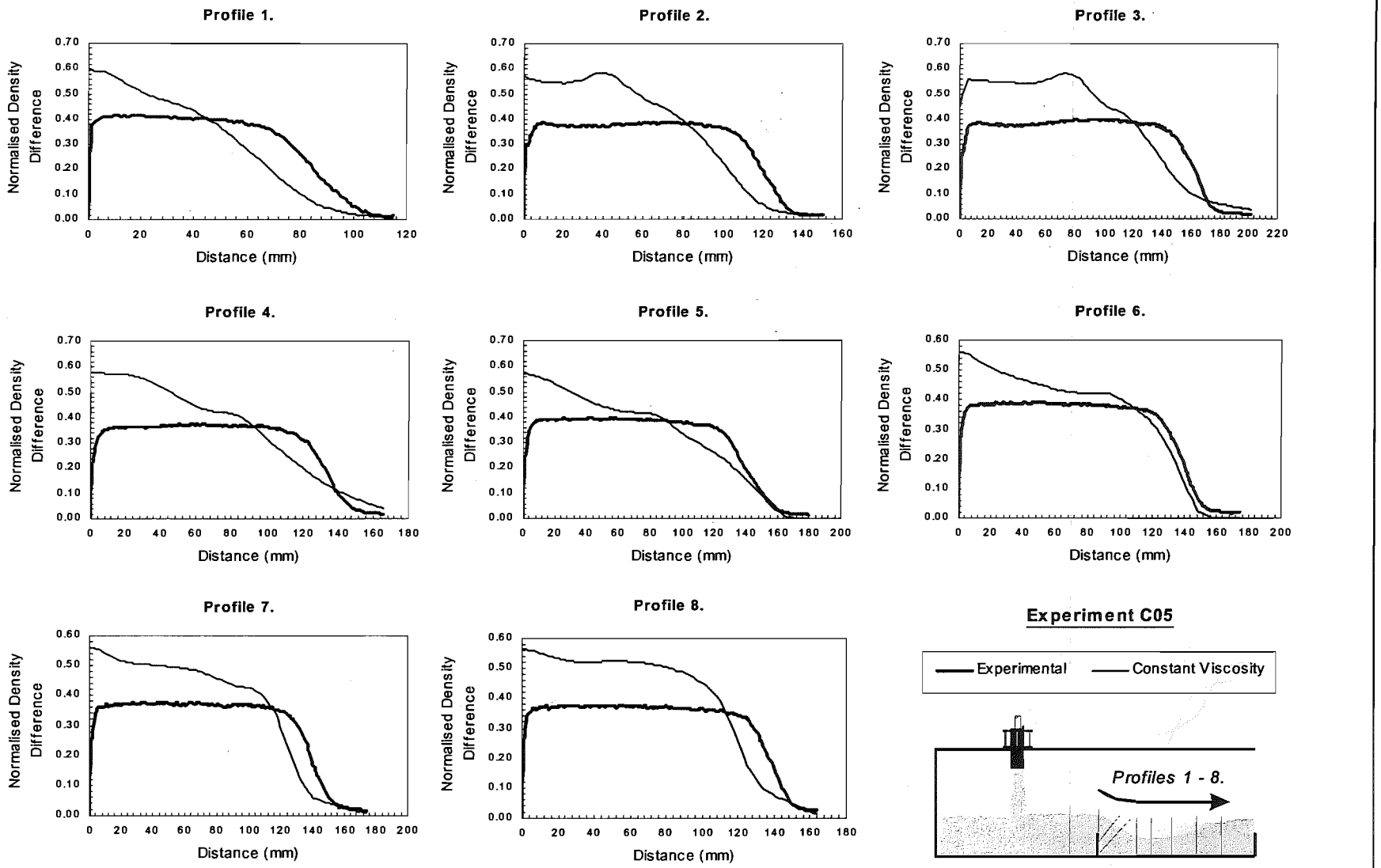
Profile 1.
Profile 2.
Profile 3.
Profile 4.
Profile 5.
Profile 6.
Profile 7.
Profile 8.
Normalised Density Difference
Distance (mm)
Experiment C05
Experimental
Constant Viscosity
Profiles 1 - 8.

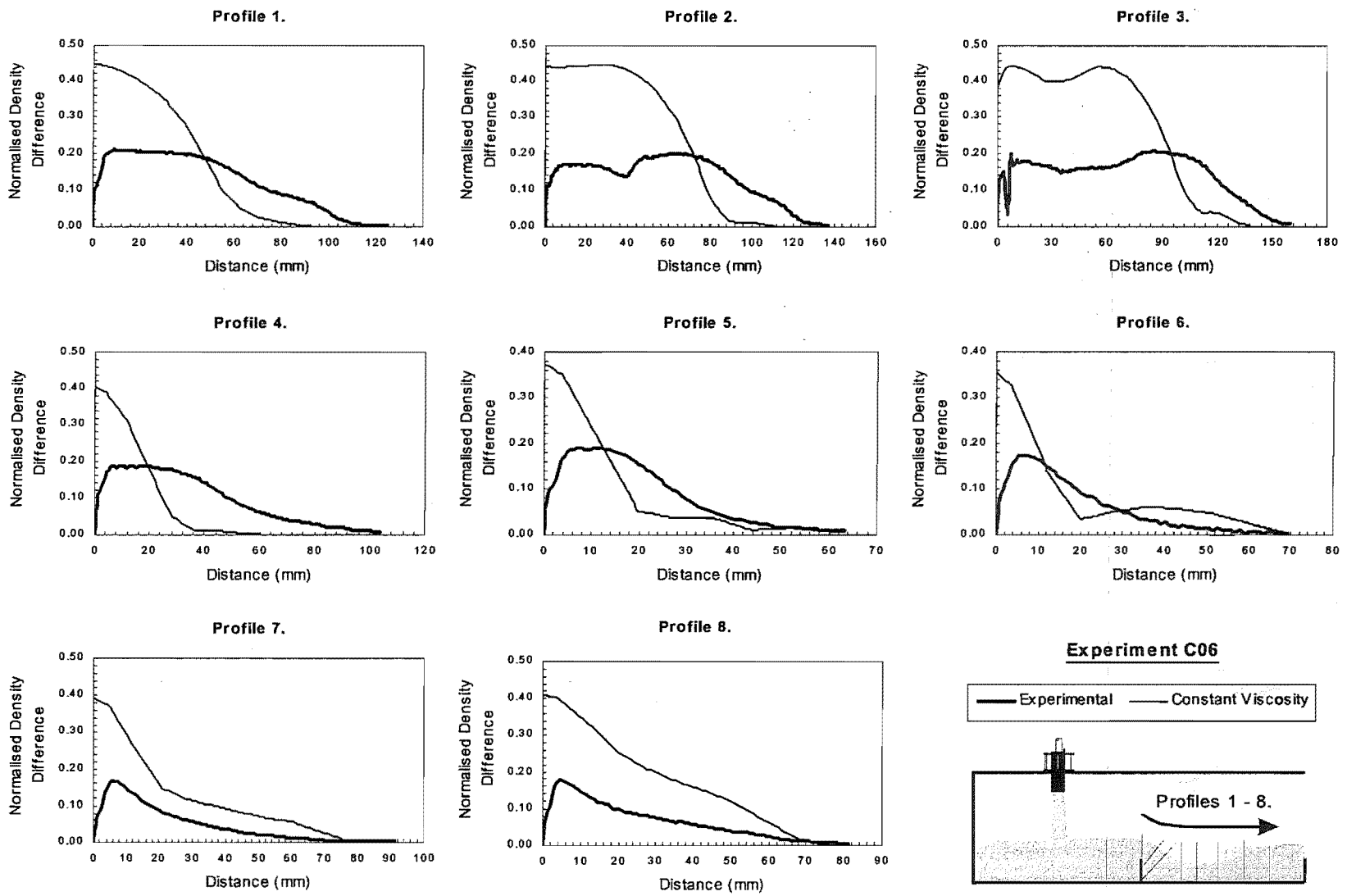
Profile 1.
Profile 2.
Profile 3.
Profile 4.
Profile 5.
Profile 6.
Profile 7.
Profile 8.
Normalised Density Difference
Distance (mm)
Experiment C06
Experimental
Constant Viscosity
Profiles 1 - 8.

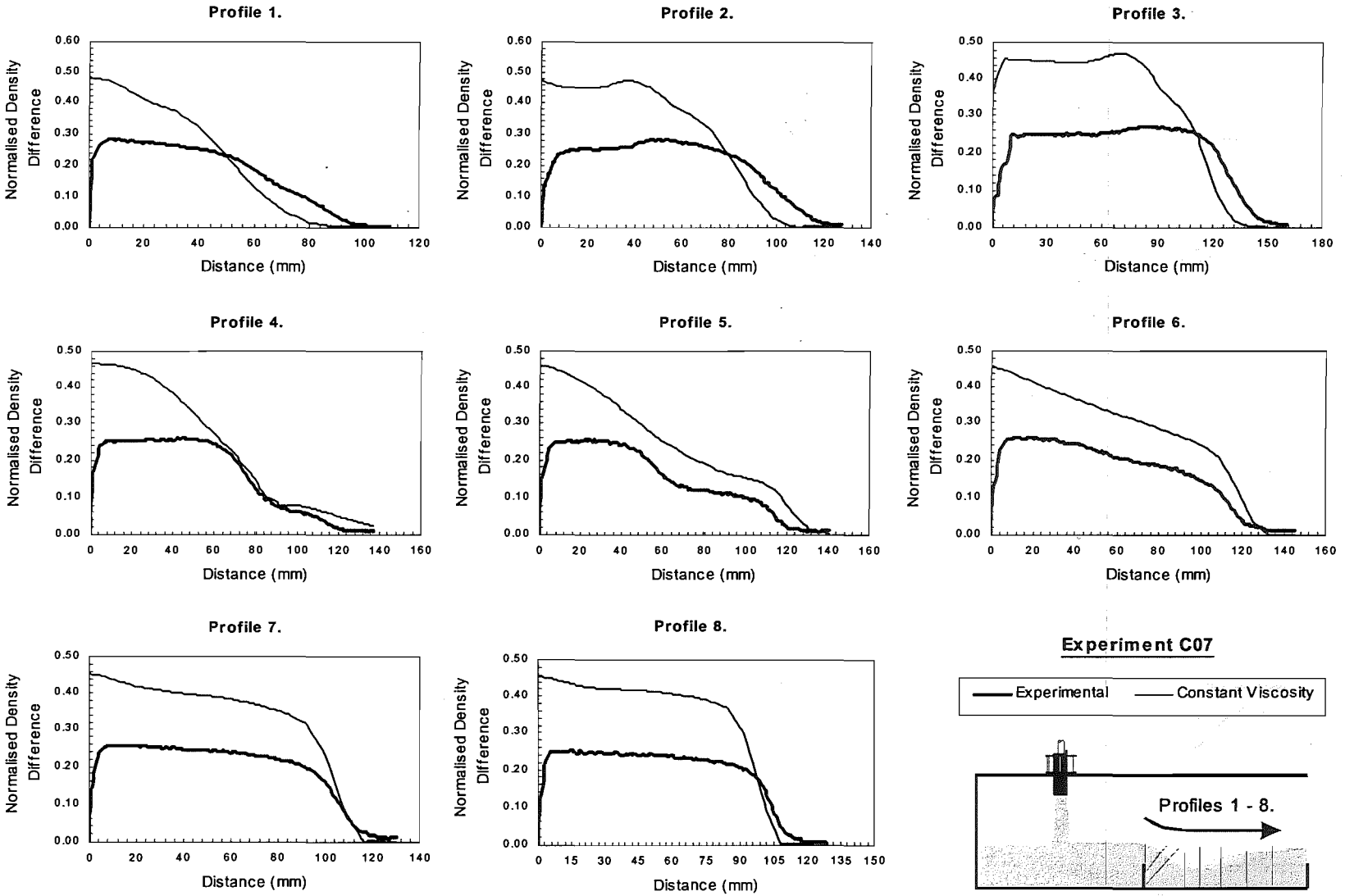
Profile 1.
Profile 2.
Profile 3.
Profile 4.
Profile 5.
Profile 6.
Profile 7.
Profile 8.
Normalised Density Difference
Distance (mm)
Experiment C07
Experimental
Constant Viscosity
Profiles 1 - 8.

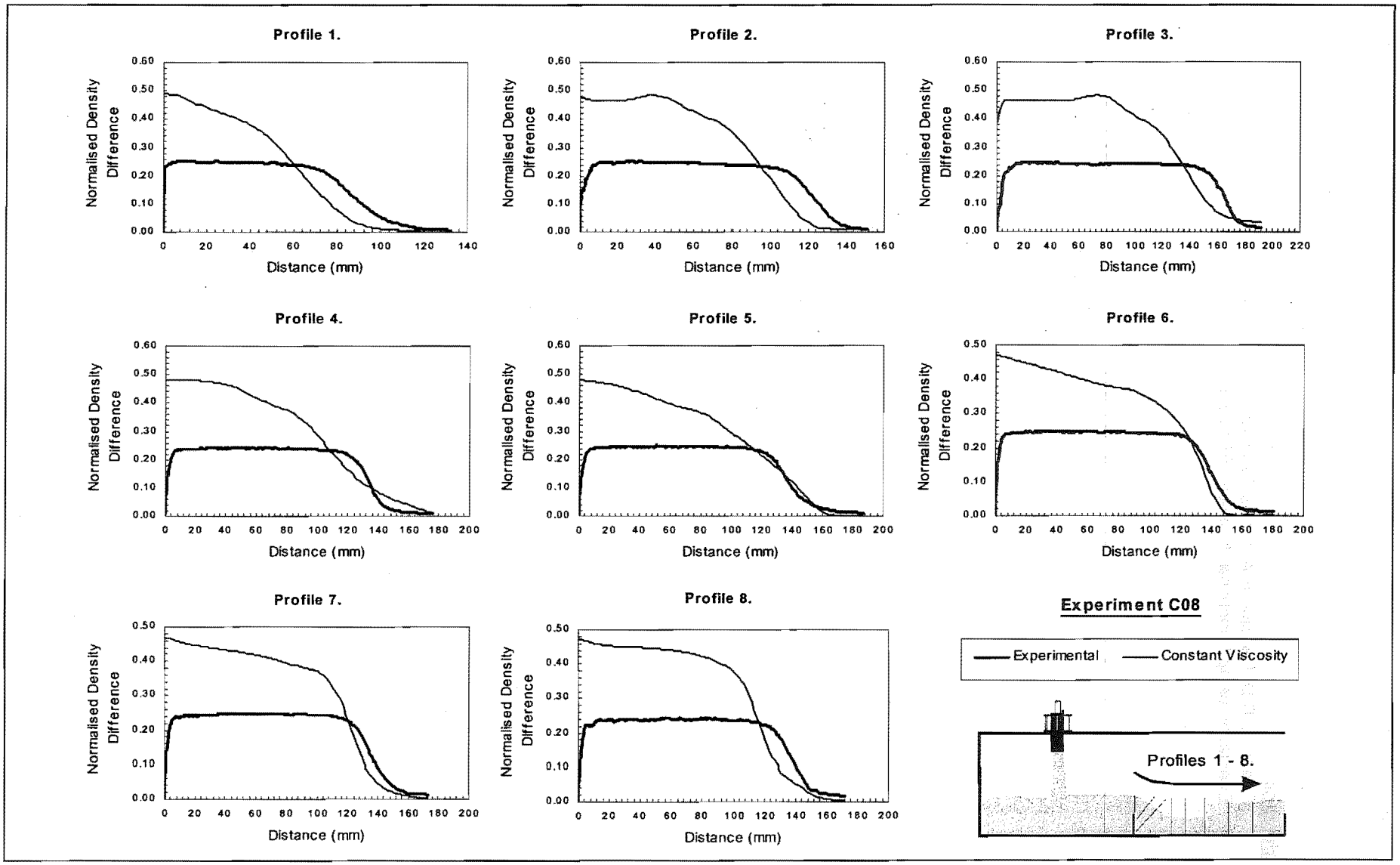
Profile 1.
Profile 2.
Profile 3.
Profile 4.
Profile 5.
Profile 6.
Profile 7.
Profile 8.
Normalised Density Difference
Distance (mm)
Experiment C08
Experimental
Constant Viscosity
Profiles 1 - 8.

Appendix 6 Functional Analysis Results

Reference

Peacock, R.D, Reneke, P.A, Davis, W.D. and Jones, W.W.,(1999) Quantifying Fire Model Evaluation using Functional Analysis, *Fire Safety Journal*, **33**, pp 167-184.

Euclidean Norm

$$\frac{\|E-m\|}{\|E\|}=\frac{\sqrt{\sum_{i=1}^{n}(E_i-m_i)^2}}{\sqrt{\sum_{i=1}^{n}(E)_i^2}}$$

Euclidean Inner Product

$$\frac{\langle E,m\rangle}{\|E\|\,\|m\|}=\frac{\sum_{i=1}^{n}E_i m_i}{\sqrt{\sum_{i=1}^{n}E_i^2\sum_{i=1}^{n}m_i^2}}$$

Euclidean Projection Coefficient

$$a=\frac{\sum_{i=1}^{n}E_i m_i}{\sqrt{\sum_{i=1}^{n}E_i^2\sum_{i=1}^{n}m_i^2}}\sqrt{\frac{\sum_{i=1}^{n}E_i^2}{\sqrt{\sum_{i=1}^{n}m_i^2}}}$$

Hellinger Norm

$$\frac{\|E-m\|}{\|E\|}=\frac{\sqrt{\sum_{i=2}^{n}\left[(E_i-E_{i-1})-(m_i-m_{i-1})\right]^2/(t_i-t_{i-1})^2}}{\sqrt{\sum_{i=2}^{n}(E_i-E_{i-1})^2/(t_i-t_{i-1})^2}}$$

Hellinger Inner Product

$$\frac{\langle E,m\rangle}{\|E\|\,\|m\|}=\frac{\sum_{i=2}^{n}\frac{(E_i-E_{i-1})(m_i-m_{i-1})}{(t_i-t_{i-1})}}{\sqrt{\sum_{i=2}^{n}\frac{(E_i-E_{i-1})^2}{(t_{i+1}-t_i)}\sum_{i=2}^{n}\frac{(m_i-m_{i-1})^2}{(t_i-t_{i-1})}}}$$

Hellinger Projection Coefficient

$$a=\frac{\sum_{i=2}^{n}\frac{(E_i-E_{i-1})(m_i-m_{i-1})}{(t_i-t_{i-1})}}{\sqrt{\sum_{i=2}^{n}\frac{(E_i-E_{i-1})^2}{(t_{i+1}-t_i)}\sum_{i=2}^{n}\frac{(m_i-m_{i-1})^2}{(t_i-t_{i-1})}}}\sqrt{\frac{\sum_{i=2}^{n}\left(\frac{E_i-E_{i-1}}{t_i-t_{i-1}}\right)^2}{\sqrt{\sum_{i=2}^{n}\left(\frac{m_i-m_{i-1}}{t_i-t_{i-1}}\right)^2}}}$$

T-Series - Smagorinsky Simulations

Exp		Profile 1	Profile 2	Profile 3	Profile 4	Profile 5	Profile 6	Profile 7	Profile 8
T01	N_E	0.21	0.26	0.37	0.43	0.52	0.56	0.50	0.39
	IP_E	0.98	0.97	0.93	0.91	0.85	0.83	0.87	0.92
	PC_E	0.96	1.00	1.00	1.08	0.98	0.92	0.93	0.94
	N_H	0.64	0.71	0.80	0.73	0.74	0.88	0.96	0.82
	IP_H	0.81	0.72	0.60	0.69	0.67	0.53	0.46	0.58
	PC_H	1.40	1.27	1.01	0.89	0.90	0.68	0.56	1.16
T02	N_E	0.20	0.33	0.53	0.71	0.87	0.97	0.93	0.67
	IP_E	0.98	0.95	0.85	0.72	0.62	0.59	0.66	0.82
	PC_E	0.96	0.96	0.92	0.81	0.62	0.52	0.55	0.70
	N_H	0.57	0.69	0.85	1.09	1.29	1.40	1.35	0.82
	IP_H	0.84	0.73	0.54	0.20	0.00	-0.07	0.00	0.58
	PC_H	1.26	1.14	0.84	0.30	0.00	-0.07	0.00	1.17
T03	N_E	0.28	0.42	0.75	0.94	1.10	1.21	1.14	0.90
	IP_E	0.96	0.91	0.70	0.54	0.42	0.38	0.47	0.66
	PC_E	0.94	0.94	0.75	0.57	0.41	0.33	0.39	0.57
	N_H	0.58	0.74	1.03	1.14	1.38	1.48	1.49	0.96
	IP_H	0.86	0.68	0.21	-0.05	-0.33	-0.42	-0.27	0.34
	PC_H	1.43	1.20	0.39	-0.10	-0.50	-0.56	-0.31	0.67
T04	N_E	0.23	0.29	0.34	0.46	0.56	0.61	0.45	0.33
	IP_E	0.98	0.96	0.95	0.91	0.89	0.89	0.95	0.98
	PC_E	0.95	0.91	0.89	0.82	0.73	0.68	0.76	0.78
	N_H	0.69	0.67	0.60	0.74	1.01	1.09	0.88	0.81
	IP_H	0.74	0.75	0.80	0.73	0.62	0.48	0.53	0.61
	PC_H	1.22	1.20	0.96	0.72	0.49	0.43	0.68	1.37
T05	N_E	0.28	0.40	0.46	0.59	0.71	0.81	0.69	0.52
	IP_E	0.96	0.92	0.89	0.83	0.79	0.74	0.84	0.92
	PC_E	0.96	0.93	0.90	0.81	0.69	0.62	0.66	0.73
	N_H	0.75	0.77	0.72	0.89	1.06	1.24	0.92	0.85
	IP_H	0.68	0.63	0.70	0.57	0.44	0.29	0.44	0.53
	PC_H	1.29	1.02	0.96	0.63	0.44	0.27	0.69	1.24
T06	N_E	0.25	0.38	0.47	0.61	0.75	0.85	0.68	0.55
	IP_E	0.97	0.93	0.89	0.84	0.76	0.75	0.85	0.91
	PC_E	0.97	0.94	0.87	0.76	0.67	0.58	0.67	0.72
	N_H	0.70	0.83	0.79	0.98	1.05	1.18	0.89	0.81
	IP_H	0.73	0.57	0.66	0.56	0.43	0.32	0.46	0.59
	PC_H	1.20	0.85	0.71	0.51	0.44	0.31	0.88	1.26

Key

N_E = Euclidean Norm
IP_E = Euclidean Inner Product
PC_E = Euclidean Projection Coefficient
N_H = Hellinger Norm
IP_H = Hellinger Inner Product
PC_H = Hellinger Projection Coefficient

T-Series - Constant Viscosity Simulations

Exp		Profile 1	Profile 2	Profile 3	Profile 4	Profile 5	Profile 6	Profile 7	Profile 8
T01	N_E	0.21	0.27	0.40	0.49	0.64	0.69	0.60	0.47
	IP_E	0.98	0.96	0.92	0.87	0.79	0.75	0.83	0.90
	PC_E	0.97	0.98	0.97	0.97	0.81	0.78	0.80	0.85
	N_H	0.62	0.69	0.82	0.76	0.89	1.04	1.06	0.83
	IP_H	0.82	0.76	0.58	0.66	0.52	0.33	0.36	0.56
	PC_H	1.43	1.37	0.99	0.85	0.68	0.43	0.41	1.17
T02	N_E	0.25	0.39	0.57	0.74	0.87	0.98	0.93	0.73
	IP_E	0.97	0.92	0.84	0.72	0.64	0.61	0.72	0.84
	PC_E	0.94	0.91	0.85	0.74	0.61	0.52	0.54	0.64
	N_H	0.58	0.72	0.85	1.15	1.36	1.45	1.32	0.82
	IP_H	0.84	0.70	0.54	0.18	0.05	-0.03	0.19	0.58
	PC_H	1.32	1.10	0.83	0.24	0.05	-0.03	0.17	1.03
T03	N_E	0.32	0.46	0.84	1.09	1.27	1.40	1.39	1.09
	IP_E	0.95	0.89	0.65	0.42	0.31	0.28	0.34	0.60
	PC_E	0.91	0.88	0.65	0.41	0.27	0.21	0.25	0.45
	N_H	0.60	0.76	1.10	1.31	1.58	1.73	1.73	0.96
	IP_H	0.83	0.65	0.14	-0.27	-0.48	-0.53	-0.44	0.37
	PC_H	1.37	1.13	0.23	-0.44	-0.57	-0.54	-0.42	0.59
T04	N_E	0.21	0.28	0.35	0.48	0.60	0.58	0.45	0.40
	IP_E	0.98	0.96	0.94	0.89	0.85	0.89	0.94	0.97
	PC_E	0.94	0.93	0.92	0.85	0.75	0.72	0.76	0.75
	N_H	0.67	0.66	0.64	0.84	0.99	0.92	0.82	0.81
	IP_H	0.74	0.76	0.77	0.64	0.57	0.57	0.60	0.59
	PC_H	1.13	1.20	0.93	0.66	0.51	0.58	0.78	1.11
T05	N_E	0.31	0.41	0.49	0.63	0.75	0.85	0.73	0.60
	IP_E	0.95	0.92	0.88	0.81	0.75	0.70	0.79	0.90
	PC_E	0.95	0.92	0.89	0.79	0.68	0.61	0.66	0.69
	N_H	0.75	0.71	0.72	0.94	1.19	1.20	0.96	0.80
	IP_H	0.68	0.71	0.70	0.50	0.27	0.26	0.36	0.62
	PC_H	1.29	1.19	0.95	0.57	0.28	0.26	0.64	1.32
T06	N_E	0.28	0.41	0.46	0.55	0.70	0.92	0.78	0.66
	IP_E	0.96	0.92	0.90	0.88	0.82	0.78	0.88	0.93
	PC_E	0.95	0.91	0.85	0.76	0.67	0.53	0.59	0.63
	N_H	0.65	0.88	0.80	0.88	0.83	1.02	0.91	0.80
	IP_H	0.79	0.52	0.67	0.68	0.64	0.48	0.43	0.60
	PC_H	1.36	0.73	0.70	0.59	0.68	0.48	0.77	1.08

Key

N_E = Euclidean Norm
IP_E = Euclidean Inner Product
PC_E = Euclidean Projection Coefficient
N_H = Hellinger Norm
IP_H = Hellinger Inner Product
PC_H = Hellinger Projection Coefficient

P-Series - Smagorinsky Simulations

Exp		Profile 1	Profile 2	Profile 3	Profile 4	Profile 5	Profile 6	Profile 7	Profile 8
P01	N_E	0.09	0.28	0.35	0.38	0.40	0.42	0.40	0.42
	IP_E	1.00	0.97	0.97	0.97	0.96	0.96	0.96	0.96
	PC_E	1.00	0.90	0.80	0.77	0.76	0.76	0.78	0.76
	N_H	0.52	0.66	0.53	0.63	0.76	0.96	1.00	1.04
	IP_H	0.86	0.75	0.85	0.84	0.83	0.79	0.78	0.75
	PC_H	1.09	1.11	0.92	0.72	0.61	0.52	0.50	0.48
P06	N_E	0.31	0.48	0.51	0.41	0.41	0.31	0.26	0.23
	IP_E	0.96	0.93	0.97	0.99	0.98	0.99	0.99	0.99
	PC_E	0.86	0.75	0.68	0.72	0.73	0.78	0.82	0.84
	N_H	0.83	0.76	0.55	0.45	0.56	0.58	0.49	0.55
	IP_H	0.59	0.65	0.84	0.94	0.92	0.89	0.91	0.87
	PC_H	0.75	0.89	0.87	0.76	0.70	0.71	0.78	0.79

P-Series - Constant Viscosity Simulations

Exp		Profile 1	Profile 2	Profile 3	Profile 4	Profile 5	Profile 6	Profile 7	Profile 8
P01	N_E	0.11	0.28	0.41	0.51	0.58	0.65	0.69	0.76
	IP_E	0.99	0.97	0.96	0.95	0.94	0.92	0.91	0.90
	PC_E	0.97	0.87	0.75	0.70	0.67	0.64	0.62	0.59
	N_H	0.54	0.72	0.72	0.90	1.18	1.51	1.80	2.02
	IP_H	0.84	0.70	0.79	0.81	0.79	0.75	0.67	0.62
	PC_H	0.97	0.85	0.68	0.54	0.44	0.36	0.29	0.25
P06	N_E	0.42	0.55	0.66	0.67	0.76	0.75	0.73	0.76
	IP_E	0.94	0.93	0.98	0.98	0.97	0.96	0.96	0.95
	PC_E	0.80	0.69	0.61	0.60	0.57	0.58	0.59	0.58
	N_H	1.01	0.90	0.82	0.91	1.26	1.51	1.71	1.79
	IP_H	0.44	0.56	0.78	0.91	0.89	0.83	0.79	0.74
	PC_H	0.49	0.62	0.60	0.53	0.43	0.37	0.33	0.31

Key

N_E = Euclidean Norm
IP_E = Euclidean Inner Product
PC_E = Euclidean Projection Coefficient
N_H = Hellinger Norm
IP_H = Hellinger Inner Product
PC_H = Hellinger Projection Coefficient

Appendix 7 Spatial Uncertainty

Spatial uncertainty of normalised density difference profiles for experiment T02.

Spatial uncertainty of normalised density difference profiles for experiment P01.

Spatial uncertainty of normalised density difference profiles for experiment C01.

Spatial uncertainty of normalised density difference profiles for experiment C03.

Spatial uncertainty of normalised density difference profiles for experiment C04.

Spatial uncertainty of normalised density difference profiles for experiment C05.

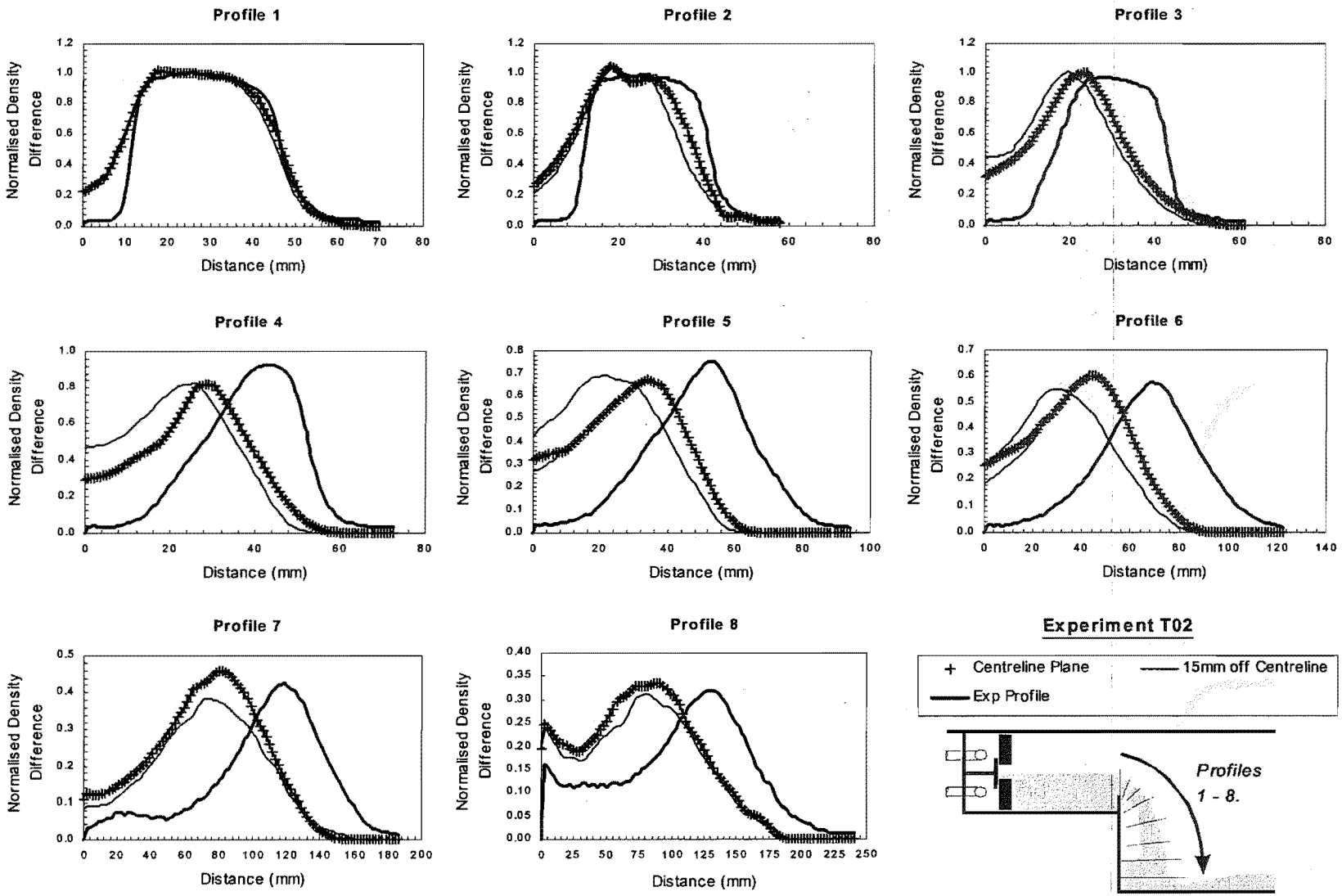
Profile 1
Normalised Density Difference
Distance (mm)
Profile 2
Normalised Density Difference
Distance (mm)
Profile 3
Normalised Density Difference
Distance (mm)
Profile 4
Normalised Density Difference
Distance (mm)
Profile 5
Normalised Density Difference
Distance (mm)
Profile 6
Normalised Density Difference
Distance (mm)
Profile 7
Normalised Density Difference
Distance (mm)
Profile 8
Normalised Density Difference
Distance (mm)
Experiment T02
Centreline Plane
15mm off Centreline
Exp Profile
Profiles
1 - 8.

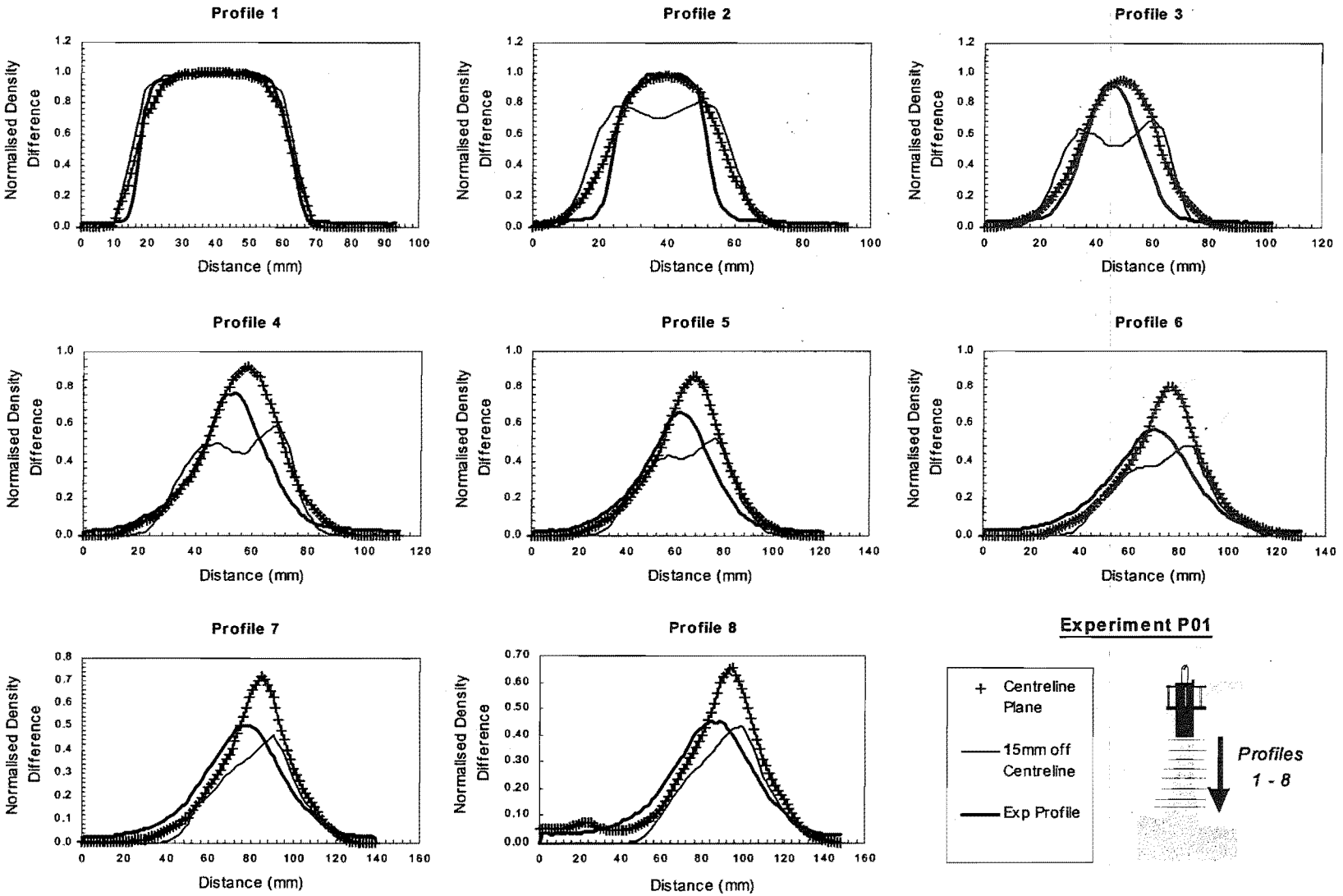
Profile 1
Profile 2
Profile 3
Profile 4
Profile 5
Profile 6
Profile 7
Profile 8
Normalised Density Difference
Distance (mm)
Experiment P01
Centreline Plane
15mm off Centreline
Exp Profile
Profiles 1 - 8

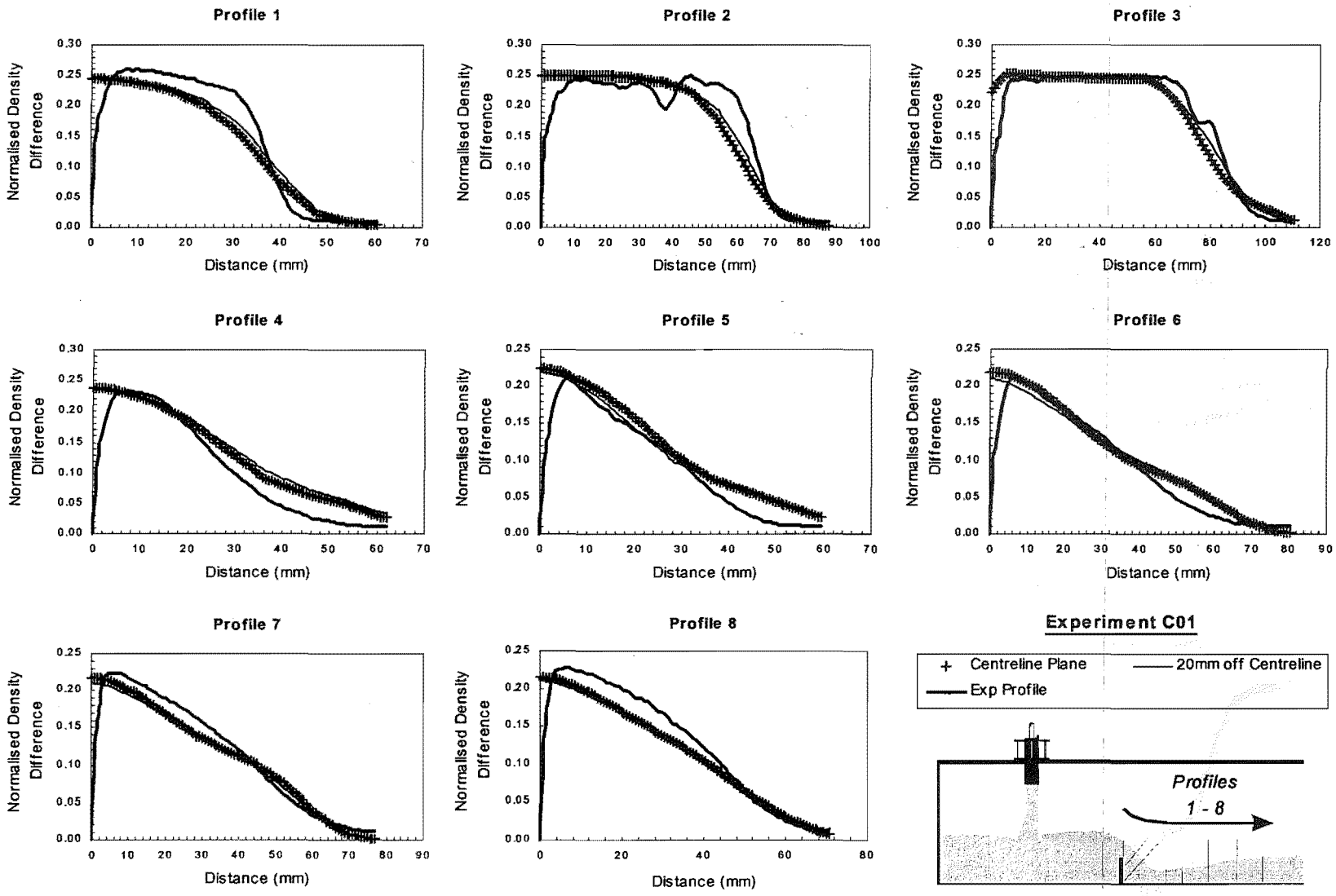
Profile 1
Profile 2
Profile 3
Profile 4
Profile 5
Profile 6
Profile 7
Profile 8
Normalised Density Difference
Distance (mm)
Experiment C01
Centreline Plane
20mm off Centreline
Exp Profile
Profiles
1 - 8

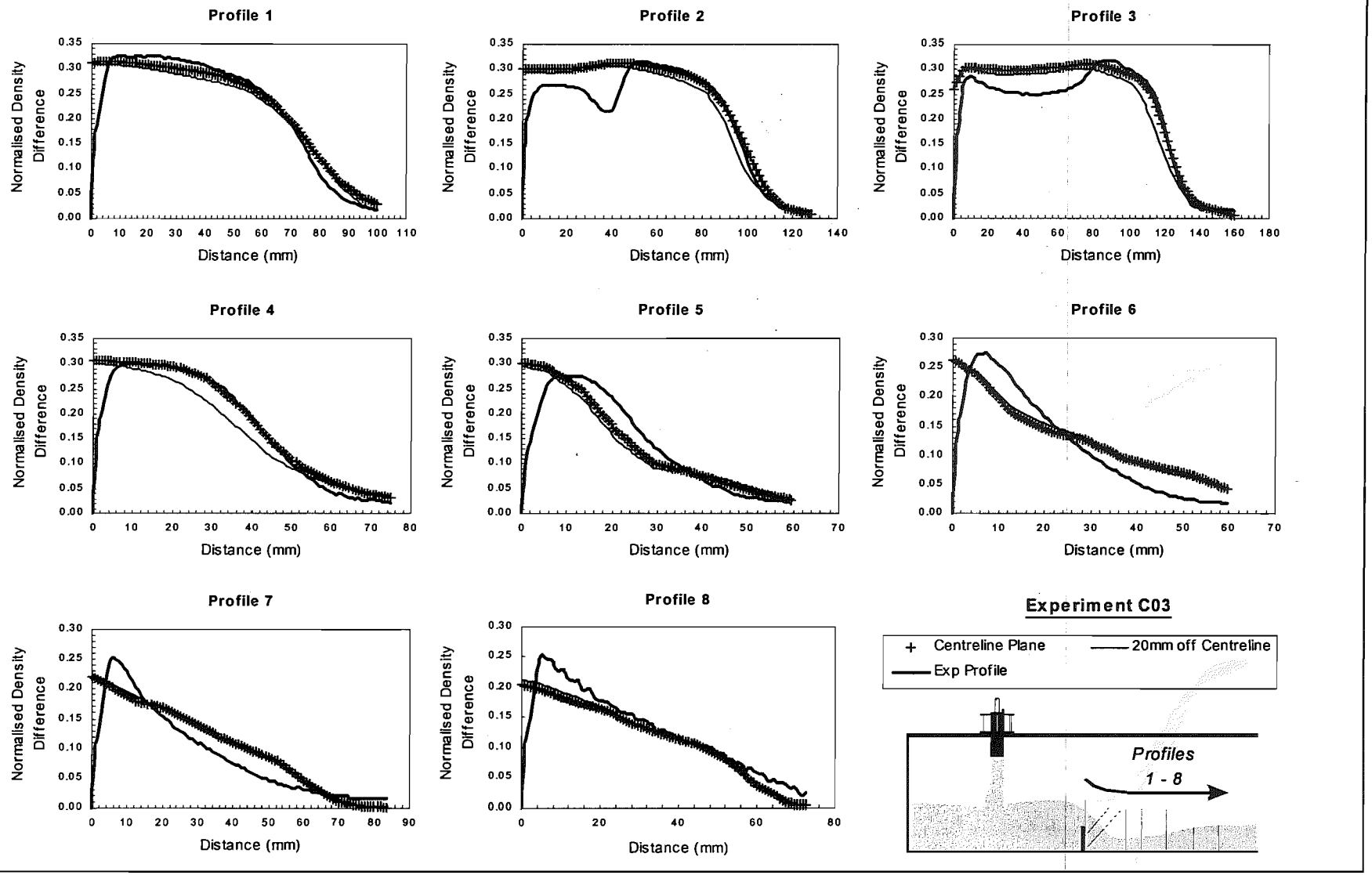
Profile 1
Profile 2
Profile 3
Profile 4
Profile 5
Profile 6
Profile 7
Profile 8
Normalised Density Difference
Distance (mm)
Experiment C03
Centreline Plane
20mm off Centreline
Exp Profile
Profiles
1 - 8

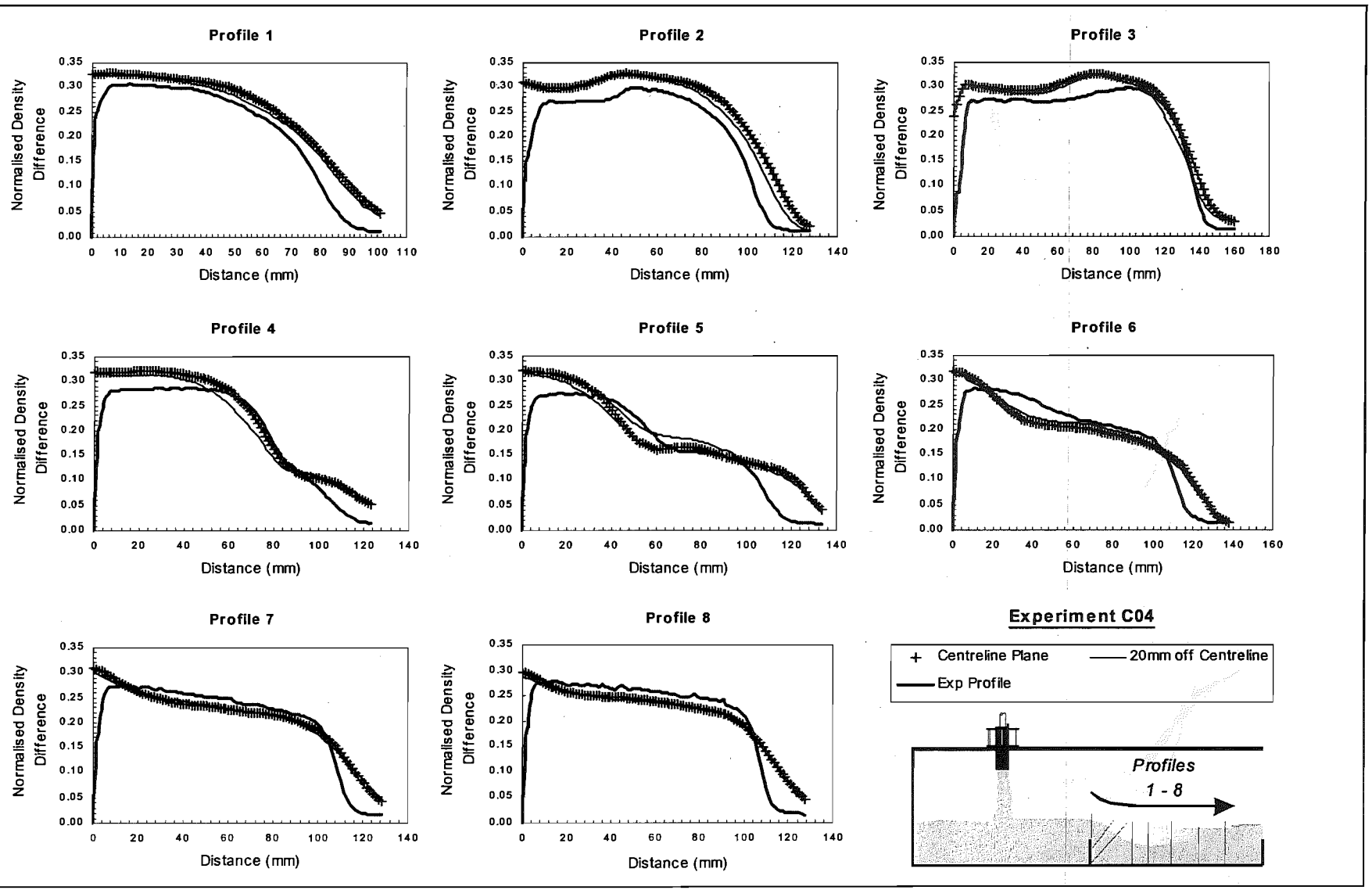
Profile 1
Profile 2
Profile 3
Profile 4
Profile 5
Profile 6
Profile 7
Profile 8
Normalised Density Difference
Distance (mm)
Experiment C04
Centreline Plane
20mm off Centreline
Exp Profile
Profiles
1 - 8

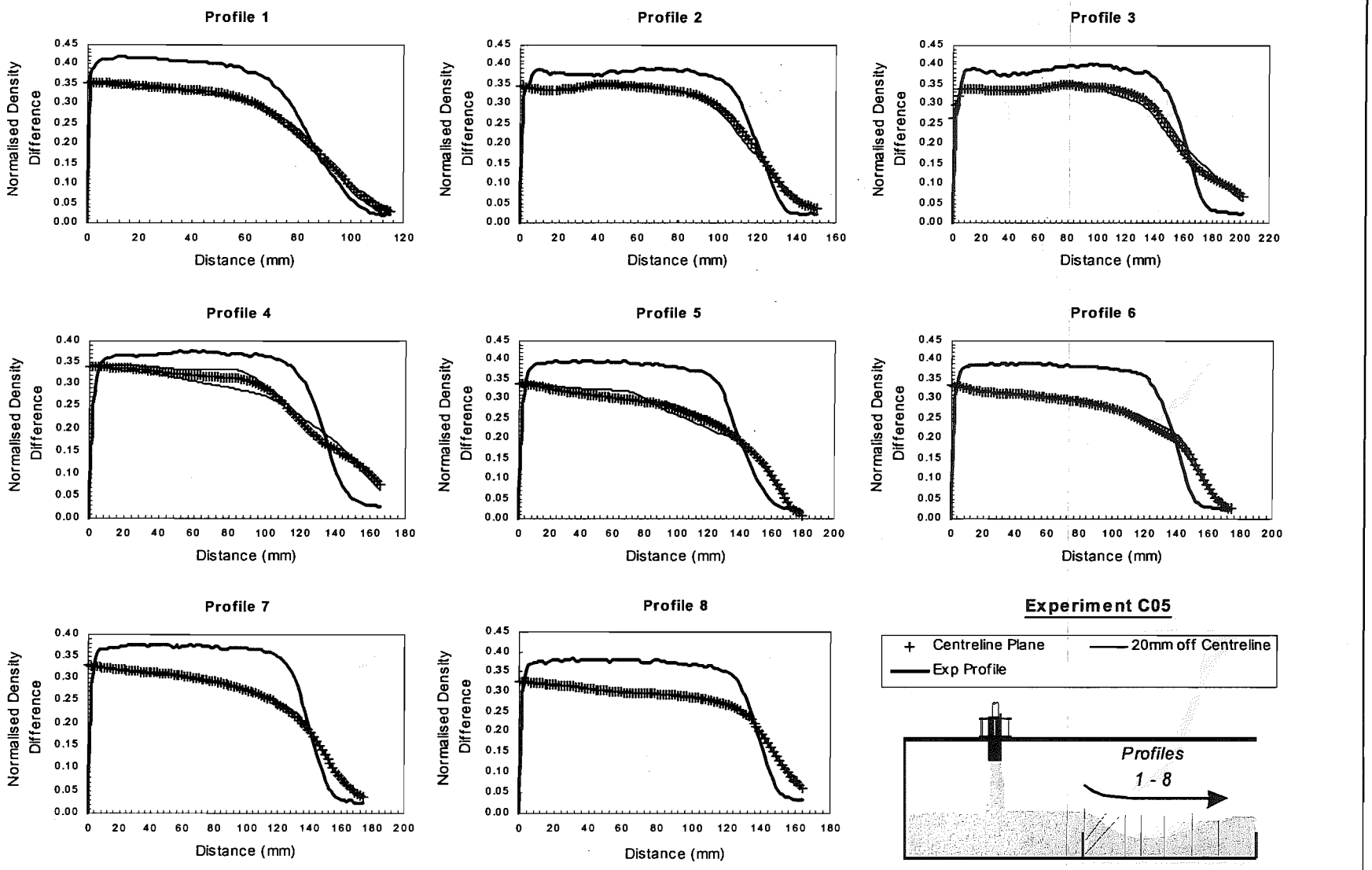
Profile 1
Profile 2
Profile 3
Profile 4
Profile 5
Profile 6
Profile 7
Profile 8
Normalised Density Difference
Distance (mm)
Experiment C05
Centreline Plane
20mm off Centreline
Exp Profile
Profiles
1 - 8

Appendix 8 Fortran Code for the Profile Program

```
      program profile
c
      parameter(idim=200)
      parameter(jdim=200)
      parameter(kdim=200)
      PARAMETER (NBD=300)
      real x(0:idim),y(0:jdim),z(0:kdim),ss(101,9),qq(101,9),xjunk(18)
      real q(idim,idim),qdum(idim,idim),qe(1000,9),se(1000,9),
     .     qout(101,18)
      INTEGER IB1(NBD),IB2(NBD),JB1(NBD),JB2(NBD),KB1(NBD),KB2(NBD)
      character*20 sfile,efile,CHID,OUTFILE
      character*40 label
      COMMON/CTRANS/ C1(0:20,3),C2(0:20,3),C3(0:20,3),CC(20,3),PC(20,3)
      COMMON/ITRANS/ NOC(3),LU4,ITRAN(3),IDERIV(20,3)
c
C Interpolation function
C
      PP(P1) = 1.-P1
      RR(R1) = 1.-R1
      AFILL(A11,A21,A12,A22,P1,R1)=
     .     (PP(P1)*A11+P1*A21)*RR(R1)+(PP(P1)*A12+P1*A22)*R1
C
      LU5  = 5
c
      write(6,*) ' Enter starting time for average (s):'
      read(5,*) tstart
c
      write(6,*) ' Enter ending time for average (s):'
      read(5,*) tend
c
      PRINT*,' Enter Job ID String:'
      READ(*,'(A)') CHID
      DO 293 I=1,30
      IF (CHID(I:I).EQ.' ') THEN
         NCHAR = I-1
         GOTO 194
         ENDIF
  293 END DO
C
  194 CONTINUE
      PRINT*,' Enter output file name:'
      READ(*,'(A)') OUTFILE
C
      LU4 = 4
      OPEN (LU4,FILE=CHID(1:NCHAR)//'.smv',FORM='FORMATTED')
C
      READ(LU4,*)
      READ(LU4,'(3I5)') IBAR,JBAR,KBAR
      READ(LU4,*)
      READ(LU4,'(6F12.5)') XBAR0,XBAR,YBAR0,YBAR,ZBAR0,ZBAR
C
      DXI   = (XBAR-XBAR0)/REAL(IBAR)
      DETA  = (YBAR-YBAR0)/REAL(JBAR)
      DZETA = (ZBAR-ZBAR0)/REAL(KBAR)
      nxp   = IBAR+1
      nyp   = JBAR+1
      nzp   = KBAR+1
```

```
C Compute transformation function
C
      READ(LU4,*)
      READ(LU4,*) NOC(1)
      DO N=1,NOC(1)
      READ(LU4,*) IDERIV(N,1),CC(N,1),PC(N,1)
      ENDDO
      DO 6 I=0,IBAR
      READ(LU4,*) IDUM,X(I)
    6 CONTINUE
C
      READ(LU4,*)
      READ(LU4,*) NOC(2)
      DO N=1,NOC(2)
      READ(LU4,*) IDERIV(N,2),CC(N,2),PC(N,2)
      ENDDO
      DO 5 J=0,JBAR
      READ(LU4,*) JDUM,Y(J)
    5 CONTINUE
C
      READ(LU4,*)
      READ(LU4,*) NOC(3)
      DO N=1,NOC(3)
      READ(LU4,*) IDERIV(N,3),CC(N,3),PC(N,3)
      ENDDO
      DO 9 K=0,KBAR
      READ(LU4,*) KDUM,Z(K)
    9 ENDDO
C
      READ(LU4,*)
      READ(LU4,*) NB
      DO N=1,NB
      READ(LU4,*)
      ENDDO
      DO N=1,NB
      READ(LU4,'(6I5)') IB1(N),IB2(N),JB1(N),JB2(N),KB1(N),KB2(N)
      ENDDO
C
      CALL SETGRID(X(1),X(NXP),Y(1),Y(NYP),Z(1),Z(NZP))
C
      write(6,*) ' Enter slice file, CHID_nn.sf'
      read(5,'(a)') sfile
      write(6,*) ' Enter coordinates of shelf edge (mm)'
      read(5,*) x0,y0
      x0 = x0/1000.
      y0 = y0/1000.
      write(6,*) ' Enter experimental file'
      read(5,'(a)') efile
      iexp = 0
      if (efile.ne.'0') iexp = 1
c
      open(20,file=sfile,form='unformatted')
c
      READ(20)
      READ(20)
      READ(20)
      READ(20) ISP1,ISP2,JSP1,JSP2,KSP1,KSP2
      if (isp1.eq.isp2) isp=1
      if (jsp1.eq.jsp2) isp=2
      if (ksp1.eq.ksp2) isp=3
c
```

```
c Compute simulated vertical averages
c
      isets = 0
   26 read(20,end=31) time
      if (isp.eq.1) read(20,end=31) ((qdum(j,k),j=1,nyp),k=1,nzp)
      if (isp.eq.2) read(20,end=31) ((qdum(i,k),i=1,nxp),k=1,nzp)
      if (isp.eq.3) read(20,end=31) ((qdum(i,j),i=1,nxp),j=1,nyp)
      if (time.lt.tstart) goto 26
      if (time.gt.tend)   goto 31
      isets = isets + 1
      if (isp.eq.1) then
      do 29 k=1,nzp
      do 29 j=1,nyp
   29 q(j,k) = q(j,k) + qdum(j,k)
      endif
      if (isp.eq.2) then
      do 39 k=1,nzp
      do 39 i=1,nxp
   39 q(i,k) = q(i,k) + qdum(i,k)
      endif
      if (isp.eq.3) then
      do 49 j=1,nyp
      do 49 i=1,nxp
   49 q(i,j) = q(i,j) + qdum(i,j)
      endif
   30 goto 26
c
   31 close(20)
c
      if (isp.eq.1) then
      do 33 k=1,nzp
      do 33 j=1,nyp
      q(j,k) = (q(j,k)/real(isets))
   33 continue
      endif
      if (isp.eq.2) then
      do 43 k=1,nzp
      do 43 i=1,nxp
      q(i,k) = (q(i,k)/real(isets))
   43 continue
      endif
      if (isp.eq.3) then
      do 53 j=1,nyp
      do 53 i=1,nxp
      q(i,j) = (q(i,j)/real(isets))
   53 continue
      endif
c
      if (iexp.gt.0) then
      open(29,file=efile,form='FORMATTED')
      read(29,*)
      le = 0
      do 63 i=1,10000
      read(29,*,end=64) (xjunk(k),k=1,18)
      le = le + 1
      do 62 ip=1,9
      se(le,ip) = xjunk(2*ip-1)
      qe(le,ip) = xjunk(2*ip)
   62 continue
   63 continue
   64 continue
```

```
      endif
c
      iframe = 0
    1 iframe = iframe + 1
      ifr = mod(iframe,4)
c
      write(6,*) ' Enter starting (x,y):'
      read(5,*) xs,ys
      xs = xs/1000.
      ys = ys/1000.
      write(6,*) ' Enter ending (x,y):'
      read(5,*) xf,yf
      if (xs.eq.xf .and. ys.eq.yf) goto 500
      xf = xf/1000.
      yf = yf/1000.
c
      xs = x0 + xs - XBAR0
      ys = y0 - ys - ZBAR0
      xf = x0 + xf - XBAR0
      yf = y0 - yf - ZBAR0
c
      dl = sqrt((xf-xs)**2+(yf-ys)**2)/real(100)
      dxx = (xf-xs)/real(100)
      dyy = (yf-ys)/real(100)
      if (isp.eq.1) then
         nt1= 2
         nt2= 3
         dx = (y(nyp-1)-y(0))/real(nyp-1)
         dy = (z(nzp-1)-z(0))/real(nzp-1)
         endif
      if (isp.eq.2) then
         nt1= 1
         nt2= 3
         dx = (x(nxp-1)-x(0))/real(nxp-1)
         dy = (z(nzp-1)-z(0))/real(nzp-1)
         endif
      if (isp.eq.3) then
         nt1= 1
         nt2= 2
         dx = (x(nxp-1)-x(0))/real(nxp-1)
         dy = (y(nyp-1)-y(0))/real(nyp-1)
         endif
c
      do 80 l=1,101
      xx = xs + dxx*(l-1)
      yy = ys + dyy*(l-1)
      ss(l,iframe) = dl*(l-1)*1000.
      xi = ginv(xx,nt1)/dx + 0.5
      yj = ginv(yy,nt2)/dy + 0.5
      i1 = xi
      j1 = yj
      qq(l,iframe) = AFILL(q(i1,j1),q(i1+1,j1),q(i1,j1+1),q(i1+1,j1+1),
     .             xi-i1,yj-j1)
   80 continue
c
      if (iexp.gt.0 .and. xs.gt.xf) then
      s0 = se(1,iframe)
      s1 = se(le,iframe)
      do 71 l=1,le
   71 se(l,iframe) = ss(101,iframe) - (se(l,iframe)-s0)
      endif
```

```
c
      goto 1
c
  500 continue
c
      do iframe=1,9
      do i=1,101
      qout(i,2*iframe-1) = ss(i,iframe)
      qout(i,2*iframe  ) = qq(i,iframe)
      enddo
      enddo
c
      open(15,file=OUTFILE,form='formatted',status='replace')
      write(15,*) 'Distance,Profile 1,Distance,Profile 2,Distance,'//
     .'Profile 3,Distance,Profile 4,Distance,Profile 5,Distance,'//
     .'Profile 6,Distance,Profile 7,Distance,Profile 8,Distance,'//
     .'Profile 9'
      do i=1,101
      write(15,"(17(F10.4,','),F10.4)") (qout(i,j),j=1,18)
      enddo
c
      stop
      end
C
C
      SUBROUTINE SETGRID(XBAR0,XBAR,YBAR0,YBAR,ZBAR0,ZBAR)
C
C Compute the polynomial transform function for the vertical coordinate
C
      PARAMETER(NDIM=20)
      DIMENSION A(NDIM,NDIM),X(NDIM,3)
      INTEGER ND(NDIM,3)
      COMMON/CTRANS/ C1(0:20,3),C2(0:20,3),C3(0:20,3),CC(20,3),PC(20,3)
      COMMON/ITRANS/ NOC(3),LU4,ITRAN(3),IDERIV(20,3)
C
      ITRAN(1) = 0
      ITRAN(2) = 0
      ITRAN(3) = 0
C
      DO IC=1,3
C
      DO N=2,NOC(IC)+1
C
      IF (IDERIV(N-1,IC).GE.0) THEN
C
      ITRAN(IC) = 1
      ND(1,IC) = 0
      IF (IC.EQ.1) THEN
      X(1,1)  = XBAR - XBAR0
      C1(1,1) = XBAR - XBAR0
      ENDIF
      IF (IC.EQ.2) THEN
      X(1,2)  = YBAR - YBAR0
      C1(1,2) = YBAR - YBAR0
      ENDIF
      IF (IC.EQ.3) THEN
      X(1,3)  = ZBAR - ZBAR0
      C1(1,3) = ZBAR - ZBAR0
      ENDIF
      ND(N,IC) = IDERIV(N-1,IC)
      IF (IC.EQ.1) CCN = CC(N-1,IC)-XBAR0
```

```
      IF (IC.EQ.2) CCN = CC(N-1,IC)-YBAR0
      IF (IC.EQ.3) CCN = CC(N-1,IC)-ZBAR0
      IF (IC.EQ.1 .AND. IDERIV(N-1,IC).EQ.0) PCN = PC(N-1,IC)-XBAR0
      IF (IC.EQ.2 .AND. IDERIV(N-1,IC).EQ.0) PCN = PC(N-1,IC)-YBAR0
      IF (IC.EQ.3 .AND. IDERIV(N-1,IC).EQ.0) PCN = PC(N-1,IC)-ZBAR0
      X(N,IC)  = CCN
      C1(N,IC) = PCN
C
      ELSE
C
      ITRAN(IC) = 2
      C1(0,IC) = 0.
      C2(0,IC) = 0.
      IF (IC.EQ.1) C1(N-1,IC) = CC(N-1,IC)-XBAR0
      IF (IC.EQ.2) C1(N-1,IC) = CC(N-1,IC)-YBAR0
      IF (IC.EQ.3) C1(N-1,IC) = CC(N-1,IC)-ZBAR0
      IF (IC.EQ.1) C2(N-1,IC) = PC(N-1,IC)-XBAR0
      IF (IC.EQ.2) C2(N-1,IC) = PC(N-1,IC)-YBAR0
      IF (IC.EQ.3) C2(N-1,IC) = PC(N-1,IC)-ZBAR0
C
      ENDIF
C
      ENDDO
      ENDDO
C
      DO IC=1,3
      IF (ITRAN(IC).EQ.1) THEN
      DO K=1,NOC(IC)+1
      DO N=1,NOC(IC)+1
      COEF = IFAC(K,ND(N,IC))
      IEXP = K-ND(N,IC)
      IF (IEXP.LT.0) A(N,K) = 0.
      IF (IEXP.EQ.0) A(N,K) = COEF
      IF (IEXP.GT.0) A(N,K) = COEF*X(N,IC)**IEXP
      END DO
      END DO
      CALL GAUSSJ(A,NOC(IC)+1,NDIM,C1(1,IC),1,1)
      ENDIF
      ENDDO
C
      DO IC=1,3
      IF (ITRAN(IC).EQ.2) THEN
      IF (IC.EQ.1) THEN
      C1(NOC(1)+1,1) = XBAR-XBAR0
      C2(NOC(1)+1,1) = XBAR-XBAR0
      ENDIF
      IF (IC.EQ.2) THEN
      C1(NOC(2)+1,2) = YBAR-YBAR0
      C2(NOC(2)+1,2) = YBAR-YBAR0
      ENDIF
      IF (IC.EQ.2) THEN
      C1(NOC(3)+1,3) = ZBAR-ZBAR0
      C2(NOC(3)+1,3) = ZBAR-ZBAR0
      ENDIF
      DO N=1,NOC(IC)+1
      C3(N,IC) = (C2(N,IC)-C2(N-1,IC))/(C1(N,IC)-C1(N-1,IC))
      END DO
      ENDIF
      ENDDO
C
      RETURN
```

```
      END
C
C
C
      FUNCTION IFAC(II,N)
C
      IFAC = 1
      DO 10 I=II-N+1,II
   10 IFAC = IFAC*I
C
      RETURN
      END
C
C
      FUNCTION G(X,IC)
C
C Vertical coordinate transform function
C
      COMMON/CTRANS/ C1(0:20,3),C2(0:20,3),C3(0:20,3),CC(20,3),PC(20,3)
      COMMON/ITRANS/ NOC(3),LU4,ITRAN(3),IDERIV(20,3)
C
      N = NOC(IC)
      IF (N.EQ.0) THEN
         G = X
         RETURN
         ENDIF
C
      IF (ITRAN(IC).EQ.1) THEN
      G = 0.
      DO I=1,NOC(IC)+1
      G = G + C1(I,IC)*X**I
      END DO
      ENDIF
C
      IF (ITRAN(IC).EQ.2) THEN
      DO I=1,N+1
      IF (X.LT.C1(I,IC)) GOTO 10
      END DO
   10 G = C2(I-1,IC) + C3(I,IC)*(X-C1(I-1,IC))
      ENDIF
C
      RETURN
      END
C
C
      FUNCTION GP(X,IC)
C
C Derivative of the vertical coordinate transform function
C
      COMMON/CTRANS/ C1(0:20,3),C2(0:20,3),C3(0:20,3),CC(20,3),PC(20,3)
      COMMON/ITRANS/ NOC(3),LU4,ITRAN(3),IDERIV(20,3)
C
      N = NOC(IC)
      IF (N.EQ.0) THEN
         GP = 1.
         RETURN
         ENDIF
C
      IF (ITRAN(IC).EQ.1) THEN
      GP = 0.
      DO I=1,NOC(IC)+1
```

```
      GP = GP + I*C1(I,IC)*X**(I-1)
      END DO
      ENDIF
C
      IF (ITRAN(IC).EQ.2) THEN
      DO I=1,N+1
      IF (X.LT.C1(I,IC)) GOTO 10
      END DO
   10 GP = C3(I,IC)
      ENDIF
C
      RETURN
      END
C
C
      FUNCTION GINV(Z,IC)
C
C Find the computational coordinate ZETA which corresponds to Z
C
      COMMON/CTRANS/ C1(0:20,3),C2(0:20,3),C3(0:20,3),CC(20,3),PC(20,3)
      COMMON/ITRANS/ NOC(3),LU4,ITRAN(3),IDERIV(20,3)
C
      GINV = Z
      N = NOC(IC)
      IF (N.EQ.0) RETURN
C
      IF (ITRAN(IC).EQ.1) THEN
      DO IT=1,10
      GF = G(GINV,IC)-Z
      IF (ABS(GF).LT.0.002) GOTO 10
      GINV = GINV - GF/GP(GINV,IC)
      END DO
   10 CONTINUE
      ENDIF
C
      IF (ITRAN(IC).EQ.2) THEN
      DO I=1,N+1
      II = I
      IF (Z.LE.C2(I,IC)) GOTO 20
      END DO
   20 GINV = C1(II-1,IC) + (Z-C2(II-1,IC))/C3(II,IC)
      ENDIF
C
      RETURN
      END
C
C
      SUBROUTINE GAUSSJ(A,N,NP,B,M,MP)
      INTEGER M,MP,N,NP,NMAX
      REAL A(NP,NP),B(NP,MP)
      PARAMETER (NMAX=50)
      INTEGER I,ICOL,IROW,J,K,L,LL,INDXC(NMAX),INDXR(NMAX),IPIV(NMAX)
      REAL BIG,DUM,PIVINV
C
      DO 11 J=1,N
   11 IPIV(J) = 0
C
      DO 22 I=1,N
      BIG = 0.
      DO 13 J=1,N
      IF (IPIV(J).NE.1) THEN
```

```
      DO 12 K=1,N
      IF (IPIV(K).EQ.0) THEN
         IF (ABS(A(J,K)).GE.BIG) THEN
            BIG = ABS(A(J,K))
            IROW = J
            ICOL = K
            ENDIF
         ELSE IF (IPIV(K).GT.1) THEN
            PAUSE 'Singular matrix in gaussj'
            ENDIF
12    ENDDO
   ENDIF
13 ENDDO
   IPIV(ICOL) = IPIV(ICOL) + 1
   IF (IROW.NE.ICOL) THEN
      DO 14 L=1,N
      DUM = A(IROW,L)
      A(IROW,L) = A(ICOL,L)
      A(ICOL,L) = DUM
14    ENDDO
      DO 15 L=1,M
      DUM = B(IROW,L)
      B(IROW,L) = B(ICOL,L)
      B(ICOL,L) = DUM
15    ENDDO
   ENDIF
   INDXR(I) = IROW
   INDXC(I) = ICOL
   IF (A(ICOL,ICOL).EQ.0.) PAUSE 'Singular matrix in gaussj'
   PIVINV = 1./A(ICOL,ICOL)
   A(ICOL,ICOL) = 1.
   DO 16 L=1,N
   A(ICOL,L) = A(ICOL,L)*PIVINV
16 ENDDO
   DO 17 L=1,M
   B(ICOL,L) = B(ICOL,L)*PIVINV
17 ENDDO
   DO 21 LL=1,N
   IF (LL.NE.ICOL) THEN
      DUM = A(LL,ICOL)
      A(LL,ICOL) = 0.
      DO 18 L=1,N
      A(LL,L) = A(LL,L) - A(ICOL,L)*DUM
18    ENDDO
      DO 19 L=1,M
      B(LL,L) = B(LL,L) - B(ICOL,L)*DUM
19    ENDDO
   ENDIF
21 ENDDO
22 ENDDO
   DO 24 L=N,1,-1
   IF (INDXR(L).NE.INDXC(L)) THEN
      DO 23 K=1,N
      DUM = A(K,INDXR(L))
      A(K,INDXR(L)) = A(K,INDXC(L))
      A(K,INDXC(L)) = DUM
23    ENDDO
   ENDIF
24 ENDDO
   RETURN
   END
```